University of Granada (Spain), June 26-28, 2006

10th European Workshop on

PHYSICAL PROCESSES IN

NATURAL WATERS

10th Europeam Workshop on
PHYSICAL PROCESSES IN NATURAL WATER

Agencia Andaluza del Agua
CONSEJERÍA DE MEDIO AMBIENTE
JUNTA DE ANDALUCIA

CAJA RURAL

Emasagra

Diputación de Granada
Red de municipios

EMASESA

Instituto del Agua

University of Granada (Spain), Junes 26-28, 2006

10th European Workshop on

PHYSICAL PROCESSES IN
NATURAL WATERS

Edited by   Francisco J. Rueda Valdivia
                Instituto Universitario del Agua
                Departamento de Ingeniería Civil
                Universidad de Granada

ORGANIZATION

Local Organizing Committee

Francisco Rueda, Chair
Victoria Amores
Inmaculada de Vicente
Enrique Moreno-Ostos
Rafael Morales Baquero
Wenceslao Martín

International Steering Committee

Adolf Stips, Joint Research Centre (Ispra, Italy)
Bertram Boehrer, UFZ-Umweltforschungszentrum (Magdeburg, Germany)
Andrew Folkard, Lancaster University (UK)
Alfred Wuest, FZL-EAWAT (Switzerland)
Nikolai Filatov, Russian Academy of Sciences (Karelia, Russia)
Arkady Terzhevik, Russian Academy of Sciences (Karelia, Russia)
Madis-Jaak Lilover, Tallinn Technical University (Estonia)
Sergei Semovski, Limnological Institute (Irkutsk , Russia)
Xavier Casamitjana , Universitat de Girona (Spain)
Lars.Bengtsson, Lund University (Sweden)
Francisco Rueda, Universidad de Granada (Spain)

Organized by
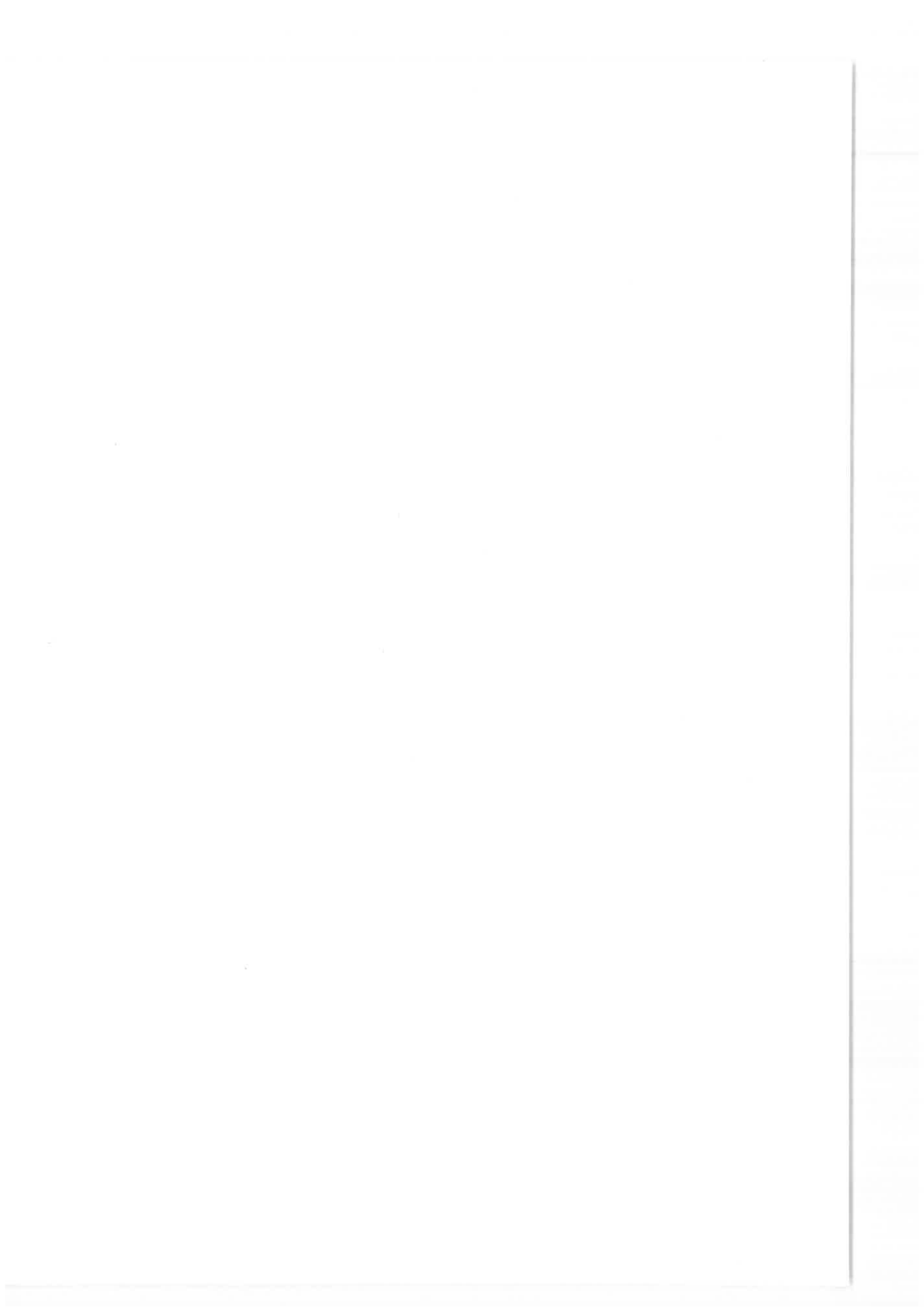
Instituto Universitario del Agua y Departamento de Ingeniería Civil. Universidad de Granada

Sponsored by

- Instituto del Agua. Agencia Andaluza del Agua. Consejería de Medio Ambiente. Junta de Andalucía
- EMASAGRA
- Fundación Caja Rural de Granada
- Diputación Provincial de Granada
- Proyecto de Excelencia RNM-772 de la Junta de Andalucía 'Patrones espaciales y temporales de acoplamiento entre hidrodinámica y plancton: impacto de perturbaciones exógenas en un embalse mesotrófico del Su· de la Península Ibérica (El Gergal, Sevilla)'

Collaborating institutions

- Fundación Empresa Universidad de Granada
- EMASESA

INDICE

DYNAMICS OF TURBULENCE IN THE METALIMNION OF A STRATIFIED LAKE

Andreas Lorke and Frank Peeters[1]

(1) Environmental Physics / Limnological Institute.
University of Konstanz. Mainaustr. 252, D-78464 Konstanz, Germany
andreas.lorke@uni-konstanz.de

The density stratification in the metalimnion of lakes supports propagating internal waves with frequencies up the local buoyancy frequency (Wüest and Lorke 2003). Laboratory experiments and numerical simulations have shown that these waves can be subject to critical reflection and breaking at the sloping boundaries of the water body and hence lead to enhanced turbulence and mixing in the bottom boundary layer at the depth of the metalimnion (e.g., Boegman et al. 2005). We present measurements of density stratification and current velocity from a steep slope at Lake Konstanz. Different techniques were applied to estimate dissipation rates of turbulent kinetic energy from the high-resolution current velocity measurements (Lorke and Wüest 2005; Wiles et al. 2005), leading to a continuous record of dissipation rates covering a period of five months. The dynamics of turbulence is discussed in relation to the meteorological forcing, basin-scale and high-frequency internal waves (Lorke et al. 2006). The unique longer-term data set further allows discussing the statistical properties of small-scale turbulence, stratification, as well as the energy transfer from the mean flow and internal waves to turbulence under natural conditions.

REFERENCES

BOEGMAN, L., G. N. IVEY, AND J. IMBERGER. 2005. The degeneration of internal waves in lakes with sloping boundaries. Limnol. Oceanogr. 50: 1620-1637.

LORKE, A., F. PEETERS, AND E. BÄUERLE. 2006. High-frequency internal waves in the littoral zone of a large lake. Limnol. Oceanogr. 51: 1935-1939.

LORKE, A., AND A. WÜEST. 2005. Application of coherent ADCP for turbulence measurements in the bottom boundary layer. J. Atmos. Oceanic Technol. 22: 1821-1828.

WILES, P. J., J. H. SIMPSON, AND T. P. RIPPETH. 2005. A novel technique for measuring mixing using Acoustic Doppler Current Profilers (ADCPs), IEEE/OES Eighth Working Conference on Current Measurement Technology.

WÜEST, A., AND A. LORKE. 2003. Small-scale hydrodynamics in lakes. Ann. Rev. Fluid Mech. 35: 373-412.

MIXING IN THE METALIMNION OF A STRATIFIED LAKE DUE TO HIGH-FREQUENCY INTERNAL WAVES GENERATED BY SHEAR IN THE SURFACE LAYER

Andrés Gómez-Giraldo, Peter S. Yeates, Jörg Imberger
and Jason P. Antenucci[1]

Presenting author: Andres Gómez-Giraldo, gomez-gi@cwr.uwa.edu.au

(1) Centre for Water Research. University of Western Australia. 35 Stirling Hwy. Crawley. 6009. WA. Australia

ABSTRACT

Data from an array of closely spaced thermistor chains was used to estimate the characteristics of high frequency internal waves observed in the crests of internal Kelvin waves in Lake Kinneret, and their vertical structure was identified from vertical velocity profiles measured with a Portable Flux Profiler. A close agreement between the characteristics of the high frequency internal waves and the results of a shear instability analysis conducted with measured density and velocity profiles, indicates that the waves were generated by shear in the surface layer induced by strong westerly winds. Some of the energy that the unstable mode gained from shear production in the surface layer was returned to the mean flow in the metalimnion due to the interaction of the Reynolds stress with the background shear, contributing to an observed metalimnetic jet. Due to the significant amplitude of the unstable mode in the metalimnion, the density profile was strained and secondary shear instabilities developed. The turbulence generated by these secondary instabilities was characterized using high-resolution simultaneous velocity and temperature microstructure profiles collected in the metalimnion using the Portable Flux Profiler. During episodes of strong high frequency internal wave activity, turbulent events with large dissipation rates and buoyancy fluxes, and overturn scales far smaller than the Ozmidov scale were observed in the metalimnion. Dissipation rates and buoyancy fluxes produced by these events were significantly higher than typical background levels, which suggests that these events may play an important role in the energy budget of lakes and in the transport of dissolved and suspended parameters between the hypolimnion and surface waters.

REFERENCES

ANTENUCCI, J. P., J. IMBERGER, AND A. SAGGIO. 2000. Seasonal evolution of the basin-scale internal wave field in a large stratified lake. Limnol. Oceanogr. 45: 1621-1638.

ANTENUCCI, J. P. AND J. IMBERGER. 2001. On internal waves near the high-frequency limit in an enclosed basin. J. Geophys. Res. 106: 22465-22474.

BOEGMAN, L., J. IMBERGER, G. N. IVEY, AND J. P. ANTENUCCI. 2003. High-frequency internal waves in large stratified lakes. Limnol. Oceanogr. 48: 895-919.

DE BAAS, A. F. AND A. G. M. DRIEDONKS. 1985. Internal gravity waves in a stably stratified boundary layer. Boundary Layer Meteorol. 31: 303-323.

GÓMEZ-GIRALDO, A., J. IMBERGER, AND J. P. ANTENUCCI. 2006. Spatial structure of the dominant basin-scale internal waves in Lake Kinneret. Limnol. Oceanogr. 51: 229-246.

HAMBLIN, P. F. 1977. Short-period internal waves in the vicinity of a river-induced shear zone in a fiord lake. J. Geophys. Res. 82: 3167-3174.

HOGG, A. M., K. B. WINTERS, AND G. N. IVEY. 2001. Linear internal waves and the control of stratified exchange flows. J. Fluid Mech. 447: 357-375.

IMBERGER, J. 1998. Flux Paths in a stratified lake: A review, p 1-17. *In* J. Imberger [ed.], Physical processes in lakes and oceans. Coastal and Estuarine Studies. V. 54. American Geophysical Union.

IMBERGER, J. AND R. HEAD. 1994. Measurement of turbulent properties in a natural system. Fundamentals and advancements in hydraulic measurements and experimentation. Am. Soc. of Civ. Eng. New York.

KUNDU, P. K., AND I. M. COHEN. 2002. Fluid Mechanics. 2nd ed. Academic Press.

MORTIMER, C. H., D. C. MCNAUGHT, AND K. M. STEWART. 1968. Short internal waves near their high-frequency limit in central Lake Michigan. Proc. 11th Conf. Great Lakes Res. II, 454-469.

SERRUYA, S. 1975. Wind, water temperature and motions in Lake Kinneret: General pattern. Verh. Int. Ver. Limnol. 19: 73-87.

STEVENS, C. L. 1999. Internal waves in a small reservoir. J. Geophys. Res. 104: 15777-15788.

SUN, C., W. D. SMYTH, AND J. N. MOUM. 1998. Dynamic instability of stratified shear flow in the upper equatorial Pacific. J. Geophys Res. 103: 10323-10337.

THORPE, S. A., J. M. KEEN, R. JIANG, AND U. LEMMIN. 1996. High-frequency internal waves in Lake Geneva. Philos. Trans. R. Soc. London. Ser A. 354: 237-257.

WIEGAND, R. C. AND E. C. CARMACK. 1986. The climatology of internal waves in a deep temperate lake. J. Geophys. Res. 91: 3951-3958.

CONVECTIVE TRANSFER GEOTHERMAL FLOWS AT THE BOTTOM OF A LAKE

Elena Roget[1] , Xavier Sánchez[1] and Iossif Lozovatsky[2, 3]

[1] Physics Department and Environmental Science Institute, University of Girona
Campus de Montilivi, edifici PII. 17071 Girona. Catalonia, Spain
[2] Environmental Fluid Dynamics Program, Arizona State University, Tempe, 85287-6106, USA
[3] P.P., Shirshov Institute of Oceanology, Russian Academy of Sciences, Moscow, 118851, Russia
elena.roget@udg.es; xavier.sanchez@udg.es; i.lozovatsky@asu.edu

INTRODUCTION

Fine-scale and microstructure measurements conducted in the regions affected by convection above the bottom of Lake Banyoles are presented and analyzed in order to better characterize fluxes and scales of convective processes. The lake, of 112 ha, is located in Catalonia, Spain, and the most important water supplies to the lake are several warm underground sources with a total inflow of about 0.5 m^3/s. Particles coming from the corrosion of the aquifer remain in suspension in the sub-basins where the underground sources are located, forming fluidized beds (Casamitjana and Roget, 1993). The fluidized beds have a vertical extension of at least several meters and present a very sharp and localized upper interface which we will refer to as the lutocline. Under stationary conditions, the particle sedimentation velocity at the lutocline level is counterbalanced by the velocity of water advection. Based on the settling velocity and the particle concentration of a sample taken from this region of the fluidized bed, the inflow can be estimated (Roget et al., 1994). Heat fluxes, which in wintertime determine general circulation of the lake (Roget et al., 1993), can also be determined measuring the temperature of the under-ground water. Therefore, microstructure measurements are not necessary to determine the geothermal fluxes into Lake Banyoles but they are needed to validate various parameterizations used to

9

determine the heat fluxes and to describe small-scale structure of the convective processes.

In this paper, we analyze data obtained at two main underground sources of the lake during 8 different field campaigns. Seven of theses campaigns were carried out at the more active underground source, which, we will refer to as basin BI according to the notation in Moreno et al. (1989). In this case, more than 250 profiles were analyzed to determine the convective heat transfer coefficient. Characteristic scales of fluctuations within the resulting convective plume are analyzed based on wavelet decomposition of microstructure temperature profiles and the energy transfer between the scales is discussed.

The 8th campaign was carried out in basin BII (see Moreno et al., 1989) where double diffusion within a diffusive layer regime was identified. Some preliminary results of this campaign were presented in PPNW9 (Sánchez and Roget, 2005); here those results are briefly reviewed and further discussion is presented.

THE LUTOCLINE

The particle settling velocity within the fluidized bed, u_{fb}, depends on the particle concentration, C, in such a way that $u_{fb}=f(C)u_s$ where u_s is the settling velocity of the particles alone (Stokes velocity) and f is a decreasing function of C. At the upper part of the fluidized bed the vertical advective velocity of the flow, u, equals u_{fb}. From the transport equation under stationary conditions, $(u - u_{sm})(dC/dz) = K_C(d^2C/dz^2)$, it is found that $d^2C/dz^2 = 0$ and therefore the lutocline is formed. The lutocline can be seen at 25.5 m depth from the turbidity profile shown in **Figure 1b**. Because the lutocline thickness is only of about 10 cm, the water column can be considered as a two-component system. In **Figure 1a,** the temperature profile corresponding to the turbidity profile of **Figure 1b** is given. The temperature drops sharply at the lutocline level and both the particle concentration and thermal interfaces are coincident However, from a gravitational point of view, the contribution of temperature and particle concentration to the density is in the opposite direction, their ratio being $R_\rho = (\gamma\Delta C)/(\alpha\Delta T)$ where γ is the particle concentration contraction coefficient, α is the thermal expansion coefficient and ΔC and ΔT are the variations of concentration and temperature across the interface. The computation of R_ρ at the lutocline gives a value of more than 100 indicating that, from a gravitational point of view, the lutocline is very stable.

10
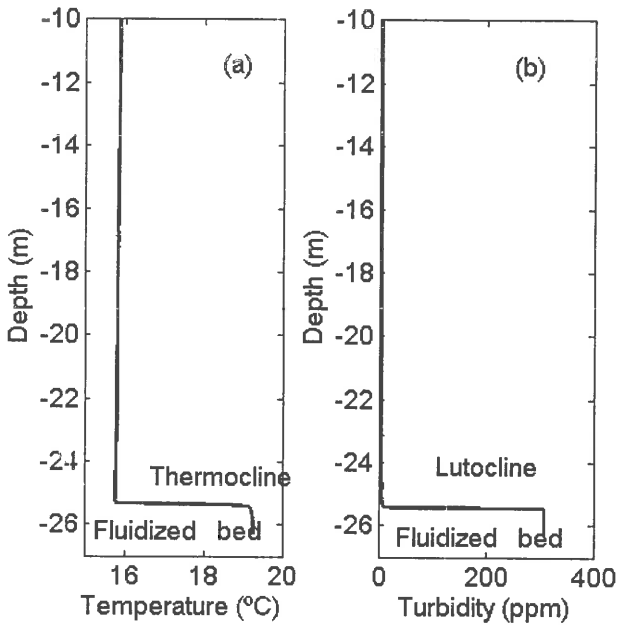
Figure 1. Characteristic (a) turbidity and (b) temperature profiles measured at source BI.

In **Figure 2,** the mean thickness of the thermal interfaces, δ, (for the 7 campaigns carried out in the basin BI) is plotted as a function of the temperature jump ΔT across the interface, along with the standard deviation calculated for the whole set of profiles obtained during each campaign. The values of ΔT vary from 1^0C (campaign 031021) to 9^0C (campaign 000303) and the interface thicknesses vary from about 10 to 30 cm. A rather good linear dependence between both variables can be observed and best fit to experimental data is found to be $\delta = 0.027\Delta T + 0.069$. The scatter around the linear trend depends on the variations of the inflow which determine the depth of the lutocline. In fact, during the two campaigns which depart more from the linear fit, the lutocline was located at about 26 m depth (campaign 200621) and 31 m depth (campaign 030916), which are extreme values for the set of studied campaigns.

11
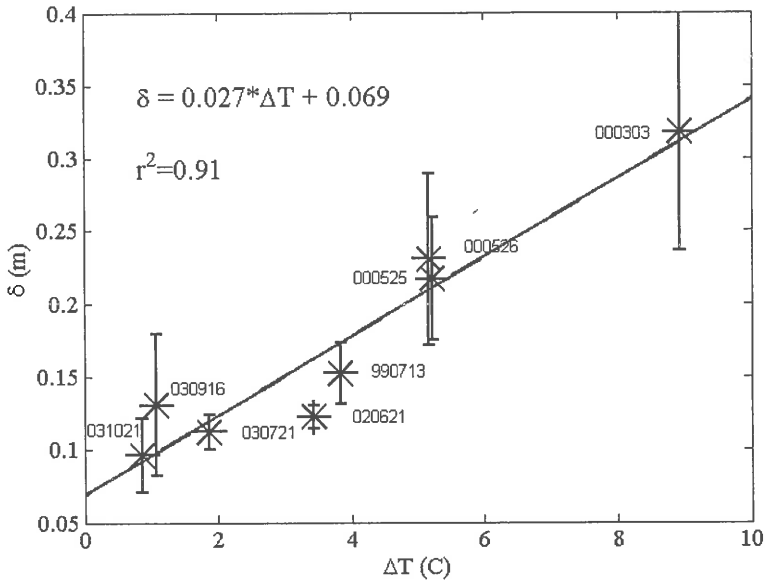
Figure 2. Thickness of the thermal interface as a function of the difference of temperature across the interface, measured during different campaigns.

CONVECTIVE FLUXES ACROSS THE LUTOCLINE

As has been shown in Figure 1, after crossing the lutocline, the underground inflow is no longer warmer than the water of the lake and we can identify an inflexion point in the temperature profile (**see Figure 3**), which results from two-component systems. Therefore, the water column can be considered as a two-component system not only with regard to the particle contents, but also from a thermal point of view.
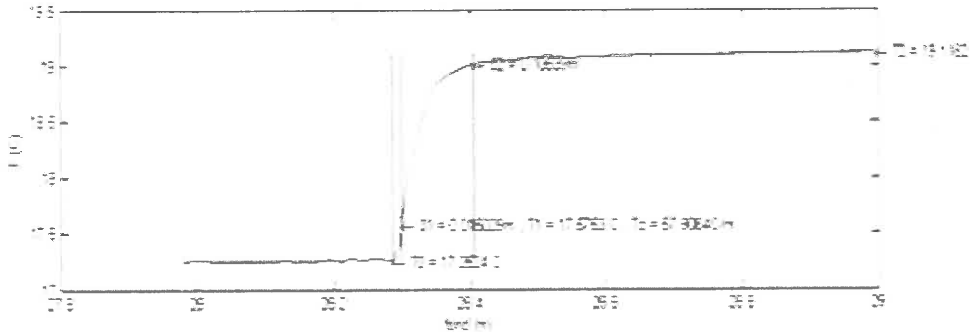
Figure 3. Detail of the thermal interface where the inflexion point, T_I, is shown.

In fact, given the high stability of the interface, the depth of the thermal inflexion point can be considered as the depth where a hypothetical plate, which is heating the lake, is located (note the small thermal disturbances above the inflection point in Figure 3).

Heat flux can therefore be related to the temperature difference which drives convection by a heat transfer coefficient. The coefficient can be thought of as the thermal resistance of a layer of fluid between the heat transfer surface and the fluid medium. Such a parameterization, known as Newton's law, has been applied to the basin BI where the thermal flux, F_T, can be determined at the diffusive inflexion point located at the core of the lutocline.

Namely, $F_T = -\kappa_T \overline{\left(\partial T / \partial z \right)}_{core}$ where κ_T is the molecular thermal diffusivity and $\overline{\left(\partial T / \partial z \right)}_{core}$ is the temperature gradient at the inflexion point (Burmesiter, 1993). The difference of temperature for Newton's law is considered between the inflexion temperature point, T_1, and the bulk temperature of the lake, T_0. **Figure 4(a)** presents the results of such computations for all the campaigns, from which a thermal coefficient of 51 W/m²K is found. Such a constant value indicates that the physical properties of the flow above the underground sources in all the campaigns are comparable.
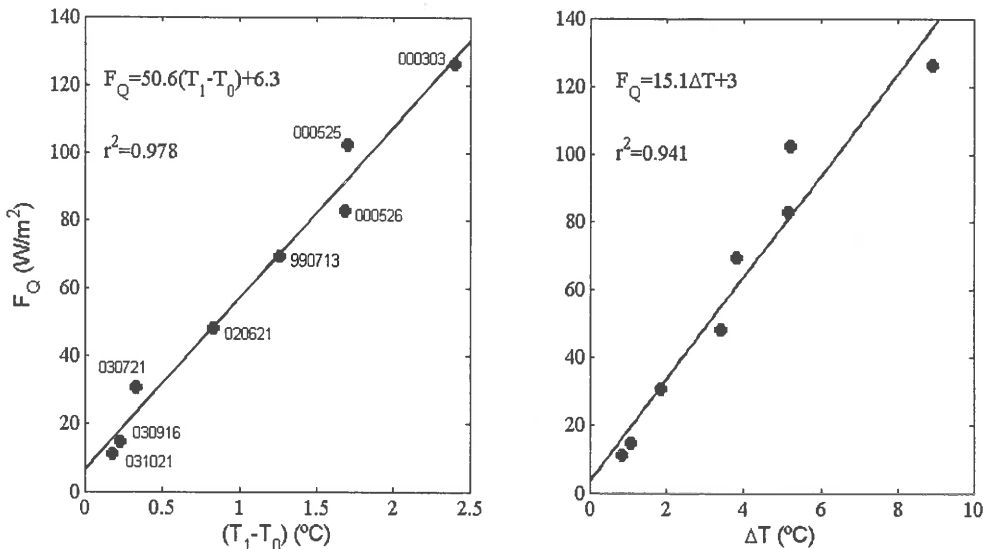
Figure 4. Newton's law for the thermal interface at the upper part of the fluidized bed when the difference of temperature considered was (a) that between the thermal inflexion point and that of the bulk water of the lake, and (b) that between the fluidized bad and the bulk water.

A similar parameterization could be suggested considering the difference of temperature between the fluidized bed ($\approx 19^\circ C$) and that of the bulk water of the lake. In this case, the correlation factor is slightly lower but the linear fit is still good (see **Figure 4(b)**). In fact, this approach is more simple as it does not require small scale measurements. For this case the thermal coefficient is found to be 15 W/m^{2}K.

Considering the mean heat flux through the underground source BI (Figure 4) and the momentum flux through source BI (Roget et al., 1994), the Morton length scale (Fisher et al. 1979) is only of a few centimeters, indicating that the advective flow is not important and a convective dynamics dominates the flow regime above the lutocline and forms a plume. The height of the plume, which depends on the background stratification, can be approximated by $h = 2.6(B_0 D)^{1/3} / N$, where B_o is the buoyancy flux ($\approx 3x10^{-8} m^2 / s^3$) and $D \approx 100\,m$ D the diameter of the source (Colomer et al., 1999), which in our case –with a background stratification corresponding to $N^2 = 4 \times 10^{-6} s^{-2}$ –gives $h = 18$ m above the lutocline, that is 14 m from the lake surface.
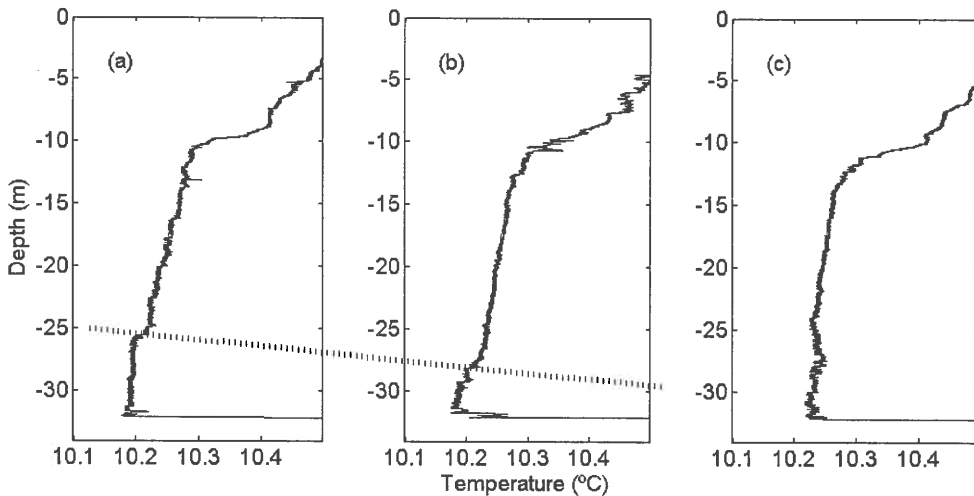
Figure 5. Characteristic temperature profiles measured during campaign 000303 at three different stations located in a radial direction within the source BI, from the most external zones (a and b) to the center (c).

Figure 5(c) shows a microthermal structure of a profile collected at the central part of basin BI. Our data however, also show a high lateral entrainment within the plume, especially at its base, as can be observed from the two profiles presented in **Figures 5(a) and 5(b).** These profiles were obtained at two different stations located

in a radial direction within BI; the profile presented in Figure 5(a) was taken at the most external station. The thickness of the intruded colder layer decreases towards the interior of the source and it is not observed at the most interior station where the profile shown in Figure 5(c) was measured. Lateral intrusions also trigger the high variability within the plume, which is only fully developed at a small central zone of the whole lutocline area.
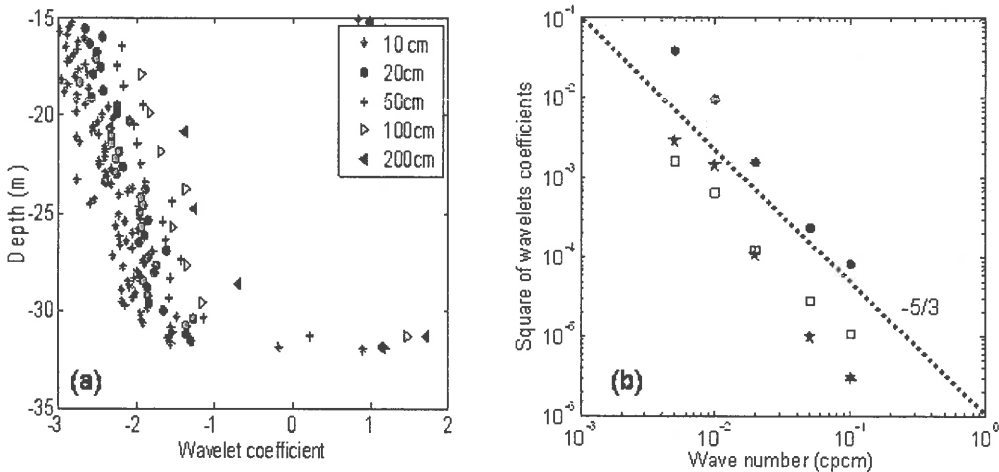
Figure 6. (a) Mean values of the coefficients of a wavelet decomposition for a series of profiles taken at the central station at the source BI during a period of 1 hour. Numbers are the real physical lengths corresponding to the scales that have been used for the decomposition utilizing db2 wavelets. (b) Squared coefficients for the wavelet decomposition for different scale (averaged within a segment of 4m) as a function of the corresponding wave number.

Characteristic overturning scales within a flow are usually based on the Thorpe scales when vertical displacements are the dominant features of the flow. In our case, however, as observed in Figure 5(c), the background stratification, although not very strong, is not monotonous. Because of this we analyze our data using wavelet decomposition of the microstructure temperature profiles obtained within the plume. In **Figure 6(a),** the mean values of the coefficients of wavelet decomposition of a series of 6 profiles recorded at the central station during a period of 1 hour are shown. Specifically, wave functions used for the decomposition were db2 and the wave scales at which data were decomposed corresponded to the wave numbers of 1/10 1/20 1/50 1/100 and 1/200 cm^{-1}. The results are presented after a smoothing procedure with a window three times exceeding each specific scale. The coefficients for all of the decomposition scales decrease from the bottom to a depth of 15 m where the inserting point of the plume was predicted. At all depths, the large-scale coefficients are larger than those for smaller scales. This suggests the existence of an active turbulent regime transferring energy from larger to smaller scales of fluctuations. In **Figure 6(b),** the square of the wavelet coefficients – which is proportional to the energy of eddies for each scale – is plotted against the corresponding wave number.

15

For each scale the coefficient is obtained after averaging of all profiles within a segment of 4 m ([19-23] *m*,[23-27] *m*, and [27-31] *m*). It appears that the dependence between the scales follows $k^{-5/3}$ in accordance with the existence of an active isotropic turbulent regime in the core of the plume transferring energy from scales of 2m (and probably above) to at least 10 cm.

CONVECTIVE FLUXES ACROSS A DOUBLE DIFFUSION STAIRCASE STRUCTURE

In this section, we discuss the microstructure temperature data recorded during another campaign in the area where the underground source BII is located and where convective layers of double diffusive origin were observed. In **Figure 7,** different parameters, which characterize the step-like structure and the turbulent processes within the convective layers, are presented.

$$\Delta T_{2-3} = 0.42 \pm 0.02$$
$$\delta_{2-3} = 0.015 \pm 0.004 \, m$$

$$F_T\big|_{2-3} = (4.2 \pm 1.3) \times 10^{-6} \, Cm/s$$

$$D_2 = 0.49 \pm 0.04$$

$$Ra_2 = (49 \pm 14) \times 10^7$$

$$\frac{dT}{ds}\bigg|_2 = 0.04 \pm 0.02$$

$$\chi_2 = (3.3 \pm 2.6) \times 10^{-7} \, C^2/s$$
$$\varepsilon_2 = (2.7 \pm 0.7) \times 10^{-9} W/kg$$
$$\overline{T'^2}\big|_2 = 7 \times 10^{-4} C^2$$
$$w'\big|_2 = 5 \times 10^{-4} m/s$$
$$L_{Th}\big|_2 = 0.135 \pm 0.039 \, m$$

$$\overline{wT}\big|_2 = (4.1 \pm 2.6) \times 10^{-6} \, Cm/s$$

$$\Delta T_{1-2} = 0.30 \pm 0.05$$
$$\delta_{1-2} = 0.021 \pm 0.013 \, m$$

$$F_T\big|_{1-2} = (2.8 \pm 1.9) \times 10^{-6} \, Cm/s$$

$$D_1 = 0.17 \pm 0.02$$

$$Ra_1 = (2 \pm 1) \times 10^7$$

$$\frac{dT}{dz}\bigg|_1 = 0.13 \pm 0.03$$

$$\chi_1 = (6 \pm 3) 10^{-7} \, C^2/s$$
$$\varepsilon_1 = (3.8 \pm 2.1) \times 10^{-9} W/kg$$
$$\overline{T'^2}\big|_1 = 10^{-4} C^2$$
$$w'\big|_1 = 3 \times 10^{-4} m/s$$
$$L_{Th}\big|_1 = 0.048 \pm 0.012 \, m$$

$$\overline{wT}\big|_1 = (2.3 \pm 1.2) \times 10^{-6} \, Cm/s$$

$$F_T\big|_{0-1} = (4.2 \pm 1.2) \times 10^{-6} \, Cm/s$$
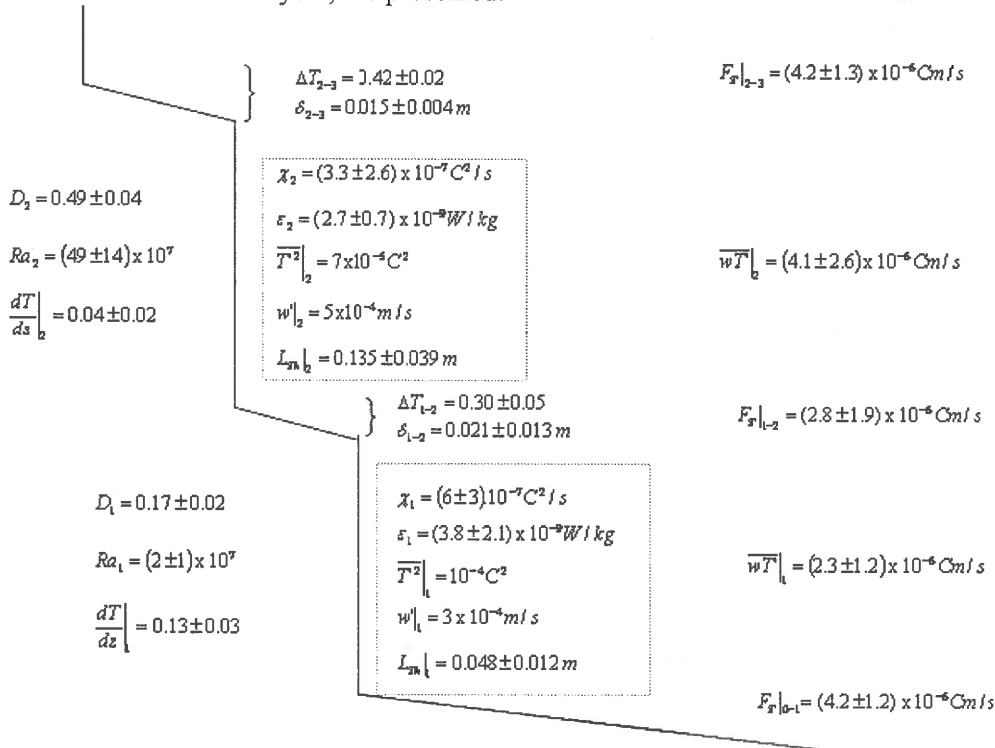
Figure 7. Mean characteristics of the double diffusive staircase structure in the basin BII.

Turbulent fluxes could be determined within the convective layers after integrating the temperature spectra (see **Figure 8**). To estimate the temperature dissipation we can use the balance equation: $-2\overline{wT'}(\partial \overline{T}/\partial z) - \chi = 0$, where $\partial \overline{T}/\partial z$ is the background temperature gradient obtained by the Thorpe sorting procedure

16

(Thorpe, 1977). Alternatively, heat flux can be computed at the diffusive interfaces. Both procedures give, within the error margin, the same result, showing a stationary mean thermal flux of 3.5×10^{-6} C m/s. This corresponds to a mean heat flux of ~ 15 W/m^2, which is within the range of values of thermal fluxes estimated in other studies for the mean flow in this basin and to the results presented here for basin BI.
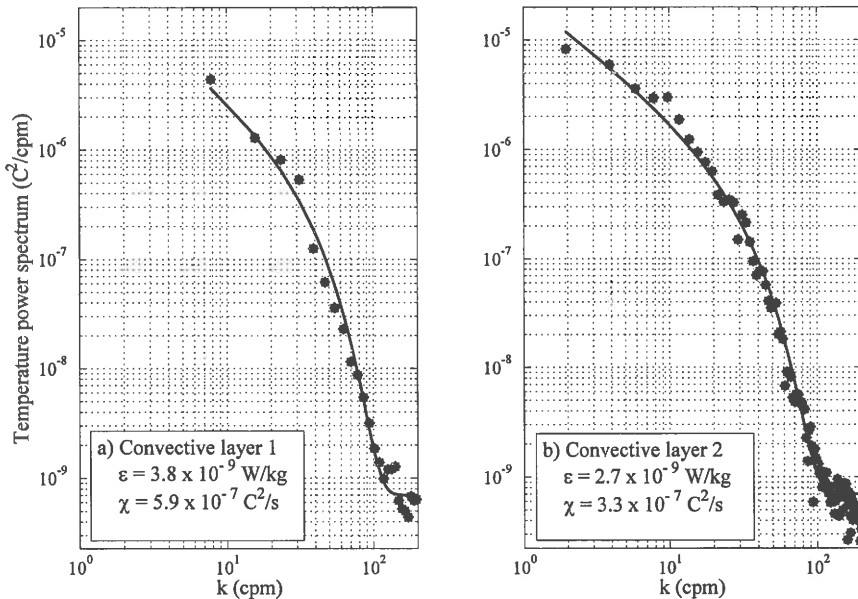
Figure 8. Thermal spectra of turbulent fluctuations within the two convective layers.

We compared fluxes estimated based on our data with the results suggested by various theoretical models and found out substantial inconsistency with some of them (i.e. Marmorino and Caldwell, 1976). However, our experimental data support Fernando's model (Fernando, 1989 a,b) for the low stability regime for double convection, where $\delta_s \approx \delta_T$ and which is in accordance with the 4/3 heat flux law for free convection. Our flux calculations also agree with the regime IV_1 of the model proposed by Grossmann and Lohse for Rayleigh-Bénard convection (Grossmann and Lohse, 2000), which keeps the 4/3 power law ($Nu \propto Ra^{1/3}$), and with the regime IV_U, which presents the dependence $Nu \propto Ra^{1/2}$. This may suggest that the double diffusion layers observed in the lake were subjected to a transitional regime between IV_1 and IV_U. In both regimes, the dissipation of the kinetic energy and of the thermal fluctuations are larger in the bulk of the convective layers than at their boundary layers, but the thickness of the thermal boundary layer for each convective cell is

17

larger than the salinity one depending on the sub-regime. It is possible that in our case both interfaces are equal. In fact such correspondence between the interfaces may be the reason why Rayleigh-Bénard's model of Kelly, which considers the shear layer thicker than the thermal one, departs from our data. Finally, if the 4/3 law is applied, we find that the parameterization proposed by Taylor (1988) for low density ratios is in good agreement with our data.

In this case, characteristic vertical displacements within convective layers could be estimated based on the Thorpe scales. It was found that the Thorpe scales are about 0.3 times the layer thickness. This result is in agreement with parameterization of Lozovatsky and Fernando (2002) who suggested that the ratio of Thorpe scale to the patch size (in this case the convective layer) depends on the buoyancy Reynolds number. For $R_b > 150$, such a parameterization gives the asymptotic value for the normalized Thorpe scale of 0.3, which is in agreement with our data (R_b in our case is around 1000).
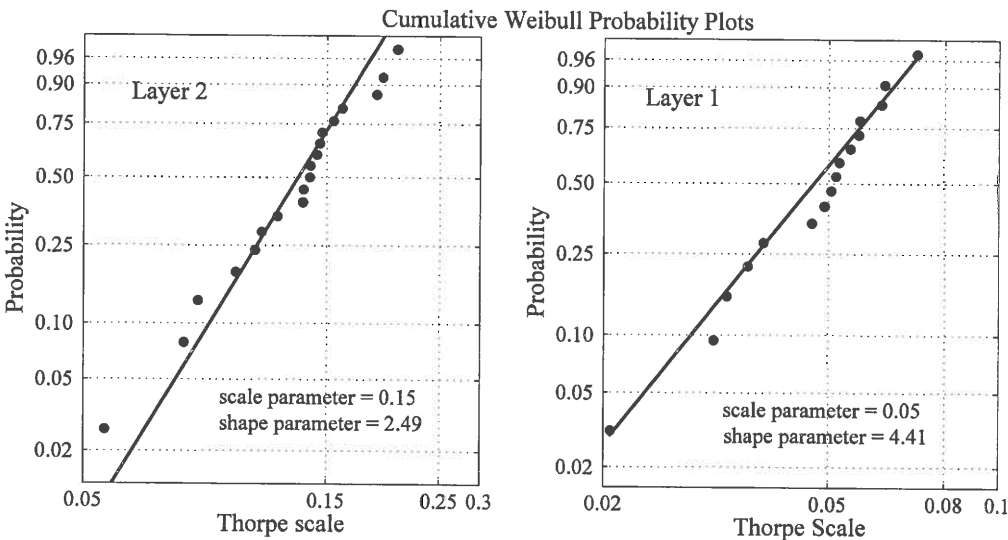
Figure 9. Cumulative distribution function of the Thorpe scales for both convective layers.

Finally, in **Figure 9**, the cumulative distribution function of the Thorpe scales for both layers are presented showing a good fit to the Weibull distribution as has been suggested by Roget et al. (in press) for active turbulence. Note that, the scale parameter is in fact in accordance with the mean Thorpe scale for each layer and the shape parameter is higher in layer 2, showing the highest asymmetry of the distribution.

18

SUMMARY

For source BI a parameterization of the thermal fluxes based on Newton's law is proposed for the cases where the lutocline ranges between 26 and 31 m depth. When the temperature difference between the fluidized bed and the bulk water of the lake is considered as the parameter which drives convection, then the heat coefficient is found to be equal to 14 W/m^2.

For the double diffusive regime which was identified in basin BII, the experimental fluxes are found to be in accordance with Fernando's law for a low stability regime and with the Grossmann-Lohse model for Rayleigh-Bénard convection and more precisely with their regime IV.

Based on wavelet analysis, the -5/3 regime of isotropic turbulence has been detected in the core of the thermal plume in basin BI at least for the scales ranging between 2 m and 10 cm at all heights of the plume.

For the double diffusive regime in basin BII the asymptotic value $L_{Th}/h_p = 0.3$ (where h_p is the thickness of the convective layer) predicted by Lozovatsky and Fernando's parameterization of the dependence of the normalized Thorpe scale on the buoyancy Reynolds number (Lozovatsky and Fernando, 2002) was found.

REFERENCES

BURMEISTER, L.C. 1993. *Convective heat transfer*, John Wiley & Sons..

CASAMITJANA, X., AND E. ROGET. 1993. Resuspension of sediment by focused groundwater in lake Banyoles. Limnol. Oceanogr., 38(3): 643-656.

COLOMER, J., BOUBNOV, B. AND H.J.S. FERNANDO. 2000. Turbulent Convection from an Isolated Sources Dynamics of Atmospheres and Oceans, 30, 125-148.

FERNANDO, H. J. S. (1989a), Buoyancy transfer across a diffusive interface, *J. Fluid Mech., 209*, 1-34.

FERNANDO, H. J. S. (1989b), Oceanographic Implications of Laboratory Experiments on Diffusive Interfaces, *J. Phys. Oceanogr., 19*, 1707-1715.

. 1979. *Mixing in inland and coastal waters.* Academ FISHER, H.B., LIST, E.J., KOH, R.C.Y., IMBERGER, J., AND N.H. BROOKS ic.

GROSSMANn, S. AND D. LOHSE (2000), Scaling in thermal convection: A unifying theory, *J.Fluid Mech,. 407*, 27-56.

KELLEY, D.E. (1990), Fluxes through diffusive staircases : A new formulation, *J. Geophys. Res., 95*, 3365-3371.

LOZOVATSKY, I. AND H.J.S: FERNANDO, HJS. 2002. Mixing on a Shallow Shelf of the Black Sea, Journal of Physical Oceanography, 32, 945-. 956.

MARMORINO, G.O., AND D.R. CALDWELL (1976), Heat and salt transport through a diffusive thermohaline staircase. *Deep-Sea Res.,* 23,59-67.

MORENO, R., AND E. GARCÍA. 1989. A new bathymetric map based on echo-sounding and morphometrical characterization of the Lake of Banyoles. Hydrobiologia 185: 83-90.

ROGET, E., CASAMITJANA, X., AND J.E. LLEBOT. 1994. Calculation of the flow into a lake from underground springs using sedimentation rates. Neth. J. Aquat. Ecol. 28: 135-141.

ROGET, E., COLOMER, J., CASAMITJANA, X. AND J. E. LLEBOT. 1993. Bottom currents induced by baroclinic forcing in lake Banyoles. Aquatic Science. 55(3):206-227.

SÁNCHEZ, X., AND E. ROGET. 2005. Convective dynamics above the upper interface of a warm and salty fluidized bed located at the bottom of a lake. 9th Workshop on Physical Processes in Natura Waters. Proceedings. Ed. Folkrad, A. and Jones, I. Geography department, Landcaster University, p: 273-279

TAYLOR, J. (1988), The fluxes across a diffusive interface at low values of the density ratio. *Deep-Sea Res.,,* 35(4):555-567.

THORPE, S.A. 1977. Turbulence and mixing in a Scottish loch. *Philos. Trans. Roy. Soc. London, A286,* 125-181.

TURBULENT AND MIXING IN STRONGLY STRATIFIED LAYERS OF NATURAL FLOWS

H.J.S. Fernando and I. Lozovatsky
Environmental Fluid Dynamics Program
Department of Mechanical and Aerospace Engineering
Arizona State University, Tempe, AZ 85287-9809

Stable stratification and turbulence are ubiquitous features in environmental flows, and the interaction between them leads to a myriad of phenomena such as internal waves, instabilities and turbulent mixing. In predictive environmental flow models, many of these small-scale phenomena cannot be resolved and hence need to be parameterized by using knowledge gained via fundamental studies. Recent attempts to understand and parameterize small-scale processes in stable layers using theoretical, laboratory, numerical and field studies will be described in this presentation, paying particular attention to mixing across sheared and shear-free interfaces and turbulent convective flows bounded by inversion layers. The application of results, in combination with meso-scale numerical modeling, to predict oceanic and atmospheric flows will also be discussed.

BENTHIC EXCITATION BY INTERNAL SOLITARY WAVES

Peter J. Diamessis[1] and Larry G. Redekopp[2]

[1]School of Civil and Environmental Engineering, Cornell University, Ithaca, NY 14853, U.S.A.
[2]Dept.of Aerospace and Mechanical Engineering, University of Southern California, Los Angeles, CA 90089-1191, U.S.A.

INTRODUCTION

A renewed interest has emerged over the last decade in the dynamics of internal solitary waves (ISW) due to their unquestionable operational and environmental importance. One aspect of ISW dynamics which still remains relatively unexplored is the associated benthic stimulation, which may drive significant dissipation and mixing of large-scale input of energy by the winds and internal tides in the ocean and lakes (Egbert and Ray 2000, Boegman et al. 2003) and resuspension of bottom-resident particulate matter (Bogucki et al. 1997, Bogucki et al. 2005).

A new mechanism based on the phenomenon of global instability has been proposed for ISW-induced benthic excitation (Bogucki et al. 1997, Bogucki et al. 2005). Diamessis and Redekopp 2006a (hereafter referred to as DR06a) employed Direct Numerical Simulations (DNS) to prove the existence of global instability in the footprint of ISW of depression and elevation. Global instability is a locally absolute instability of the separation bubble created by the decelerating velocity field of the wave in a frame of reference moving with the ISW phase speed. The instability occurs spontaneously (i.e. no external or upstream excitation is required), whenever the wave Reynolds number, $Re_W = C_0 H / \nu$ (C_0 and H are the ISW phase speed and waveguide depth, respectively) amplitude, α_0 (given by the maximum isopycnal display-cement normalized by H) exceed supercritical values. The separation bubble is fragmented into coherent vortices which are quasi-periodically ejected high into the water column at a frequency characteristic of the instability. The critical wave amplitude decreases with increasing Re_W and is in the range [0.2,0.3] for oceanically and limnologically relevant Reynolds numbers of $O(10^6\text{-}10^7)$ suggesting that global instability is indeed operational in stratified natural water bodies (DR06a).

DR06a observed that, in contrast to lower Re_W simulations, at $Re_W = 10^5$, the vortex shedding was arrested after eight to ten vortex ejection events and the separation

23

bubble was annihilated. Although the bubble appeared to reconstruct itself, the runs could not be extended further in time due to the re-entry of shed vortices into the streamwise periodic domain. In addition, the wave forcing used by DR06a was fixed in time, and thus, interactions with the bed could not modify the energetic content of the ISW. Therefore two questions may be posed, which this note aims to answer: Is the destabilization of the bed only a transient feature of wave evolution? Can global instability induce levels of bottom dissipation so high that further propagation of the ISW is impeded?
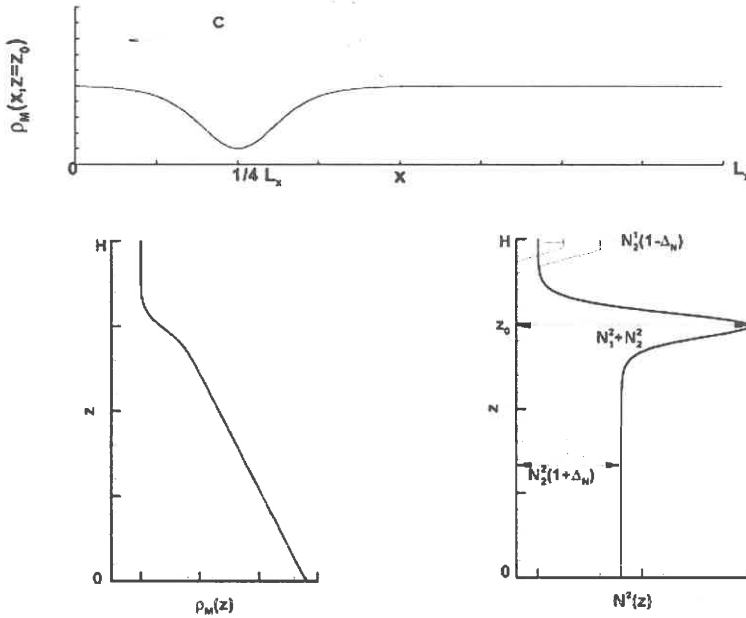
Figure 1. Schematic of solitary internal wave of depression propagating with phase velocity C through a structured thermocline. Top panel: Typical solitary wave isopycnal displacement at the center of the seasonal thermocline. Bottom panel: Vertical profiles of mean density (left) and Brunt-Vaisala frequency(right).

The base flow considered here is similar to that of DR06a. This study focuses on a weakly non-linear mode-1 ISW of depression propagating with phase velocity C along a wave guide containing a structured thermocline in a region of uniform finite depth H (figure 1) with no ambient current. In contrast to DR06a, the center of the wave is now positioned at $x/L_x=1/4$, where L_x is the length of the domain, and the domain dimensions are $20HxH$. The numerical method used is a spectral multidomain penalty method scheme (DR06a). This investigation considers simulations at $Re_W=2x10^4$ and 10^5 with corresponding critical wave amplitudes, $\alpha_{0cr}=0.46$ and 0.38, respectively. To illustrate the effect of amplitude criticality on the questions posed in the introduction, a weakly and strongly supercritical value are chosen for each Re_W

(i.e. α_0=0.48 and 0.6 and α_0=0.4 and 0.48 for Re_W=2x10^4 and 10^5, respectively). The grid resolutions and spectral filters used are identical to those described in DR06a.

RESULTS

A visualization of the formation and subsequent destabilization of separation bubble induced by a mode-1 ISW of depression at Re_W=10^5 and α_0=0.48 is shown in figure 2. The regular separation bubble in the footprint of the ISW spontaneously undergoes a global instability and emits instability waves both upstream and downstream (figure 2a).

(a) tC_0/H=3.25

(c) tC_0/H=8

(b) tC_0/H=5

(d) tC_0/H=11
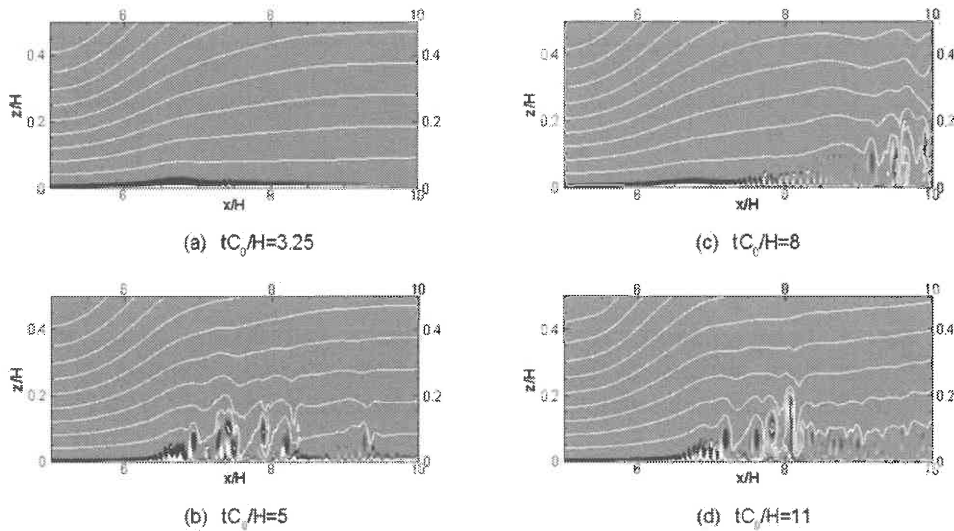
Figure 2. Visualization of global instability of mode-1 solitary wave of depression at α_0=0.48.
The wave propagates from right to left. Total density isopycnals (white line contours) vs.
perturbation vorticity (grayscale contours, with dark being positive). Shown is the bottom half of the water column with the wave center located at x/H=5.

The bubble is rapidly fragmented into coherent vortices which are shed high into the water column (as high a 20% of the total depth above bottom). In contrast to the Re_W=2x10^4 simulations, characterized by quasi-periodic vortex shedding up to tC_0/H=20 (Diamessis and Redekopp 2006b, hereafter referred to as DR06b), at Re_w=10^5, the bubble is annihilated at tC_0/H=7 but proceeds to reconstruct itself as it continues to emit instability waves downstream (figure 2c). At time tC_0/H=9, a new string of vortex ejections is initiated which lasts until tC_0/H=12 (figure 2d), when the separation bubble once again is annihilated. Vortex shedding then resumes at tC_0/H=13.5. Thus, benthic excitation by ISW at high Re_W is characterized by an alternation between periods of excitation, where a finite number of vortices are

ejected into the water column, and periods of calm, where the separation bubble rebuilds itself.
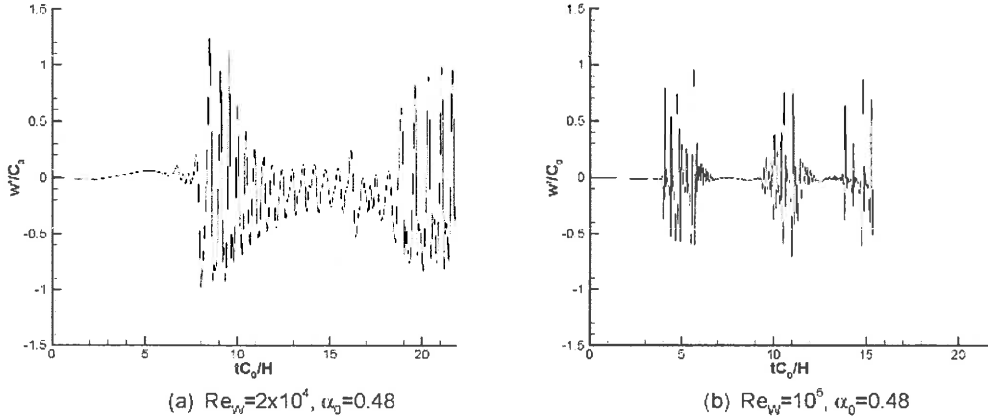
Figure 3. Timeseries at different Re_W and for α_0=0.48 of vertical perturbation velocities sampled near the bed at $z/H=0.075$ and at a fixed streamwise location corresponding to the rear end of the separation bubble upon the onset of global instability.

Figure 3 shows timeseries of vertical perturbation velocities w' (where the ISW velocity has been subtracted from the instantaneous value) sampled at a fixed streamwise location on the rear end of the separation bubble and at $z/H=0.075$ above the bed. The timeseries for $Re_W=2\times10^4$ and $\alpha_0=0.48$ exhibit two distinct frequencies (figure 3a): A high frequency, characteristic of the global instability and the rate of vortex shedding, and a low-frequency envelope, associated with the oscillatory translation of the separation bubble in the streamwise direction (DR06b). The timeseries exhibits a distinct symmetry around $tC_0/H=15$ indicating that the separation bubble translation is a form of amplitude modulation on the high frequency signal of the global instability. In contrast, $Re_W=10^5$ timeseries at the same wave amplitude (figure 3b) are characterized by periods of near-zero w' values alternating with bursts of intensely fluctuating velocities commensurate with the ISW phase speed. Note that corresponding timeseries at $Re_w=10^5$ but with $\alpha_0=0.4$ demonstrate an equally intermittent character where the benthic eruptions have a similar duration and equal number of vortex ejections but are spaced further apart in time (see DR06b).

26
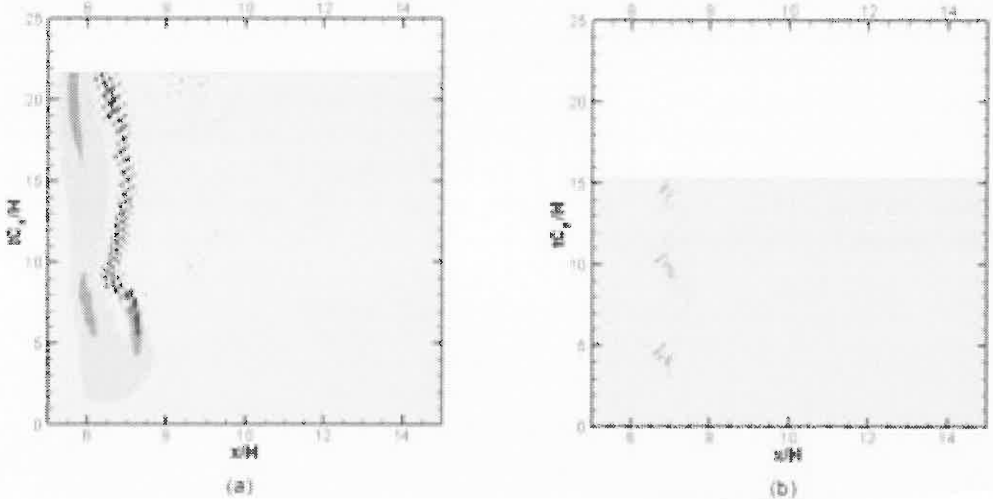
Figure 4. Streamwise position versus time contour maps of perturbation bottom shear stress, $\tau_0 = \mu \partial u' / \partial z \big|_{z=0}$ at $\alpha_0 = 0.48$. (a): $Re_w = 2 \times 10^4$ and (b) $Re_w = 10^5$.

Spacetime contour plots of the bottom perturbation shear stress $\tau_0 = \mu \partial u' / \partial z \big|_{z=0}$ are shown in figure 4 for the moving reference frame and the same values of Re_W and α_0 considered in figure 3. The temporal resolution of these plots corresponds to the separation between adjacent minima and maxima in figure 3. The oscillatory streamwise translation of the separation bubble and its high shear stress tail end is immediately visible for the $Re_w = 2 \times 10^4$ case in figure 4a. This quasi-periodic translation clearly breaks down at $Re_w = 10^5$, where the contour plot consists of temporally localized regions of enhanced τ_0 associated with benthic eruptions (figure 4b). The maximum shear stress magnitude in the destabilized separation bubble scales with the thickness of the boundary layer, i.e. as $Re_W^{-1/2}$ (DR06a), as indicated by a value greater by a factor of two in the $Re_w = 2 \times 10^4$ data. However, the relative increase of τ_0 along the wave footprint, from the laminar section of the ISW-induced boundary layer to its destabilized part, is enhanced with increasing Re_W. A $O(10^2)$ increase is observed in the $Re_W = 10^5$ data which may be even greater for higher Reynolds numbers. A comparable enhancement of the spatiotemporal variability of τ_0 with increasing Re_W is also observed.

The integral of τ_0 over the entire length of the domain provides the value of drag force per unit width, F_D. Application of conservation of momentum over a control volume delineating the entire computational domain, which is periodic in the streamwise direction and impermeable in the vertical, shows that the only external transfer of momentum is done through the action of the drag force at the bottom boundary. Thus, $F_D C_0$ is the rate of work of the drag force, which serves as a two-dimensional

27

estimate of the rate of viscous dissipation of kinetic energy of the wave due to its interaction with the bed. Figure 5 shows the integral of $F_D C_0$ from time t=0 up to a given time t=T, i.e. the total energy lost due to the wave-bed interaction, normalized by the total kinetic energy of the temporally invariant wave, which is computed using the strict Boussinesq approximation (DR06b). For across-shelf propagation of over roughly 15 to 20 waveguide depths, the ISW dissipates 3.5% to 4.5% of its total kinetic energy, which would correspond to an energy loss of near-negligible consequences for a time-dependent ISW.
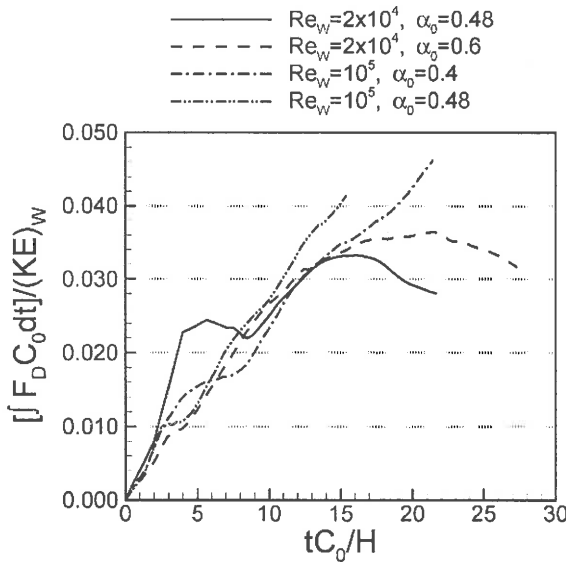
Figure 5. Timeseries of time-integrated dissipation rate, i.e. energy lost by the wave to work done by bottom drag, as a function of Re_W and α_0.

DISCUSSION

Based on the results presented above, the annihilation of the separation bubble at high Re_W, presumably caused by the break-down of its oscillatory streamwise translation due to the enhanced non-linearity of the global instability, is only temporary. The destabilization of the ISW-induced boundary layer is a quasi-permanent feature of the evolution of an internal solution as it propagates across the shelf. The benthic excitation by an ISW may be best described as a set of intermittent benthic eruptions, where vortex shedding is accompanied by elevated bottom shear stress and near-bed vertical velocities suggesting a potential mechanism for significant episodic particulate resuspension. Finally, the results of figure 5 imply that for a typical continental shelf of $O(100m)$ depth and $O(10km)$ length an ISW may dissipate roughly 20% of its initial energy through bottom interactions. Thus, despite

28

its instantaneously weaker levels of benthic dissipation, the global-instability of the ISW-induced boundary layer is a phenomenon that persists over the entire ISW evolution and thus may have a time-integrated effect, in contrast to wave-breaking.

REFERENCES

BOEGMAN, L., J. IMBERGER, G. N. IVEY, AND J. P. ANTENUCCI. High-frequency internal waves in large stratified lakes. Limnol.Oceanogr., **48** (2), 895–919, 2003.

BOGUCKI, D., T. DICKEY, AND L. G. REDEKOPP, Sediment resuspension and mixing by resonantly generated internal solitary waves. J. Phys. Oceanogr., **27**, 1181–1196, 1997.

BOGUCKI, D., L. G. REDEKOPP, AND J. BARTH. Internal solitary waves in the Coastal Mixing and Optics Experiment 1996: Multimodal structure and resuspension. J. Geophys. Res., **110** (C2), Art. No. C02,024, 2005.

DIAMESSIS, P. J., AND L. G. REDEKOPP. Numerical investigation of solitary internal wave-induced global instability in shallow water benthic boundary layers, J. Phys. Oceanogr., **36** (5), 784–812, 2006a (Referred to as DR06a in the text)

DIAMESSIS, P. J., AND L. G. REDEKOPP. Benthic Excitation by Internal Solitary Waves: Temporal Intermittency, Bottom Dissipation and Implications for Field Measurements. (In preparation for J. Geophys. Res., Oceans), 2006b (Referred to as DR06ab in the text).

EGBERT, G. D., AND R. D. RAY. Significant dissipation of tidal energy in the deep ocean inferred from satellite altimeter data.Nature, **405**, 775–778, 2000.

DIRECT MEASUREMENTS OF WIND INDUCED INTERNAL MOTIONS IN LAKES USING AN ACOUSTIC DOPPLER CURRENT PROFILER

John Simpson, Phil Wiles, Michael Ridgill and Matthew Lewis
University of Wales Bangor,
School of Ocean Sciences,
Menai Bridge, Anglesey, UK, LL59 5AB

INTRODUCTION

The internal flow field induced by surface wind stress in small lakes is weak with peak current speeds of only a few centimeters per second. Such flows are generally not well resolved by conventional current meters and, in the past, internal motions have mostly been deduced from the vertical display-cement of isotherms from temperature chain measurements. (e.g. Munnich et al. 1992) The advent of broad band acoustic Doppler current profilers (ADCPs) allows measurements of velocity on a 1m scale with a single ping uncertainty $\sim$ 1cm/s. By averaging over $\sim$100s or more the noise can be reduced to <1mm/s. In this contribution, we report on a series of measurements with a bottom mounted ADCP in two lakes which demonstrate the ability of such instruments to determine the response of lakes to wind forcing over a wide range of frequencies and to identify the principal modes of oscillation.

METHODOLOGY

A broad band ADCP operating at 1.2 MHz (RDI Workhorse) was deployed in a pyramid frame alongside a chain of thermistor sensors in water depth of ~20m.
The ADCP was configured to have a bin size of Δz=1m and to ping at 0.5 Hz with an average velocity recorded every 4 seconds with an r.m.s. noise of 2.1cm/s. By averaging for 5 minutes (20 minutes) this uncertainty is reduced to 2.4(1.2) mm/s.

RESULTS

Deployment 1: Rostherne Mere, Cheshire England
This small lake(fig.1) has a mean depth of 15m and a length of 1.1km. It is somewhat sheltered from the wind by surrounding woodland and rising ground.
Wind speed and direction data were available from the nearby Manchester airport.
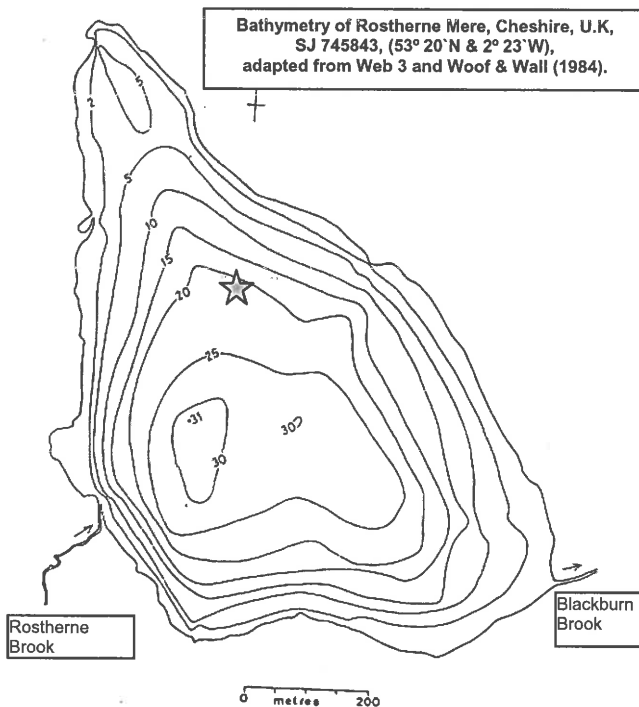
Figure 1. Rostherne Mere

The lake experiences strong seasonal stratification with a surface to bottom temperature difference of $\Delta T \sim 7°C$ evident at the start (17/5/05) of our observations increasing to $\Delta T \sim 12°C$ to at the finish on 10/8/05. The temperature time series from the thermistor chain (fig.2) illustrates the evolution of the temperature structure and shows that, during the observation period, the bottom temperature increases by only a fraction of a degree from its value of 6°C in May. The clear implication is that there is only limited mixing through the metalimnion suggesting generally weak flows in the interior of the basin. Following bursts of wind stress, however, significant oscillations of the isotherms are apparent with vertical displacements of ~2m. for example during periods A-C in fig.2.

32
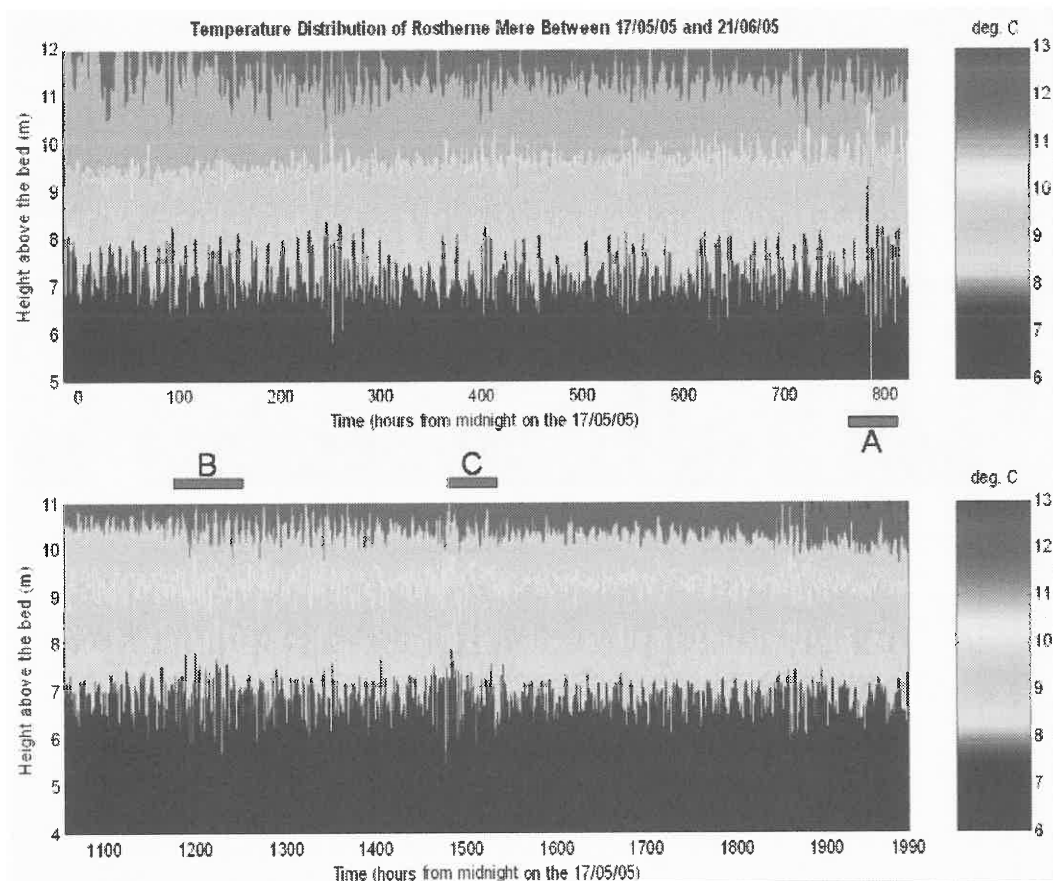
Figure 2. Time series of temperature from thermistor chain in Rostheren Mere 17/5 -10/8/05. Pink bars indicate periods following intensified wind forcing

An expanded plot of the isotherms in parallel with the N-S component of velocity and the wind field during period A (fig3) shows regular oscillations of the flow matching the vertical movements of the isotherms with a dominant period of ~1.5 hours most evident in the lower layers. Peak velocities reached 3cm/s following a strong pulse of wind stress (W~11m/s) from the west around t=783 hours. After this impulsive excitation, the lake continued to "ring" for ~40 hours although the wind speed reduced to much lower levels.

33
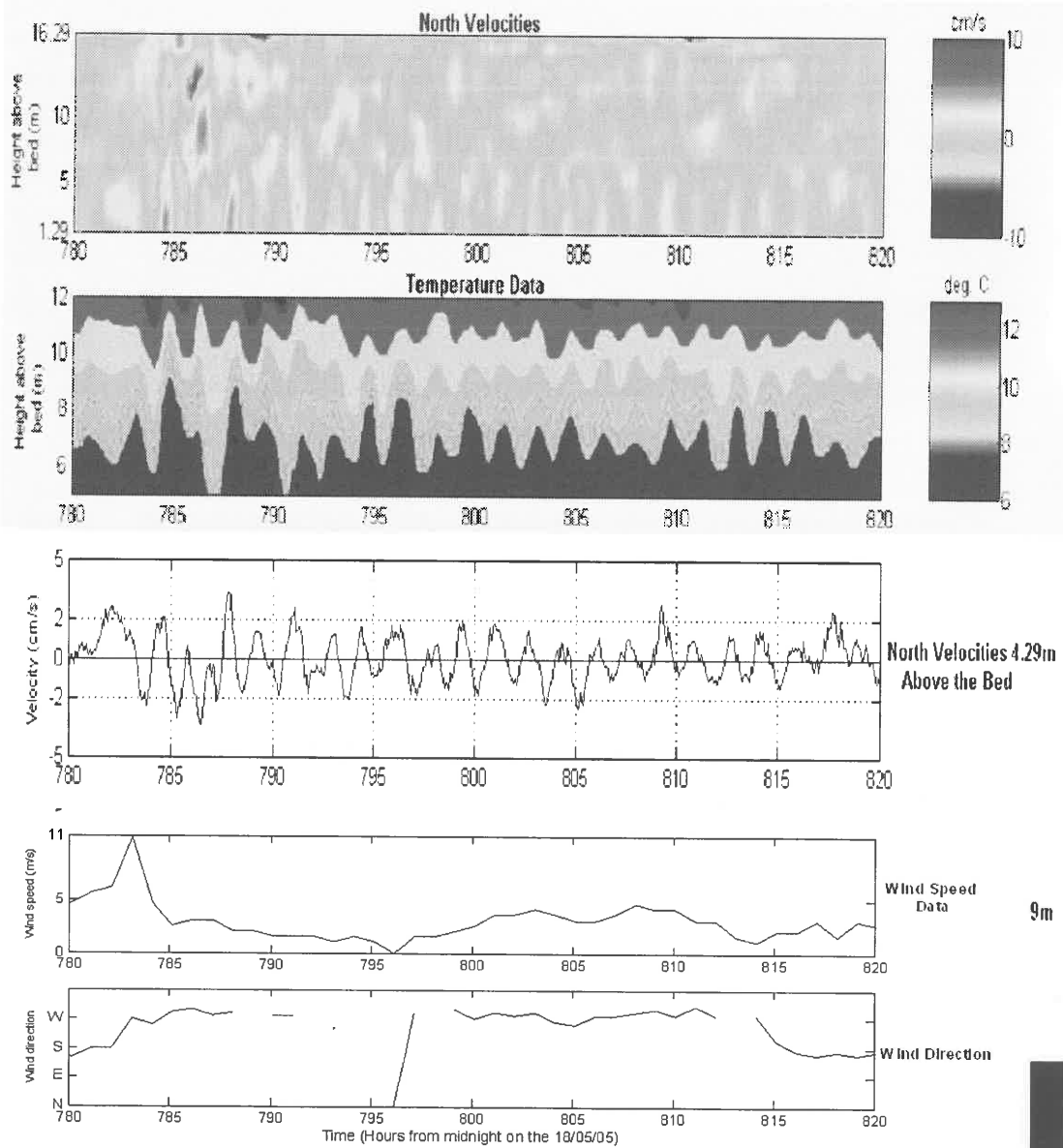
Figure 3. Evolution of temperature and N-S velocity in Rostheren Mere during period A following wind pulse.

Power spectrum analysis of the data from this period indicates a pronounced peak at a frequency of close to 0.6 c/h. Here we show in fig.4 the cross-spectrum between the velocity at each level and that in the lowest bin. This analysis improves the signal to noise ratio and allows determination of the coherence and phase of the two time

34

series. The phase at f=0.6 c/h is seen to switch by ~180 degrees between the upper and lower halves of the water column with significant coherence in upper and lower layers. This behavior is consistent with the flow being that of the first vertical mode. Comparing the frequency with the phase speed calculated from the density structure using Klinck (1999) for the lowest vertical mode suggests an effective length scale of ~ 450m which would indicate that this is the v1h1 mode.

A second mode of oscillation is also apparent in the cross-spectrum at f~0.24c/h. The phase distribution here indicates that this is the second vertical mode (v2h1) with the mid-water flow 180 degrees out of phase with the near bottom and near surface layers. There are also indications of a weaker oscillation with first mode structure at a frequency of ~0.9c/h.

Figure 4. Cross-pectrum of velocity at each depth with velocity in the lowest bin for period A in Rostherne Mere.

Later in the observation period, as stratification intensified, the frequency of oscillation was also observed to increase somewhat. This increase in frequency can be seen in the cross-spectral plot of a second wind stress event (fig 5) which shows the same two principal modes v1h1 and v2h1 with frequencies of 0.65 and 0.26 c/h respectively and confirms the phase structure observed in fig.4.

North Cross-Spectra for period: 1180 to 1240 hrs after 15/5/2005 2400.
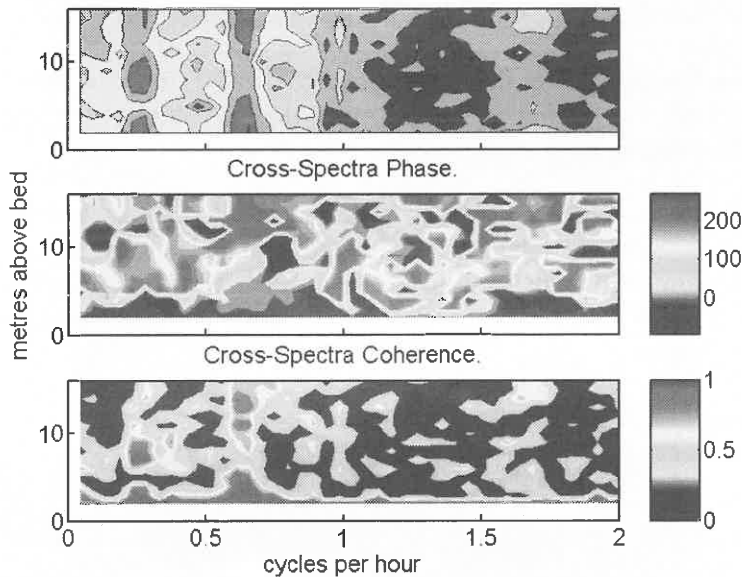
Figure 5. As for figure 4 but data for period B

DEPLOYMENT 2: LYN TEGID (BALA) NORTHWALES

In a recent study, the same combination of bottom-mounted ADCP and thermistor chain has been deployed in a larger lake, Llyn Tegid (Lake Bala) in North Wales. This lake is ~5km long and has an approximately rectangular shape with a maximum depth of 40m. (fig 6). There is rather little sheltering from wind stress by the surrounding topography and the lake experiences full exposure to winds from the south-west which blow along the its axis. To optimize coverage of the water column, the ADCP, which has a range of ~20m, was deployed close to the 20m contour at a position approximately one third of the way from the SW end of the lake (fig. 6). Vertical bin size was set to 0.5m. and data was recorded from single pings at intervals of $\Delta t=1.3s$ The temperature chain was located close by the ADCP with the 8 sensors spaced to cover the water column with a maximum spacing of 2.5m.

36

SW———————+————NE

GLASLLYN
LLANUWLLYN
20   30   40   30   20
C
B
A
BALA
R.DEE

0   1   2
SCALE;KILOMETRES   DEPTH IN METRES
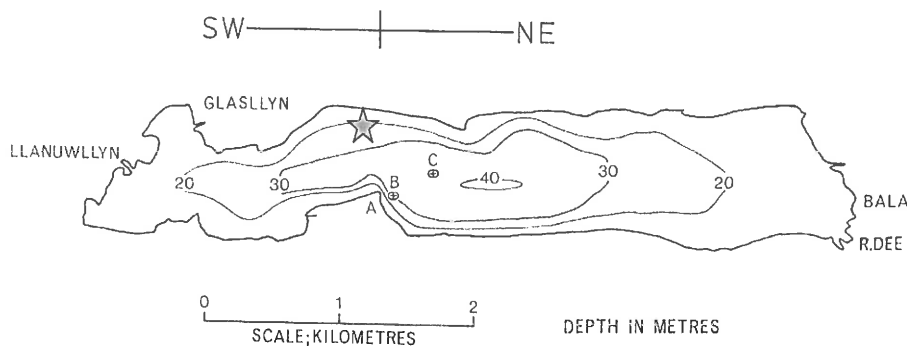
Figure 6 Llyn Tegid bathymetry

Observations commenced on 17/5/06 (day 129) when thermal stratification was already established with $\Delta T \sim 4°C$ (fig.7) although a strong wind event (W~ 10m/s) on days 136-137 increased mixing and reduced the temperature difference to $\Delta T \sim$ 2°C. During the subsequent calm period, the surface layer warmed again.
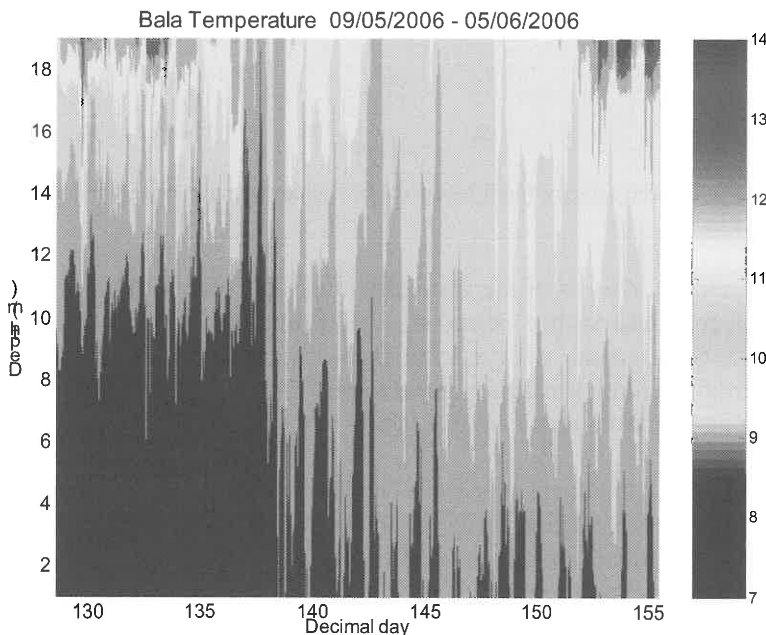
Figure 7. Temperature (°C) evolution in Llyn Tegid May-June 2006

The wind stress event produced a significant response in the currents as indicated in fig.7 which shows the axial velocity component, averaged over 30 minutes (r.m.s.

37

uncertainty ~1mm/s), together with the wind. Initially the wind induced a near surface flow in the same direction as the wind with a speed of up to 10cm/s but later the flow reversed and a flow against the wind developed and extended down to ~20m. This sequence was repeated following a second, weaker wind pulse on day 142.
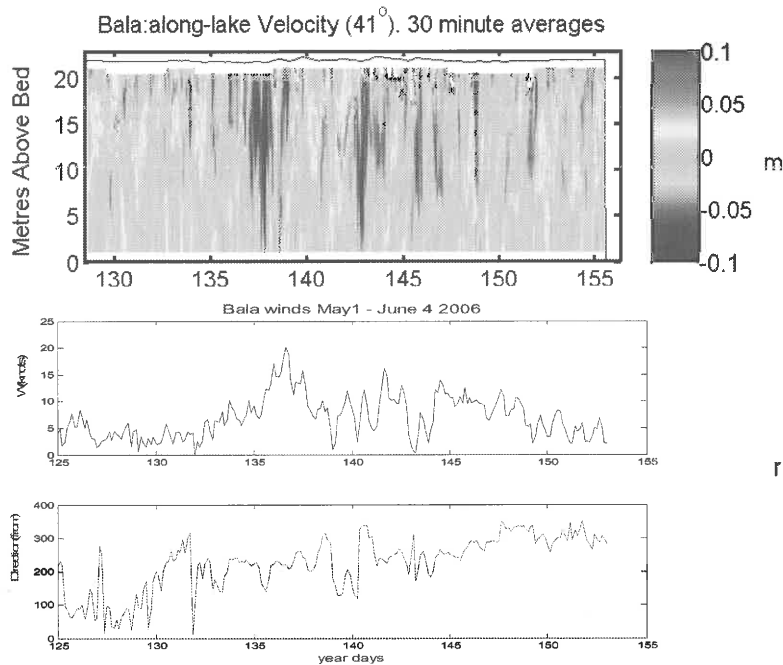
Figure 8. Llyn Tegid axial velocity (m/s) based on 30 minute averages with wind speed (knots) and direction

Power spectrum analysis of the vertically integrated flow (fig 9a) indicates a first mode external response with a period of ~ 12.8 minutes (f=4.68 c/h) in agreement with parallel measurements with a level recorder at the SW end of the lake. The principal internal oscillation is again found to be a first vertical mode (v1h1) as can be seen from the co-spectrum analysis of fig.9b.

The increase in coherence in a band centered on f = 0.046c/h (period 22.2 h) is accompanied by a well-defined change in phase by 180° at a depth of ~12m. Calculation of the normal mode eigenvalues (Klinck 1999) gives the phase velocity of the lowest mode c = 0.096 and 0.113 m/s at the beginning and end of the recording period which correspond to a periods of 23.1h and 19.7h respectively.

Bala:Spectra of along-lake (41°) velocity(depth mean)

External 1st mode
T~12 minutes

$m^2 s^{-2}/cph$

cycles per hour
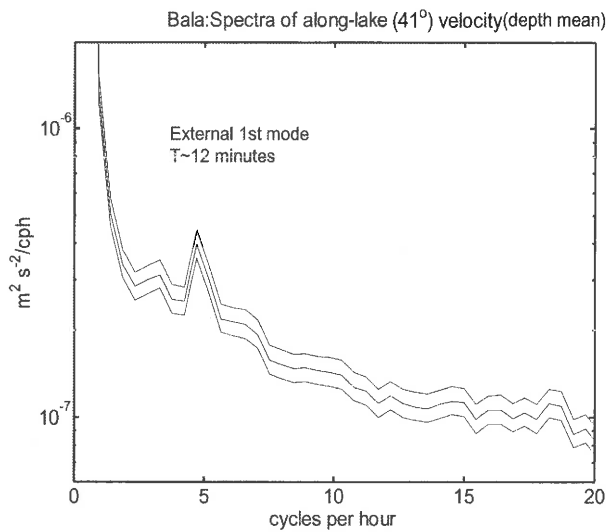
Figure 9(a). Spectrum of vertically integrated velocity based on 30s averages showing the external mode with a period of 12.8 minutes

v1h1

Along-Lake velocity Cross-Spectra.

Along-Lake velocity Spectra Phase.

metres above bed

Along-Lake velocity Spectra Coherence.

cycles per hour
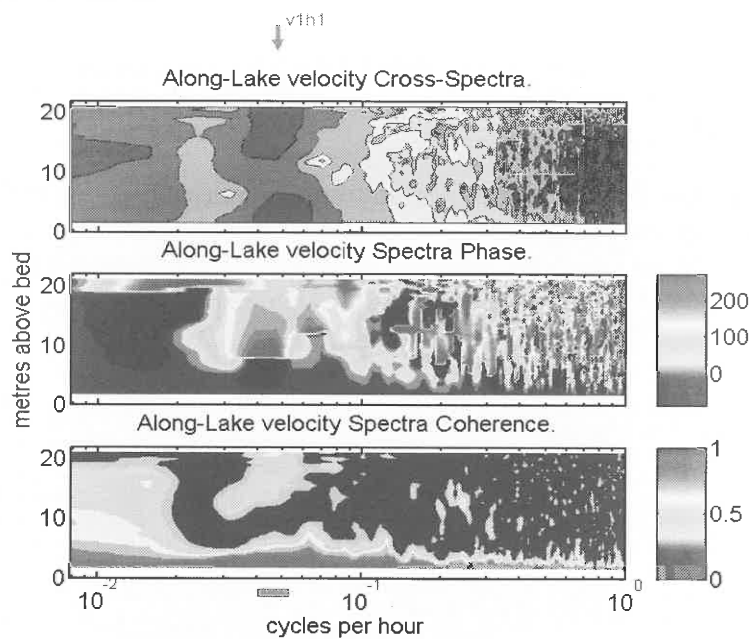
Figure 9(b). Co-spectrum based on 30 min average velocities. Note first vertical mode with two layers moving in antiphase at f = 0.046c/h

39

CONCLUSIONS

Using a standard broad band ADCP, we have been able to resolve the principal components of the wind-induced flow in two lakes of relatively small scale where the velocities associated with internal oscillations are ~1cm/s and not accessible to rotor and propeller current meters. In the smaller lake (Rostherne Mere) we found first and second vertical modes of oscillation predominating after periods of significant wind stress forcing. The structure of these modes (v1h1 and v2h1) was confirmed by determination of the phase and coherence through cross-spectral analysis. In the larger lake, Llyn Tegid , we also identified a much longer v1h1 mode with a period of 22.2h which is long enough to require consideration of the influence of the earth's rotation which will tend to give the waves a progressive component. The external seiche mode could also be observed in this case. Spectral analysis of the depth mean velocities indicated a period of 12.8 minutes.

In Rostherne Mere, the observations were of sufficient endurance (84 days) for us to observe the decrease of the periods of oscillation as stratification intensified. The periods of oscillation were consistent with estimates of the phase velocity based on a normal modes analysis (Klinck 1999).

REFERENCES

KLINCK J.(1999). Matlab Script for solution of normal modes problem (see Gill Atmosphere-Ocean Dynamics, 1982, p160)

MUNNICH M., WUEST A., AND IMBODEN D.M. (1992). Observations of the second vertical mode of the internal seiche in an alpine lake. Limnology and Oceanography 37(8), 1705-1719.

IMPLICATIONS FOR RAY WAVES IN ISLAND COPPER MINE LAKE, B.C., CANADA

Bertram Boehrer[1] and Craig Stevens[2]

(1) UFZ-Umweltforschungszentrum Leipzig-Halle GmbH, Magdeburg, Germany.
Bertram.Boehrer@ufz.de
(2)New Zealand National Institute for Water and Atmospheric Research, PO Box 14-901 Kilbirnie, Wellington New Zealand. C.stevens@niwa.co.nz

ABSTRACT

Observational proof for ray waves, or internal wave beams, as the more recent oceanographic literature tends to call the observed phenomenon, has long been searched for in the aquatic environment. Though through mathematical approach and laboratory experiments these waves are well understood, the observational proof has eluded us until recently. We only know implications for such waves from measurements of the internal tide created on critical continental slopes. However, the special basin shape of Island Copper mine pit-lake and its sharp salinity stratification make it an ideal place to look for ray waves. The first-mode internal seiche oscillates the deep water vertically over the regular bench structure of the side-walls at a distinct frequency. Theoretical considerations show the disturbances result in internal wave beams traversing the stratified water body at a known angle. Steep side-walls prevent the ray beams from being trapped in the beach zone. Instead the reflection at the extremely strong pycnocline creates a vertical interference pattern. We numerically derive the vertical length scale of this interference, which will be shown to agree well with the repeated turbulence pattern discovered underneath the pycnocline.

REFERENCES

STEVENS C., T.S.R. FISHER, AND G.A. LAWRENCE (2005), Turbulent layering beneath the pycnocline in an strongly stratified pit lake. *Limnol. Oceanogr. 50*, 197-206.

BOEHRER, B., AND C. STEVENS (2005), Ray waves in a pit lake, *Geophys. Res. Lett., 32*, L24608, doi:10.1029/2005GL024678.

SEASONAL EVOLUTION OF THE INTERNAL WAVE FIELD IN TWO MEDITERRANEAN RESERVOIRS

Javier Vidal [1] Xavier Casamitjana[1] and Francisco Rueda[2]

(1) Institut de Medi Ambient. Universitat de Girona. Campus de Montilivi. 17071 Girona – Spain
(2) Instituto del Agua & Civil Engineering Department – Universidad de Granada. C/Ramón y Cajal, 4. 18071 Granada – SPAIN

INTRODUCTION

The seasonal evolution of the internal wave field as a response to forcing winds of two Mediterranean reservoirs (Sau and Beznar) was analyzed. The internal seiches and their vertical structure are determined to a large extent by stratification patterns and wind forcing with a marked 24 h periodicity. In these conditions the reservoirs behave as forced, damped oscillators. They respond to these periodic winds with water currents with the same period. However, when stratification allows that one of the natural periods of the reservoir is close to the forcing periods, the energy transfer from the wind is higher and resonance occurs. In Sau reservoir the forcing winds have periods of 12 h and 24 h and the resonance response to these forcing winds for the period analyzed are the modes V2 and V3 respectively. In Beznar reservoir the response to the forcing wind with a 24 h period are the higher modes V3, V4 and V5; however, when the 24 h wind pattern is disrupted, modes V1 and V2 are excited.

Although there are many studies on internal seiches in lakes, very few are focused on learning how the internal seiches are excited as a response to forcing winds. We present an example of two Mediterranean reservoirs in which the modal response to forcing winds is analyzed. Both are elongated reservoirs with the wind blowing along their main axis with a marked 24 h periodicity, usually land-sea breezes blowing along the inundated river valleys. The reservoirs develop thick metalimnetic layers in response to warming heat fluxes through the free surface, which occur during the spring and summer periods together with the river inflow action and selective withdrawal processes through deep outlet structures. Internal seiches can be divided into different categories depending on the nodal points (ViHj) where i and j are the number of vertical and horizontal nodes. The most commonly observed, the V1H1, has one vertical and one horizontal nodal point. In this paper we will only consider vertical modes and use the notation Vi, omitting Hj. The wind forcing combined with stratification, allows the reservoir to present higher vertical mode response that goes until V3 for Sau reservoir and until V5 for Beznar reservoir.
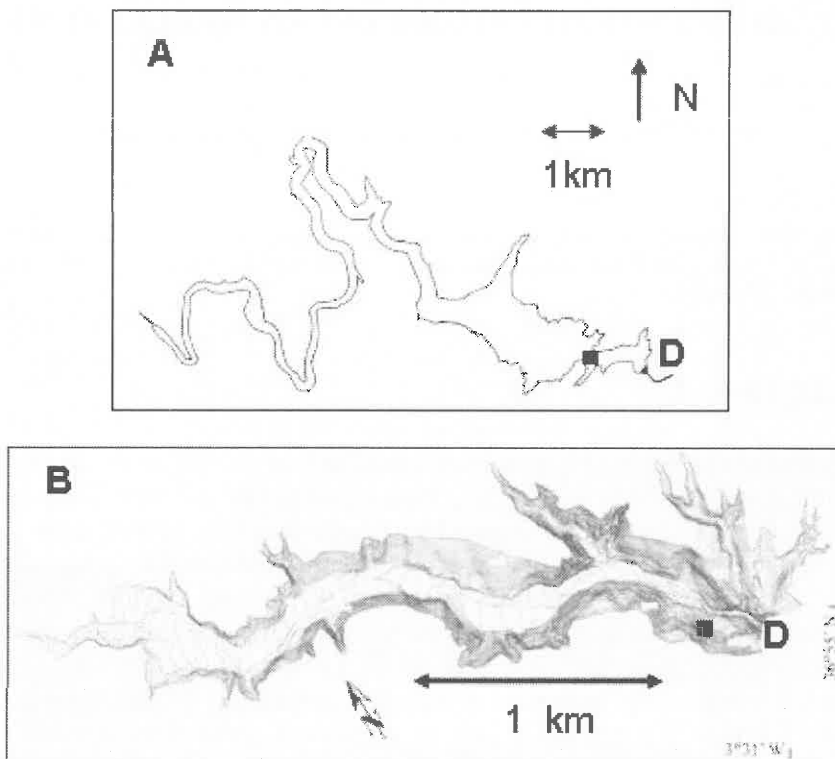
Figure 1. (A)- Schematic maps of Sau Reservoir and (B) Beznar reservoir. The filled black squares shows the position of the measuring station and D is the position of the dam.

SAU RESERVOIR

Sau is a canyon shaped reservoir 18225 km long situated in the central part of the river Ter, which is 200 km long with its source in the Pyrenees in NE Spain (Armengol et al. 1999). The length of the widest part of the reservoir is 3600 m. The maximum width is 1300 m and the maximum depth is ~ 60 m (Fig. 1). We present the results of different surveys carried out in the period July 2004 to October 2004, during the stratification period of the reservoir. An acoustic Doppler current meter (ADCP) and a thermistor string (TS) were deployed at station 1 (Fig. 1). The ADCP was active from 20 July 2004 to 4 August 2004 and from 7 to 9 September, and the TS from 8 July to 5 September and from 9 September to 9 October. Wind data was obtained from a meteorological station located near the lake. The ADCP (RDI 600 kHz Workhorse Sentinel) was deployed at the water surface with the beams facing downwards. Between 8 July and 5 September the available temperature records

obtained with the TS corresponded to the following depths: 3 m, 4 m, 5 m, 6 m, 7 m, 8 m, 9 m, 11 m, 15 m, 16 m, and 17 m. Between 9 September and 9 October the depths of the sensors were changed to fit the new stratification better. At that time, the available temperature records were obtained at 8 m, 10 m, 11 m, 12 m, 13 m, 14 m, 16 m, 20 m, 21 m, 22 m, 27.5 m, 30 m, 32.5 m and 37.5 m depth.

Figure 2A shows the evolution of the wind power spectral density for the 2004 stratified period. The spectral analysis was carried out every two days over a period of ten days. The wind velocity was projected following the main axis of the reservoir. A dominant 24 h period can be clearly seen as well as a secondary sub-daily mode of 12 h. While the 24 h periodicity could be anticipated given the daily wind pattern, the 12 h periodicity is not so obvious, although changes in the wind direction are probably the cause of this sub-daily wind pattern. Fig. 2B shows the power spectral density evolution of the potential energy per unit of volume calculated as:

$$PE\ (t) = \frac{1}{2} N^2(t)\ \rho_0(t)\ \xi^2(t)$$

where

$$N^2 = -\frac{g}{\rho_0} \frac{d\rho}{dz}$$

is the buoyancy frequency, g is the gravity acceleration, ρ is the water density and ξ is the displacement of a selected isotherm. In Fig. 2B it can also be seen that the 12 h and 24 h periods dominate the internal wave field.
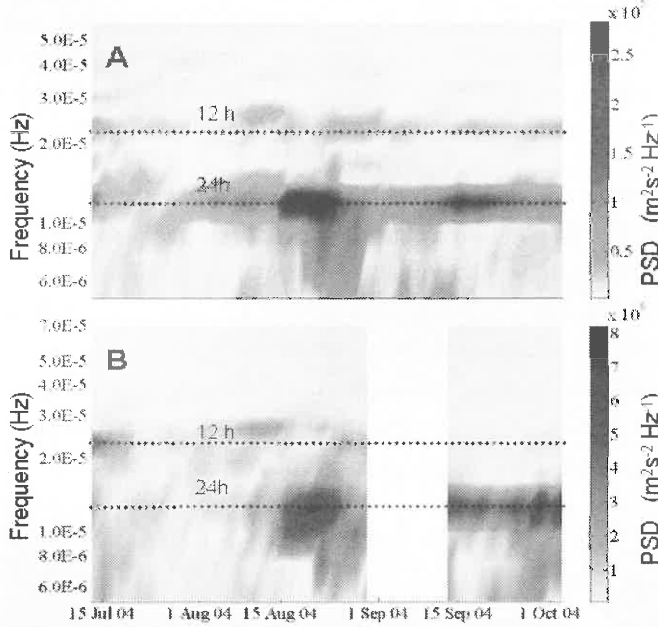
Figure 2. (A) Evolution of the power spectra density for the projected wind velocity along the main axis in Sau reservoir and (B) evolution of the potential energy per unit of volume (see the text).

Sau reservoir responds to the periodic winds of 12 h and 24 h patterns with water movements the same periods (Fig. 2B). However, when stratification allows that one of the natural periods of the reservoir is close to the forcing periods, the energy transfer from the wind is higher because of the resonance. As the numerical model ELCOM shows (Hodges et al. 2000), this happens in mid-July for mode V2 and at the end of August and the end of September for mode V3. There are other periods (see for example the beginning of August in Fig. 2B) with strong wind forcing of ~24 h, and less at ~12 h, which do not cause a marked response in the reservoir. In these periods the model calculations show that the oscillation modes of the reservoir are far from 12 h and 24 h.

BEZNAR RESERVOIR

Beznar reservoir is located in southern Spain (Fig. 1B), draining a watershed that occupies the south-western portion of Sierra Nevada. The river reach that is inundated by the reservoir is approximately 4400 m long and rather steep, with a maximum depth of ~ 100 m. In 2005, in order to characterize the evolution of the internal wave field on seasonal time scales, a thermistor chain was deployed and left in the reservoir

46

from Julian day 95 to 217. Thermistors were deployed at the surface, and at 2 m, 4 m, 6 m, 10 m, 15 m, 20 m, 25 m, 30 m, 50 m and 80 m depth. Meteorological and hydrological records were provided by government agencies.
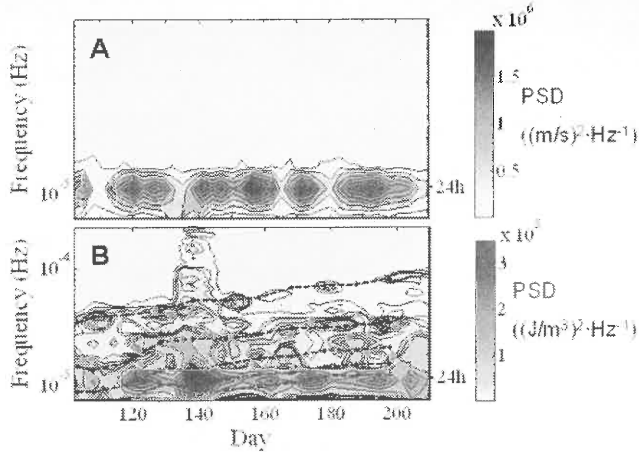
Figure 3. (A) Evolution of the power spectra density for wind velocity in Beznar reservoir and (B) evolution of the potential energy per unit of volume (see the text). Dashed lines show the predicted evolution of modes V1 (upper line) to V5 (lower line).

Fig. 3A, as in Fig. 2 for Sau reservoir, shows the evolution of the wind power spectral density for the 2005 stratified period for Beznar reservoir. In addition, a dominant period of 24 hours can be clearly seen. In Fig. 3B, the power spectral density evolution of the potential energy per unit of volume shows a strong response coinciding with the 24 h period. The dashed lines show the evolution of modes V1 to V5 calculated using the 2D model described in Vidal et al. (2005). Examples of the predicted modes for day 198 are shown in Fig. 4. At the beginning of the stratified period, by day 120 (see Fig. 3), the 24 h wind excites a V3 mode which also has a period of 24 h and therefore resonance enhances the reservoir's response. By day 160 the stratification changes and the modal response of the reservoir also changes to V4. Finally, by day 190 the modal response is V5. Furthermore, by days 110, 130, 165, 180 the 24 h wind pattern is disrupted and V1 and V2 are excited.
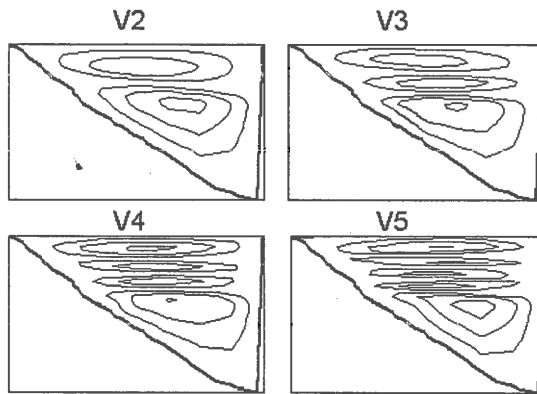
Figure 4. Streamlines predicted by the model, corresponding to modes V2, V3, V4 and V5 for Beznar reservoir

REFERENCES

ARMENGOL, J., AND OTHERS. 1999. Longitudinal processes in canyon type reservoir: The case of Sau (N.E. Spain), p. 313–345. *In* J. G. Tundisi and M. Straskraba [eds.], Theoretical reservoir ecology and its applications. Backhuys Publishers.

HODGES, B. R., J. IMBERGER, A. SAGGIO, AND K. WINTERS. 2000. Modeling basin-scale internal waves in a stratified lake. Limnol. Oceanogr. **45:** 1603–1620.

VIDAL, J.,X. CASAMITJANA, J. COLOMER AND T. SERRA, 2005. The internal wave field in Sau reservoir: Observation and modeling of a third vertical mode. Limnol. Oceanogr., **50:** 1326–1333

NON LINEAR INTERNAL SEICHES DEGENERATION IN A IN A DEEP SUB-ALPINE LAKE

Yannis Cuypers [1], Brigitte Vinçon-Leite [1],
Michel Poulin [2], Bruno Tassin [1]

(1) CEREVE, Centre d'Enseignement et de Recherche Eau-Ville-Environnement, ENPC, 6 av. Blaise Pascal, Champs sur Marne, F-77455, France (cuypers@cereve.enpc.fr)
(2) CIG, Centre d'informatique géologique, ENSMP, 5 rue Saint Honoré, Fontainebleau, F-77305, France

Internal waves are ubiquitous in lakes and oceans. From the physical point of view, comprehension and modelling of internal waves dynamics is a fascinating challenge. From the ecological point of view, internal waves forcing is an important factor in ecosystems equilibrium, mainly because turbulent mixing resulting of non linear internal waves dynamics can sustain biogeochemical turbulent fluxes (Macintyre *et al* 1999). Therefore, characterization of the internal wave weather is a crucial step in lacustrine ecosystem understanding and modelling.

Recently nonlinear processes leading to high frequency waves generation have focused much attention, leading to theoretical, experimental and field studies (Horn *et al* 2001, Horn *et al* 2002, Boegman 2005). Such high frequency waves are indeed expected to play an important role in mixing processes because they can shoal at lake boundaries leading to important turbulent mixing in the metalimnion, a region where direct forcing by the wind is usually inefficient for turbulence generation

The work presented in this article focuses on the modelling and understanding of nonlinear degeneration mechanism of basin scale wave, and their implication for lake Bourget ecology.

I STUDY SITE AND DATA COLLECTING

Lake Bourget (Fig.1) is long (18 km), narrow (2.5 km) and deep (maximum depth 145 m, mean depth 80 m). East and West lake slopes orthogonal to the lake main axis are very steep, whereas slopes at the southern and northern ends are shallower. The lake lies within a relict glacial valley and is sheltered by mountains parallel to its axis.

Consequently the winds which blow on its surface are essentially directed along the main axis North-South. Winds can get strong 15 ms^{-1} and are characterized by a daily return period from June to October. From spring to autumn, the lake is thermally stratified.
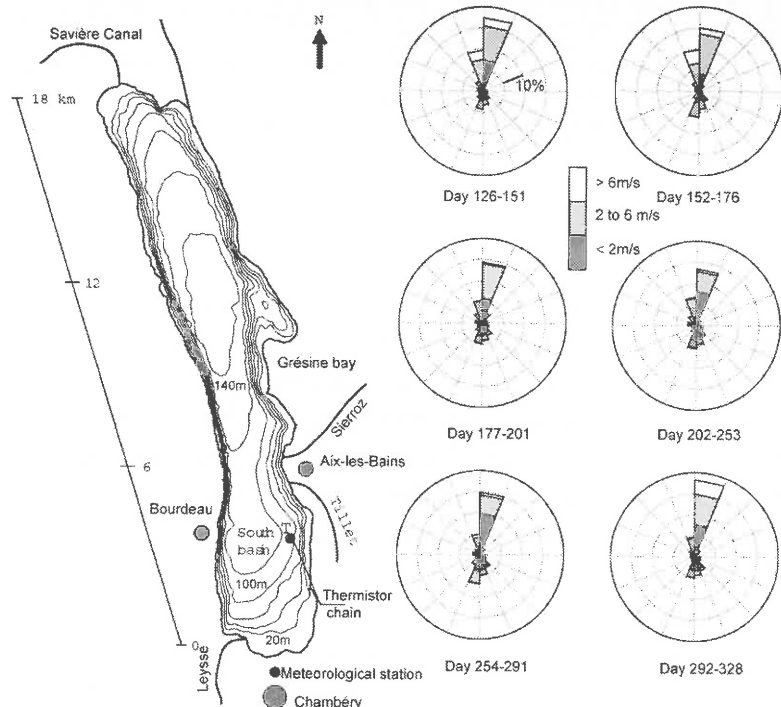
Fig 1. Lake Bourget bathymetry and wind regime

Field data were recorded between 6 May 2004 (day 126) and 24 November 2004 (day 328) which represents main of the stratification period of year 2004. Meteorological data are provided by Voglans meteorological station at the southern end of the lake (Fig.1). Air temperature wind force and directions are collected every 6 mn. Temperature profiles were recoded at point T (90 m depth) in the south basin of the lake with an array of 20 Aanderaa thermistors, spatially fitted to catch the strong temperature gradient in the metalimnion.

II INTERNAL WAVES FIELD

From day 126 to day 200 the lake is heating and the stratification is increasing progressively, until it reaches its maximum around day 200. The cooling of the lake starts around day 250 with a progressive deepening of the thermocline. Two isotherms series obtained from linear intrapolation are shown in figure 2 from spring heating period, day 164.7-169.3, and from fall cooling period, day 273-277.6. Each of the record shows strong evidence of vertical mode 1 waves with a period close to 24 hours. Comparison of the wave periodicity with a linear model modelling the stratification as 20 layers (Monismith 1985) shows these waves to be of the V1H1 mode (first vertical mode, first horizontal mode).

However, isotherms of the first serie of figure 2 a, as well as those of figure 3 show strong asymmetrical shape with a gradual rise of the isotherms followed by an abrupt. Such asymmetrical waves known as internal surges are characteristic of nonlinear processes which are affecting internal waves field in spring in Lake Bourget.
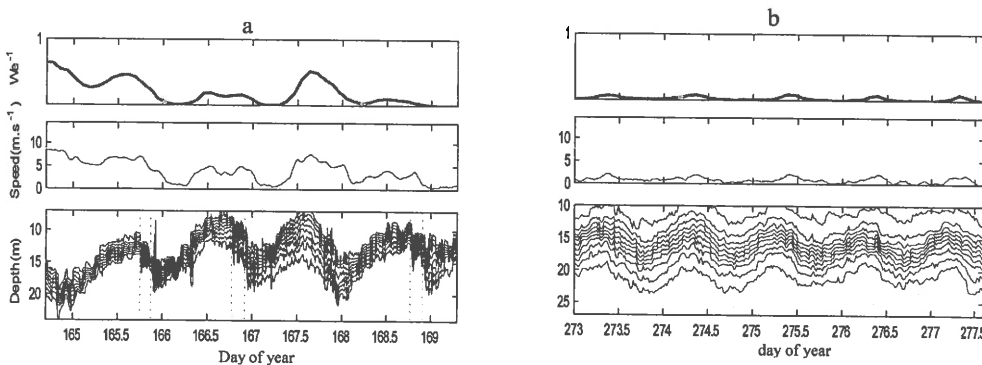
Fig2. isotherms series wind strength and invert of the Weddreburn number for 2 periods showing linear standing V1H1 seiches (left) and non linear surges (right). Vertical lines mark incident and reflected fronts

The observed surges are followed by a train of high frequency waves with strong vertical coherence. A second abrupt fall of the isotherms always occurs a few hours after the first one, again followed by high frequency waves. Internal surges have a ubiquitous nature, they have been characterized in several lakes (Thorpe 1971, Hunkins and Fliegel 1972, Farmer 1978, Saggio 1998). The characteristic second abrupt fall observed in the isotherm series in Lake Bourget is characteristic of a surge reflection at the southern basin end. Similar surge reflection characterized by the two

wave front of depression has already been observed, for instance, by Appt *et al* (2004) in Lake Constance, as well as in laboratory experiments of Horn et al (2001).

A KORTEWEG DE VRIES MODELLING

Generally, the high frequency wave train is composed of several internal solitary waves, followed by a dispersive sinusoidal wave train. Such solitary waves are a particular solution of the Korteweg de Vries (denoted KDVin the following) equation and generation of internal surge and high frequency waves have been interpreted in lakes in the Korteweg de Vries framework (Hunkins and Fliegel 1972, Farmer 1978, Boegman 2001, 2005). The Korteweg de Vries equation is a weakly non linear, weakly dispersive propagation equation. Modelling the stratification in a lake as a simple two layer structure, this equation reads:

$$\frac{\partial \eta}{\partial t} + c_0 \frac{\partial \eta}{\partial x} + c_1 \eta \frac{\partial \eta}{\partial x} + c_2 \frac{\partial^3 \eta}{\partial x^3} = 0,$$

with $c_0 = \sqrt{g' h_1 h_2/H}$, $c_1 = -3 c_0 (h_2 - h_1)/(2 h_1 h_2)$, $c_2 = c_0 h_1 h_2 / 6$

The surge formation can be interpreted as a steepening of the seiche under the influence of the non linear term. For a lake $h_1 < h_2$ and $\alpha < 0$ so that the surge is a wave of depression, in agreement with observations. As the wave steepens, higher harmonics compose the wave elevation η and dispersive effects increase. A balance between dispersive and non linear effects may then lead to solitary wave formation with a *sech²* profile. An important property of internal solitary is that they can propagate without altering their shape. Horn et al (2001) have performed laboratory experiments reproducing V1H1 seiche motion in a rectangular tank where stratification was modelled by two layers of different density. Owing to experimental facilities, they were able to explore different regimes by increasing the initial tilting of the interface. They showed that experimental observed regimes (linear standing seiches, internal surge and solitary waves) were well predicted by comparison of the characteristic time scales of non linear steepening, as derived from equation 1, and bottom turbulent friction damping of seiches, as derived from empirical laws. From these results they proposed a classification of the expected regime in a lake as function of two parameters, the upper layer to lake depth ratio h_1/H and the invert of the Wedderburn number $We^{-1} = \eta_0/h_1$, where η_0 is the maximum seiche amplitude. Regimes predicted by this classification were in general in good agreement with field observations.

Modelling lake Bourget stratification as a 2 layers structure of upper layer thickness h1, we find that $0.2 < h_1/H < 0.35$ from spring to late autumn, leading to a critical value of $We^{-1} \approx 0.2$ for apparition of non linear surge and solitary waves. Such a critical value of We^{-1} is easily reached under moderate wind forcing in spring when the epilimnion is thin and stratification is weak, leading to large amplitude internal surges as shown in figure 2a and figure 3.

Because of its quite regular bathymetry, and the relative simplicity of wind forcing which is guided along the lake axis, Lake Bourget appears as a natural laboratory to study seiche motions. Therefore we expect that a direct modelling in the Korteweg de Vries framework could reproduce non linear waves features observed during spring.

In order to deal with degeneration of standing internal seiches in a closed basin, where characteristics reflect at basin ends 0 and L, one has to consider the sum of 2 KDV equations that model propagation along each characteristics x-ct and x+ct (Horn *et al* (2002)) . Since the stratification in spring significantly differs from a 2 layer structure, we use a formulation of the Korteweg de Vries equation where the coefficients c_0, c_1 , c_2 takes into account the continuous character of stratification (Benney 1966).

Finally we add effect of damping by turbulent friction at the bottom. To model the turbulent friction we use a quadratic Chezy friction term in the form ρ k u|u|, as used for instance by Holloway to model turbulent friction in internal tide driven solitary waves (Holloway *et al* 1997}, where k is the Chezy friction coefficient. We choose $k=0.002$, a typical value for Chezy friction in a lake. Finally we us the Korteweg de Vries in the following form:

$$\frac{\partial \eta}{\partial t} + c_0 \frac{\partial \eta}{\partial x} + c_1 \eta \frac{\partial \eta}{\partial x} + c_2 \frac{\partial^3 \eta}{\partial x^3} + \frac{kc_0^{\,2}}{c_1} \eta |\eta| = 0 \quad (2)$$

We choose a classical numerical method to integrate this equation as a pseudo spectral method coupled with a 4th order Runge-Kutta scheme for the time integration. This Korteweg de Vries modelling still requires important assumptions, we neglect variation of the bathymetry, we consider that the motion is still weakly non linear as stated by the Korteweg de Vries equation, we neglect the wind forcing as soon as the thermocline relaxes, finally we make the assumption of weak non linearity.

We choose to reproduce the internal surge event occurring between day 137 and day 140. From day 135 to day 136.7 a strong wind characterized by an almost constant direction from the north blew. The tilting of the thermocline under the wind action appears clearly on the isotherms records at point T (Fig.3) where the thermocline deepens of 10 m between day 135.7 and day 137. After day 136.7 the wind falls abruptly, and the shear is expected to decrease rapidly, leading to a relaxing of the thermocline an initiation of seiche motion around day 137.

In the numerical computation, we set an initial linear tilted interface profile on day 137 in the form: $\eta(x,0)=\eta_0-2(\eta_0/L)x$ with $\eta_0=h_1 We^{-1}=17$ m , where We^{-1} was set to the maximum value of 1 reached around day 136.35. The simulation of $\eta(x=x_T,t)$, the temporal displacement at a virtual point T is compared to isotherms displacement recorded at point T in figure 3. The simulation compares fairly well with field observations over more than 2 periods of the linear V1H1 mode. The simulation reproduces well the global shape of the isotherms displacements, notably the strong damping of the large scale wave motion under turbulent friction at the bottom. The 2 abrupt falls of the isotherms marking the incident and the reflected surge on day 138.27 and day 138.54 are well reproduced, as well as the travel time of 6.5 hours separating the two fronts. The simulated high frequency waves packet following the first internal front also shows a good agreement with observations. The mean frequency of the simulated high frequency wave packet following the first internal front is $9.3.10^{-4}$ Hz whereas observed high frequency waves packet shows a close mean frequency of $8.3.10^{-4}$ Hz. Leading high frequency waves show a characteristic solitary wave shape with wide crests and narrow troughs both on the field records and simulated data. However, the maximum amplitude of the simulated high frequency internal wave is around a ≈ 6 m, whereas field recorded high frequency waves has maximum amplitude a ≈ 4 m. This discrepancy may partially results from the fact that our sampling rate of 5 mn is too slow to catch accurately the profile of the high frequency waves. Leading high frequency waves show a characteristic solitary wave shape with wide crests and narrow troughs both on the field records and simulated.
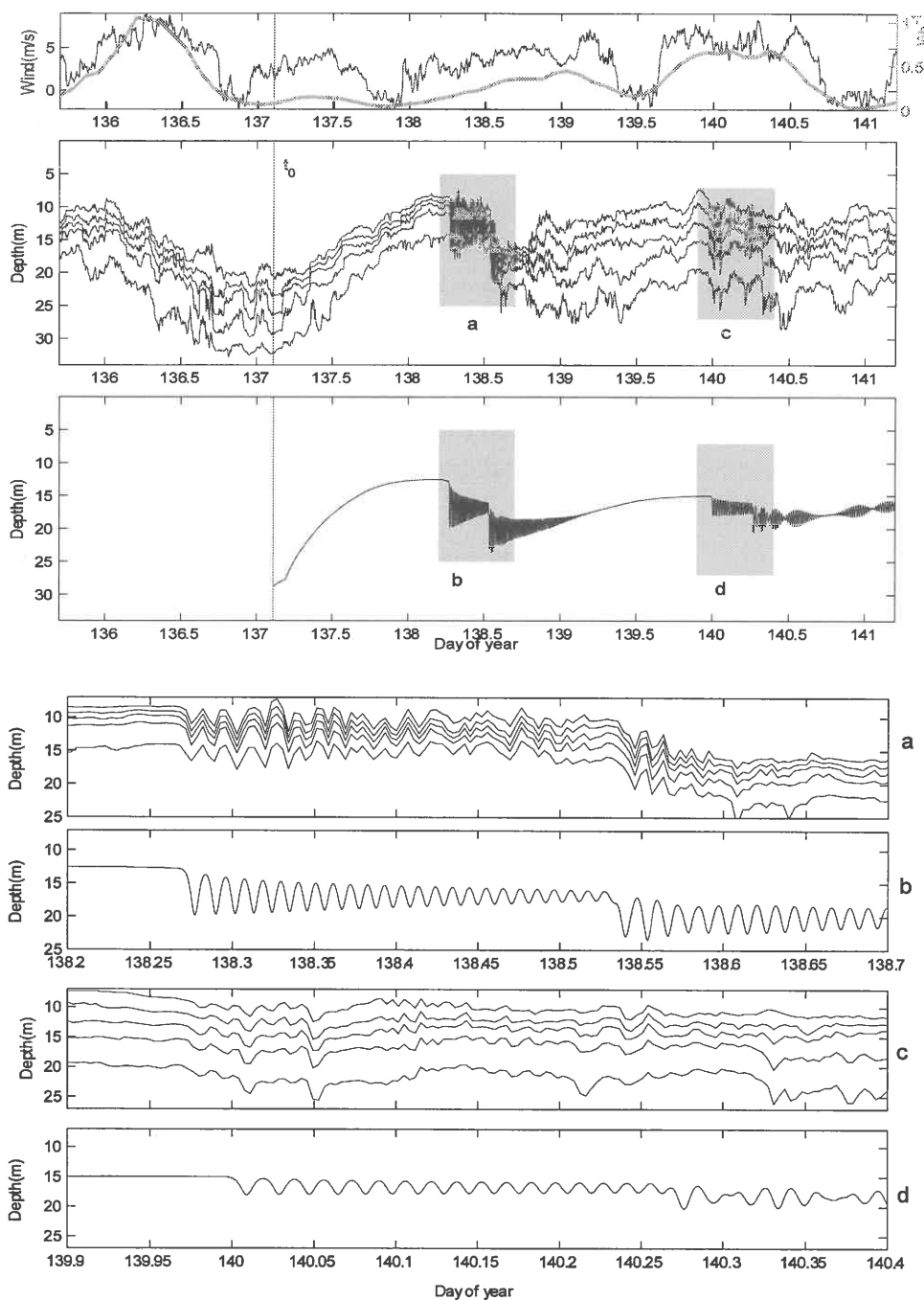
Fig 3. Comparison of time series recorded at point T and simulated using Korteweg de Vries equation, upper panel shows wind record and Wedderburn number, graph a, b, c and d show magnified view of shaded regions.

55

III DISCUSSION

Conditions for generation of non linear surges and solitary waves are easily reached in spring for moderate winds in Lake Bourget. Main features of the observation of an internal surge and high frequency waves were fairly well reproduced using a numerical simulation based on the KDV equation for the evolution of the interface. We can therefore infer that the combination of steepening of the initial seiche and dispersive effects is the mechanism leading to high frequency wave sin Lake Bourget, evidence of solitary waves type have also been shown.

High frequency non linear waves evidenced here are likely to shoal on the lake shores. Boegman *et al* 2005 have derived empirical laws from laboratory experiments for the ratio of the incident energy to reflected energy and for mixing efficiency as a function of the Iribarren number:

$$\xi = \frac{S}{(a/\lambda)^{1/2}}$$

(where S is the lake slope λ the wave length and a the wave amplitude). From these laws and estimation of the incident energy, we find that around 5% of the incident high frequency waves energy is converted into an increase of potential energy by turbulent mixing. Although this ratio may appear modest, rough estimation shows that it can lead to drastic intermittent increase of the turbulent dispersion up to 10^{-3} m^2/s at the depth of the pycnocline compared to usual observed values around 10^{-6} m^2/s derived from microstructure measurements at the centre of the lake (data not shown). Such high turbulent dispersion rate may lead to important nutrient fluxes at the lake shores and sustain unexplained cyanobacterial blooms in Lake Bourget.

REFERENCES

ANTENUCCI, J. P., IMBERGER, J., AND SAGGIO, A. 2000. Seasonal evolution of the basin scale internal wave field in large stratified lake. Limnol. Oceanogr. **45**(7):1621-1638.

APPT, J. IMBERGER, J. AND KOBUS, H. 2004. Basin scale motion in stratified upper lake Constance. Limnol. Oceanogr. **49**(4): 919-933.

BENNEY, D. J. 1966. Long non linear waves in fluid flows. Journal of Mathematics and Physics **45**: 52-63.

BOEGMAN, L., IMBERGER, J., IVEY, G. N. AND ANTENUCCI J. P. 2003. High frequency internal waves in large stratified lakes. Limnol. Oceanogr. **48**(2): 895-919.

BOEGMAN, L., IMBERGER, J., IVEY, G. N. 2005. The degeneration of internal waves in lakes with sloping topography. Limnol. Oceanogr. **50**(5): 1620-1637.

FARMER, D. M. 1978. Observations of long non linear internal waves in a lake. J. Phys. Oceanogr.**8**:63-73.

HOLLOWAY, P. E., PELINOVSKY, E., TALIPOVA, T. AND BARNES, B. 1997 A nonlinear model of internal tide transformation on the australian north west shelf. J. Phys. Oceanogr. \textbf{27}: 871-896.

HORN, D. A., IMBERGER, J. AND IVEY, G. N. 2001. The degeneration of large scale interfacial gravity waves in lakes. J. Fluid Mech. **434** 181-207.

HORN, D. A., IMBERGER, J., IVEY, G. N. AND REDEKOPP, L. G. 2002. A weakly nonlinear model of long internal waves in closed basins. J. Fluid Mech. **467**:269-287.

HUNKINS, K., FLIEGEL, M. 1973. Internal undular surges in Seneca lake: a natural occurence of solitons. J. Geophys. Res. **78**(3): 539-548.

MACINTYRE, S., FLYNN, K. M., JELLISON, R. AND ROMERO, J. R. 1999. Boundary mixing and nutrient fluxes in Mono Lake, California. Limnol. Oceanogr.**44**(3): 512-529.

MONISMITH, S. G. 1985. Wind-forced motions in stratified lakes and their effects on mixed-layer shear. Limnol. Oceanogr. **30**: 771-783.

SAGGIO, A. AND IMBERGER, J. 1998. Internal wave weather in a stratified lake. Limnol. Oceanogr. **43**(8): 1780-1795.

THORPE, S. A. 1971. Asymmetry of the internal seiche in Loch Ness. Nature, **231**, 3

SEICHE-INDUCED CONVECTION
IN UPPER SEDIMENTS

C. Engelhardt, S. Golosov, P. Casper, M. Hupfer, G. Kirillin[1]

(1) Leibniz-Institute for Freshwater Ecology and Inland Fisheries, Berlin, Germany.
corresponding author:kirillin@igb-berlin.de

ABSTRACT

Series of vertically resolved temperature measurements in lake sediments were performed in the shallow zone of small stratified Lake Stechlin, Germany. The results indicate periodical appearance of unstable temperature stratification driven by seiche upwelling of the cold metalimnion water into the littoral. The upward heat flux from sediments during the periods of instability exceeds to some orders of magnitude the molecular heat exchange rate. Analysis in terms of the Nusselt and Rayleigh numbers reveals convective character of the heat exchange. Periodic development of convection in sediments is associated with mass flux into the bottom waters and can contribute essentially to the internal loading of dissolved nutrients. The mechanism is to expect in the majority of stratified lakes with gradual topography.
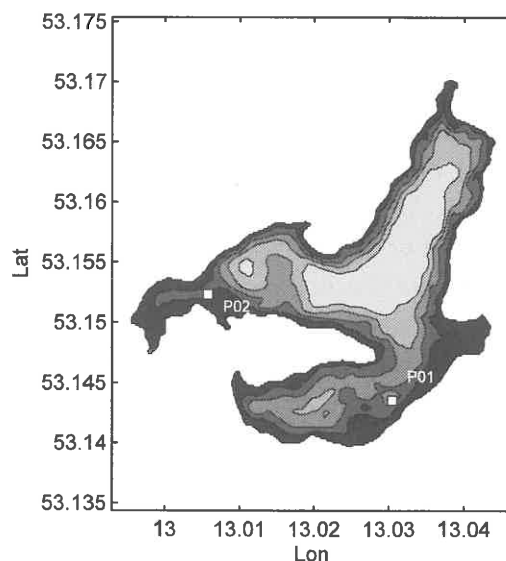
INTRODUCTION

The bottom boundary layer in stratified lakes is strongly affected by internal seiches. One of the seiche effects on near-bottom dynamics consists in periodical seiche-driven upwelling of cold hypolimnion water at the bottom slopes. It was recently shown that the cold water upwelling in coastal zones of the ocean superimposed by formation of the shear boundary layer produces an unstable vertical temperature distribution near the bottom (Moum et al. 2004). The vertical density instability is formed here by deceleration of the upwelling water by bottom friction in the vicinity of the water-sediments interface and creeping of colder water just above the friction layer. A similar effect was reported to take place in stratified lakes on account of seiche oscillations (Lorke et al. 2005). The resulting convection contributes essentially to the mass and heat exchange at the bottom, especially in lakes, where it has periodical character. However, the same upwelling mechanism should result in even higher density instability in the upper sediments covered

periodically by cold upwelling water. This instability can potentially cause convection, which would be though less intense than in water, but can contribute significantly to nutrients release from sediments to lake water. This effect has not been yet investigated, though convection development in upper sediments was previously reported in shallow lakes during autumn cooling with vertical temperature gradients comparable to that caused by seiche-driven upwelling (Lappalainen 1982, Golosov and Ignatieva 1999). Our study was aimed at evaluation of seiche-induced heat transfer in upper sediments of a strongly stratified lake and estimation of its possible impact on nutrients release from lake sediments.

MATERIALS AND METHODS

Study site: The domestic, oligotrophic Lake Stechlin (53° 10′N, 13° 02′E; surface area 430 ha, mean depth 22.8 m, maximum depth 69 m) is situated approximately 120 km north of Berlin, Germany (Koschel and Adams 2003). Relatively high depths and small horizontal dimensions result here in strong stratification normally lasting from May to the end of November. During the entire stratified period internal seiches dominate the lake dynamics, whose characteristics are perplexed by irregular lake shape and bottom topography. The lake consists of three virtually isolated sidearms (conveniently called North, South and West Basins) of nearly the same area (Fig. 1) giving rise to a number of different horizontal and vertical seiche modes.
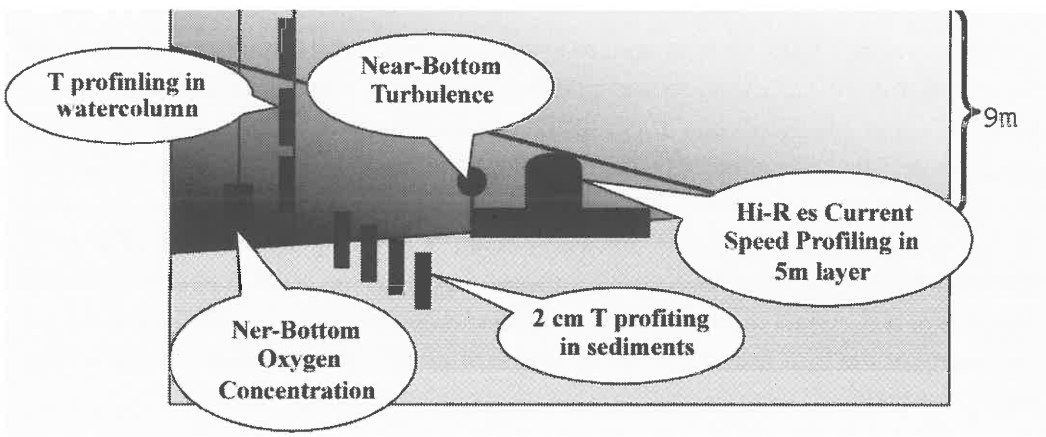
Figure 1. (Top) bathymetry of Lake Stechlin (10, 20, 30 and 40m isobathes are shown), location of two experimental sites and (bottom) measurements setup.

Analysis of basin-scale oscillations pattern on seasonal time scales have shown that starting from early summer the 2nd vertical mode seiches with daily period dominate in the lake, what conditioned by the resonance with the with diurnal oscillations in wind forcing. An important consequence of this resonance consists in high (up to 5m) seiche amplitudes and, as a result, in a wide margin zone at the lake shore flooded periodically by the cold metalimnion water. The 1st vertical mode seiches with higher frequencies prevail in the lake during the early spring and late autumn, when the thermocline layer is too thin or too deep to generate the 2nd vertical mode oscillations. In addition, strong 1st vertical mode oscillations emerge if the prevailing south-west wind coinciding with the main axis of the North Basin changes its direction and the 2nd mode oscillations cease.

DESIGN OF FIELD EXPERIMENTS

One consequence of the high-amplitude seiches is the unstable temperature stratification at the water-sediments boundary of the near-shore zone appearing periodically on account of colder deep water covering warmer sediments. In order to investigate the thermal characteristics of the unstable layer, series of field experiments were perfor-med in the near-shore zone of Lake Stechlin. Two locations were chosen, P01 and P02 (see Fig. 1) with depths 11 and 9 meters correspondingly that agrees approximately with the undisturbed thermocline depth. Four 2-week measurement series were performed, two at each site, one in May, two in August and

61

one in November 2005. 10 temperature loggers (RBR T-1050, Canada) were installed on a bottom-mounted measurement platform, with 2cm vertical resolution covering 10cm of upper sediments and 10cm of the overlaying water. Temperature data were sampled at 10s rate with 0.002K accuracy. Additional data were provided by thermistor strings in the water column using the same RBR T-1050 loggers, acoustic current velocity profiling in the 5m near-bottom layer using 2MHz NORTEK ADP and near-bottom oxygen concentration measurements using RBR XR-420 CTD+O2 logger (see right panel in Fig. 1). Following discussion is confined with the short-term variability of the heat transfer in the upper 10cm of sediments, so that information on bottom currents and oxygen concentration is excluded from consideration.

RESULTS AND DISCUSSION

The temperature data indicate periodical cooling of the upper sediments in all three observational series in May, August and November. The strongest temperature gradients as well as the longest periods of cooling were observed in August at the measurement point P02 (Fig. 1). During this period, evolution of isotherms within the sediments reveals quasi-regular pattern (Fig. 2, top panel): relatively short cooling events intermit sediments heating from above and disturb the stable temperature stratification with frequency close to the daily one.
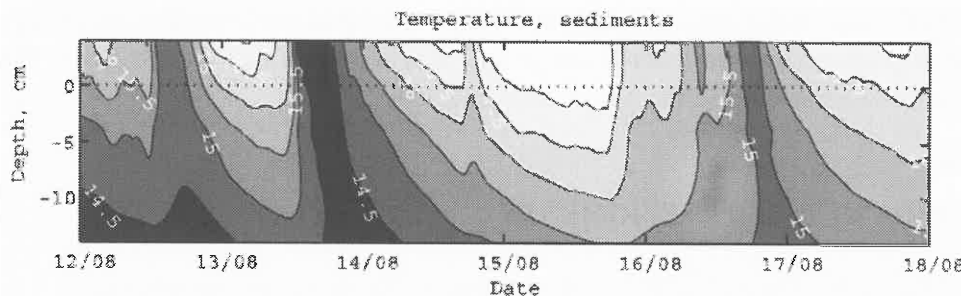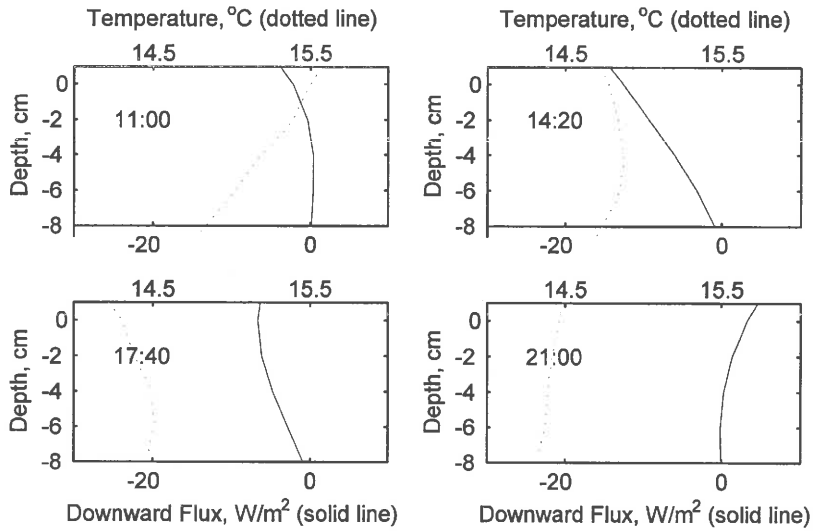
Figure 2. (Top) Temperature evolution in the upper sediments of Lake Stechlin, August 2005. (Bottom) Successive temperature and vertical heat flux profiles in sediments on 13 Aug 2005, averaged over every 200 min.

62

Temperature, °C (dotted line)

Downward Flux, W/m² (solid line)

In the starting phase of all cooling episodes (e.g. 13-14 August 2005 and 16-17 August 2005 in Fig. 2) isotherms have negative slope suggesting unstable temperature profiles in sediments. The unstable stratification is followed by fast development of vertically-mixed layer that is characteristic for convective behaviour. Successive profiles of temperature and vertical heat flux for the cooling event on 13 August 2005, presented in Fig. 2 (bottom panel), support the convective character of mixing. Heat flux was estimated in this case from 1-D heat transfer equation assuming no horizontal heat transport and negligible heat transfer below the deepest measurements depth. According to the profiles, an unstable stratification develops in the upper 5 cm of sediments with vertical temperature gradient about $1°C·m^{-1}$ (Fig. 2, bottom panel, 14:20 local time), followed almost immediately by increase of the upward heat flux up to several tens $W·m^{-2}$. Several hours after the formation of unstable stratification (Fig. 2, profiles at 17:40), mixing spans over the entire sediments layer that suggests penetrative character of convection. Comparison of the vertical heat flux at the water-sediments boundary with that provided by the molecular heat diffusion (Fig. 3, top panel) demonstrates close values of both estimations in case of stable conditions suggesting diffusive mechanism of the downward heat transport within the sediments.
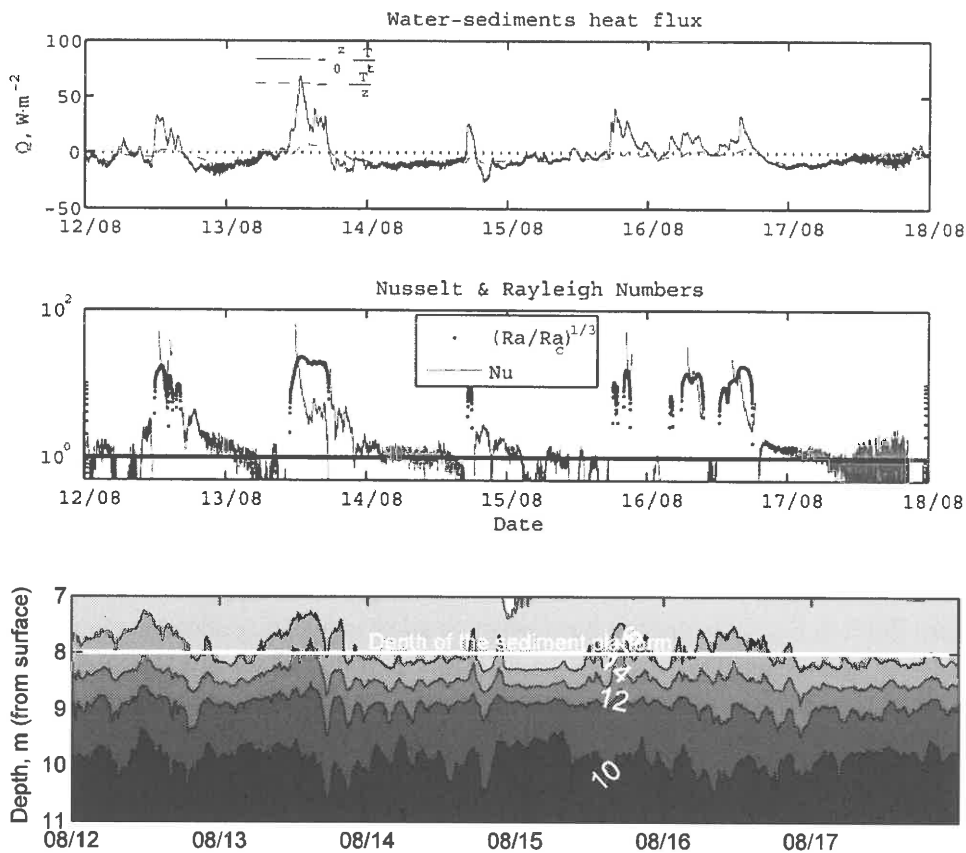
Figure 3. (Top) Evolution of the vertical heat flux across the water-sediments boundary during the August experiment. Dashed line is the flux value estimated from the temperature gradient assuming molecular diffusivity. (Middle) Nusselt Number (ratio of real and "molecular" fluxes) at the water-sediments boundary. Points are scaled values of the Rayleigh Number calculated for instable conditions (see text). (Bottom) Isotherms displacements in water from a thermal chain installed in the center of the West Basin.

The upward flux values, in their turn, exceed up to 100 times the estimations given by the diffusion law. Appearance of the upward fluxes is strongly correlated with unstable stratification events within the upper sediments. When compared to the Rayleigh Number, the dimensionless heat flux (Nusselt number) scales favorably against $Nu = \left(Ra/Ra_c \right)^{1/3}$ (Fig. 3, mid panel). Here, the critical Rayleigh Number is chosen as $Ra_c \approx 10^3$, and

$$Ra = \frac{g\alpha\Delta T h^3}{\kappa\nu}$$

64

where h is the thickness of the unstable layer of sediments, ΔT is the temperature jump across it, κ, ν, α are the molecular diffusivity, the molecular viscosity and the heat expansion coefficient of water, correspondingly. The scaling suggests the heat loss from sediments be due to developed convection, driven by the unstable temperature gradient. When compared to the isotherms displacement in the west basin, a strong correlation can be revealed between seiche-driven rise of isotherms and the instability events (cf. the $16°$ C isotherm in bottom panel of Fig. 3 and the water-sediments heat flux curve in the top panel of the same figure). Thus, the seiche-driven upwelling can be regarded as the driving force for the convection in sediments.
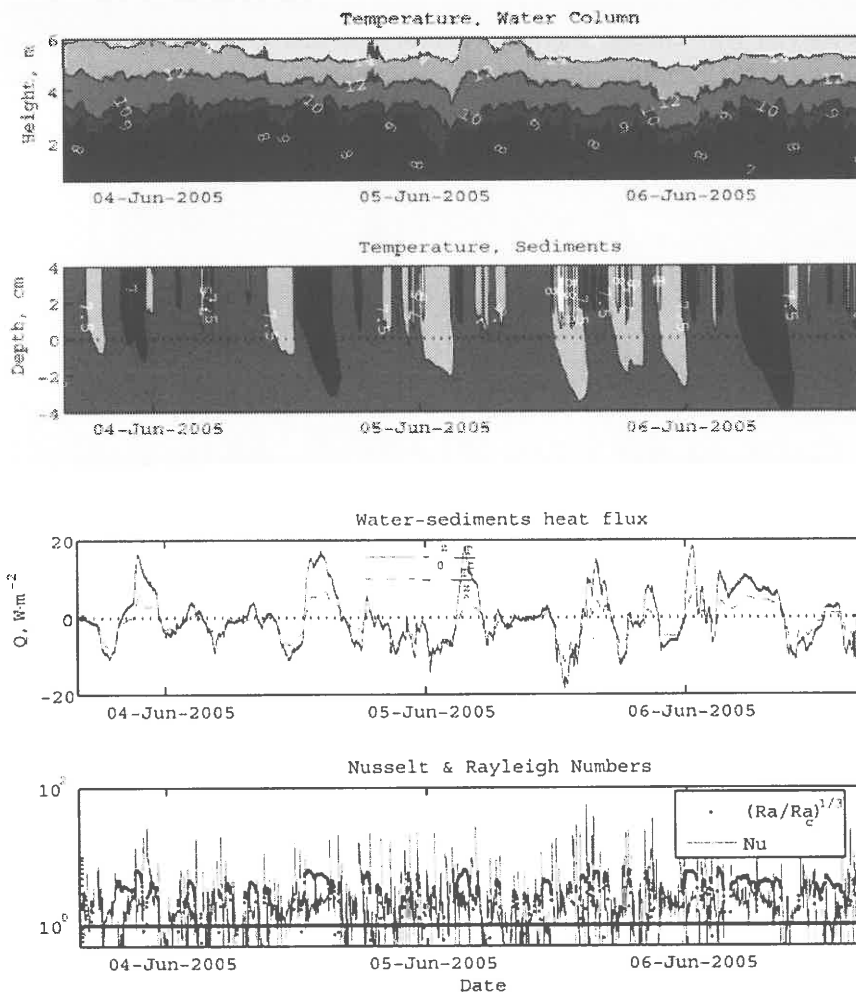
Figure 4. From top to bottom: (i) Isotherms displacements in water and (ii) in sediments at the measurements site P01 during the May experiment; (iii) vertical heat flux and (iv) Rayleigh and Nusselt Numbers at the water-sediments interface (see caption to Fig. 3)

65

The fact that the seiches pattern in August is characterized by dominating of the 2nd vertical mode explains the quasi-diurnal character of the convection development. Thus, the measurement series performed in May 2005, when the 1st vertical mode prevails in basin-scale oscillations (Fig. 4, top panel), reveals different time scales of convection events than that from the August measurements. Again, the inverse temperature stratification develops here driven by seiche upwelling (Fig. 4, second panel) and the resulting upward heat flux sufficiently exceeds the molecular values (Fig. 4, third panel). However, the timing of the convection events is shorter according to higher frequency of the seiche oscillations and the absolute values of heat flux are smaller conditioned by the weaker stratification in the spring. The scaling between Nusselt and Rayleigh numbers is less evident here on account of rapid changes in the heat flux and difficulty in definition of the convective layer.
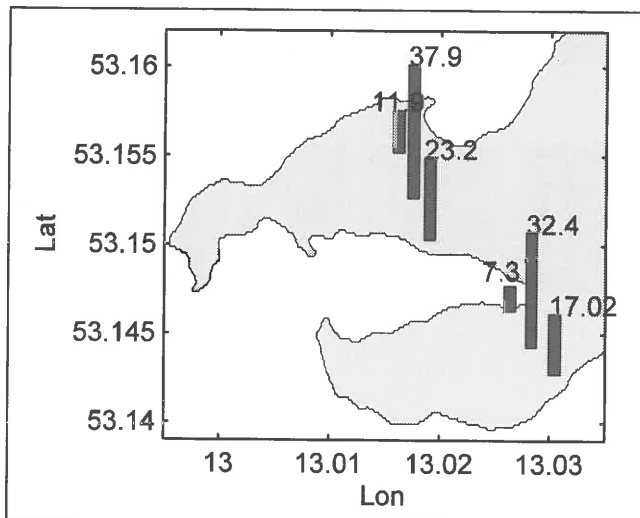
Figure 5. Dissolved inorganic phosphorus concentrations (μgl^{-1}) in the upper 5 cm of bottom sediments of Lake Stechlin.

One of the most important consequences of the periodic convection development in lake sediments consists in vertical transport of the dissolved substances in pore water by convective water motions. Strong impact of convection on nutrients release from sediments during autumn cooling in shallow lakes has been previously reported (Lappalainen 1982, Golosov and Ignatieva 1999). The present results suggest contribution of this effect into water-sediments matter exchange at bottom slopes during the entire stratified period. The shoreward decrease in nutrients concentrations observed in lakes (Fig. 5), which is usually associated with the washout of the matter

66

by near-bottom currents, or by the so-called focusing effect resulting in accumulation of material in the deepest parts (Michel et al. 2001), can however serve also as indirect evidence of the convection contribution to the internal nutrients loading.
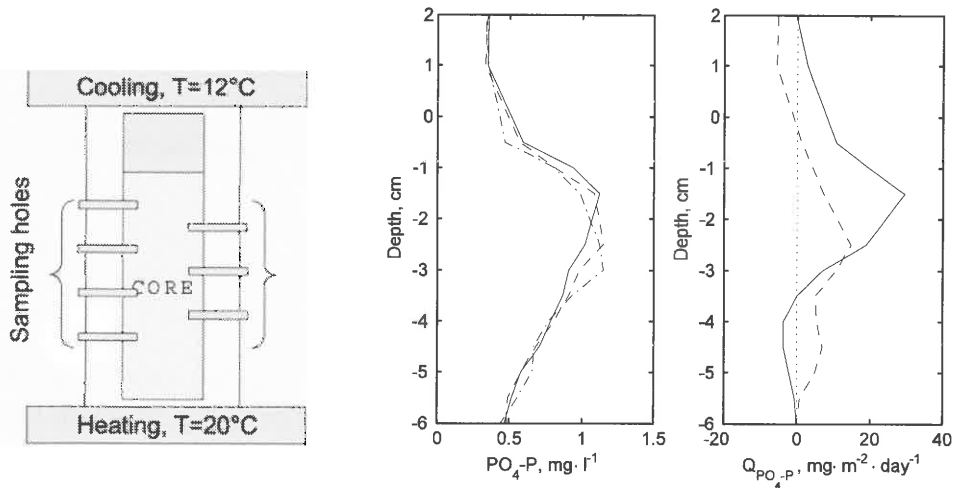
Figure 6. From left to right: (i) laboratory setup for simulation of the convective mass transfer in sediments; (ii) vertical phosphorus profiles: solid line - at experiment's start, dashed line - after 1 hour of cooling, dash-dotted line - after 3 hours of cooling; (iii) vertical mass flux: solid line - after one hour of cooling, dashed line - after 3 hours of cooling.

Direct *in situ* estimation of the convectively-driven mass transfer in sediments is cumbersome. Therefore, a laboratory experiment was performed imitating convective conditions in upper sediments of Lake Stechlin. A sediment core was taken at the site P01 (see Fig. 1) and put into a thermostat with constant temperatures hold at the upper and the lower boundaries (Fig. 6i). The unstable temperature gradient across the core was kept for 3 hours at $8°$ C (an upper estimate taken as the average temperature jump across the thermocline). Microsamples of the pore water were taken at different depths in the core and the dissolved phosphorus concentration was estimated. First results demonstrate diffusion of the dissolved phosphorus profile apparently by the convection (Fig. 6ii). Estimation of the vertical mass flux from the profile evolution (Fig. 6iii) provides with values about 4 mg m^{-2}day^{-1}, which is about 5 times larger than typical values for Lake Stechlin and are comparable to fluxes produced by anoxic phosphorus release. It suggests an important role of the mechanism in phosphorus dynamics in oxic conditions of oligotrophic lakes (Gonsiorczyk et al. 2001).

REFERENCES

GOLOSOV, S. D. AND IGNATIEVA, N. 1999. Hydrothermodynamic features of mass exchange across the sediment-water interface in shallow lakes. *Hydrobiologia* 408/409:153-157.

GONSIORCZYK T., CASPER, P., AND KOSCHEL, R. 2001. Mechanisms of phosphorus release from the bottom sediment of the oligotrophic Lake Stechlin: Importance of the permanently oxic sediment surface. *Arch.Hydrobiol.* 151:203-219.

KOSCHEL, R. AND ADAMS, D. (EDS) 2003. Lake Stechlin - an Approach to Understanding an Oligotrophic Lowland Lake, volume 58 of *Archiv Hydrobiologie - Advances in Limnology.*

LAPPALAINEN, K. M. 1982. Convection in bottom sediments and its role in material exchange between water and sediments. *Hydrobiologia (Historical Archive)* 86:105-108.

LORKE, A., PEETERS, F., AND WÜEST, A. 2005. Shear-induced convective mixing in bottom boundary layers on slopes. *Limnol. Oceanogr.* 50:1612-1619.

MICHEL, H., BARCI-FUNEL, G., ARDISSON, G., CASPER, P., AND EL-DAOUSHY, F. 2001. Plutonium-238, 239-240 inventories in sediment cores from Stechlin Lake, Germany. *J. Radioanalyt. and Nucl. Chem.* 250:159-164.

MOUM , J. N., PERLIN, A., KLYMAK, J. M., LEVINE, M. D., BOYD, T., AND KOSRO, P. M. 2004. Convectively driven mixing in the bottom boundary layer. *J. Phys. Oceanogr.* 34:2189-2202.

EMPIRICAL MODE DECOMPOSITION:
A NEW TOOL TO ANALYSE TIME SERIES

Johann Ilmberger and Christoph von Rohden[1]

(1) Institut für Umweltphysik, Im Neuenheimer Feld 229, D-69120 Heidelberg, Germany
Johann.Ilmberger@iup.uni-heidelberg.de

ABSTRACT

Data analysis is an essential part in research and much effort has to be taken to extract from measurements information about ongoing processes. The fairly new method "empirical mode decomposition" (EMD) and instantaneous frequency calculations was introduced by N.E. Huang. The method is based on the identification of the intrinsic oscillatory modes by their characteristic time scales in the data empirically, and decompose the data accordingly. The advantage of the EMD is, that data of non stationary and non linear systems can be analysed.

This method, which is still discussed controversial, is presented and the application to measured time series of temperature and water currents shows the ability of the method to analyse non stationary processes.

Usual data analysis assumes linear and stationary processes. At a first order approach many systems can be treated linear. Restricting the analysis to appropriate time scales, also the stationary assumption holds and one gets acceptable results.

In recent years methods were developed to analyse non linear systems and also non stationary processes. For the interpretation of non stationary data for example wavelet analysis or short term Fourier transform is used.

As data of natural systems are quite often both non linear and non stationary, a useful tool to analyse these data is the Hilbert-Huang transform (HHT) (Huang et al. (1996, 1998, 2005).

The HHT consists of two parts: The empirical mode decomposition (EMD) and the Hilbert transformation. The Hilbert transformation allows to calculate the instantaneous frequency from a given time series, but only on a signal which has a narrow frequency band. Using the EMD a signal can be decomposed into such narrow

bands. So the first step is the decomposition of the signal and the second is the application of the Hilbert transformation. The decomposition is based on the assumption that any time series consists of different simple intrinsic modes of oscillations. Each intrinsic mode is a simple oscillation, linear or nonlinear, which will have the same number of extrema and zero-crossings.

The definition of the intrinsic mode functions (IMF) is:

(1)   in the whole dataset, the number of extrema and the number of zero-crossings must either equal or differ at most by one, and
(2)   at any point, the mean value of the envelope defined by the local maxima and the envelope defined by the local minima is zero.

The IMFs compare to the simple harmonic functions when using Fourier transformation, but are more general. They can have variable amplitudes and frequencies as function of time.

To find the IMFs, a procedure which is called sifting process is applied to the data. This is an iteration process, where the first step is: find all maximum values of the data (test data see figure 1) and envelope them with a cubic spline (Figure 2). Second: construct a lower envelope through all local minimal values and again a cubic spline. The mean value of the two spline functions is drawn red in figure 2.
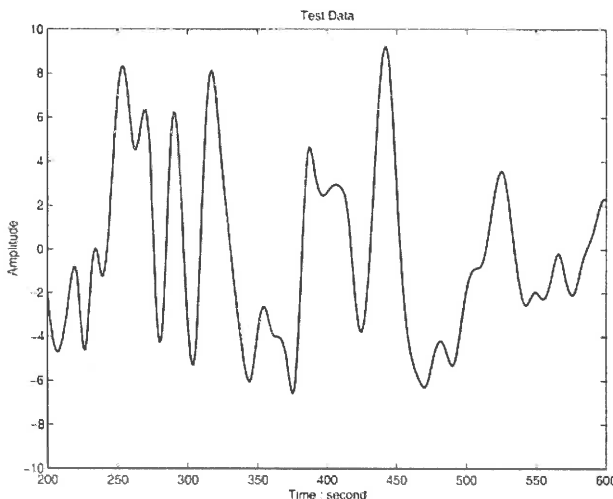
Figure 1. A test signal versus time. (Figure after Huang et al. 2005)

70
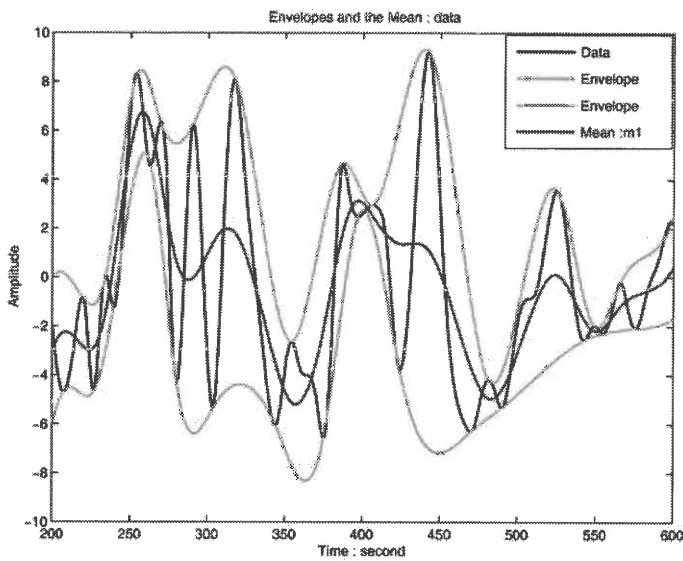
Figure 2. The signal versus time, the upper and lower cubic spline envelope and the mean of these envelopes. (Figure after Huang et al. 2005)

This mean value doesn't fulfil the definition (1) for an IMF, which states that the number of zero crossings and maxima must match. This is not the case (see red curve in figure 2). So the iteration process of connecting the maxima via a cubic spline and also the minima and calculating the mean has to be continued.
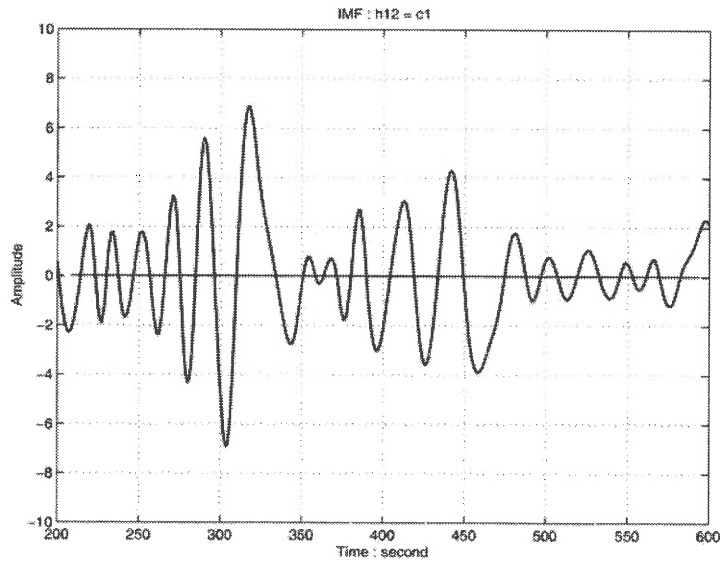
Figure 3. The first IMF after 12 iteration steps. (Figure after Huang et al. 2005)

The sifting process has to get the signal more symmetric and to remove riding waves. Figure 3 shows the result of the sifting process after 12 iterations, when the difference was accepted as IMF. The problem is the stopping criteria. One possibility is an upper bound for a quadratic deviation of two successive functions. The problem is, that an value for the deviation has to be set. Another criteria used is a fixed number of iterations after the number of zero crossings and the number of extrema stays the same and are equal or differ at most by one.
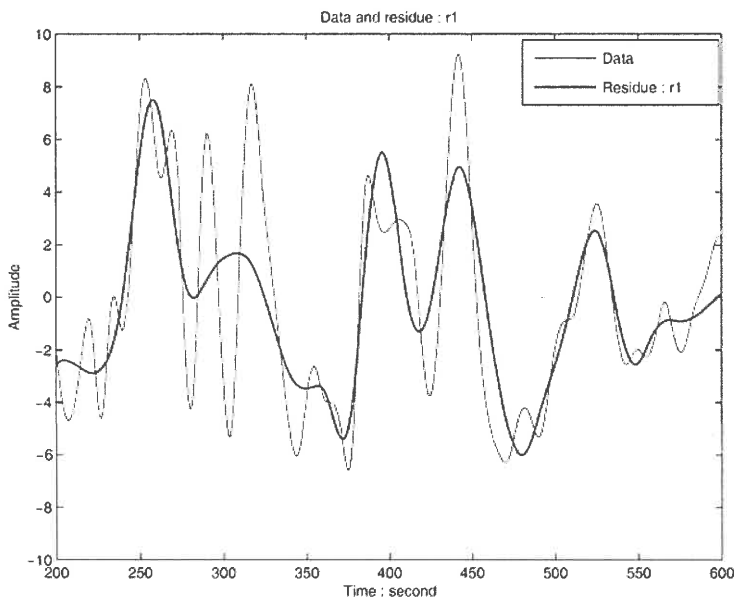
Figure 4. The original signal versus time and the residue i.e. the difference between the data and the first IMF. (Figure after Huang et al. 2005)

When the stopping criteria is met and an IMF is found, the residual, i.e. the difference between the signal and the IMF is calculated (figure 4). Now the sifting process is applied to the residue and the calculations are continued till the final residue is a trend, a constant value or small compared to the signal.

TESTING THE METHOD

To test the procedure two scenarios are performed. First a time series with changing frequency was created. There, after 150 seconds, the frequency changes linearly with time. The results are shown in the figures 5, 6 and 7. Figure 5 shows the time series, Figure 6 shows the intrinsic mode functions of this time series. There are

only few IMFs and the main signal is in the first one. The other ones are very small in amplitude and can't be recognised on that scale.
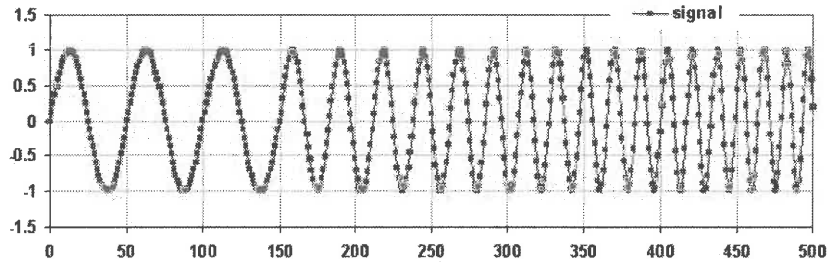
Figure 5. Test time series. Linear increase of the frequency after 150 s.
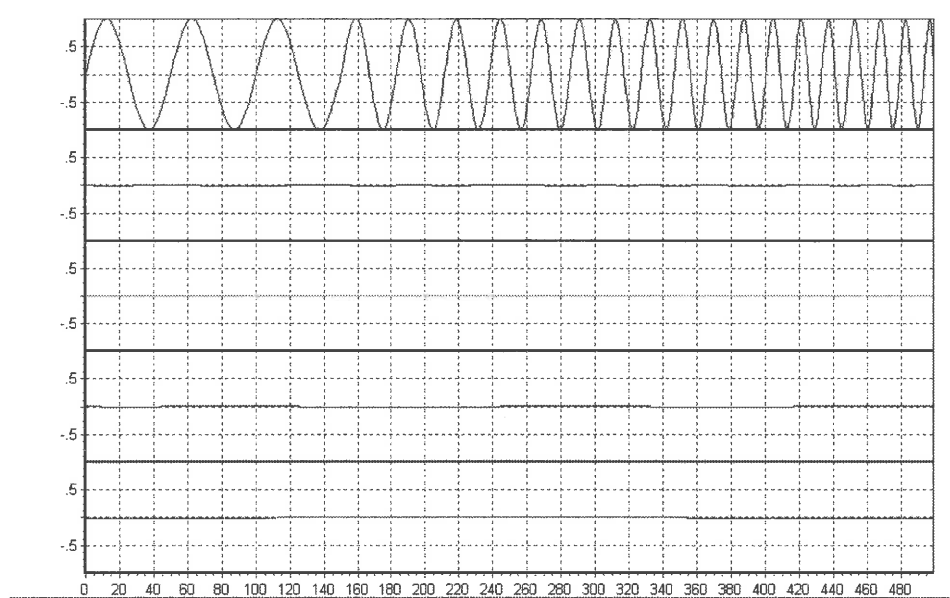
Figure 6. The intrinsic mode functions IMF1 to IMF4 and the residue of the above test time series. In this simple case the complete time series is in the first IMF. The amplitude of the other are very small.

73
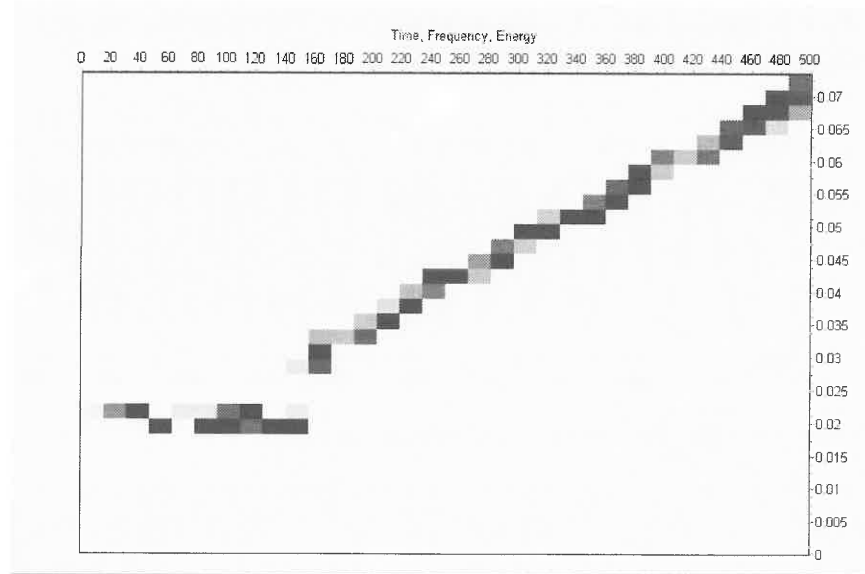
Figure 7. Hilbert spectrum of the test time series of figure 5. It is the time series of the instantaneous frequency, which increases linearly after 150s. The color scale is a measure for the current amplitude

The second test time series is a sinus signal with a random signal added. The amplitude of the random signal is 20% of the main signal's amplitude. The figures 8, 9 and 10 show the results.

Figure 8 shows the time series created as test signal. Figure 9 displays the IMFs calculated from the time series. The first two IMFs comprise the random noise and the third is the original sine wave. The next figure (fig 10) is the instantaneous frequency, calculated by the Hilbert transformation.
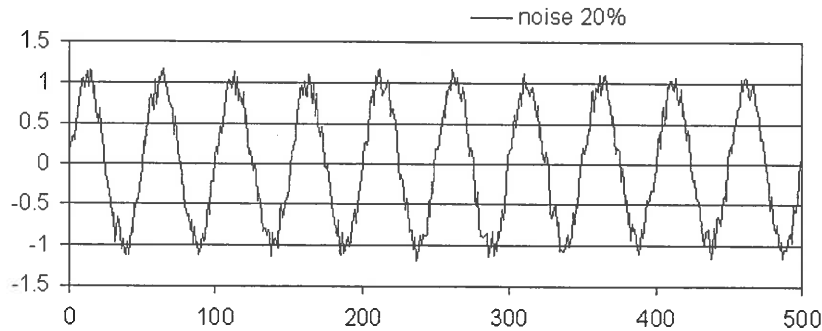
Figure 8. Sinus signal plus random signal. The random signals amplitude is 0.2 at most.

74
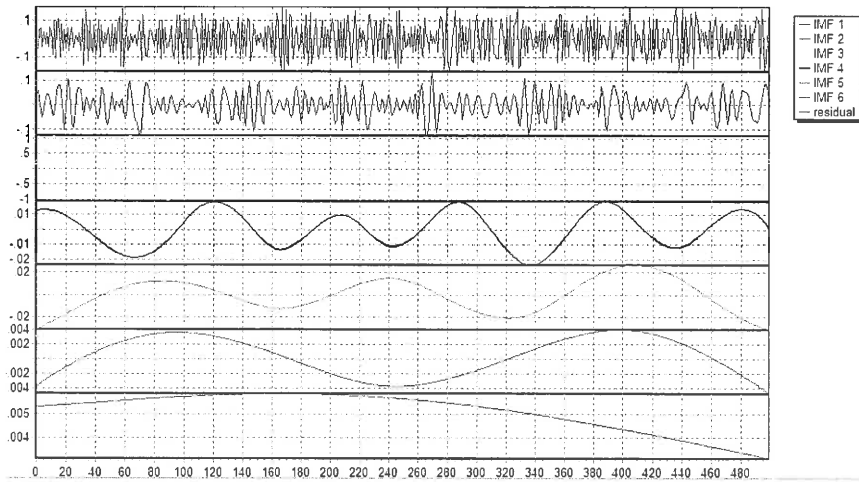
Figure 9. The panels show the IMFs, calculated from the time series shown in figure 8. The first two IMFs can be addressed to the noise, which might be not fully random. IMF 3 gives the undistorted signal and 4,5 and 6 some underlying signal. The 7th panel shows the residue. The different panel are on different scales!
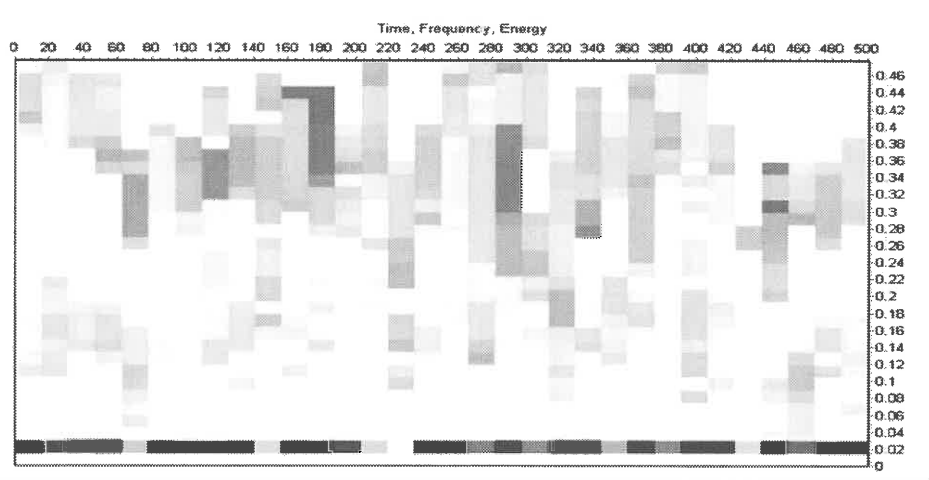
Figure 10. The instantaneous frequency, calculated via Hilbert transformation. The axes are time and frequency. The color scale is a measure for the amplitude.

We performed only two rather simple tests to show how the method works. There are many publications, where different tests are recorded e.g. Huang et al (1998), Flandrin et al (2004), Wu and Huang (2004). There are also some publications about applications of the empirical mode decomposition and the Hilbert transformation e.g. Oonincx and Hermand (2004), Cummings et al (2004), Flandrin and Goncalves (2004).

APPLICATION TO FIELD DATA

In the following we give two examples for the application of the method to field data. The first is a time series of current measurements in a small stratified lake in the Rhine valley. In 2004 we performed current measurements in this lake using a acoustic current profiler (ADCP). The currents in the lake are very low and the signal is rather noisy. Figure 11 shows a record of the north component of the current velocity at a water depth of 4.4 m. The signal is a 5 min mean, very noisy and doesn't show much of a structure. To analyse this signal, the empirical mode decomposition was applied. The whole set of the resulting IMFs and the residue is shown in figure 12. The first IMF, or may be the first and second IMF, can be addressed to the signal's noise, while the third and fourth clearly show a structure in the data, which is quite intermittent and wave package like.
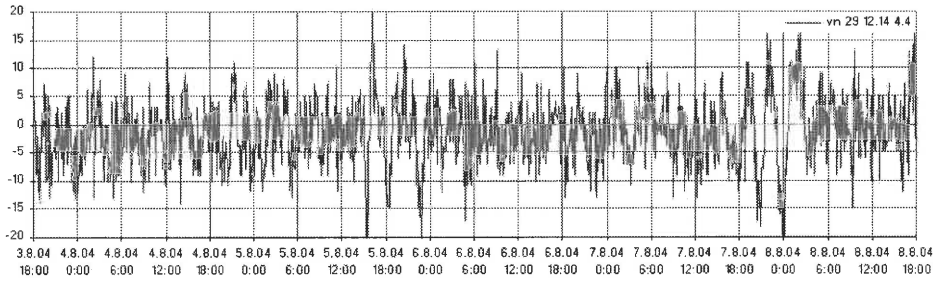
Figure 11. Time series of the north component of the water current velocity in a small stratified lake.
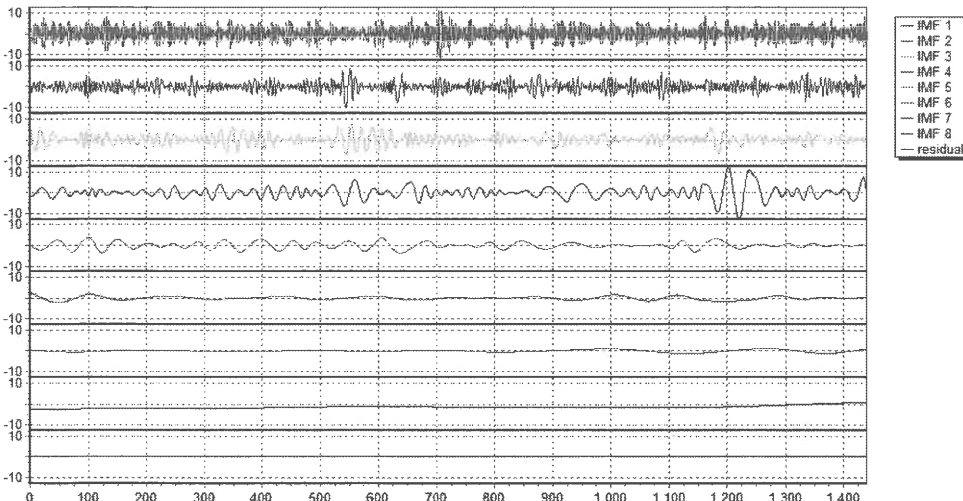
Figure 12 The panels show the intrinsic mode functions of the time series of figure 12. IMF 1 and 2 can be addressed to the signal's noise, while IMF 3 and 4 show a structure. IMF 5 to IMF 8 and the residue are of minor importance.

76

The second example is a time series of 1 hour mean temperature data, measured at 9m water depth in lake Überlinger See (a part of lake Constance). The record starts at 15.5.1995 and ends at 4.8.1995 (see figure 14). Figure 15 shows the eight resulting IMFs. Figure 16 displays the measured data, IMF8, the sum of IMF5 to IMF8 and the intrinsic mode function 4.

The sum of the IMFs give already a good approximation of the data except for the time period form 14.7. to about 20.7. There one needs the IMF4 to get a better approximation. The time scale of the IMF4 is about two days.
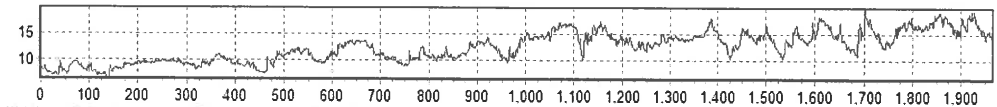
Figure 14. Time series of water temperature at 9m water depth in lake Über-lingen. The time scale is hours starting at the 15.5.1995. The y-axis is temperature in°C.
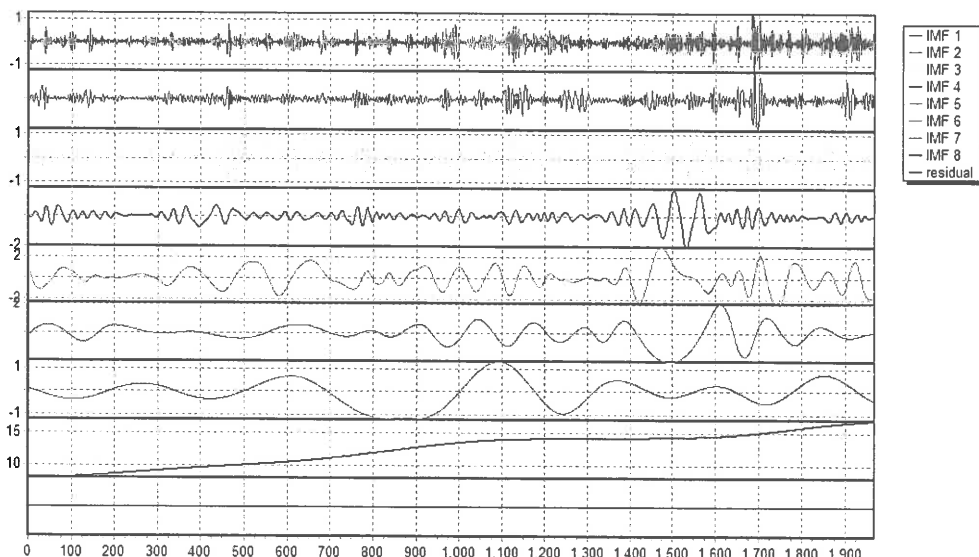
Figure 15. Intrinsic mode functions of the time series of figure 14.The time scale is hours starting at the 15.5.1995. The y-axis is temperature in°C
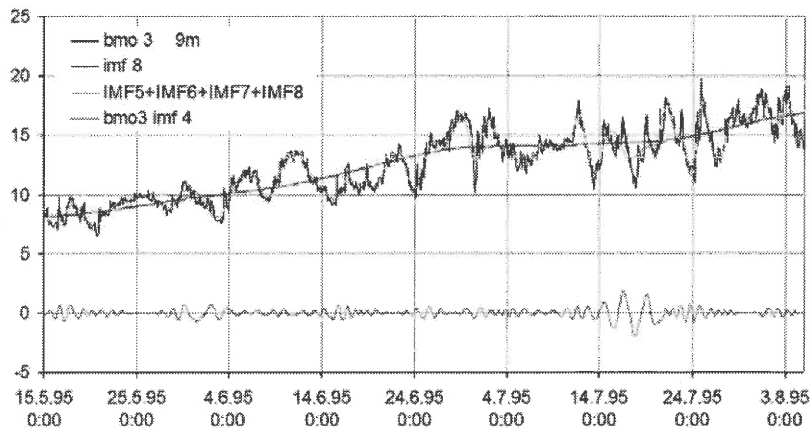
Figure 16. The figure shows the same temperature data as figure 14 and the sum of IMF 5 to 8, which is already a good approximation for the data. From the 14.7. to about the 20.7. the IMF 4 shows a rather high amplitude. The y-axis is temperature in°C

CONCLUSIONS

The method seems to have the ability to give an insight to field data, by decomposing the signal into the intrinsic mode functions. This is very useful for the still very important 'by eye' data analysis. The decomposition into non liner and non stationary functions is great, but only if they are physical meaningful. To judge whether this is the case or not, one needs a lot of experience, but this is the same , when using other tools to analyse data.

There are other problems for example: the IMFs are not orthogonal, i.e. they are actually no basis, and at the beginning and end of a data set the cubic splines do not work well so we get distortions there.

The Hilbert transformation for the calculation of the instantaneous frequency is theoretical and mathematical fully developed and gives the current frequency. But also here one has to have the physical understanding of the system to interpret the results.

All the calculations (IMF, Hilbert transformation) in this contribution were performed with the software developed and distributed by N. Huang et al.

78

REFERENCES

CUMMINGS D., R. IRIZARRY, N. HUANG, T. ENDY, A. NISALAK, K. UNGCHUSAK AND D. BURKE, 2004: Travelling waves in the occurrence of dengue haemorrhagic fever in Thailand, NATURE, VOL 427, 22 JANUARY 2004

HUANG, N. E., 2005: Introduction to Hilbert-Huang transform and its associated mathematical problems. 1-32, *Hilbert-Huang Transform in Engineering*, Ed. N. E. Huang and N. Attoh-Okine, 2005, CRC Press, New York.

HUANG, N. E., S. R. LONG, AND Z. SHEN, 1996: The mechanism for frequency downshift in nonlinear wave evolution. Adv. Appl. Mech., 32, 59–111.

HUANG, N. E., Z. SHEN, S. R. LONG, M. C. WU, H. H. SHIH, Q. ZHENG, N.-C. YEN, C. C. TUNG, AND H. H. LIU, 1998: The empirical mode decomposition and the Hilbert spectrum for nonlinear and non-stationary time series analysis. Proc. R. Soc. London, Ser. A, 454, 903–995.

FLANDRIN, P. AND P. GONCALVES, 2004: "Empirical Mode Decompositions as a Data-Driven Wavelet-Like Expansions," Int. J. of Wavelets, Multires. and Info. Proc., Vol. 2, No. 4, pp. 477-496

FLANDRIN, P., G. RILLING AND P. GONCALVES, 2004: "Empirical Mode Decomposition as a Filter Bank," IEEE Sig. Proc. Lett., Vol. 11, No. 2, pp. 112-114.

OONINCX, P.J., AND HERMAND, J.P., . 2004: Emperical mode decomposition of ocean acoustic data with constraint on the frequency range, Proceedings of the Seventh European Conference on Underwater Acoustics, Delft.

WU, Z., AND N. E. HUANG, 2004: A study of the characteristics of white noise using the empirical mode decomposition method. Proc. R. Soc. London, Ser. A, 460, 1597–1611.

THE EFFECT OF THE DRIVING WIND FIELDS ON THE ACCURACY OF WAVE MODELLING IN THE BLACK SEA

Nikolay Valchev [1], Nadezhda Valcheva [1],
Miroslav Petrov [2], Veneta Ivanova [2]

(1) Institute of Oceanology – Bulgarian Academy of Sciences, Varna

(2) National Institute of Meteorology and Hydrology, Varna branch

INTRODUCTION

The importance of the wind waves is marked as they define the sea state representing the surface, which divides the ocean and atmosphere – the two most important subsystems controlling the climate dynamics. They affect many human activities related to navigation, gas and oil industry, and hydro-technical construction. Moreover, the waves have major impact on human and environmental security in the coastal zone. Therefore, wind waves gain strategic geophysical significance and their observation and forecasting are relatively well-developed.

Availability of realistic input information on spatial and temporal distribution of driving forces affects significantly accuracy of wave simulations. In recent years a number of studies (Cardone et al., 1995; Günther et al., 1998) arrived to the conclusion that the wind fields derived from global models either in operational mode or by means of reanalysis tends to reproduce with no sufficient accuracy the real conditions. In the present study this problem is brought to the geographical frames of the Black Sea where long-term observations in open sea areas are extremely rare. This shortage impedes the global models from getting proper solutions of the atmospheric circulation. Hence, there is need data of atmospheric pressure or surface wind from different sources to be compared and suitable regional model capable to reasonably reproduce the driving fields to be selected.

DATA AND MODELS

Results derived for the Black Sea region through a couple of regional atmospheric models (RAM) both forced with the major reanalysis (ECMWF and NCEP/NCAR) data are considered. These models are: REMO, designed in the Max Planck Institute, and the one developed in the St. Petersburg branch of State Oceanographic Institute (SPB SOI). While REMO is a hydrostatic circulation model that calculates three dimensional atmospheric fields of many meteorological parameters (Feser et al., 2001) driven in this case by the NCEP/NCAR global wind reanalysis, the SPB SOI model is primarily designed to estimate the wind input (Davidan, 1995) and currently is run using atmospheric pressure reanalysis data.

Three wave models that have proved their viability and are widely exploited in the world prognostic centers are adopted. WAM (cycle 4) and WAVEWATCH-III are third-generation wave models, which solves the wave transport equation explicitly without any assumptions on the shape of the wave spectrum. They are comprehensively described in Komen et al. (1994) and Tolman (1999). The Spectral Parametric Model (the latest version issued in 2001 is employed) is an improved second-generation model. It parameterizes feasibly weak non-linear wave interactions and accounts for wave induced stresses in the boundary layer (Davidan, 1996).

NUMERIC EXPERIMENTS

The models are implemented on the Black Sea spherical grid, which is extended from 27.0°E to 42.0°E and from 41.0°N to 47.0°N. Wind input is provided by REMO with spatial resolution of about 50km (Feser et al., 2001). These wind data are believed to be homogeneous enough to serve wave modeling. Wind fields are derived also using SPB-SOI model driven by both NCEP/NCAR and ECMWF (ERA project) reanalysis with 0.5° spatial resolution. The output wind fields have been stored at every hour. Besides, information drawn from synoptic maps is used for extreme storms.

Wave models WW-III and SPM are implemented with the same resolutions using the SPB-SOI model output. WAMC4 is forced both with the REMO/NCEP and SPB-SOI wind fields with 0.5° spatial resolution. Integrated parameters and total sea and swell spectra output are obtained at every 3h. The wave models are run for deep water

case using frequency-directional spectrum with 25 frequencies and 24 directional bands.

DISCUSSION

Analysis is carried out taking into account two issues: evaluation of input wind forcing quality and resulting accuracy of wave simulations. Therefore, wind speed time series, simulated for two of the severest storms in the Black Sea during last 50 years, are compared with meteorological stations records. Comparison between the regional atmospheric models output concerns extreme storm events occurred during 16 – 22 February, 1979 and 3 – 10 February, 2005. The model results are evaluated against the wind speed measurements carried out at the hydro meteorological station Kaliakra. It is situated on the most jutting out cape along the Western Black Sea coast. Storms were distinguished with powerful and continued inrush of cold air masses from northeast. The high waves during the first event was coupled with persistent storm serge, which combined effect led to catastrophic consequences for the Bulgarian coast.
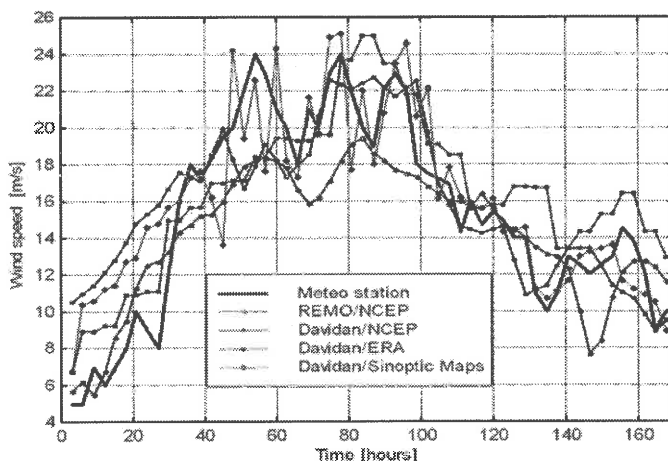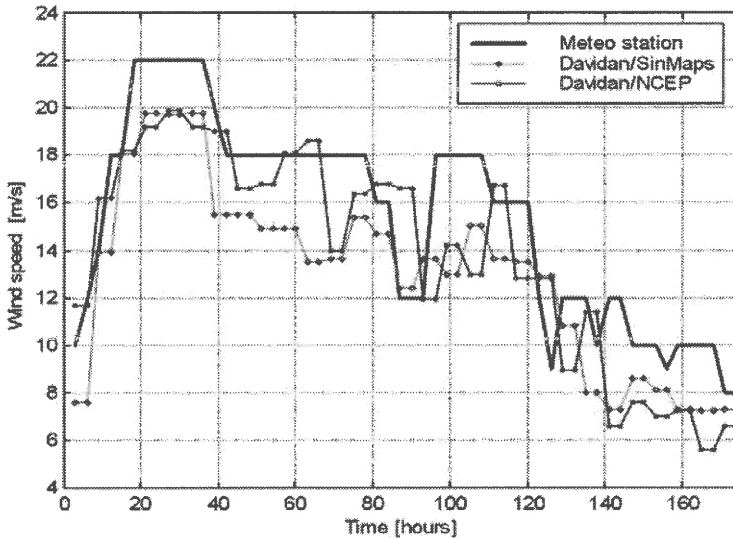
Figure 1. Accuracy of input wind fields: RAM outputs for the closest to cape Kaliakra deep water grid point for two storm events in February, 1979 (top) and February, 2005 (bottom).

During the developed stage of the first storm (see Fig. 1a) wind speed reaches 24m/s twice. The three observed peaks are caught by model when driven with synoptic maps' data, and the differences do not exceed 1-3m/s. In the Davidan/ERA and Davidan/NCEP series first peak is not apparent and the computed speed is 5-6 m/s lower compared to measurements. The second and third peaks cannot be well discerned, but the quality of simulation is high with slight overestimation (Davidan /ERA) or underestimation (Davidan/NCEP) of observed values. The best agreement is noted for the mentioned series. As for the REMO/NCEP one, the degree of underestimation is higher – about 6 m/s. Similar performance is indicated during entire phase of storm growth.
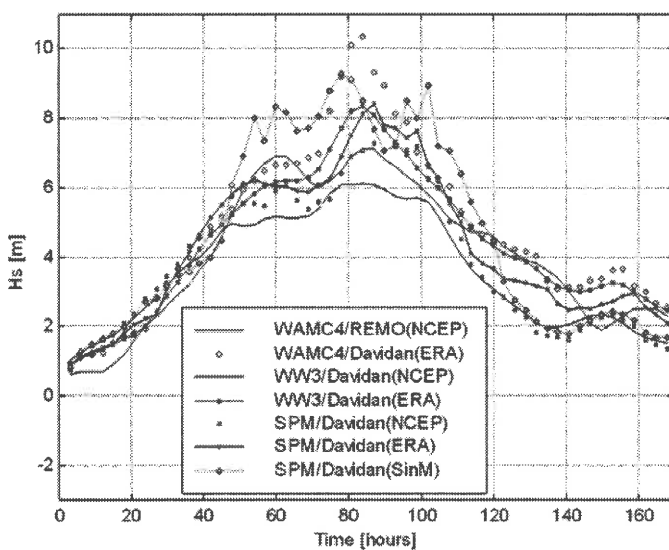
Estimated error statistics indicates that wind speed simulated with the SPB-SOI model deviate less, in particular using NCEP reanalysis (bias 0.13m/s) and synoptic maps' (RMSE 2.66m/s) data, while through the ECMWF reanalysis errors result higher: bias -0.86m/s, RMSE 3.30m/s. The same statistics for the REMO series are even larger and read 1.87m/s and 3.36m/s, respectively.

With respect to the second storm it is obvious that models slightly underestimates the observed wind speed in particular in the phase of very rapid storm growth (see Fig. 1b). During this stage simulations based on synoptic maps are better whilst for the rest of the storm interval reanalysis driven wind fields appear to be more realistic. This fact indicates the high feasibleness of used forcing data, namely NCEP/NCAR sea level pressure reanalysis product.

It is important to be noted that estimated for 10-year period (1972-1981) REMO wind speed series RMSE is 3.83m/s and for the SPB-SOI – 3.70m/s. These values are about 1.5 - 2 times grater than those simulated with similar models basing on ECMWF reanalysis for the North (Komen et al., 1994) and the Baltic Sea (Lavrenov, 1998). The main reason should be sought in deficiency of data for the Black Sea open areas for assimilation into the RAMs.

Further, the effect of the wind data feasibility on the accuracy of the modeled significant wave height is considered by comparison with buoy measurements. The first step is to model the wave field during storms discussed above. Simulation results can be seen in Fig. 2. In the case of first storm we do not dispose with measurements for that particular location but regarding the second one some visual observations are available that allow general comparison to be done.

Given the development of atmospheric situation for the period of the first storm, one could guess that wave simulation with SPM based on synoptic maps data reproduces best the wave growth (see Fig. 2a). Similar results are obtained with WW-III and again SPM when they are forced with sea level pressure data. The highest waves are simulated with WAMC4 but not in the case in which the NCEP/NCAR wind reanalysis serves as input source. As a whole little divergence could be found between results obtained through reanalysis and synoptic maps' data except for the storm peak, which is important enough to be taken into consideration.
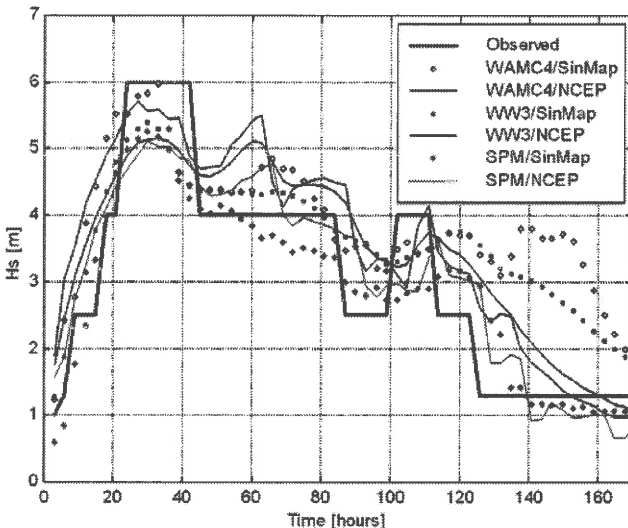
Figure 2. Wave models output for the same as in the previous figure grid point for studied storm events in February, 1979 (top) and February, 2005 (bottom).

As for the second storm, in its first stage the most realistic are WAMC4 simulations when the model is forced with synoptic maps' input while in the decay phase better agreement is noted for series reproduced with SPM despite of the origin of driving force information (see Fig. 2b). Contrasting with the previous storm, larger discrepancies between different series is noted but mostly at some stage in decay and due to the second peak (63rd hour) emerging at the NCEP reanalysis driven simulations. It does not appear neither in observations nor in synoptic maps based wave simulations. Therefore, it can be concluded that models performed accurately enough.

Second option for assessment of wave models accuracy is comparison against directional buoy data set obtained in the northeastern part of the Black Sea. An underestimation of measured H_s prevails with respect to WAMC4 simulations driven with the REMO wind fields. However, since WAMC4 has proved world wide its excellence and is positively validated against both wave measurements and other wave models performance, the main reason for the result in this case study is attributed to the limited quality of Black Sea wind fields, calculated on the basis of global wind reanalysis.

86
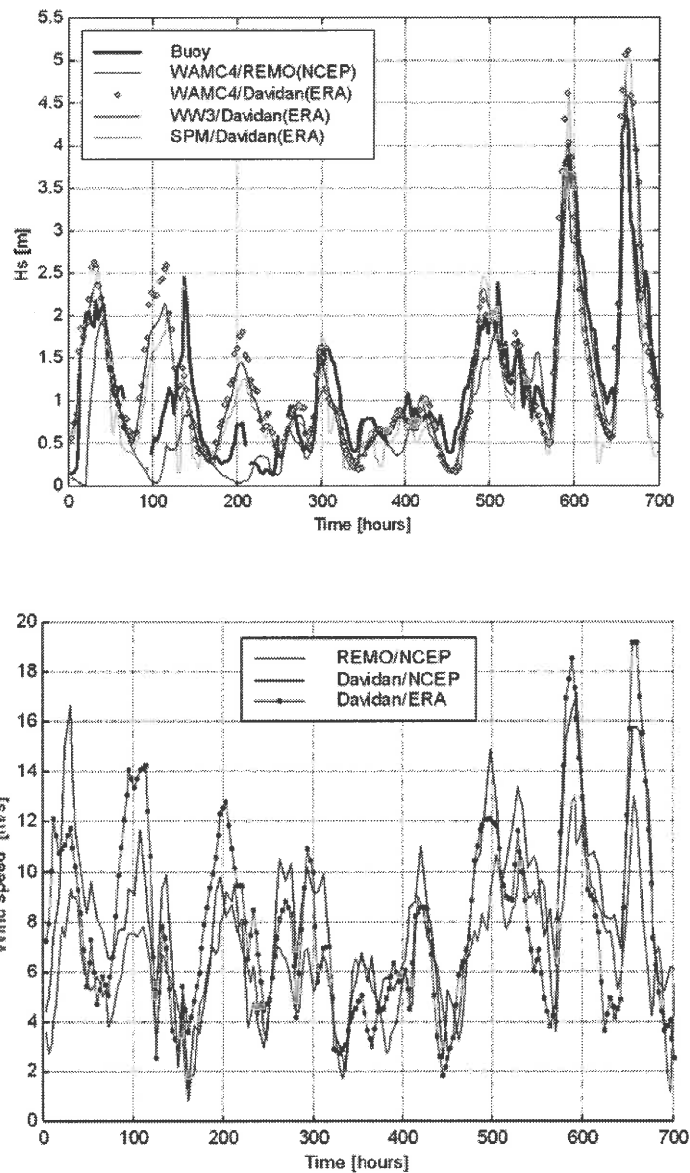
Figure 3. Wave models accuracy: simulated vs. buoy H_s, measured off Gelendzhik (top), taking into account of the driving winds (bottom) for the period January 10th-Febraury 3rd, 1997.

If wave models are run with wind input coming from the SPB-SOI model a better reconstruction of H_s field is obtained. Example for wind speed simulations are shown in Fig. 3b. During the second part of the period all wave models reach proper performance although differences in the input wind speed still exist. This is the reason

why Lavrenov (1998) points that wave field can be considered as a filter, which smoothes the wind input errors.
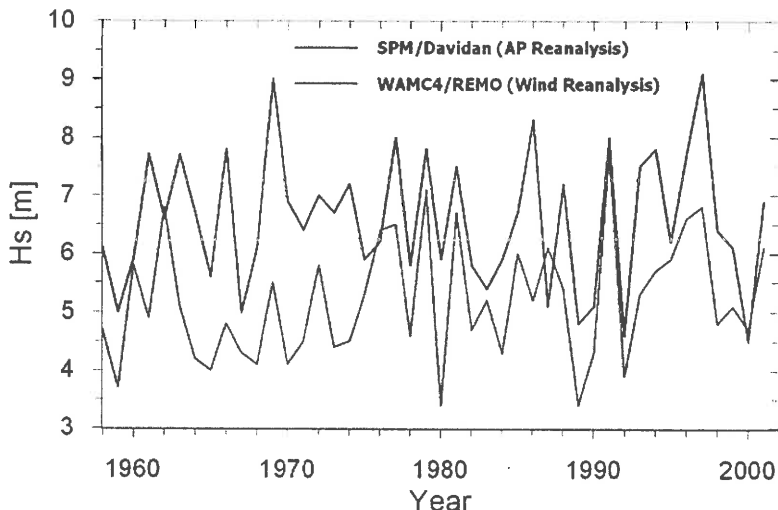
Figure 4. 43-year simulated H_s series for the closest to cape Kaliakra grid point.

The advantage of sea level pressure reanalysis application is further corroborated by comparison of significant wave heights hindcast with two of adopted models – WAMC4 and SPM – and driven with different input wind data as indicated in Fig. 4. The period spans 43 years (1958-2001). In wave climatic aspect, the difference between annual maxima significant wave heights calculated using these sets exceeds 20%.

CONCLUDING REMARKS

It is found that more realistic wave fields are simulated using the atmospheric pressure field reanalysis rather than the reanalysis of surface wind. This is substantiated by assessment of both regional atmospheric and wave model output as well as providing wave climatic features. Identified errors are quite due to atmospheric models input than to the wave models themselves. Reanalysis of wind fields significantly underestimates the wind speed, whilst the atmospheric pressure reanalysis appears to be more reliable source for wave modeling purposes.

By developing potentials of the global reanalysis through enhanced data assimilation and spatial resolution, REMO considerably improves the quality of wind

source information but still not sufficiently in regards to the Black Sea part of the domain. With this respect, the issue how far the products of certain RAM could be extended, given the scarce availability of data for assimilation and validation, arises. Taking into account quite good results, the use of data originated from quality synoptic maps, which are not considered in the reanalysis process itself, is found to be suitable alternative for resolving some extreme storms. This fact also confirms the convenience of using the sea level pressure reanalysis rather than the surface wind one.

With respect to wave modeling, WW-III and WAMC4 simulate very well H_s in particular for higher waves. Using SPM, sound outcomes are at hand as well. The less computer time consumption of this wave model converts it in suitable option for operational use in the Black Sea.

ACKNOWLEDGEMENTS

REFERENCES

CARDONE, V. J., H. C. GRABEN, R. E. JENSEN, D. A. T. COX, T. RESIO, V. R. SWAIL (1995). In search of the true surface wind field in SWADE IOP-1, The Global atmosphere and ocean system, 3(2-3), 107-150.

DAVIDAN, I. N. (Ed.) (1995). Problems in investigation and numerical modelling of wind waves, Gidrometeoizdat, St. Petersburg, 472 (in Russian).

DAVIDAN, I. N. (1996). New results on wind wave growth, Met. and Hydr., 4, 65-72 (in Russian).

KOMEN, G.J., L. CAVALERI, M. DONELAN, K. HASSELMANN, S. HASSELMANN, P.A.E.M. JANSEEN (1994). Dynamics and Modelling of Ocean Waves, Cambridge University Press, UK.

FESER, F., R. WEISSE, H. VON STORCH (2001). Multi-decadal atmospheric modeling for Europe yields multipurpose data, EOS Transactions, 82, 305-310.

LAVRENOV, I. (1998). Numerical modeling of wind waves in spatially heterogeneous ocean, Gidometeoizdat, St. Petersburg, 449 (in Russian).

TOLMAN, H. L. (1999). User manual and system documentation of WAVEWATCH-III version 1.18, NOAA/NWS/NCEP/OMB Technical Note 166, 110.

FATE AND TRANSPORT OF STORM-RIVER-WATER IN A SMALL ULTRA-OLIGOTROPHIC LAKE: TOOLIK LAKE (ALASKA)

Francisco J. Rueda[1], Sally MacIntyre[2] and George W. Kling[3]

(1) Departamento de Ingeniería Civil & Instituto del Agua - Universidad de Granada. C/ Ramón y Cajal, 4. 18071. Granada – Spain.
(2) Marine Science Institute, University of California, Santa Barbara, California 93106-6150. USA.
(3) Department of Ecology and Evolutionary Biology, University of Michigan, Ann Arbor, Michigan 48109

INTRODUCTION

External sources of nutrients, usually entering as pulses (during storms), may control the primary production and, in general, the biogeochemical behaviour of oligotrophic freshwater lakes (Fee et al. 1996; MacIntyre et al. 2006). For example, the temporal changes of the biological community in a small ultra-oligotrophic aquatic system located at 3000 m in southern Spain, with negligible river inflows, can be explained in terms of episodic events of atmospheric depositions (Morales-Baquero et al., 2005). For lakes with larger contributing watersheds, hence, with larger riverine inflows, the impact of atmospheric sources on the nutrient status of inland aquatic systems will depend on the magnitude of atmospheric versus riverine fluxes and the nutrients supplied by each mechanism. While atmospheric sources, deposited in the surface layers, can be immediately available for primary production in the surface layers, the exact flow paths of river-borne nutrients and their availability for algal-growth will depend on whether the storm-river water penetrates to the hypolimnion, inserts in the metalimnion or remains on the surface layers, and whether it is rapidly mixed with overlaying water or remains as definable structures. These pathways, in turn, will strongly depend on features such as lake geometry, stream density relative to lake water (e.g. Fischer et al. 1979), stream hydraulics (e.g. Fleenor 2001) and on the hydrodynamics and mixing away from river inlets (e.g. Fischer and Smith 1983). They will further depend upon volume of the discharge and prevalence of heating versus cooling at the surface both during and after the inflow event. The fate of river water in channelized lakes and reservoirs with simple geometry has been well studied in the literature (e.g. Johnson et al, 1988). However, in lakes of complex geometry, the pathways of riverine inflows are not well known.

The extent of the intrusions, their persistence, and the time scales at which water will reach the different parts of the lake will have considerable importance for ecosystem function. Combined modelling and field studies are thus of considerable importance for developing generalizations as to inflow behaviour.

Our goal is to elucidate and quantify, using a numerical approach and guided by experimental observations, the pathways of storm river-nutrients in a small lake characterized by complex bathymetry (Toolik Lake, Alaska) as physical forcing varies. Our focus on storm events is justified in that a large proportion of riverine nutrient loads into Toolik Lake enters during runoff events. MacIntyre et al. (2006), in a recent study in 1999, estimated that loading of inorganic N from the stream during five days enclosing a storm event was c.a. 40% of the loading that occurs in a typical season (i.e., mid-May to the end of August). Hence, in order to analyze factors affecting growth in such ecosystems, it is appropriate to establish the space-time distribution of river nutrient loadings during and after inflow events. Here, we will illustrate the mechanisms of river water distribution in lakes that, as Toolik Lake, have several basins separated by moraines and sills that restrict lateral motion and assess the spatial and temporal distribution of river-water in the lake.

STUDY SITE

Toolik Lake, Alaska (68°38'N, 149°38'W) -, in the northern foothills of the Brooks Range is an oligotrophic multibasin kettle lake with a surface area of 1.5 km^2, mean depth of 7.1 m, and maximum depth of 25 m (Fig. 1). Air masses affecting local climate come from the Bering Sea to the southwest and from the Arctic front to the north. High winds are associated with the former and cold air masses with the latter (Miller et al. 1986). Due to high concentrations of chromophoric dissolved organic matter in the lake, attenuation of light is relatively high ($k_d \sim 0.5$ m^{-1}), although epilimnetic chlorophyll concentrations are low (Miller et al. 1986). The basic limnology of the lake is reviewed in O'Brien et al. 1997nutrient limitation is discussed in Levine and Whalen (2001); and MacIntyre et al. (2006) discuss physical pathways of nutrient supply in the ice free season
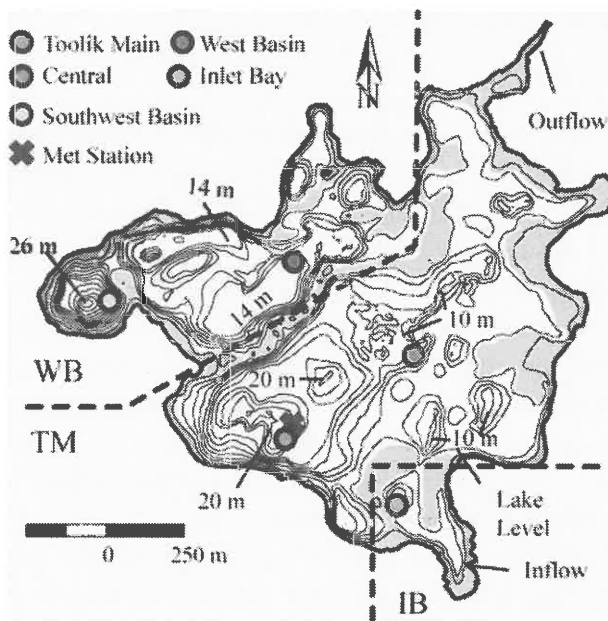
Figure 1. Bathymetric map of Toolik Lake, with isobaths shown every 2 m. Gray areas mark shallow zones, or moraines, which separate the Toolik basin in sub-basins (divisions shown by dashed lines – IB = Inlet Bay; TM = Toolik Main; WB = West Basins). The dots mark deployment locations and sites where model results are checked. (Our thermistor chain in the West Basin was located further to the west; to the left of the 1 of 14m. Consider moving the red dot.)

MATERIALS AND METHODS

Approach - We analyzed the space-time distribution of river water, as it flows into Toolik Lake, in simulated tracer experiments. First, a three-dimensional model of the hydrodynamics of Toolik Lake was validated against field data collected during the ice free period on 2004. Then the storm-river-water flow paths in Toolik Lake were studied by simulating the dispersion of a passive tracer released at the river inflow section at different times during three storm events. During this first set of numerical experiments, the tracer was released continuously at all times when the river inflow Q was larger than 2 m^3s^{-1} (Q> 2 m^3s^{-1}). The river water is presumed to have a constant tracer concentration which is set to an arbitrary value of 100 mmol m^{-3}.

Experimental data - The experimental data set consists of time series of water temperature collected at different depths (colored marks in Fig. 1), meteorological variables, lake-water level and river water inflows and temperature during the ice-free

period of several years. Details of the experimental set up can be found in MacIntyre et al. (2006).

Numerical simulations – Numerical simulations of circulation and transport in Toolik were conducted with a three-dimensional (3-D) free surface hydrodynamic model (e.g. Smith 1997; Rueda and Cowen, 2005). To make sure that the model provides a valid representation of inflow and mixing processes in Toolik Lake a validation exercise was conducted. A period of 32 days in 2004, starting on day 188, which includes three inflow events, was simulated with the model. The simulated time series of temperature profiles at Toolik Main station was then compared with the temperature observations collected at those same points and during that same period (see Fig. 3). The model was forced using observed temperatures and estimated inflow rates in Toolik Inlet, heat and momentum fluxes calculated from local atmospheric variables from on lake measurements following calculation procedures in MacIntyre et al. 2002). From observed water level fluctuations in the lake (Fig. 1), rainfall and inflow rates the outflow rate was estimated and used as boundary condition at the outflow section. Using the velocity field from the simulations for the selected periods, a series of tracer release experiments were conducted. The computations were conducted on a domain that includes all Toolik Lake, using 20 x 20 x 0.5 m grid cells. The time step was set to 30s, for stability purposes.

RESULTS

Meteorological data - The ice-free season in Toolik Lake is marked by periods of heating interspersed with cold fronts, during which rainfall and inflow events occur (Fig. 2) which have the potential to perturb the nutrient climate in the lake. The exact distribution of river-borne nutrients, i.e. the fate of river water in the lake, will strongly depend on the sequence of hydrodynamic events during and after the event, which are forced by meteorological conditions. Cold and wet fronts are associated to winds with medium to strong magnitude (of up to 9 ms^{-1}) from the North to Northwest, which result in energetic mixing and deepening of the surface layers. The strongest winds, with gusts of up to 15 ms^{-1}, are, though, from the south and also induce strong mixing events in the water column. The strongest wind event during 2004 was from day 202 to 204 and, during that time, the surface mixed layer deepened between 1 and 2 m (see Fig. 2). During the heating periods, incoming shortwave radiation had daily maxima approaching 800 Wm^{-2}, and under relatively calm conditions, with winds of at most 4 ms^{-1} usually from the south, the water column stratifies.

94

Temperature data and intrusion depth – Three events occurred with high discharge. All were associated with cold fronts, but air temperatures dropped considerably below lake temperatures for the first and third and the water column cooled. Intrusion depth could be, a priori, estimated by comparing the inflow temperature against the temperature profiles. According to this ad-hoc and simplistic (for ignoring mixing processes) procedure river inflow would intrude at the depth where river temperature equals that of the water column. Figure 2 (bottom) shows, in color, time series of isotherm depths, together with a thick black line marking the theoretical depth of intrusion at each time.
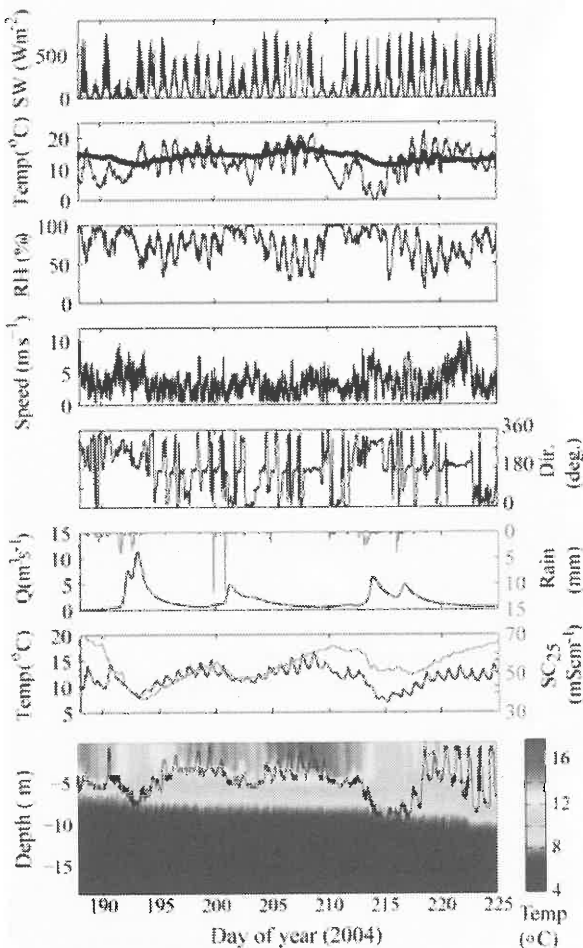
Figure 2. A) Short wave radiation, B) air and surface water temperatures (thick black line), C) relative humidity, D) wind speed, E) wind direction, F) stream discharge Q and rainfall (note the rain is upside down) G) stream temperature and conductivity normalized to 25oC, and F) water temperatures with a thick black line indicating intrusion depth were it only a function of stream temperature for Toolik Lake in 2004.

95

Model Validation against field data – Figure 3 shows daily averaged simulated (line) and observed (dots) temperature profiles, every two days, during the simulation periods for 2004 respectively. Observed and simulated temperatures are for Toolik Main station (Fig. 1). The Root Mean Squared Error (RMSE), a norm of the model error (see Rueda and Schladow, 2002 for a definition), of the simulations for 2004, estimated by comparing observed and simulated daily-averaged temperature profiles (a total of 30 profiles with 25 points each corresponding to all but the first and last day of simulations), is 0.1486°C.
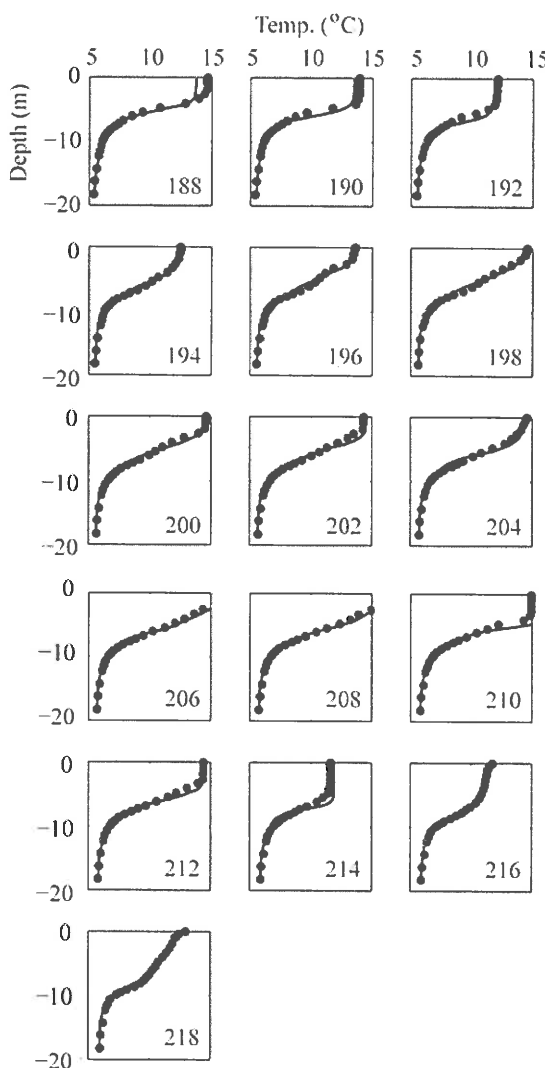
Figure 3. Simulated (continuous line) and observed (dots) daily-averaged temperature profiles at Toolik Main, shown every two days during the study period in 2004.

Inter-basin exchange mechanisms over moraines – River water injected into a given sub-basin of Toolik Lake, will reach the other basins, separated by moraines, if

1) *Shallow overflow* - Inflow intrusion occurs shallow enough, i.e. above 3 m of depth.

2) *Overflow exchange mechanism* - Inflow intrusion occurs deeper, but still, the inflow volume is such that the intrusion structure thickens until it reaches the level of the moraines. We will refer to this mechanism as overflow route, one that is purely advective.

3) *Vertical mixing pathway* - Inflow intrusion is deep, but cooling/mixing occurs, inducing an upwards transport of river plume waters to the surface layers. Once in the surface layer, it will be subject to lateral wind driven transport processes.

4) *Internal displacement pathway* - Inflow is deep, but, strong enough winds from the West or North act on the surface, inducing partial upwelling of deeper metalimnetic waters, until they reach the level of the shallow moraines and above.

Shallow overflows – Examination of the time series data in Fig. 2 indicates that this mechanism will likely only be most important when the water column is well stratified, stream temperatures do not change much during inflow events, and when atmospheric cooling is minimal. Later we will discuss the implications of the volume of discharged water.

Overflow exchange mechanism – Presuming an inflow intrusion with a level of neutral buoyancy at 8 m (see Fig. 2), the volume that needs to be filled in order to reach the 3 m depth, which is the level of the submerged moraines, and the time it takes to fill, are determined by the particular bathymetry of the sub-basin and the inflow rate. For the purposes of analyzing mechanisms of inter-basin exchange, Toolik Lake was sub-divided into three sub-basins: Inlet Bay (IB), Toolik Main (TM) and Western Basins (WB). For IB, the volume between 3 and 8 m depth is 71320 m^3, while for TM it is 2488780 m^3. For the inflow event in 1999, one of the largest in the experimental data set, the inflow rate was above 2 $m^3 s^{-1}$ during 2 days, and was characterized by an average inflow rate of 7.43 $m^3 s^{-1}$ and maximum values of c.a.16 $m^3 s^{-1}$. At the average inflow rate, IB would fill in 2.67 h and then start spilling water to the other adjacent basins, while TM would fill only after about 4 days. Hence, it is

97

only in the smallest sub-basins or depressions existing near the inlet, that the overflow mechanism is responsible for inter-basin exchange during inflow events.

Internal-displacement above moraine level – Internal displacement mechanism is, by its own nature, intermittent. The occurrence of internal-displacement exchanges above moraine levels will be will be examined with the aid of the simplest possible model of wind effects on a lake, consisting of a two-layer stratified fluid contained in a rectangular box and subject to an impulsively applied wind stress. In this model it is further assumed that rotational effects and wind stress variability are negligible. According to linear theory, the magnitude of the thermocline displacement z_{max} can be found as

$$z_{max} = -L / Ri^*$$ (2)

where L is the fetch length of the lake, and Ri^* is the bulk Richardson number, given by

$$Ri^* = \frac{\alpha g \Delta T h}{u_*^2}$$ (3)

Here, h is the depth of the surface layer, α is the thermal coefficient of expansion, ΔT is the temperature difference across the thermocline, and u^* is the water friction velocity due to wind stress τw. Presuming that (1) the bottom of the surface layer is located at 5 m with temperature jump of c.a. 5°C, and (2) TM basin is roughly 1000 m long in the EW direction, one can estimate the magnitude of the westerly winds that will induce internal displacements with excursions of 2 m (the difference between the depth of the moraines and that of the bottom of the surface layer – see Fig. 3), and hence, exchange of a river intrusion over the WB-TM moraines. The minimum wind speed to induce isotherm displacements, large enough to bring river intrusions in TM over the moraines and inject them in WB is between 6 and 7 ms^{-1}. The 6ms^{-1} wind speed threshold is only reached, for example, during the first event in 2004 (lasting 3 days from day 192 to 195), in 15% of the time (11 h) and, in particular, on 5 occasions of less than 3 hours each.. Though, simplistic, this model suggests that the internal-displacement route is infrequent and possibly not important, which leaves the vertical mixing route as the most plausible mechanism by which river water is able to reach the western basins of Toolik Lake.

Vertical Mixing – Figure 4 shows, as a contour plot, the time series of area-average tracer concentration (mmols m^{-2}) for three basins in which Toolik Lake has

been discretized: Inlet Bay, Toolik Main and the Western Basins. The averaged concentration profiles were plotted for the three inflow events in the period of study in 2004. In all cases, river water starts as a mid-depth intrusion, and rapidly flows to the bottom of Inlet Bay. Once the first inflow event finished (after day 195), river water in IB remained attached to the bottom, slowly diffusing to the after-storm river water above.. It is not until the last flushing event (e.g. that starting on day 215) that water from the first and second events were flushed from Inlet basin. In Toolik Main, inflow occurred as a metalimnetic intrusion during the first storm event, with concentrations which remained above their upper and lower values for at least 15 days after the end of the event on day 195. Similar to the Inlet basin, the intrusion structure only faded away after the flushing event on day 215. In the Western Basins, the concentration initially peaked at 7-8 m below the free surface, indicative of deep intrusions probably fed by upwelling of intrusion structures in Toolik Main. Shortly afterwards, the tracer concentration became uniform in the first 5 m at values which are near concentrations in Toolik Main. These results suggest vertical mixing followed by wind-driven advection as the most plausible interbasin exchange mechanism between TM and the Western Basin. For the other events, inflows were at 5 and 8 m respectively and mixed with the overlying water within a few days. Concentrations in WB increased after the mixing began in Toolik Main again supporting the role of vertical mixing combined with horizontal advection in inducing exchange of water across the moraine.

In summary, the fate of river water in multiple basin lakes is highly dependent upon the volume of the discharge and the meteorological forcing which accompanies the storms. Only when discharge is appreciable, as in 1999, is the overflow exchange mechanism dominant enabling much of the incoming water to reach basins separated by shallow features such as sills and moraines. During moderate and low discharge events, much of the water remains trapped in the inlet basin. The percentage remaining will be dependent upon the degree of surficial cooling. The fate of incoming nutrients during low discharge events will be highly dependent upon their timing of release from the landscape and we hypothesize a greater proportion of those released early in a discharge event will be likely to reach the euphotic zone. In contrast, during high discharge events, much of the inflowing water will reach the larger basins as an intrusion with the availability of the nutrients to the euphotic zone dependent upon subsequent cooling events.
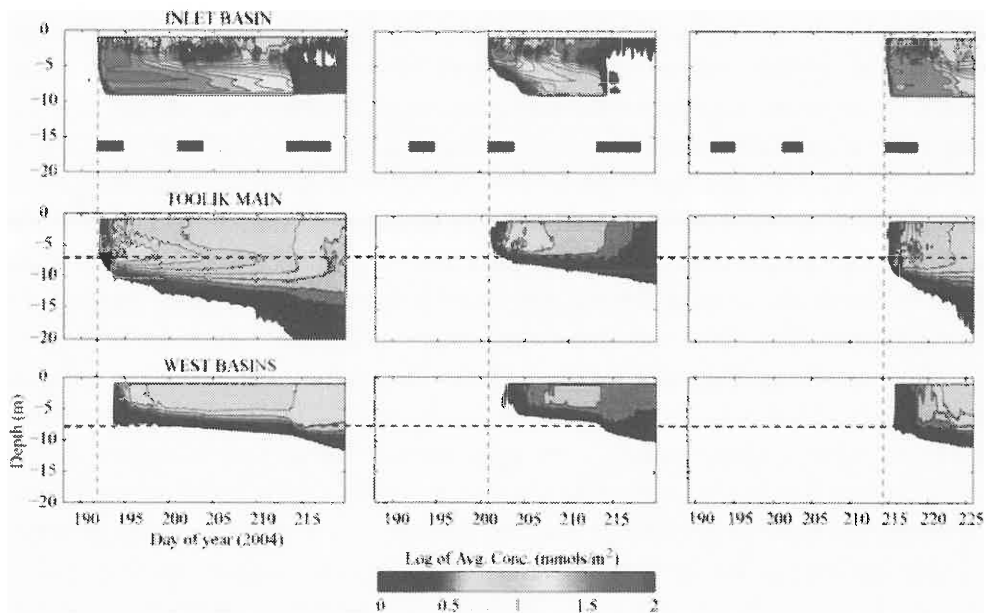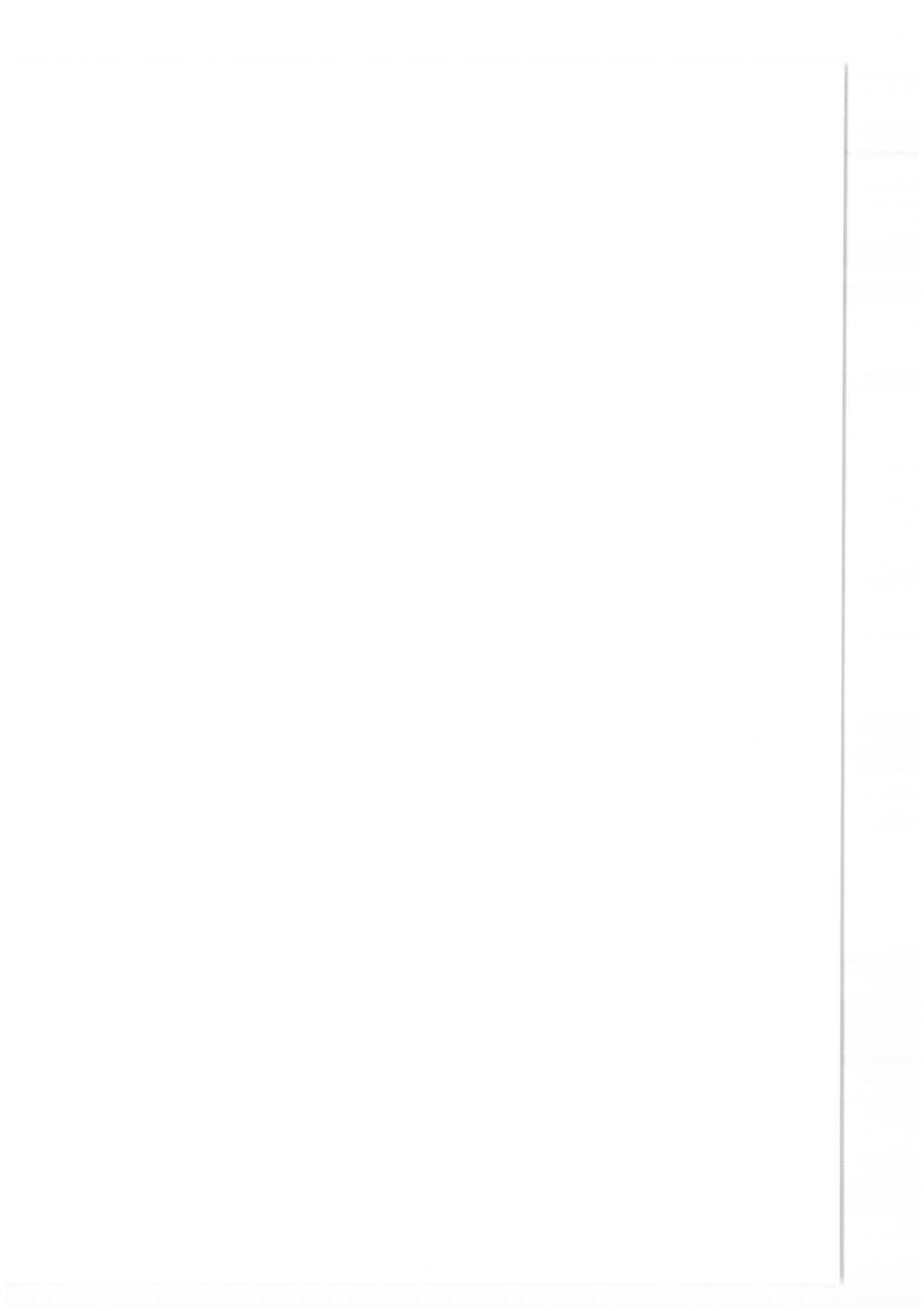
Figure 4. Profiles of average concentration (mmols/m^2) of tracer in the Inlet Basin, Toolik Main and West Basins. Moraines separate the three basins. The black squares indicate the duration of the inflow events, when water is marked with tracer. The lines are shown here for reference and comparison among events.

REFERENCES

FEE, E.J., R.E. HECKY, G.W. REHEHR, L.L. HENDZEL AND P. WILKINSON. 1994. Effects of lake size on nutrient availability in the mixed layer during summer stratification. Can. J. Fish. Aquat. Sci. 51: 2756-2768.

FISCHER, H.B., LIST, E.J., KOH, R.C.Y., IMBERGER, J. AND BROOKS, N.H., 1979. Mixing in Inland and Coastal Waters. Academic Press.

FISCHER, H.B. AND SMITH R.D., 1983. Observations of Transport to Surface Waters from Plunging Inflow to Lake Mead. Limnol. Oceanogr., 28 (2): 258-272.

FLEENOR, W.E., 2001. Effects and Control of Plunging Inflows on reservoir Hydrodynamics and Downstream Releases, Dissertation, University of California, Davis. 2001.

JOHNSON, T.R., ELLIS, C.R. AND STEFAN, H.G., 1988. Experimental Study of buoyancy induced plunging into reservoirs and coastal regions. Project Report No. 245, St. Anthony Falls Hydraulics Laboratory, University of Minnesota, Minneapolis, MN.

LEVINE, M.A. AND S.C. WHALEN. 2001. Nutrient limitation of phytoplankton production in Alaskan arctic foothill lakes. Hydrobiologia 455: 189-201.

MACINTYRE, S., J. R. ROMERO, AND G.W. KLING. 2002. Spatial-temporal variability in mixed layer deepening and lateral advection in an embayment of Lake Victoria, East Africa. Limnol. Oceanogr. 47: 656-671.

MACINTYRE, M, J.O. SICKMAN, S.A. GOLDTHWAIT AND G.W. KLING. 2006. Physical pathways of nutrient supply in a small, ultraoligotrophic arctic lake during summer stratification. *Limnol. Oceanogr.,* 51(2), 2006, 1107–1124

MILLER, M.C., P. SPATT, P. WESTLAKE, D. YEAKEL, AND G.R. HATER. 1986. Primary production and its control in Toolik Lake, Alaska. Arch. Hydrobiol. Suppl. 74: 97-131.

MORALES-BAQUERO, R., PULIDO-VILLENA, E. AND RECHE, I., 2005. Atmospheric inputs of phosphorus and nitrogen to the Southwest Mediterranean region: Biogeochemical responses of high mountain lakes. Limnol. Oceanogr., In press.

O'BRIEN, W. J., M. BAHR, A.E. HERSHEY, J.E. HOBBIE, G.W. KIPPHUT, G.W. KLING, H. KLING, M. MCDONALD, M.C. MILLER, P. RUBLEE, AND J. R. VESTAL. 1997. The limnology of Toolik Lake. *In* A.M. Milner and M.W. Oswood, [eds.], Freshwaters of Alaska. Ecological Studies volume 119. Springer-Verlag.

RUEDA, F.J. AND E.A. COWEN. 2005. The residence time of a freshwater embayment connected to a large lake. Limnol. Oceanogr. 50(5), 1638–1653.

SMITH, P. E. 1997. A three-dimensional, finite-difference model for estuarine circulation, Department of Civil and Environmental Engineering. University of California.

ADVERSE SUPERPOSITION OF EUTROPHICATION AND ATMOSPHERIC WARMING – EFFECTS ON DEEP WATER STRATIFICATION IN THE UNIQUE ECOSYSTEM OF LAKE OHRID

Andreas Matzinger[1]; Alfred Wüest[1]; Zoran Spirkovski[2]; and Suzana Patceva[2]

(1) Swiss Federal Institute of Aquatic Science and Technology (Eawag) - Limnological Research Center, CH-6047 Kastanienbaum, Switzerland
(2) Hydrobiological Institute, MK-6000 Ohrid, Macedonia

Lake Ohrid (surface area ~358 km^2, volume ~55 km^3) in south-eastern Europe is one of the few ancient, long-lived lakes of the world, harboring more than 200 endemic species. Based on internal and external nutrient monitoring a progressing eutrophication was detected, which led to a ~3.5 fold increase in phosphorus (P) concentration of the lake over the past century. Fortunately, the lake is still oligotrophic with high concentrations of dissolved oxygen (DO), which in turn is the prerequisite for the vast endemic bottom fauna. In this contribution, we concentrate on the question whether Lake Ohrid could potentially loose one of its unique properties of having high oxygen concentrations even in the deepest ranges of the 288 m deep water body. The high level of oxygen in the deep water could be jeopardized by changes in the stratification persistency and strength, caused by salinity and temperature gradients. Salinity can build up in the deep water layers by production-induced dissolution of calcite and organic matter. In addition, temperature gradients in deep natural waters could form, if the atmospheric warming would consistently increase to such an extent, that the top-bottom temperature differences can not be eliminated on sub-decadal basis or be compensated by deep heat input, e.g., from geothermal sources. Coupling a k-ε turbulence scheme with a bio-geochemical lake model it was found that the hypolimnetic DO is very sensitive (i) to changes in anthropogenic P load via mineralization of organic material and (ii) to atmospheric warming via decrease of mixing and the reduction of the occurrence of complete deep convection. Moreover running different scenarios combing the two impacts indicated that they amplify each other. In order to prevent anoxia over the next decades, P load must be decreased significantly. In more concrete and absolute terms: To keep DO > 4 mg/L (an arbitrarily chosen limit) over the next decades, the P load must be

decreased by 50%, if the currently predicted atmospheric warming of 0.04 °C/yr is used as a boundary condition. It is important to realize, that the increase in stratification (leading almost to a long-term isolation of the deep water) is triggered by the warming and not the higher absolute temperatures per se. In contrast, deep convective mixing would be even more frequent than today under higher temperature equilibrium, as a result of the temperature dependence of the thermal expansivity of water. After the introduction to the unique lake system, different model scenarios will be presented and conclusions will be drawn relative to the unique endemism associated with the high oxygen level at great depth.

THE HYDROGRAPHY OF ALFACS BAY. AN STUDY OF INTER-ANNUAL VARIABILITY

J. Solé, A. Turiel, C. Llebot, M. Estrada, D. Blasco,
M. Delgado, M. Fernandez, J. Diogéne

The Alfacs bay is a semi-enclosed estuary placed in the south of the Ebro river delta. This area represent not only a scientific interest from the physical and ecological point of view but also a great economic interest for the shellfish cultures. The hydrography of the bay has been studied in different published works and from the early 80's to now a monitoring of the main physical and biological variables is maintained. The present study is a preliminary view of the hydrographic data collected between 1990 and 2004. The time series used in this study are the salinity (Fig. 1) and temperature (Fig. 2) of water at bottom (5 m depth) and at surface (1 m depth) we have calculated the stratification (Fig. 3) and we also have analyzed the meteorological data for the same period, which includes air temperature (Fig. 4), pressure at sea level (Fig. 5), anomaly of precipitation (Fig. 6), and wind (Fig. 7,8). To relate these different time series we use the Empirical Mode Decomposition (EMD), the EMD method, developed by Huang et al. [1998,2004], is used to produce a linear decomposition of series in non-linear modes, which are called Intrinsic Mode Functions (IMF). IMFs are intended to represent partial Hilbert transforms of the signal, and so they posses special properties such as the smoothness in both frequency and amplitude modulation. The method is based on the local time scales of the data, giving a precise meaning to local frequencies and removing spurious harmonics (typical in Fourier analysis) to represent nonlinear and non-stationary signals [Coughlin and Tung, 2004]. The essence of the method is to empirically identify oscillatory modes in the data by means of their local extrema. For this work we have used a MatLab implementation of the algorithm, provided by Patrick Flandrin and collaborators [Rilling et al., 2003]. The code can be retrieved at the following URL: *http://perso.enslyon.fr/patrick.flandrin/emd.html.*

Given two time series, $s^1(t)$ and $s^2(t)$, which have a IMF decomposition: $s^1(t) = \Sigma_n c^1_n(t)$; $s^2(t) = \Sigma_m c^2_m(t)$ where $c^1_n(t)$, $c^2_m(t)$ are the IMFs of each series. We compare the phase differences of two given IMFs: $c^1_n(t)$ and $c^2_m(t)$. To obtain the phase of each IMF we take the Hilbert transform of each mode, which gives a set of complex

modes $c^1_n(t)$ and $c^2_m(t)$: $c^1_n(t) = a^1_n(t) \exp(i\, \Theta^1_n(t))$; $c^2_m(t) = a^2_m(t) \exp(i\, \Theta^2_m(t))$. We are interested in $\Delta\Theta_{nm}(t) = \Theta^1_n(t) - \Theta^2_m(t)$: $\exp(i\, \Delta\Theta_{nm}(t)) = c^1_n(t) \cdot (c^2_m(t))^* / (|c^1_n(t)| |c^2_m(t)|)$; then, we can define $\delta_{nm}(t) = \cos(\Delta\Theta_{nm}(t)) = \mathrm{Re}(\exp(i\, \Delta\Theta_{nm}(t)))$ we take the variance of $\delta_{nm}(t)$ ($\mathrm{var}[\delta_{nm}(t)]$) as an indicator of a constant phase shift, having $\mathrm{var}[\delta_{nm}(t)] = 0$ for constant phase shift and $\mathrm{var}[\delta_{nm}(t)] = 0.5$ for modes have different local frequencies. We choose a threshold of 0.3 for $\mathrm{var}[\delta_{nm}(t)]$ to select the couples of modes with a reasonable time span of constant phase shift.

The results with the different couples are shown in table 1. There are the modes that have a $\mathrm{var}[\delta_{nm}(t)]$ less than the threshold chose. In the figure 9 we can see the modes of water and air temperatures and in 10 the $\delta_{44}(t)$ we observe a constant local phase shift between the two modes of 0. In the figure 11 the couple of water temperature (mode 4) and pressure at sea level (mode 5) and in figure 12 the corresponding $\delta_{45}(t)$. Finally for the coupling between the air (mode 5) and water (mode 5) temperatures (Figs. 13 and 14) we can see an inter-annual oscillation with period of three years.

Using the EMD we have been able to decompose the different time series in a set of modes that can be related in order to find the phase shift between each couple of modes. We observe a reasonable constant phase shift between the modes of the series of: water and air temperature, water temperature and air pressure and stratification and air temperature. We also observe an inter-annual oscillation pattern in the series of water temperatures and air temperatures. Future work can be addressed in to analyze specific periods of the time series and in to improve the IMF separation, which is the key point to find a good phase shift for each couple of series.

Table 1. Couples of modes bellow the threshold. X means variance more than 0.3.

	Temp.	Pres.	Wind E-W	Wind N-S	Precip.
Strat.	6 vs. 4	6 vs. 5	X	X	X
Temp. Bot.	4 vs.4 5 vs.5	4 vs. 5	3 vs. 4	3 vs. 4	
Temp. Sur.	4 vs. 4 5 vs. 5	4 vs. 5	4 vs. 4	4 vs. 4	7 vs. 7
Sal. Bot.	6 vs. 6	5 vs. 5	X	X	X
Sal. Sur.	X	X	X	X	X
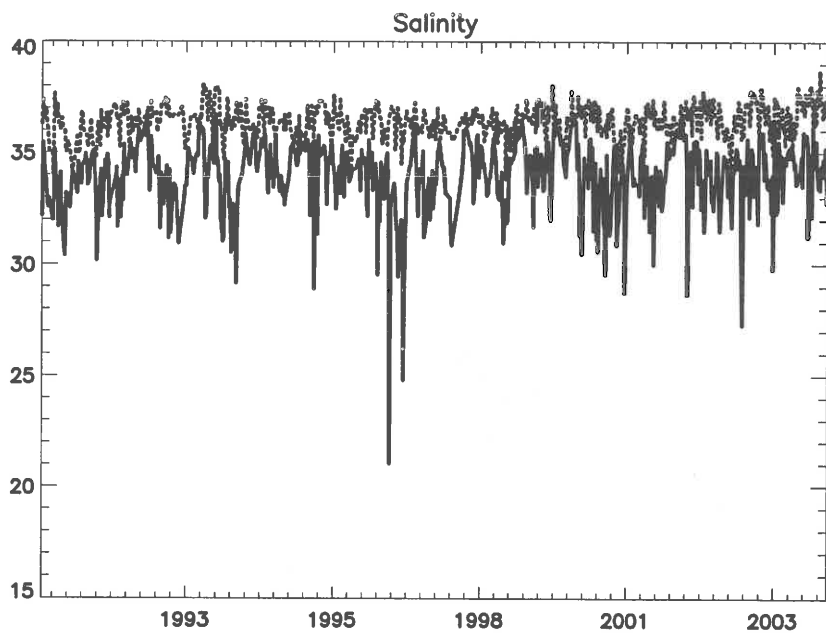
Figure 1. Salinity at center of Alfacs bay from 1990 to 2004.
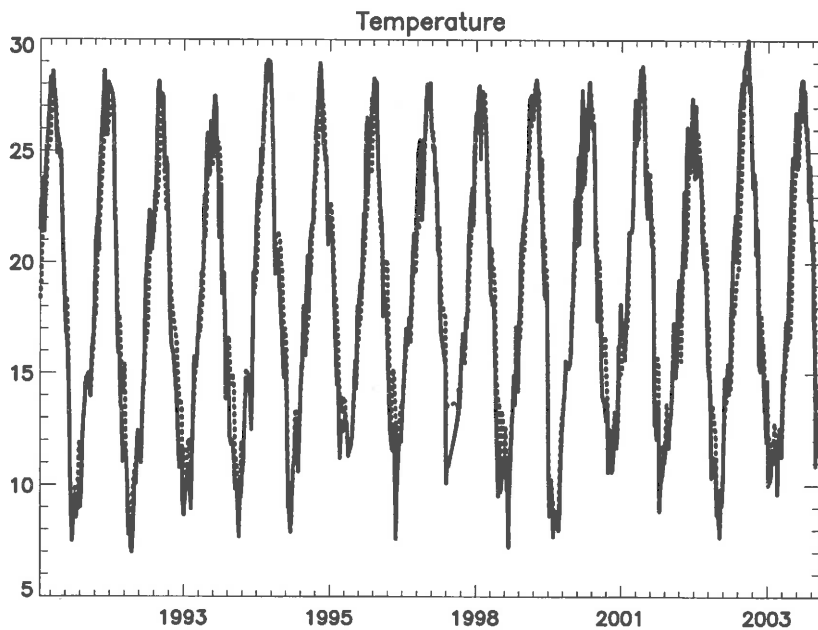
Figure 2. Temperature at center of Alfacs bay from1990 to 2004.
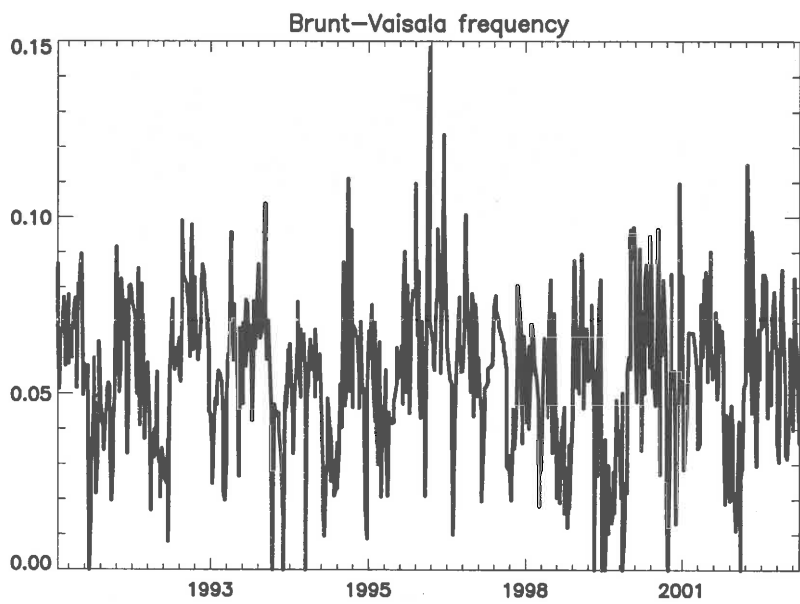
Figure 3. Evolution of stratification index from 1990 to 2004.
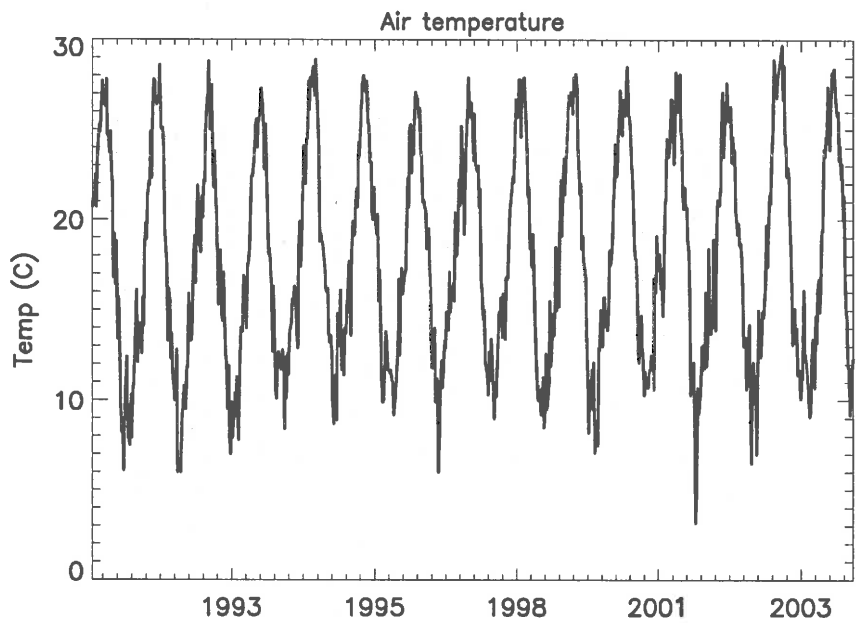
Figure 4. Evolution of air temperature from 1990 to 2004.

108
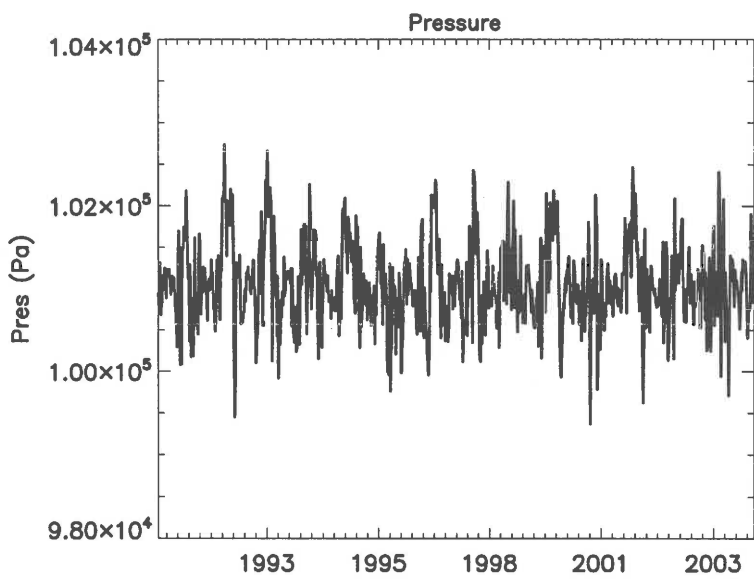
Figure 5. Evolution of air pressure at sea level from 1990 to 2004.
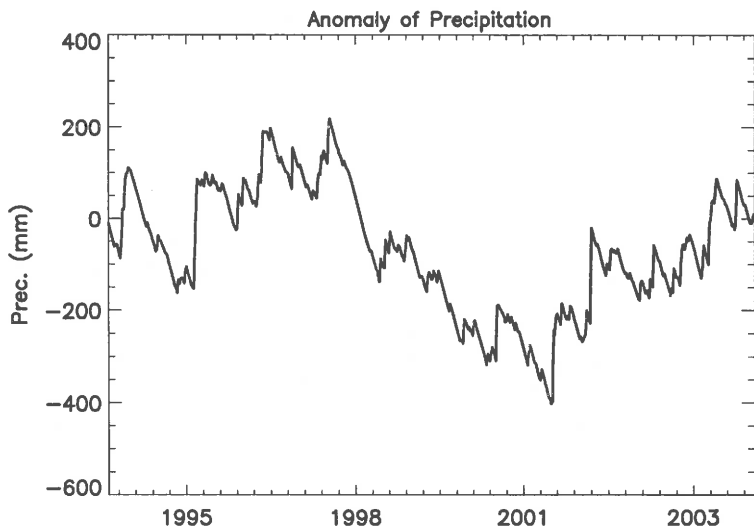
Figure 6. Evolution of precipitation anomaly. Years 1994-2004.

109
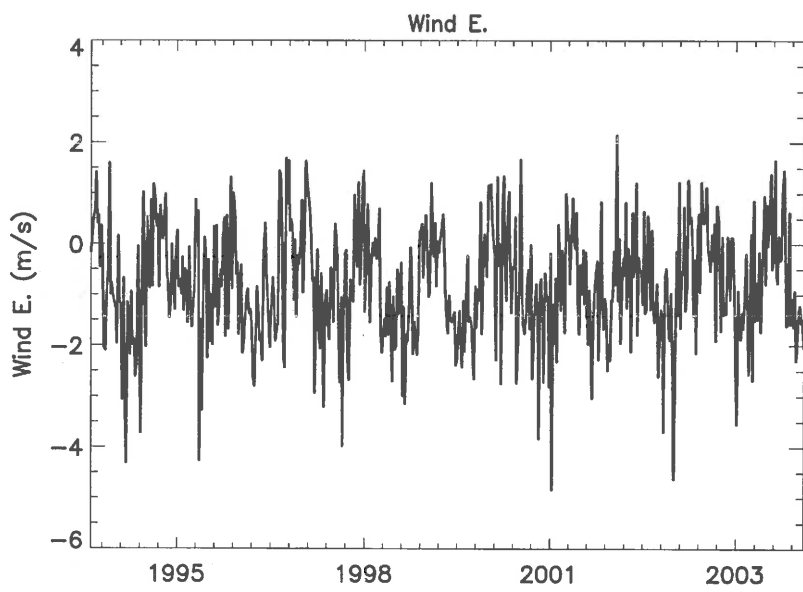
Figure 7. Evolution of Wind: East component. Years 1994-2004.
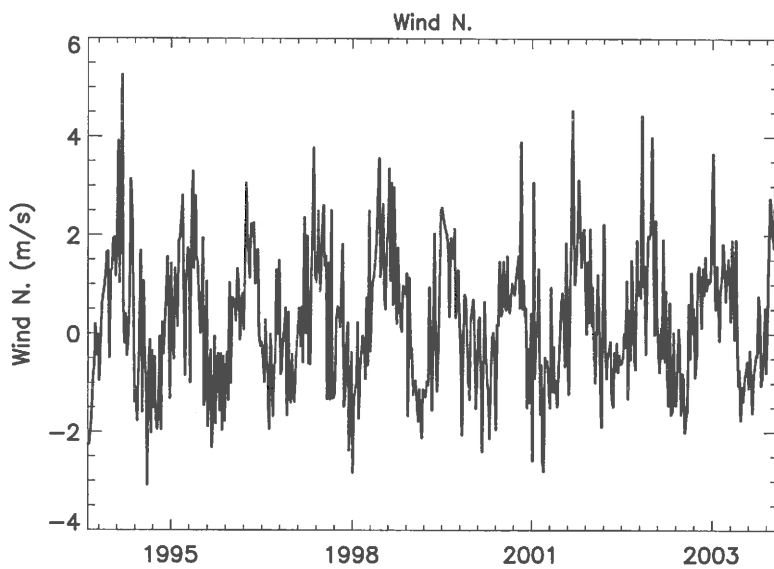
Figure 8. Evolution of Wind: North component. Years 1994-2004.

110
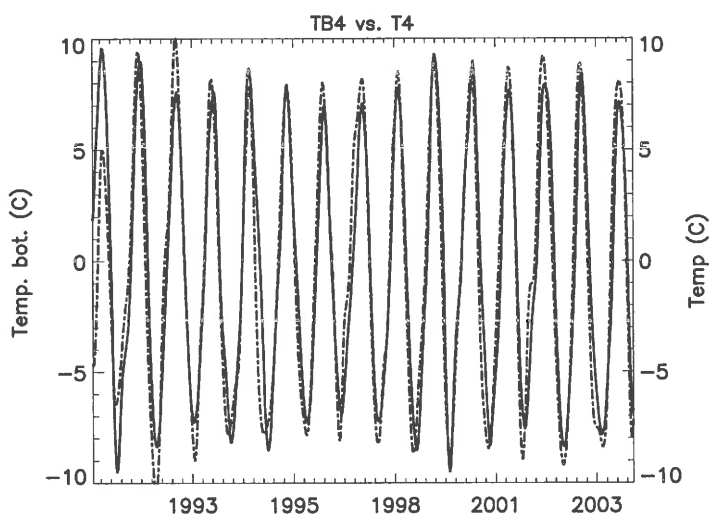
Figure 9. Mode 4 of temperature at bottom vs. mode 4 of air temperature.

Figure 10. δ_{44} (t) for the fig. 9.

111
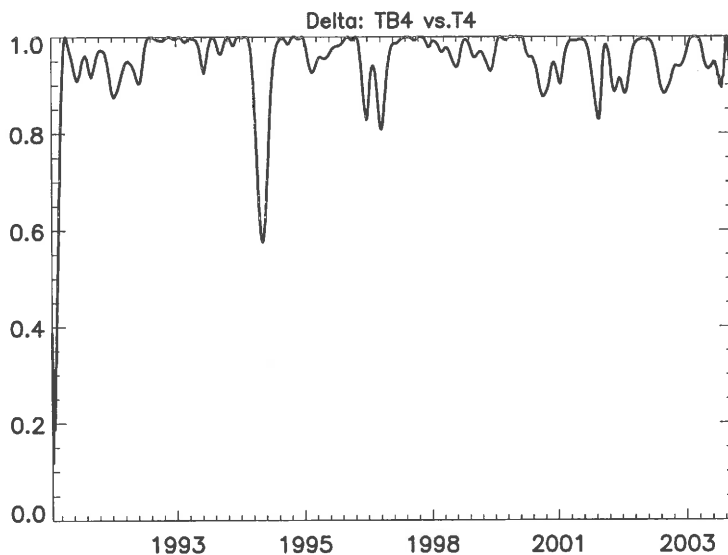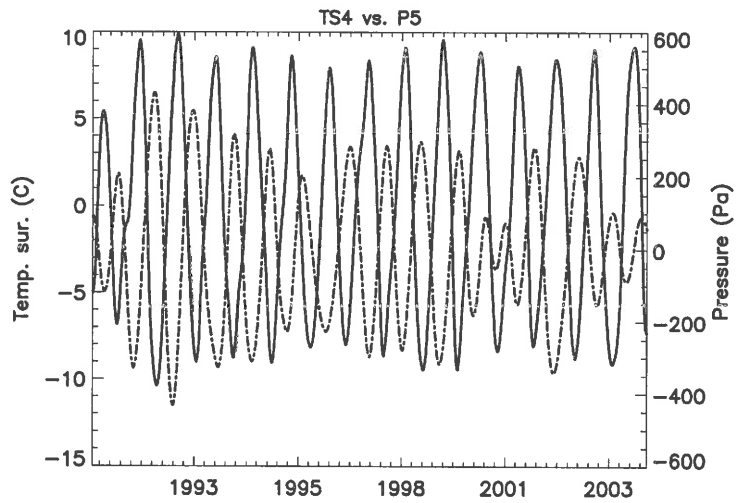
Figure 11. Mode 5 of temperature at surface vs. mode 5 of air temperature.
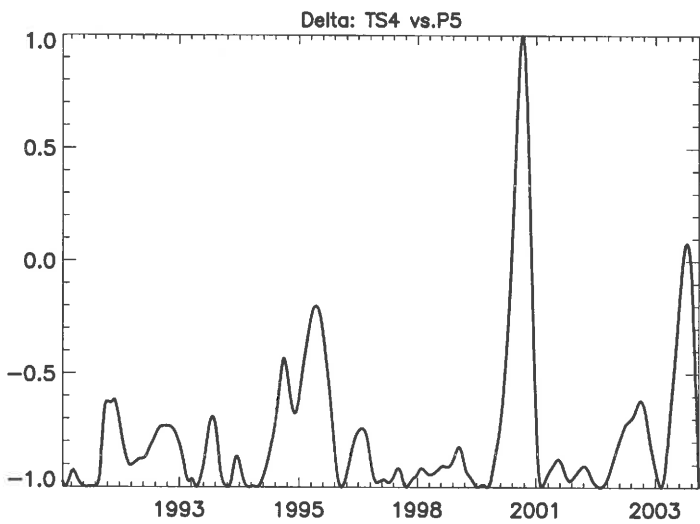
Figure 12. δ_{45} (t) for figure 11.
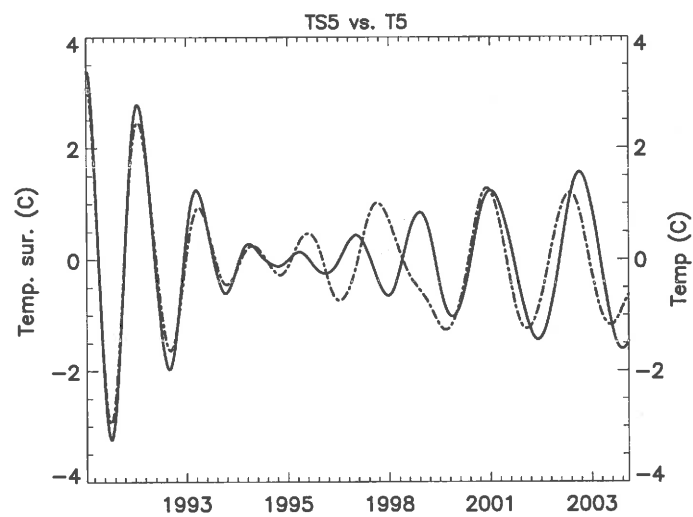
Figure 13. Mode 5 of temperature at surface vs. mode 5 of air temperature.
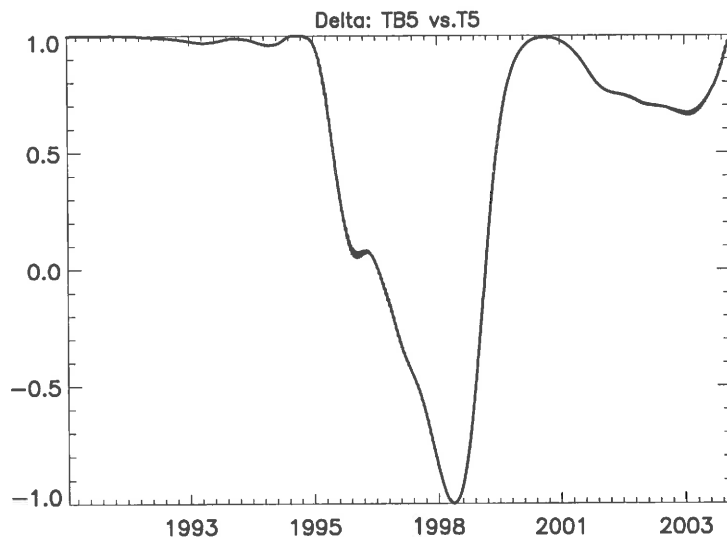
Figure 14. $\delta_{55}(t)$ for figure 13.

113

REFERENCES
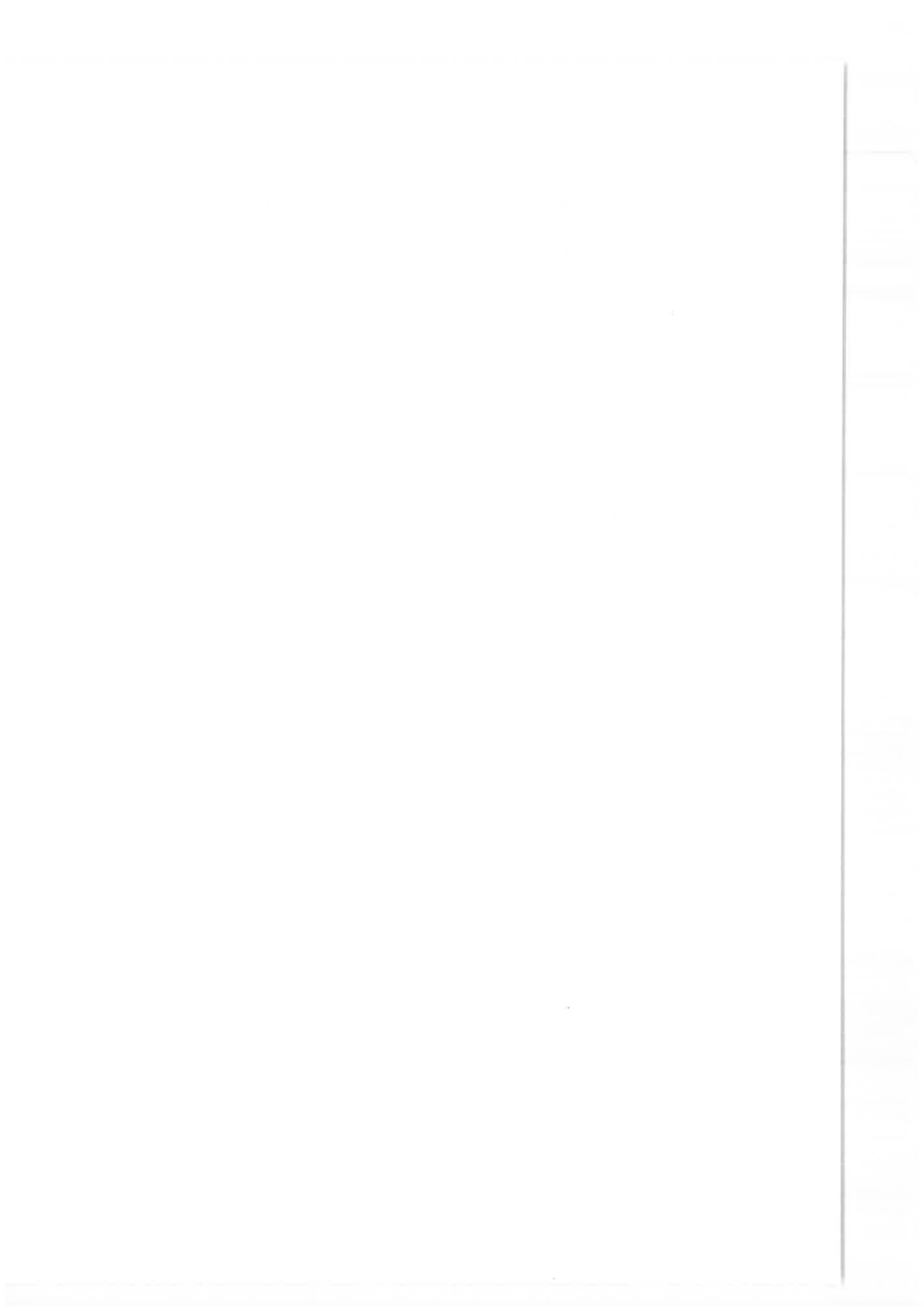
COUGHLIN, K., AND K. TUNG (2004), 11-year solar cycle in the stratosphere extracted by the empirical mode decomposition method, Advances in Space Research, 34, 323 329.

FLANDRIN, P., G. RILLING, AND P. GONÇALVÈS (2004). Empirical mode decomposition as a filterbank. Signal Processing Letters, IEEE, 11, 112-114.

HUANG, N., Z. SHEN, S. LONG, M.WU, H. SHIH, Q. ZHEN, N. YEN, C. TUNG, AND H. LIU (1998), The empirical mode descomposition and the Hilbert spectrum for nonlinear and non-stationary time series analysis, Proceedings of the Royal Society of London, 454, 903 995.

HUANG, N., M. WU, S. LONG, S. SHEN, W. QU, P. GLOERSEN, AND K. FAN (2003), A confidence limit for the empirical mode decomposition and Hilbert spectral analysis, Proceedings of the Royal Society of London, 459, 2317-2345.

THE EFFECT OF HYPOLIMNETIC OXYGENATION ON WATER QUALITY IN CARVIN'S COVE RESERVOIR

Gantzer, P., Lee Bryant and John C. Little[1]

(1) 418 Durham Hall, Department of Civil & Environmental Engineering. Virginia Polytechnic Institute and State University. Blacksburg, Virginia 24061-0246, USA.

Carvin's Cove is a 24.2 hm^3 water-supply reservoir maintained by the Western Virginia Water Authority (WVWA). It is a shallow monomictic eutrophic lake with a maximum depth of 21.3 meters that traditionally experiences hypoxia in both the hypolimnion and metalimnion during summer stratification. The reservoir has chronic summer algal blooms in the epilimnion coupled with elevated manganese levels in the hypolimnion. Despite having multiple elevations to withdraw water, the algae and manganese cause significant problems during the water treatment process. During the summer of 2005, a linear bubble-plume diffuser was installed to improve raw water quality by adding oxygen. The goal was to eliminate manganese and minimize internal loading of phosphorous which exacerbates seasonal algae blooms. The diffuser consists of two 610-m sections placed 30-m apart in the deepest section of the lake and has a maximum design flow rate of 70 Nm^3 h^{-1}. Observations during the first year of diffuser operation included 1) significant increase in DO levels throughout the entire hypolimnion, including at the sediment water interface approximately 0.5 m below the diffuser, 2) elimination of the metalimnetic minimum, 3) significant reduction in dissolved manganese, and 4) no noticeable fall algal bloom following turnover. Despite the observed success, the rate at which manganese was removed was slower than observed in Spring Hollow Reservoir, another water supply reservoir with a linear bubble-plume diffuser managed by the WVWA. Water chemistry in both lakes is similar with the exception of alkalinity, hardness, and pH; which are all lower in Carvin's Cove. The slow Mn removal appears to be related to pH. Experimental data shows slow removal during summer stratification and low pH (~6.0 – 6.3) compared to faster removal following fall turnover and corresponding increased pH (~7.2 – 7.5).

TRANSIENT VARIATION IN SEDIMENT OXYGEN DEMAND AS A FUNCTION OF DIFFUSER-INDUCED TURBULENCE

Lee Bryant and John Little[1]

(1) Department of Civil and Environmental Engineering, 418 Durham Hall, Virginia Tech, Blacksburg, Virginia

Dissolved oxygen (DO) concentrations have been identified as one of the most critical ecological factors controlling water quality and consequent environmental conditions (Hondzo et al. 2005). Aquatic ecosystems, drinking water quality, and hydropower plants are all negatively impacted by depleted levels of DO. Water quality standards typically target DO > 5 mg/L to protect aquatic life, and hydropower plants are usually required to meet these minimum DO levels in the water they discharge downstream. It has recently been found that long-term DO depletion in fish habitats can cause significant declines in fish populations as a result of endocrine system disruptions and subsequent reproductive impairment, with low DO possibly having even more of an effect than anthropogenic chemicals (Wu et al. 2006). Organic or nutrient loading of thermally stratified lakes and reservoirs may lead to significant depletion of DO in the lower hypolimnetic water. Hypolimnetic oxygen depletion may result in the release of iron (Fe) and manganese (Mn) from the sediments, thereby decreasing water quality and increasing drinking water treatment costs. Orthophosphate release can promote excessive algal growth which stimulates eutrophication and leads to additional oxygen consumption as settled algal detritus is degraded. Oxygen depletion is largely controlled by sediment oxygen demand (SOD), which in turn depends on microbial and chemical reactions occurring within the sediment. Understanding these processes is crucial for accurately quantifying SOD, optimizing water quality, and successfully managing lakes and reservoirs (Beutel 2003; Lorke et al. 2003).

SOD is a fundamental parameter that is frequently used to define the overall quality of a water body (Wetzel 2001). Often, SOD measurements based on conditions that are assumed constant are taken as representative of the entire lake or reservoir, with little thought given to the influence of transient processes (Adams et al. 1982; Gelda et al. 1995; Lavery 2001; Beutel 2003). However, SOD and other sediment-water flux measurements obtained under specific environmental conditions may not apply year-round, or even at other locations in the same water body, due to changes in parameters like sediment accumulation, oxygen concentration, and turbulence at the sediment-water interface. Although SOD is typically considered to be governed by the concentration of

organic matter (OM) in the sediment, with high concentrations of OM resulting in an increased oxygen demand, recent work suggests that OM degradation may actually be dominated by sediment loading rates and oxygen exposure time (Kalin et al. 2003; Dittrich et al. 2004; Meckler et al. 2004). Fluctuating turbulence levels in the water column have also been shown to have a significant impact on rates of oxygen diffusion into the sediment (Gundersen et al. 1990; Lorke et al. 2003; Agrega et al. 2005). Because these variable processes may cause significant changes in SOD, recent literature has suggested that there is a need for work focusing on transient oxygen fluxes into the sediment (Nogami et al. 2000; Higashino et al. 2004).

Hypolimnetic oxygenation systems (e.g., bubble-plume diffusers), used increasingly by drinking water and hydropower utilities to replenish DO while preserving stratification, may impact SOD via diffuser-induced turbulence and increased DO concentration gradients (McGinnis et al. 2002). Unfortunately, reservoir-specific SOD measurements are rarely available and oxygenation systems are often designed based on oxygen depletion rates measured prior to installation of the diffusers (Mobley et al. 1997). It has been found that after the diffusers are turned on they are sometimes unable to meet the reservoir oxygen consumption rate, possibly because of the additional diffuser-induced demand that they cause (Beutel 2003). Little work has been done to actually quantify how diffuser use impacts SOD, oxygen penetration into the sediment, and fluxes at the sediment-water interface.

We have performed a series of field and laboratory experiments that focus on how SOD is impacted by diffuser-induced changes in near-sediment oxygen concentrations and turbulence levels. Corresponding variations in trace metal (Fe, Mn) concentrations at the sediment-water interface were also studied. The main objectives of this research were (1) to investigate the impact of hypolimnetic oxygenation on oxygen penetration into the sediment and SOD, (2) to examine the specific influences of elevated DO concentrations and turbulence on SOD, and (3) to evaluate subsequent effects on the water quality of the overlying water-column.

MATERIAL AND METHODS

Study and sampling sites - Our research is focused on two drinking-water-supply reservoirs, Spring Hollow Reservoir (SHR) and Carvin's Cove (CC), that are managed by the Western Virginia Water Authority (WVWA) to supply drinking water to the city and county of Roanoke, Virginia. These reservoirs are quite different in age, bathymetry, flow characteristics, and sediment composition (Table 1 and Figure 1); thus, we have the ability to collect and compare data from two very different field sites. CC is an old, stream-fed lake that has been managed by WVWA as a drinking-water-supply reservoir

since the late 1940's. Due to its age, there is significant sediment accumulation in CC. SHR is a young reservoir with minimal sediment accumulation that was constructed by WVWA in 1996. SHR is filled by pumping from the Roanoke River. The water quality in both CC and SHR is preserved by bubble-plume-diffuser oxygenation systems installed to replenish oxygen depleted during summer stratification. Hence, we have the ability to carefully control the oxygen and turbulence (mixing) conditions in both reservoirs via diffuser operations. The diffuser systems can deliver either air or pure oxygen gas over a wide range of flow rates, providing considerable operational flexibility for control of hypolimnetic DO and turbulence.

	SHR	CC
Maximum depth (m)	62	23
Surface area (km^2)	0.6	2.5
Volume (m^3)	13×10^6	24×10^6
Avg. length × width (m)	1500 × 450	8000 × 600
Diffuser length (m)	620 (1 diffuser line)	1250 (2 × 625 m diffuser lines)

Table 1. Comparison of bathymetry and oxygenation system characteristics at Spring Hollow Reservoir (SHR) and Carvin's Cove (CC).
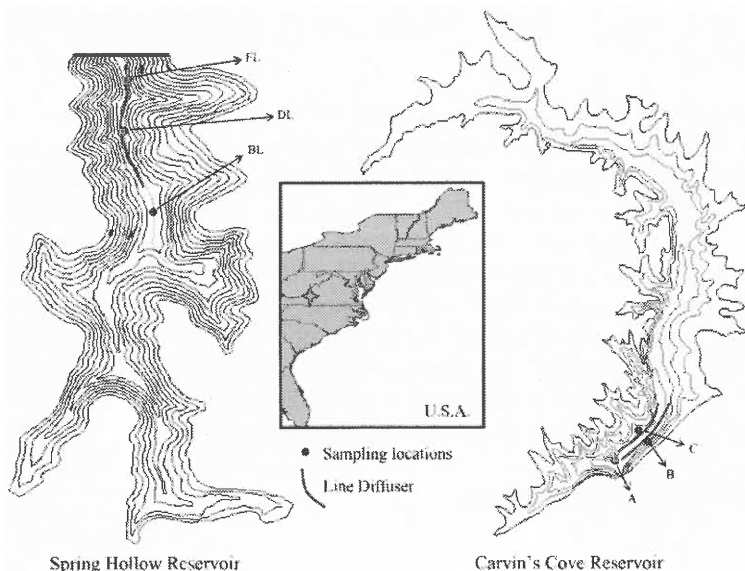
Fig. 1. Map of Spring Hollow Reservoir and Carvin's Cove showing locations of the sampling sites and linear diffusers.

Experimental setup - We collected data to characterize fluxes at the sediment-water interface as a function of oxygenation using sediment cores, oxygen microsensors, and in-

situ porewater samplers ("peepers") (Lewandowski 2002). Corresponding water column data was obtained via profiling with a CTD probe (Seabird). Sediment, porewater, and water column data was collected prior to, during, and following diffuser use. Through controlled diffuser operations, fluxes at the sediment-water interface were studied as conditions at the sediment surface ranged from anoxic (before diffuser use) to highly aerobic (during diffuser use). Concentration gradients of DO, Fe, and Mn in the water column immediately above the sediment and within the first several centimeters of porewater were measured using DO microsensors and peepers to capture variations over time.

DO profiles – Sediment cores were obtained routinely (every 1-2 weeks during peak stratification and monthly during destratification) throughout diffuser operations at the three sampling sites at each reservoir (Figure 1) using a ball corer (Uwitec), with a core tube diameter of 90 mm. Following extraction, the sediment cores were profiled within approximately one hour using Clark-type oxygen microsensors (Unisense A/S OX-100 sensors), which have an internal reference and a guard cathode. The OX-100 microsensor has an outer tip diameter of 100 μm. The microsensors were controlled by a manual micromanipulator (World Precision Instruments, Inc. M3301R) and were connected to a high-sensitivity picoammeter (Unisense A/S PA2000) during profiling. Measurements were obtained in picoamps and the data were converted to DO concentrations using calibration data. For each sediment core profiled, a linear calibration of the microsensors was obtained using DO concentrations in the overlying core water column, as determined via Winkler titration, and in the anoxic sediment (Roy et al. 2004).

Porewater measurements – Peepers were used to obtain in-situ porewater data. We constructed peepers in accordance with the principle of Hesslein's peeper, with a single column of 40 sampling chambers (Hesslein 1976; Lewandowski et al. 2002). The height of each chamber and the distance between each chamber was 1 cm; hence, a vertical profile resolution of 1 cm was obtained. The peeper chambers were initially filled with distilled water and covered with 0.45μm Durapore HV membrane (Millipore). Each peeper was inserted into an aluminum frame which, upon deployment, positioned the peeper vertically into the sediment so that half of the peeper chambers were exposed to the overlying water column and half of the chambers were exposed to the underlying sediment porewater. Two peepers have been deployed for 2-4 weeks at a time at each reservoir (sample sites CC-A and SHR-BL) throughout our experiments. Following retrieval, samples were obtained from each peeper chamber, acidified, and analyzed via inductively coupled plasma (ICP) spectroscopy.

Profile analyses – Oxygen fluxes (J) across the sediment-water interface were calculated from sediment core DO profiles using Fick's Law for diffusion within the sediment (Lavery 2001).

$$J = -\varphi D_s \, (dC/dz) \qquad (1)$$

where D_s is the effective diffusion coefficient for DO in the sediment (m^2/s), φ is the sediment porosity (m^3 porewater/m^3 bulk sediment), and dC/dz is the oxygen concentration gradient at the sediment/water interface ((g/m^3)/m). SOD for steady-state conditions is equivalent to the diffusive flux of oxygen into the sediment (Higashino et al. 2004). Overall, oxygen and turbulence conditions in the reservoirs were changing relatively slowly and quasi-steady-state conditions were assumed. Frequently, oxygen fluxes at the sediment-water interface are calculated based on the thickness of the diffusive boundary layer (DBL) immediately overlying the sediment surface, rather than oxygen diffusion within the sediment, as this allows DO consumption processes within the sediment to be ignored (Rasmussen et al. 1992; Steinberger et al. 1999; Lorke et al. 2003; Higashino et al. 2004). However, because we are currently obtaining our DO profiles from extracted sediment cores, the DBL is not adequately preserved in our profiles. Hence, we have determined SOD from the concentration gradient of the sediment DO profile immediately at the sediment-water interface (Lavery 2001; House 2003; Higashino et al. 2004). SOD values calculated using oxygen profiles within the sediment have been checked by performing parallel SOD analyses using incubated cores in a laboratory batch system (Rasmussen et al. 1992; Agrega et al. 2005).

SOD, which is a function of both diffusion and biological and chemical reactions within the sediment (House 2003; Higashino et al. 2004), was estimated from the near-surface oxygen concentration gradient because the rate of oxygen consumption due to sediment biological and chemical processes within our system is not currently known. To obtain some insight into these consumption processes, both Monod and zero-order oxygen uptake kinetic models were applied to our sediment core profile data (Bouldin 1968; Lewandowski et al. 1991; House 2003; Higashino et al. 2004).

RESULTS

Impact of oxygenation on SOD – DO penetration and the corresponding DO gradient into the sediment increased during periods of oxygenation (Figure 2). While oxygenation systems are designed to remediate problems with SOD and subsequent DO depletion, our results show that they cause SOD to increase (Figure 3). Oxygenation increases the DO concentration gradient between the bulk water and the sediments and possibly also reduces the thickness of the diffusive boundary layer (DBL), the viscous sub-layer of

water at the sediment-water interface that determines the rate-limiting step for oxygen transfer into the sediments (Jorgensen et al. 1985; Lorke et al. 2003).
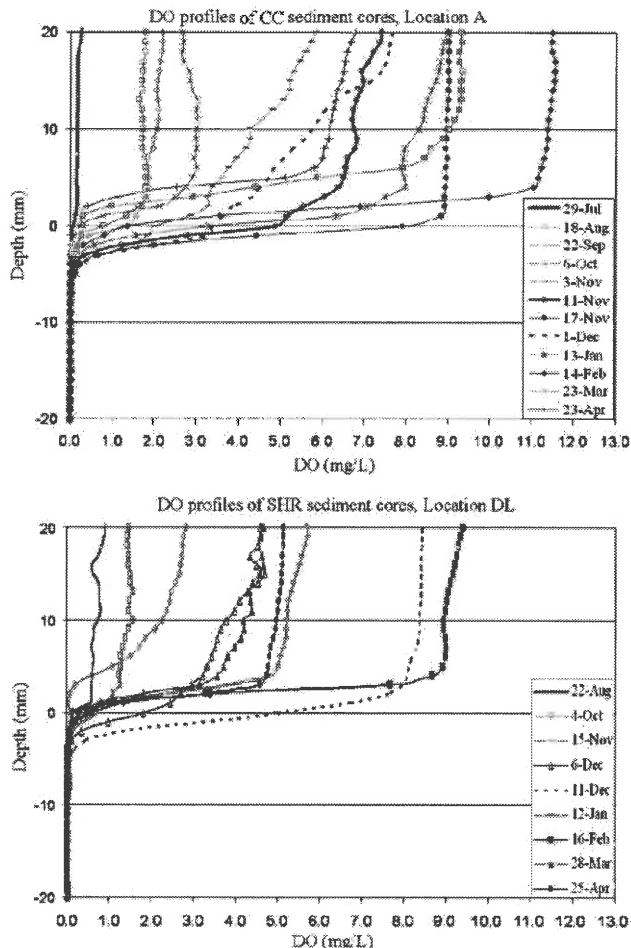
Fig. 2. Changes in sediment core DO profiles as a function of diffuser use. In the CC data set (top plot), the dashed-line profile (12/1/05) was the sole profile obtained during the period when both diffusers were turned off. In the SHR data set (bottom plot), the dashed-line profile (12/11/05) was the sole profile obtained when the diffuser was turned on at this sampling location (DL).

122
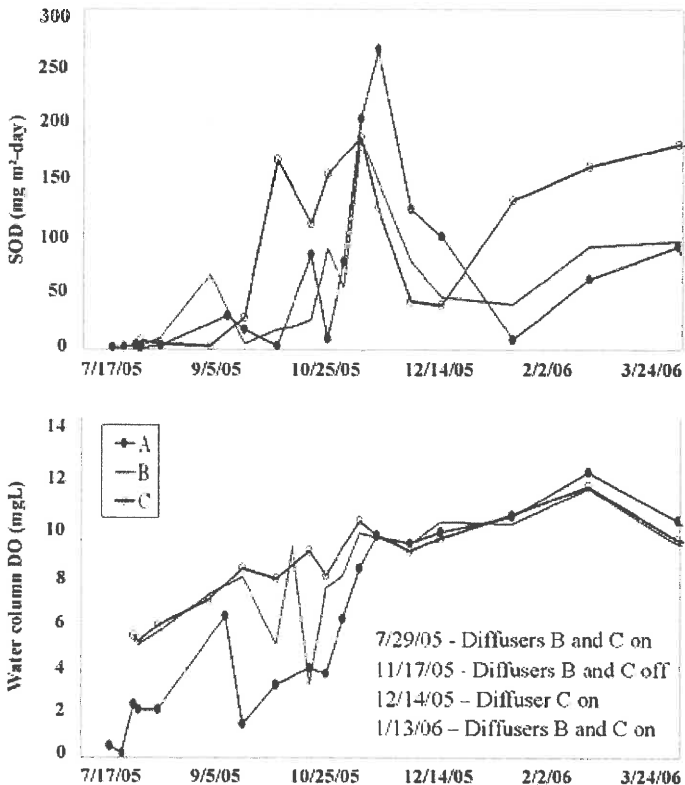
Fig. 3. Comparison of SOD variations over time as a function of diffuser use with DO concentrations in overlying water column (DO data measured 5 cm above sediment core surface via Winkler titration and verified with in-situ CTD data) in CC. Note significant increase in SOD and DO in water column during diffuser use. Importance of turbulence suggested by sharp decrease in SOD during period when diffuser is turned off (11/17-12/14) while the DO 5-cm above sediment surface remains high. Similar trends were observed in SHR (not shown).

Using equations presented by Bouldin (1968) and House (2003), we found that zero-order oxygen uptake kinetics described our experimental data quite well, suggesting that oxygen consumption within the sediments is constant. Monod maximum consumption rates (μ) and half-saturation constants (K_s), calculated using methods presented by Lewandowski et al. (1991), showed significant variation over the duration of our experiments and thus did not describe our data as well as zero-order kinetics. Monod parameters should be constant for a given microbial population; however, sediment microbial communities change in terms of both the microbial population size and type as a function of oxygen availability and penetration into the sediment (House 2003). Thus, if the sediment microbial populations within our reservoir systems are varying as a result of diffuser activity, this could result in fluctuating consumption rates. Future experiments

123

will focus on quantifying changes in microbial populations and also identifying changes in the structure of the microbial community (e.g., Fe- and Mn-oxidizers/reducers) as a function of diffuser activity.

Effect of DO and turbulence on SOD – As shown in Figure 3, a strong correlation between diffuser use and increased SOD is evident up to the point that the diffusers were turned off in mid-November; this increase also corresponds with increasing DO in the overlying water column. The importance of diffuser-induced turbulence is revealed during the period from mid-November to mid-December when the diffusers were turned off and mixing no longer occurs. A sharp decrease in SOD is evident during this absence of turbulence although the DO in the water column remains high. Thus, this data suggests that turbulence is a significant factor in driving oxygen down to the sediment surface, upon which the DO diffuses into the sediment.

Supplementary laboratory experiments were performed to see how re-establishing the DBL in the sediment cores via a mini-diffuser would impact DO penetration and the corresponding SOD. Using a small pump and a bubbling stone, air was bubbled into the sediment core water-column at a flow rate of 25 cm^3/s. Preliminary data from these experiments show that a DBL is formed at the core sediment-water interface by the mini-diffuser. Over time, continuous mini-diffuser activity resulted in increased DO concentrations in the water column and increased DO penetration into the sediment (Figure 4).
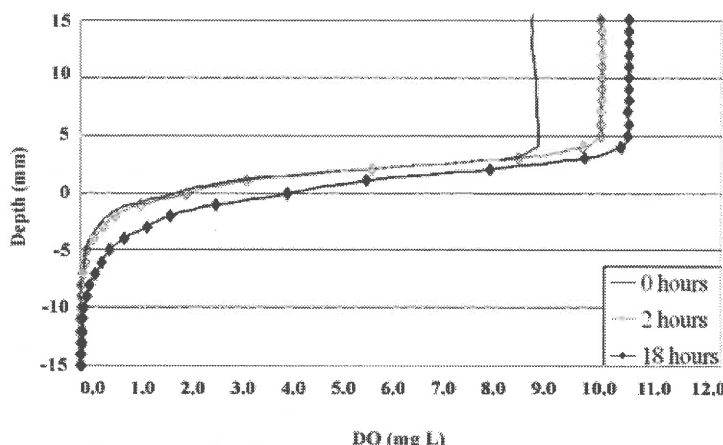
Fig. 4. Variations in sediment core DO profiles and the formation of a DBL as a result of mini-diffuser use.

Impacts on water quality – From a drinking-water standpoint, one of the main goals of oxygenation systems is to decrease levels of soluble Fe and Mn by oxygenating the

water column and increasing the oxidized zone within the sediments to suppress soluble Fe and Mn fluxes (Beutel 2003). During our diffuser operations, we found that concentrations of soluble Fe and Mn decreased significantly in the water column.

Peeper data showed increasing maximal peaks of soluble Fe and Mn just below the sediment surface in correlation with diffuser activity. These peaks of increasing concentrations of Fe and Mn may be a result of several processes. Increased oxidation of sediment organic matter could result in reductive remobilization of Fe and Mn (Zhang et al. 1999). As increased levels of particulate Fe and Mn precipitate out of the oxygenated water column, these particles may also be a source of soluble Fe and Mn upon reaching the less oxygenated environment present at the sediment-water interface. Fe and Mn flux analyses that parallel those focusing on DO fluxes during this study will be performed in future work, thus allowing us to determine whether the influence of oxygenation has a similar effect on other sediment-water fluxes.

CONCLUSION

Through a series of analyses using DO microsensors and sediment cores, we monitored oxygen penetration into the sediment as a function of diffuser use and subsequent oxygen conditions. These measurements were used to determine how diffusion-controlled DO fluxes into the sediment, and the corresponding SOD, were specifically impacted by diffuser-induced turbulence. In-situ porewater data was also obtained in order to quantify the overall impact of diffuser activity and variations in SOD on Fe and Mn cycling. During this study, we acquired experimental data using sediment cores, oxygen microsensors, and peepers; however, we are currently expanding our suite of sampling equipment to include an in-situ miniprofiling lander and sediment traps. With this equipment, we will perform similar analyses using in-situ DBL and sediment flux data obtained with the lander and will use sediment trap data to study the impacts of sedimentation on SOD and nutrient fluxes. Future work will also include biochemical studies of changes in the sediment microbial populations, analyses of Fe and Mn fluxes parallel to those performed on oxygen fluxes during this study, and the development of a computer model that will enable accurate predictions of spatial and temporal variations in SOD and sediment-water biogeochemical fluxes.

SOD is one of the key parameters governing hypolimnetic DO levels and sediment-water fluxes. Lacustrine processes like transient sediment accumulation and composition, oxygen concentration, and turbulence may lead to considerable variations in SOD. This transience could have significant implications when evaluating SOD measurements without taking environmental conditions at the time of testing into consideration. Understanding the impacts that variations in lacustrine processes have on sediments and
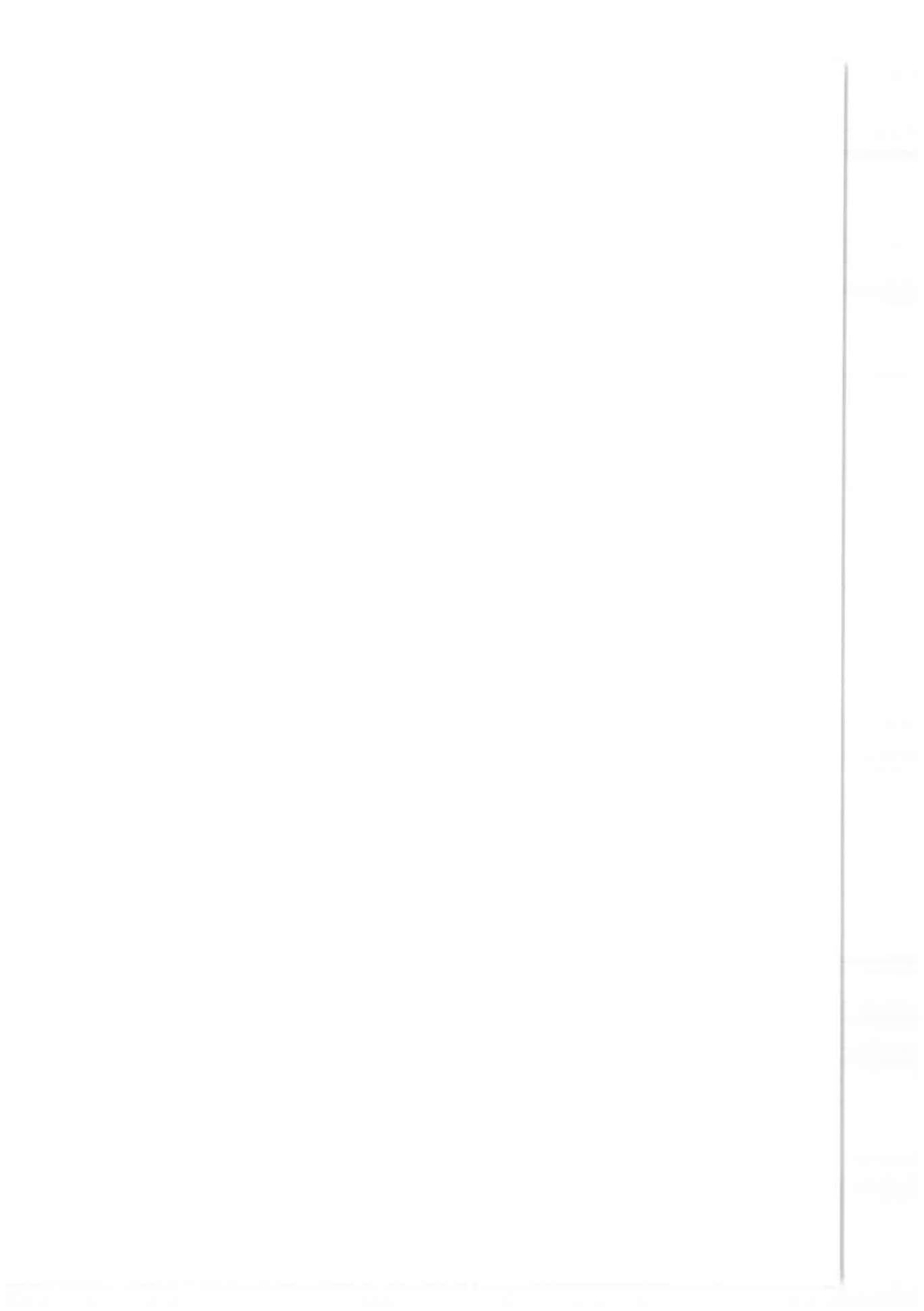
the overlying water column is crucial for accurately quantifying SOD, optimizing water quality, and enhancing our ability to manage lakes and reservoirs.

REFERENCES

ADAMS, D. D., G. MATISOFF, ET AL. (1982). "Flux of reduced chemical constituents (Fe2+, Mn2+, NH4+, and CH4) and sediment oxygen demand in Lake Erie." Hydrobiologia 92: 405-414.

AGREGA, F. AND J. H. W. LEE (2005). "Diffusional mass transfer at sediment-water interface of cylindrical sediment oxygen demand chamber." J. Env. Engr. 131(5): 755-766.

BEUTEL, M. W. (2003). "Hypolimnetic Anoxia and Sediment Oxygen Demand in California Drinking Water Reservoirs." Lake and Reservoirs Management 19(1).

BOULDIN, D. R. (1968). "Models for describing the diffusion of oxygen and other mobile constituents across the mud-water interface." J. Ecol. 56: 77-87.

DITTRICH, M., B. WEHRLI, ET AL. (2004). "Lake sediment modeling over different time scales." in press.

GELDA, R. K., M. T. AUER, ET AL. (1995). "Determination of sediment oxygen demand by direct measurement and by inference from reduced species accumulation." Mar. Freshwater Res. 46: 81-88.

GUNDERSEN, J. K. AND B. B. JORGENSEN (1990). "Microstructure of diffusive boundary layers and the oxygen uptake of the sea floor." Nature 345: 604-607.

HESSLEIN, R. (1976). "An in-situ sampler for close interval pore water studies." Limnology and Oceanography 21(6): 912-914.

HIGASHINO, M., C. J. GANTZER, ET AL. (2004). "Unsteady diffusional mass transfer at the sediment/water interface: Theory and significance for SOD measurement." Wat. Res. 38(1): 1-12.

HONDZO, M., T. FEYAERTS, ET AL. (2005). "Universal scaling of dissolved oxygen distribution at the sediment-water interface: A power law." Limn. and Ocean. 50(5): 166-1676.

HOUSE, W. A. (2003). "Factors influencing the extent and development of the oxic zone in sediments." Biogeochemistry 63: 317-333.

JORGENSEN, B. B. AND N. P. REVSBECH (1985). "Diffusive boundary layers and the oxygen uptake of sediments and detritus." Limnology and Oceanography 30(1): 111-122.

KALIN, L. AND M. M. HANTUSH (2003). Evaluation of Sediment Transport Models and Comparative Application of Two Watershed Models. Cincinnati, Ohio, EPA National Risk Management Research Laboratory: 81 pp.

LAVERY, P. S., OLDHAM, C.E., GHISALBERTI, M. (2001). "The use of Fick's First Law for predicting porewater nutrient fluxes under diffusive conditions." Hydrol. Process. 15: 2435-2451.

126

LEWANDOWSKI, J. (2002). "Peeper supplementary info." Environ. Sci. Technol.: S2-S6.

LEWANDOWSKI, J., K. RUTER, ET AL. (2002). "Two-dimensional small-scale variability of pore water phosphate in freshwater lakes: results from a novel dialysis sampler." Environmental Science & Technology 36(9): 2039-2047.

LEWANDOWSKI, Z., G. WALSER, ET AL. (1991). "Reaction kinetics in biofilms." Biotechnology and Bioengineering 38: 877-882.

LORKE, A., B. MULLER, ET AL. (2003). "Breathing sediments: The control of diffusive transport across the sediment-water interface by periodic boundary-layer turbulence." Limn. and Ocean. 46(6): 2077-2085.

MCGINNIS, D. F. AND J. C. LITTLE (2002). "Predicting diffused-bubble oxygen transfer rate using the discrete-bubble model." Water Research 36: 4627-4635.

MECKLER, A. N., C. J. SCHUBERT, ET AL. (2004). "New organic matter degradation proxies: Valid in lake systems?" in press.

MOBLEY, M. H., G. E. HAUSER, ET AL. (1997). Diffuser System Modeling and Design for Dissolved Oxygen Enhancement of Reservoirs and Releases. Proceedings of the 27th IAHR Congress, San Francisco, CA.

NOGAMI, M., T. MATSUNO, ET AL. (2000). "Estimation of oxygen consumption rate using T-DO diagram in the benthic layer of Ohmura Bay, Kyushu, Japan." Journal of Oceanography 56: 319-329.

RASMUSSEN, H. AND B. B. JORGENSEN (1992). "Microelectrode studies of seasonal oxygen uptake in a coastal sediment: role of molecular diffusion." Marine Ecology Progress Series 81: 289-303.

ROY, H., M. HUETTEL, ET AL. (2004). "Transmission of oxygen concentration fluctuations through the diffusive boundary layer overlying aquatic sediments." Limn. and Ocean. 49(3): 686-692.

STEINBERGER, N. AND M. HONDZO (1999). "Diffusional mass transfer at sediment-water interface." Journal of Environmental Engineering 125(2): 192-200.

WETZEL, R. G. (2001). Limnology: Lake and River Ecosystems. San Diego, Academic Press.

WU, R. S. S., B. S. ZHOU, ET AL. (2006). "Aquatic hypoxia is an endocrine disruptor and impairs fish reproduction." Environ. Sci. Technol. submitted.

ZHANG, H., W. DAVISON, ET AL. (1999). "Remobilisation of major ions in freshly deposited lacustrine sediment at overturn." Aquat. Sci. 61: 354-361.

127

FLOW AND TURBULENCE CHARACTERISTICS IN THE PRESENCE OF A DISCONTINOUS LIGULATE SEAGRASS PRAIRY

Antonino Maltese[1]; Eleanor Cox[1]; Giuseppe Ciraolo[1]; Andrew M. Folkard[2], Giovanni B. Ferreri[1] and Goffredo La Loggia[1]

(1) Dipartimento di Ingegneria Idraulica ed Applicazioni Ambientali, Università di Palermo, Viale delle Scienze, 90128 Palermo, Italy. Email: giuseppe@idra.unipa.it; Fax: +390916657749
(2) Department of Geography, University of Lancaster, Lancaster, LA1 4YB, United Kingdom.

INTRODUCTION

Aquatic vegetation affects the transport of dissolved and particulate matter by altering the hydrodynamic conditions (e.g., Fonseca and Kenworthy 1987; Nepf 1999; Ghisalberti and Nepf 2002), furthermore it is crucial for coastal protection and biodiversity. Hence modeling circulation and transport in coastal waters requires the quantification of flow-vegetation interactions.

Seagrasses are arguably the most important type of vegetation in coastal waters. Several important species, for example *Posidonia oceanica*, are ligulate (long, thin and flexible leaves). *P. oceanica* colonizes sandy bottoms in the Mediterranean Sea, with a density varying (Mazzella *et al.* 1995) from 1200 shoots·m^{-2} in shallow water (1-5 m deep) to 100 shoots·m^{-2} in deeper water (up to 40 m). Its shoots have 6-8 leaves, the outermost being oldest and longest, and the innermost youngest and shortest. The leaves are $\approx$ 0.2 mm thick, $\approx$1 cm wide and up to 1.5 m long. The shoots emerge from rhizomes, which grow vertically and horizontally, and form extensive "prairies" which are an ideal habitat for many species of fauna. The prairies are a food source, provide nursery and shelter beds, and are significant contributors to water oxygenation. The prairies are actually constituted by "islands", "barriers" or "rings" of vegetation separated by bare substrate ("gaps"). The alternation of vegetated and non-vegetated areas produces important effects on the flow field, in terms of both mean flow and turbulence. In fact it affects drag, velocity profiles, turbulence source and sink terms and suspended particulate matter budgets.

In the present study, the patterns of mean flow and turbulence in a canopy of ligulate seagrass, in the presence of a gap, is examined by processing experimental laboratory velocity measurements. In the light of the above remarks, this study is useful in the perspective of an incorporation of the results into numerical simulation models.

About flow in the presence of vegetation, previous studies (e.g. Gambi *et al.* 1990; Cheng and Castro 2002) demonstrated that on a roughness sublayer a inertial sublayer lies, in which the velocity profile follows the well known Karman-Prandtl logarithmic profile, implying a local balance between turbulence production and dissipation. However, Nepf and Vivoni (2000) found that logarithmic profiles does not exist above canopies that occupy a fraction of the water depth larger than 2/3.

METHODOLOGY

The experiments were carried out in a horizontal laboratory flume, 26.3 m long and 77 cm wide, using artificial plants. The latter imitated *P. oceanica*, and their leaves were made by strips of polyethylene 1 cm wide and 0.2 mm thick, whose mechanical properties proved to be analogous to those of the actual ones (Folkard, 2005). These leaves were collected together in groups of six: the external pair, the intermediate pair and the inner pair, respectively 50 cm, 25 cm and 12.5 cm long.

The shoots were fixed on wooden panels reaching a density of 1037 plants m^{-2}, which is within the range of densities found in nature. The panels were laid on the flume bottom in an intermediate stretch 9.6 m long (Fig.1). The upper layer of the panels ("canopy bottom") was 5 cm above the flume bottom. The 1 m long gap was created by removing a panel approximately 5.5 m downstream from the start of the vegetated stretch.
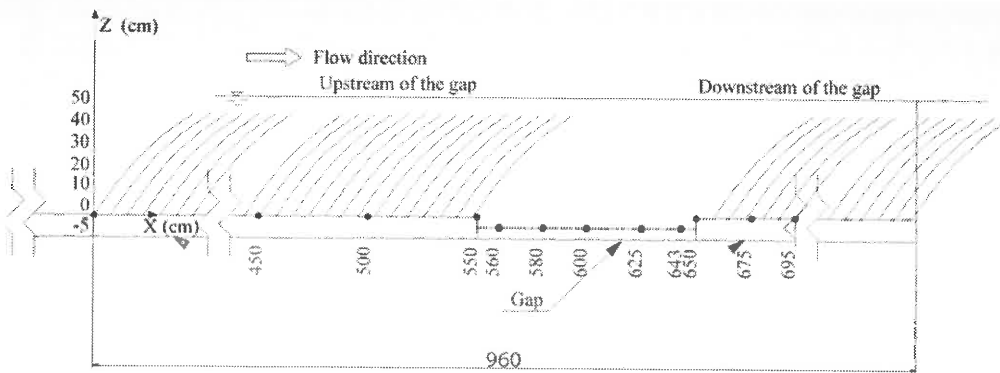
Figure 1. Longitudinal section of the flume

130

Velocity measures were collected along eleven verticals in the central longitudinal plane of the flume. Each vertical is identified by a number that indicates its distance in centimeters from the beginning of the vegetated stretch (Fig. 1). The instrument used was an Acoustic Doppler Velocimeter (ADV), with a maximum sampling volume of 0.73 cm^3 and a sampling rate of 25 Hz. Velocity measures were acquired for four minutes at each measurement point. The flow had a depth of about 46 cm and a mean velocity of about 5.5 cm s^{-1}, similar to that caused by peak tidal flows observed in a shallow coastal lagoon with a fragmented *P. oceanica* prairie (Nasello and Ciraolo 2004). Since the flow had a Horizontal Sub-critical Accelerated profile (H2), the water depth slightly decreased downstream.

The first measurement vertical was positioned 4.5 m downstream of the start of the vegetated stretch, followed by others every 50 cm. Within the gap, the measurement verticals were on average every 20 cm, in order to allow a more detailed hydro-dynamic investigation. For each vertical, the measurements were taken every 2 cm in the canopy from 37 cm down to 1 cm above the bottom, and in the gap from 42 cm down to 1 cm above the bottom.

Since in-canopy flow measurements using ADV probes may be affected by errors caused by leaf disturbance, data with correlation values lower than 70% and SNR < 15 dB have been filtered out.

VELOCITY PROFILES ANALYSIS

During the experiment, the plants were submerged and gently swaying between the heights 15 and 23 cm. The velocity profiles in the canopy (Fig. 2) showed the well-known *S*-shape (Nepf and Vivoni, 2000). In the canopy, both upstream and downstream of the gap, there is a layer of near-zero flow extending from the bed up to about 15 cm. Between about 15 and 23 cm, where the leaves oscillate, there is a layer with strong shear whose velocity profile presents an inflection point. This implies the presence of a Kelvin-Helmholtz instability (KHI) (Holmes *et al.* 1998), and therefore vortex formation (Ghisalberti and Nepf 2002). This layer presents the characteristics of a mixing layer (Nepf and Vivoni, 2000). Higher up, the velocity field develops a typical logarithmic boundary layer profile, since the total flow depth exceeded 1.5 times the canopy height (Nepf and Vivoni, 2000). The sharp delineation of these sections of the velocity profile occurs because of the strong obstruction of the flow due to dense vegetation.

131
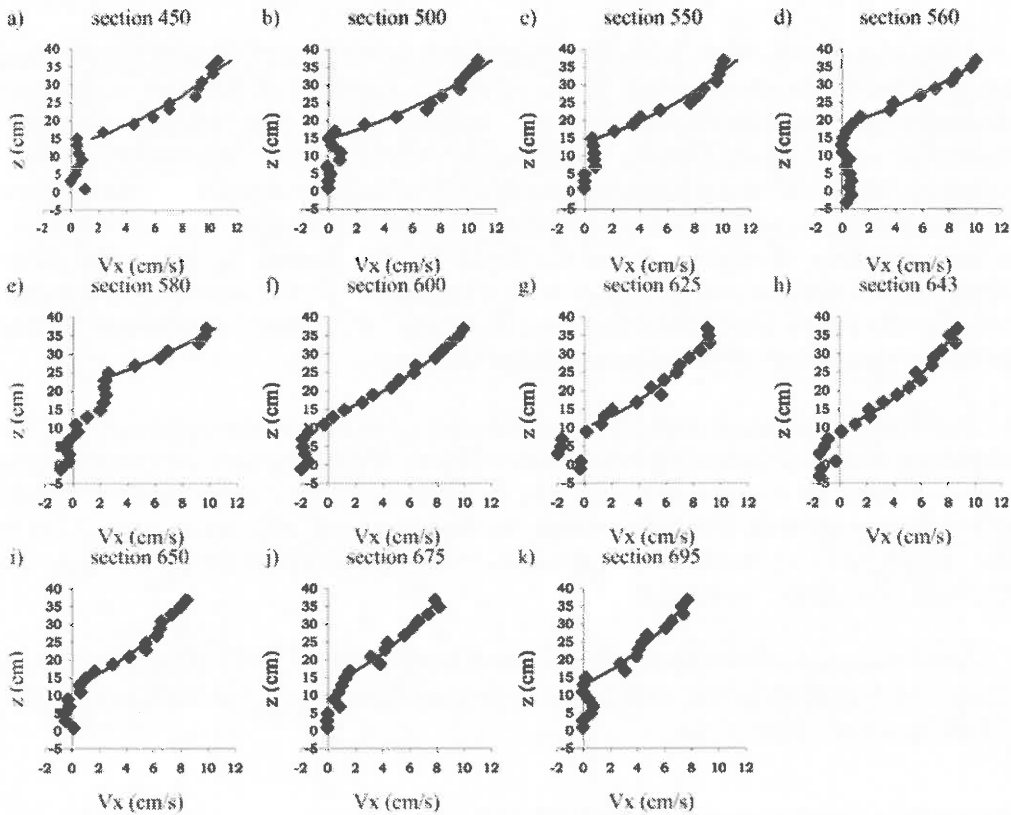
Figure 2. Velocity profiles along the stream

Approaching the upstream gap edge (vertical 550), the layer of near-zero flow begins to expand upwards (e.g., it reaches 20 cm in vertical 560). In the lower part of the gap, where the overhanging plants shade the lower part of the flow, a recirculation cell characterized by low upstream velocities occurs (starting from vertical 580), whose edge cannot be exactly defined because of the uncertainties in low velocities measurements. In the upper zone, the flow continues downstream with relatively fast velocities.

REYNOLDS STRESS ANALYSIS

The vertical momentum transfer, as it is usual, has been studied by means of the distribution of the quantity

$$\frac{\tau_{xz}}{\rho} = -\overline{u'(t)w'(t)} \qquad (1)$$

132

where τ_{xz} = the Reynolds stress, ρ = the water density, $u'(t)$ and $w'(t)$ are, respectively, the horizontal and vertical instantaneous fluctuations from the mean velocity at time t

Fig.3 shows the contour plot of $-\overline{u'(t)w'(t)}$ which synthesizes the general behavior along the flume. Upstream of the gap (verticals 450 to 550) the $-\overline{u'(t)w'(t)}$ presents a maximum just above the top of the canopy since this is the main region of turbulence production, in accordance with many other studies (e.g., Raupach *et al.* 1996; Finnigan 2000; Nepf and Vivoni 2000). The lower layer, of course, presents $-\overline{u'(t)w'(t)}$ values close to zero. In verticals 560 and 580, the height of the maximum $-\overline{u'(t)w'(t)}$ increases significantly (from ~25 cm in verticals 500 and 550 to ~30 cm), coherently with the rising of the edge of the near-zero flow layer. Because of the presence of the recirculation cell, the remaining verticals in the gap (600 – 650) show raising $-\overline{u'(t)w'(t)}$ values while the "fast" layer expands.

Downstream of the gap (verticals 650 onwards), the stress profile returns to the form found upstream (verticals 450 to 550).
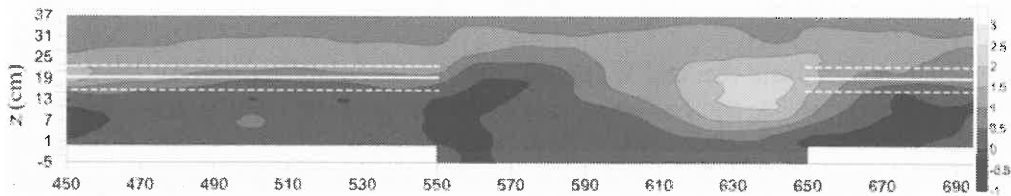
Figure 3. Reynolds stress contour plot

FLUX OF VERTICAL KINETIC ENERGY

Since the vertical transport of both dissolved and particulate nutrients is produced by the vertical component of the velocity, namely the instantaneous fluctuations w'. In particular, vertical transport of matter occurs at the expense of the water vertical kinetic energy. Therefore it is appropriate to study the distribution of the kinetic energy transport along the vertical, defined using the scalar quantity

$$KEF_z = w'^2\, w' = w'^3 \tag{2}$$

which, excluding the factor $\gamma/2g$ (where γ is the specific weight and g is acceleration due to gravity), represents the instantaneous flux of vertical kinetic energy per unity area or the vertical kinetic power per unit area available for vertical transport. This quantity is positive when w' is upward and negative when w' is downward.

Fig.4 shows the contour plot of the local mean values $\overline{KEF_z}$ along the flume. The figure shows that generally the mean flux increases with elevation. A line separate an

133

upper zone characterized by upward mean fluxes (positive $\overline{KEF_z}$ values) and a lower one characterized by downward mean fluxes (negative $\overline{KEF_z}$ values). The most intense KEF_z negative values occur in the gap, approximately in the recirculation cell. The latter is therefore a sedimentation zone, which traps significantly sediments.
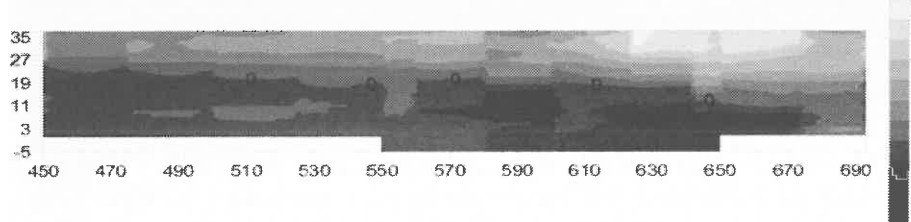
Figure 4. Flux of vertical kinetic energy contour plot

QUADRANT ANALYSIS AND VORTICES EVOLUTION

Quadrant analysis (Lu and Willmarth 1973) is an important tool for the study of turbulent phenomena, and has been used widely in research on turbulence generated by, for example, sub-aerial canopy flow (e.g., Finnigan 2000) and fluvial bedforms (e.g., Roy *et al.* 1996). It assigns each instantaneous recorded "event" of turbulent velocity fluctuations $u'(t)$ and $w'(t)$ to one of the four quadrants in the u'-w' plane, denoted as Q_i ($i = 1,\dots, 4$). In Q_1 ($u'(t) > 0$ and $w'(t) > 0$), we find "outward interaction" events; in Q_2 ($u'(t) < 0$ and $w'(t) > 0$) "ejection" events, indicating upward transport of relative slow flowing fluid; in Q_3 ($u'(t) < 0$ and $w'(t) < 0$) "inward interaction" events; and in Q_4 ($u'(t) > 0$ and $w'(t) < 0$) "sweep" events, indicating downward transport of relatively fast flowing fluid. So, we can quantify the contribution of the events belonging to each quadrant in determining the mean value of a "phenomenon" due to the turbulence (i.e. Reynolds stress, turbulent transport of dissolved and particulate matter, turbulent transport of energy as heat and kinetic energy, etc.), and then to recognize the "dominant" quadrant that mainly contributes to the total main value. For example, if in a point the Reynolds stress is positive (mean velocity increasing with elevation z) the major contributors are quadrants Q_2 and Q_4 (sweeps and ejections), while if it is negative (mean velocity decreasing with elevation z) the major contributors are quadrants Q_1 and Q_3.

In order to identify the dominant quadrant for a given measurement location, the number of fluctuations in each quadrant may be counted (e.g., Lu and Willmarth 1973; Nakagawa and Nezu, 1977). However, a larger number of events in a quadrant does not necessarily imply—the dominance of this quadrant in terms of the phenomenon intensity (Finnigan, 2000). Therefore, counts should be weighted in

134

terms of the studied quantity (Reynolds stress, kinetic energy, etc.). For Reynolds stress τ_{xz} and vertical kinetic energy flux KEF_z the respective contributions of the quadrant j-th are:

$$\tau_{xz,j} = \frac{\sum_{i=1}^{m(j)} -u'(t_i)w'(t_i)}{N} \quad \text{and} \quad KEF_{z,j} = \frac{\sum_{i=1}^{m(j)} w'(t_i)^3}{N} \qquad (3)$$

where $m(j)$ is the number of fluctuations in quadrant j-th, and N the total number of fluctuations in the considered measurement point, used to normalize the data. The maximum values of $\tau_{xz,j}$, or $KEF_{z,j}$, are used to determine the most representative quadrants. We carried out the quadrant analysis both for Reynolds stress τ_{xz} and vertical kinetic energy flux KEF_z, but here we report the KEF_z analysis only (the general pattern is similar).

Of course, the results within the canopy are affected by some uncertainties due to the very low velocity values. In the first half of canopy, in the upper region, where the vertical velocity profiles follow the logarithmic law, quadrant Q_2 (ejections) dominates (Fig. 5), while just below, where a mixing layer occurs and Reynolds stresses are highest, quadrant Q_4 dominates (sweeps). This result matches those of other studies for terrestrial canopy air flows (e.g., Finnigan, 2000). The presence of a sweep-dominated region overlain by an ejection-dominated region implies that coherent vortices dominate the vertical exchange of momentum.

In the gap, the sweep-dominated zone expands vertically (Fig. 5) covering the locations of the highest Reynolds stress (Fig. 3) and the recirculation cell (Fig. 2). It reaches the bed in the middle of the gap, while it never reaches the free-surface. In fact, on this region we again find a relatively thin ejection layer (Q_2 dominion), which expands downwards approaching the second canopy stretch. Just downstream of the drop (between sections 550 and 600), in the overhanging plants shade zone, quadrant Q_2 dominates too.

In the second half of the canopy (starting from section 650), the sweep-dominated zone shrinks, mainly for the rising of its lower edge due to flow trend to the re-establishment of a flow field analogous to that of the first canopy half (Fig.5).

The fact that the ejection-dominated upper zone (Q_2) extends for all the length suggests that the coherent vortices formed at the top of the upstream canopy continue

to be present in the gap, at a height indicated by the boundary between the sweep-dominated region and the overlying ejection dominated region.
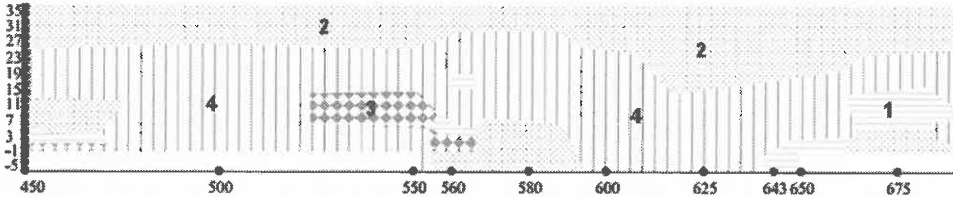
Figure 5. Dominant quadrants in terms of vertical turbulent kinetic energy flux

The evolution of the coherent vortices has been studied by determining the vortices size and the locations of their centers. For the sake of brevity, we report here only some indication of this application and we skip the theoretical treatment. The turbulence pattern described by the figures above is produced by the presence of coherent vortices, as the comparison with previous results (e. g., Finnigan, 2000) allows us to recognize. Thus, the vortex-centers were assumed as lying on the separation interface between the regions dominated by ejections and sweeps (Fig. 5), in accordance with the analysis criterion adopted (τ_{xz} or KEF_z).

In order to compute the vortex size evolution along the flume, the Kelvin-Helmholtz instability theory has been applied. Along the measured section of the upstream canopy, the vertical size of the vortices grows from 8 to 11 cm. Downstream of the gap, the latter assumes the same range of values.

To further aid in identifying the evolution of the vortices within the gap, the temporal correlation of the longitudinal velocity fluctuations $u'(t)$ has been quantified by calculating the autocorrelation function, representing the time τ over which $u'(t)$ is auto-correlated (Velasco *et al.* 2003). Upstream of the gap, the autocorrelation function shows maximal values at the top of the canopy, coincident with Reynolds stress maxima. Inside the canopy, it decreases as the development of large scale turbulent structures is constrained. Within the gap, it grows reaching a maximum (τ_{max}=1.6 s) that is approximately coincident with the global maximum in the Reynolds stress field located at the end of the gap (Fig. 3). This increased autocorrelation suggests that the coherent eddies formed at the top of the upstream canopy not only persist but grow longitudinally as they move across the gap.

DISCUSSION AND CONCLUSIONS

The velocity profiles measured in the simulated canopy upstream of the gap showed the S-shape observed in many previous studies on flows in the presence of both

136

terrestrial and aquatic vegetation (e. g., Raupach *et al.* 1996; Ikeda and Kanazawa 1996; Ghisalberti and Nepf 2002). The flow consists of three layers having distinct characteristics. The lowest layer, totally contained in the canopy, presents near-zero mean flow; coherent turbulent eddy structures do not form and Reynolds stress is therefore near-zero too. Within this layer quadrant analysis is essentially meaningless, and the formation of coherent turbulent eddying structures is not possible. The second layer, which occupies the region around the canopy top, is a mixing layer, characterized by the formation of coherent eddies due to a Kelvin-Helmholtz instability. In this layer, the highest Reynolds stress values occur, with the maximum just at the canopy top, and there is a pre-dominance of sweep events (quadrant Q_4). The upper layer is characterized by the mean velocity profile taking on the form as in a logarithmic boundary layer. In this region, flow velocities are much higher than in the first two layers, and ejection events (quadrant Q_2) pre-dominate.

Within the gap, the shear layer separates from the top of the canopy and forms a recirculation cell which characterizes the mean flow field. This process is "delayed" by the presence of the canopy overhanging the upstream end of the gap. As a result a quasi-stagnant region forms beneath the overhanging canopy, and the recirculation cell is located in the downstream part of the gap, impinging on the onset of the second half canopy. The turbulence structure, outlined by the quadrant analysis, of a sweep-dominated region at the height of the canopy top overlain by an ejection-dominated region persists into the gap.

Both in the canopy and in the gap, the dominance of sweeps, in terms of vertical kinetic energy power available for vertical sediment transport, allows one to recognize that seagrass canopies capture sediments and nutrients while reduce significantly their re-suspension, and this process is not mitigated by the presence of the gaps (e.g., Terrados and Duarte 2000).

However, these important sedimentary and biological implications have to be better investigated. Therefore, further field and laboratory experiments and two-phase (fluid-particle) flow modeling (Folkard *et al.* 2006) need to be carried out in order to determine in detail the nature of deposition and resuspension phenomena especially within these gaps.

REFERENCES

CHENG, H, AND CASTRO, I.P. (2002). "Near wall flow over urban-like roughness." *Bound. Lay. Meteorol.* 104 (2), 229-259.

FINNIGAN, J.J. (2000). "Turbulence in plant canopies." *Ann. Rev. Fluid Mech.*, 32, 519-571.

FOLKARD, A.M. (2005). "Hydrodynamics of model Posidonia oceanica patches in shallow water." *Limnol. and Oceanogr.* 50 (5), 1592-1600.

FOLKARD, A.M., MALTESE, A., CIRAOLO, G. AND LA LOGGIA, G. (2006). "Laboratory flume studies of hydrodynamics at downstream seagrass canopy edges: implications for particulate matter." Submitted to *Estuarine, Coastal and Shelf Science*.

FONSECA, M. S., AND KENWORTHY, W. J. (1987). "Effects of current on photosynthesis and distribution of seagrasses." *Aquat. Bot.,* 27, 59-78.

GAMBI, M., NOWELL, A., AND JUMARS, P. (1990). "Flume observations on flow dynamics in *Zostera marina* (eelgrass) beds." *Mar. Ecol. Prog. Ser.,* 61, 159-169.

GHISALBERTI, M. AND NEPF, H.M. (2002). "Mixing layers and coherent structures in vegetated aquatic flows." *J. Geophys. Res.,* 107(C2),1-11.

GHISALBERTI, M, AND NEPF, HM, 2004. "The limited growth of vegetated shear layers." *Water Resources Research* 40 (7): Art. No. W07502.

HOLMES, P., LUMLEY, J.L., AND BERKOOZ, G. (1998). *Turbulence, Coherent Structures, Dynamical Systems and Symmetry*, Cambridge University Press, New York.

IKEDA, S., AND KANAZAWA, M. (1996). "Three-dimensional organized vortices above flexible water plants." *J. Hydraul. Eng. - ASCE*, 122(11), 634-640.

LU, S.S., AND WILLMARTH, W.W. (1973). "Measurements of the structure of the Reynolds stress in a turbulent boundary layer." *J. Fluid Mech.,* 60, 481–511.

MAZZELLA, L., BUIA, M.C., GAMBI, M.C., LORENTI, M., RUSSO, G.F., SCIPIONE, M.B. AND ZUPPO, V. (1995). "A review on the trophic organization in the Posidonia oceanica ecosystem." In: Cinelli, F., Fresi, E., Lorenzi, C., and Mucedola, A. (Eds), *La Posidonia oceanica – Un contributo per la salvaguardia del principale ecosistema marino del Mediterraneo*. Rivista marittima, Rome, Italy, 40-47.

NAKAGAWA, H. AND NEZU, I. (1977). "Prediction of the contributions to the Reynolds stress from the bursting events in open-channel flows." *J. Fluid Mech.,* 80, 99-128.

NASELLO, C. AND CIRAOLO, G. (2004). "Misure idrodinamiche nello Stagnone di Marsala." *Proc., XXIX Convegno di Idraulica e costruzioni idrauliche*, Editoriale Bios, Cosenza, Italy, 1(A3), 699-706.

NEPF, H.M. (1999). "Drag, turbulence and diffusion in flow through emergent vegetation." *Water Resour. Res.,* 35(2), 479-489.

NEPF, H.M., AND VIVONI, E. (2000). "Flow structure in depth-limited, vegetated flow." *J. Geophys. Res.,* 105(C12), 28,547-28,557.

NEZU, I., AND NAKAGAWA, H. (1993) *Turbulence in Open-Channel Flows*. IAHR Monograph Series, Rotterdam, Netherlands: A. A. Balkema, 16.

RAUPACH, M., FINNIGAN, J. AND BRUNET, Y. (1996). "Coherent eddies and turbulence in vegetation canopies: The mixing-layer analogy." *Bound. Lay. Meteorol.,* 78, 351-382.

138

ROY, A.G., BUFFIN-BÉLANGER, T., AND DELAND, S. (1996). "Scales of coherent flow structures in a gravel-bed river." Ashworth, P.J., Bennett, S.J., Best, J.L, and McLelland, S.J. (Eds.), *Coherent Flow Structures in Open Channels*. Chichester, UK: Wiley, 147-164.

TERRADOS J. AND DUARTE C.M. (2000). "Experimental evidence of reduced particle resuspension within a seagrass (*Posidonia oceanica* L.) meadow." *J. Exp. Mar. Biol. and Ecol.* 243 (1), 45-53.

VELASCO, D., BATEMAN, A., REDONDO, J.M. AND DEMEDINA, V. (2003). "An Open Channel Flow Experimental and Theoretical Study of Resistance and Turbulent Characterization over Flexible Vegetated Linings." *Flow, Turbulence and Combustion*, 70: 69-88.

EFFECTS OF A STRONG CONNECTION TO LAKE ONTARIO, A LARGE WATERSHED, AND DYNAMIC PLANT POPULATIONS ON THE HYDRODYNAMICS AND RESULTING WATER RESIDENCE TIMES OF A SMALL COASTAL EMBAYMENT

Alexandra T. King, Robert L. Johnson, and Edwin A. Cowen[1]

INTRODUCTION

Coastal embayments and wetlands, as mediators between their watersheds and deeper lakes or the ocean, filter watershed runoff, alter its temperature, and provide habitat and breeding grounds for aquatic species that are often important to the ecosystem of the deeper water body.

Physical Processes: The time-dependent velocity and temperature fields and resulting transport time scales of coastal embayments and wetlands are determined by boundary conditions including surface wind stress, surface heating and cooling, and barotropic and baroclinic forcing from the watershed and the larger water body, and by internal conditions including bathymetry, bed roughness, and aquatic vegetation.

Residence Time: Water residence time, defined as the amount of time a water parcel remains in an aquatic system, is a bulk measure of embayment hydrodynamics. Residence time is a function of starting time and location, $(t, \vec{x})$, and for a given $(t, \vec{x})$, is a stochastic variable described by a *residence time distribution* (RTD – Monsen et. al. 2002). Mean residence time tends to be set by the time scales of physical processes driving exchange with adjacent systems and the time scales of mixing within the system itself (Rueda and Cowen, 2005b).

The RTD at time t and location $\vec{x}$ may be measured directly by releasing an instantaneous pulse of a passive and conservative tracer at $(t, \vec{x})$ and monitoring the tracer flux out of the system (Hilton et. al. 1998). If the system has only one outlet,

and if the tracer is well-mixed across that outlet, then the RTD is given by Eq. 1, where $r(t)$ is the RTD, $Q(t)$ is volumetric flow rate out of the system, $C(t)$ is the concentration of the tracer at the outlet, and V_0 is the total volume of tracer released.

$$r(t) = \frac{Q(t)C(t)}{V_0}$$

(1)

As discussed in Hilton et. al., $r(t)$ is not technically the RTD in cases where tracer re-enters the system, but it always has the same mean, and we will loosely refer to $r(t)$ as the RTD. The time integral of $r(t)$, defined as $R(t)$ in Eq. 2, is the fraction of tracer which no longer remains in the system at time t, and we will loosely refer to $R(t)$ as the *cumulative residence time distribution* (CRTD).

$$R(t) = \int_0^t r(\tau)d\tau$$

(2)

Study Site: Sterling Pond (SP) is a small and shallow freshwater embayment that drains Sterling Creek, bordering wetlands, and a large watershed ($210km^2$) into Lake Ontario (LO) through a long, narrow, and shallow manmade channel ($100m \times 17m \times 3m$) – a bathymetric map of SP is provided in Fig. 1. From late spring through early fall, SP is home to diverse populations of submerged aquatic vegetation (macrophytes) which undergo one or more periods of dense growth.

Objective and Approach: Because of its small size, large watershed, strong connection to LO, and highly variable macrophyte populations, the hydrodynamics and resulting water residence times of SP result from the interaction of all of the physical processes discussed above. To decipher these processes and to characterize the residence time scales of SP, dye studies were conducted in synchrony with extensive macrophyte surveys and continuous monitoring of temperature, water surface elevation, channel flow rate, and meteorological conditions. The results of these studies comprise a benchmark data set for investigation of flow through macrophyte-dominated coastal embayments.

MATERIALS AND METHODS

Dye Release Studies: The two dye release studies discussed in this paper commenced on May 15, 2002 and September 18, 2003. The 2002 experiment was conducted during a period of high watershed flows following a spring snow-melt event. The 2003 experiment was conducted during a period of intermittent coastal upwelling in LO and high lake level oscillations instigated by high winds following hurricane Isabel.

142
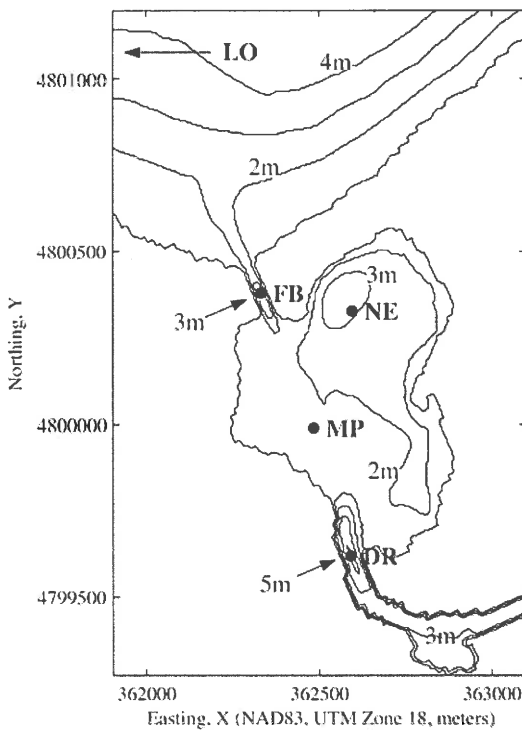
Figure 1. Bathymetry of Sterling Pond and equipment locations. The LO site is located $1.5km$ to the west on the $6m$ isobath of Lake Ontario.

Each experiment began with the release of a plug of $3.79L$ (2002) or $7.57L$ (2003) of Rhodamine WT (20% by weight solution) through a vertical line-source diffuser at site DR (see Fig. 1). After the release, the volumetric flow rate, $Q(t)$, from SP to LO was continuously monitored at site FB as was the concentration of RWT, $C(t)$.

Flow rate was measured as follows – a vertical velocity profile was measured in the center of the channel with an RDI $1200kHz$ Workhorse Monitor acoustic Doppler current profiler (ADCP) looking upward from the bed. The horizontal boundary layers were characterized in a separate experiment, and combining the results of this experiment with measured channel bathymetry and the vertical centerline velocity profiles, an accurate estimate of $Q(t)$ was obtained (King, unpubl. M.S. thesis).

Concentration was measured with a Turner Designs 10-AU flow-through fluorometer. The fluorometer intake tube was positioned in the center of the channel to sample water exiting SP near the ADCP. The sampling intervals for concentration and velocities were between 0.33 and $5sec$ – time series were ensemble averaged over a time scale longer than the longest turbulent time scale but shorter than the high

143

energy barotropic oscillations (see Lohrmann et. al. 1990), determined from longitudinal velocity spectra (not shown) to be $2min$ in 2002 and $8min$ in 2003.

Continuous Monitoring: Throughout the dye studies, water temperatures in SP and LO were monitored in vertical profiles with chains of Sea Bird Electronics SBE-39 thermistors recording at $1\text{-}2min$ time intervals. Thermistor chains were located in Lake Ontario (site LO in Fig. 1), at the dye release site (DR), at the midpoint of the pond (MP), at the deepest point in the northeast lobe (NE), and in the channel connecting SP to LO (FB). Water surface elevation in SP was monitored at $1\text{-}2min$ intervals with an SBE-39 temperature/pressure recorder on the bed at DR. Meteorological conditions, including wind speed, wind direction, air temperature, atmospheric pressure, relative humidity, and short wave radiation were recorded in $15min$ intervals at a station located $1km$ west of SP on the shore of neighboring Little Sodus Bay. Together with these measured variables, flow rate from SP to LO, monitored as part of the dye release study described above, completes the measured history of external hydrodynamic forcing and the internal response of SP during the dye studies.

Macrophyte Surveys: Macrophyte abundance, height, and species composition were sampled in 41 $100m\times100m$ quadrates in SP on a monthly (and sometimes more frequent) basis throughout the 2002 and 2003 growing seasons. Macrophytes were hand-harvested by diving and cutting the stems at the substrate-water interface. Samples were taken from a $0.25m$ square frame randomly tossed in each quadrate. Plant heights were measured in the field. Species were separated in the lab and dried for 48 hours at $105^{o}C$ to determine dry biomass on a per-species basis.

ANALYSIS AND RESULTS

Hydrodynamic Forcing: A summary of the forces driving hydrodynamics and resulting water residence times in SP during the two dye studies is provided in Fig. 2. In order to decipher to some extent the relative impact of barotropic forcing from the watershed and LO, the bulk velocity in the channel, u, was decomposed into a $12hr$ moving average time series, $<u>$, and the root $12hr$-mean square residual, $<u'^2>$. The $12hr$ averaging period was chosen to distinguish the barotropic modes of LO from the longer time-scale watershed processes (Hamblin 1982, Rueda and Cowen 2006b). The magnitude of barotropic forces (per unit width) from the watershed and from LO were then estimated by Eqs. 3 and 4, respectively, where ρ is water density and H is the time-dependent water depth at site FB. The baroclinic force (per unit width) from LO was estimated from the bulk density difference between site DR and LO by Eq. 5. The wind force may also be estimated, but its effect is thought to be small compared to that of the other forces (Andradóttir and Nepf 2000b, Rueda and

small compared to that of the other forces (Andradóttir and Nepf 2000b, Rueda and Cowen 2005b). Note that these are simple order-of-magnitude estimates and that the ratio of the barotropic to baroclinic forces is the square of the Froude number.

$$F_{Bt,w} = \rho <u>^2 H \tag{3}$$
$$F_{Bt,L} = \rho <u'^2> H \tag{4}$$
$$F_{Bc,L} = g(\rho_{LO} - \rho_{DR})H^2 \tag{5}$$
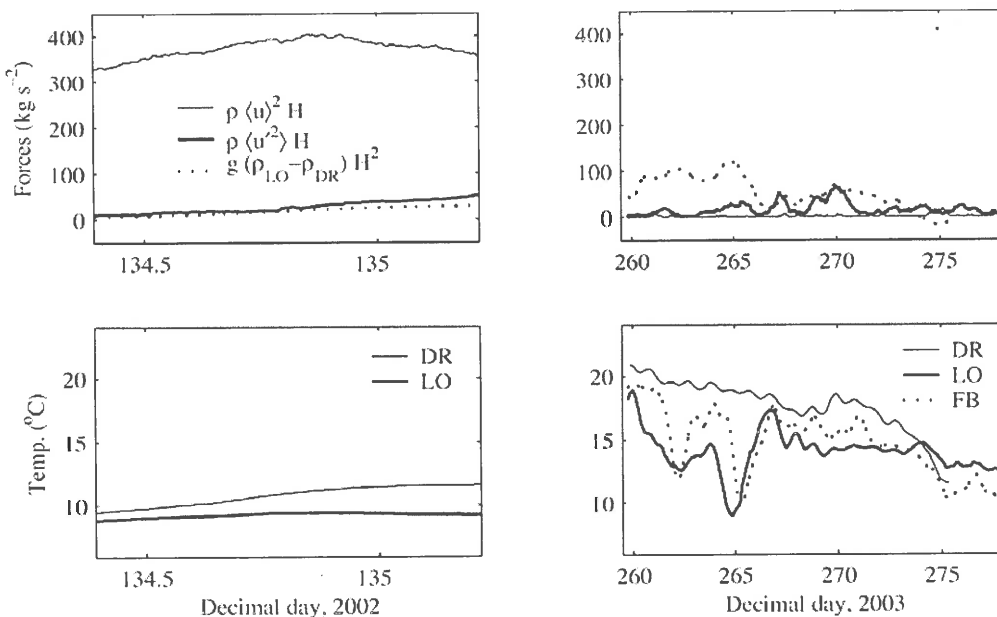
Figure 2. Barotropic forcing from the watershed, barotropic forcing from Lake Ontario, and baroclinic forcing from Lake Ontario (see Eqs. 3-5) during the 2002 and 2003 dye experiments are plotted in the top two panels. The temperatures at sites DR and LO are plotted in the bottom two panels. For the 2003 experiment, the temperature at site FB is also plotted. All temperatures are averaged over the top $3m$ of the water column.

In Fig.2, we see that during the 2002 dye study, barotropic forcing from the watershed dwarfed all forcing from LO. In contrast, during the 2003 study, barotropic forcing from the watershed was extremely weak and baroclinic and barotropic forcing from LO were of moderate magnitude. The effect of these forces on the dynamics of SP is not immediately clear, but the temperature time histories plotted in Fig. 2 give some indication of the impact of baroclinic forcing – we see that during coastal upwelling of LO (days 260-267), cold hypolymnetic water from LO appears to enter

Macrophyte Distributions: As shown in Fig. 3, macrophytes were sparse during the 2002 dye study, although some biomass was located in the northeast lobe of the pond and near the channel, whereas during the 2003 study, macrophytes were both thick and relatively uniform in density. Species composition (not shown) in SP is highly dynamic – during the 2002 study, dense patches consisted primarily of *C. demersum*, *E. nuttalli*, and *P. crispus*; during the 2003 study, the west side of the pond was dominated by *N. obtusa* while *C. demersum* and *E. nuttalli* occupied the northeast lobe. Efforts are underway to characterize the frontal area per unit volume and the drag coefficient for these macropyhte species and to investigate the importance of vegetative drag and longitudinal dispersion (see Nepf 1999, Lightbody and Nepf 2006).

Biomass ($50 \, g \, m^{-2}$)

Day 142, 2002

```
            0   1
         0  1   1   1
         0  0   2   2
0   0    5  0   1   2
0   0    0  1   1
0   0    0  0   0   0
0   0    0  0   0   1
         1  0   0   0
            0   0   1
               0
```

h/H

```
                0    0.7
             0  1    1    1
             0  0    0.7  0.7
1   0   0.6 0.8  0.8  0.9
0   0.7 0.7 0.7  0.6
0.5 0   0.8 0.7  0.6  0
0   1   0.7 1    0.9  0.7
        1   0.9  0.6  0
            0    0.7  0.7
                  1
```

Day 267, 2003

```
            7
      0  5  3  0
      0  0  5  5
8  3  6  7  5  1
4  9  4  3  10
2  3  8  2  3  5
2  6  3  5  1  1
      4  2  5  3
         3  1  0
            6
```
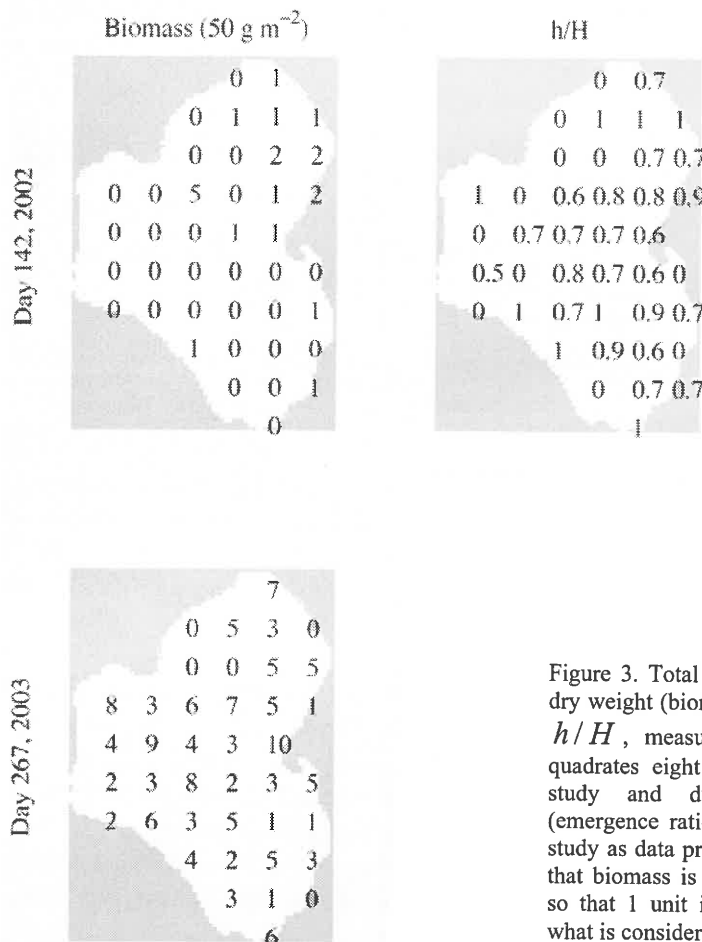
Figure 3. Total above-ground macrophyte dry weight (biomass) and emergence ratio, h/H, measured in 41 $100m \times 100m$ quadrates eight days after the 2002 dye study and during the 2003 study (emergence ratio not shown for the 2003 study as data processing is ongoing). Note that biomass is plotted in units of $50gm^{-2}$ so that 1 unit is near the lower limit of what is considered "dense" vegetation.

146

Residence Time: For each experiment, $r(t)$ was computed from $Q(t)$ and $C(t)$ measured at site FB using Eq. 1. Uncertainty due to bias error, precision error, and errors correlated over intermediate time scales were considered separately so that uncertainty in time-integrated statistics, such as $R(t)$ and mean residence time could be estimated accurately (King, unpubl. M.S. thesis). The raw time series of $r(t)$ are plotted in Fig. 4 and the time series of $R(t)$ with error bars are plotted in Fig. 5. Roughly 60% of the dye exited SP during each of the studies. In order to compute statistics of residence time, $r(t)$ had to be extrapolated until over 99% had left. The standard procedure is to fit an exponential tail – this is reasonable if the embayment is well-mixed toward the end of the experiment, resulting in exponential decay toward zero. For these two studies, however, such a fitted exponential tail predicts that significantly less than 100% of the dye leaves the embayment. An alternative method is to extrapolate $R(t)$ by finding the decay rate k which minimizes the mean-square residual for Eq. 6 under the constraint that all of the mass eventually exits the embayment. This constraint requires that r_0 and k satisfy Eq. 7 where t_N is the time of the final measurement. For each study, $R(t)$ was extrapolated by this method, and mean residence time was estimated from the corresponding extrapolated time history of $r(t)$.

$$R(t) = 1 - r_0 e^{-kt} \qquad (6)$$
$$r_0 = \left[1 - R(t_N)\right] e^{kt_N} \qquad (7)$$
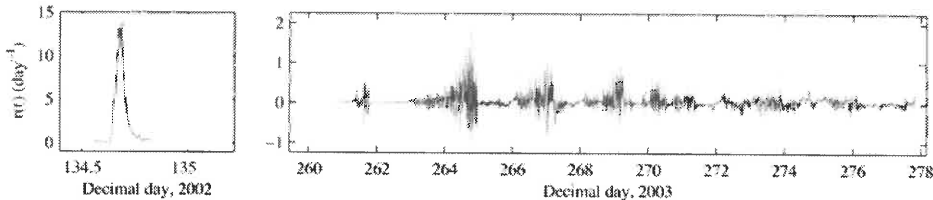
Figure 4. Measured RTD's for the 2002 and 2003 dye studies. Each time series begins at the time of dye release. Note that error bars are not shown because they would obscure detail – see Fig. 6 for instantaneous uncertainty in the 2002 RTD, and see Fig. 5 for cumulative uncertainty in both experiments.

There are two types of error implicit in this extrapolation method. The first is error in the exponential model – this error is clearly present because if the embayment were indeed fully mixed toward the end of the experiment as the exponential model assumes, then a straightforward fit to the tail of $r(t)$ would predict that all of the mass exits the embayment, and this condition had to be imposed artificially. The second error propagates from the measured data. This error was estimated by

147

be to stochastically fit the curve accounting for the time correlation of the various contributions to uncertainty in $R(t)$, but fitting the upper and lower bounds gives a first order uncertainty estimate. The upper bound was extrapolated linearly to obtain a more conservative lower bound on the mean residence time. The resulting mean residence times with upper and lower bounds estimated from measurement error are given in Table 1. The model error is not accounted for here but is explored in the next section by using a more physically valid model to extrapolate the 2002 RTD.

	exponential/linear	dead-zone
2002	{0.22, 0.56, 0.79}	0.88
2003	{16.1, 18.1, 19.9}	–

Table 1. Estimates of mean residence time (*days*) for each dye experiment and each extrapolation method.
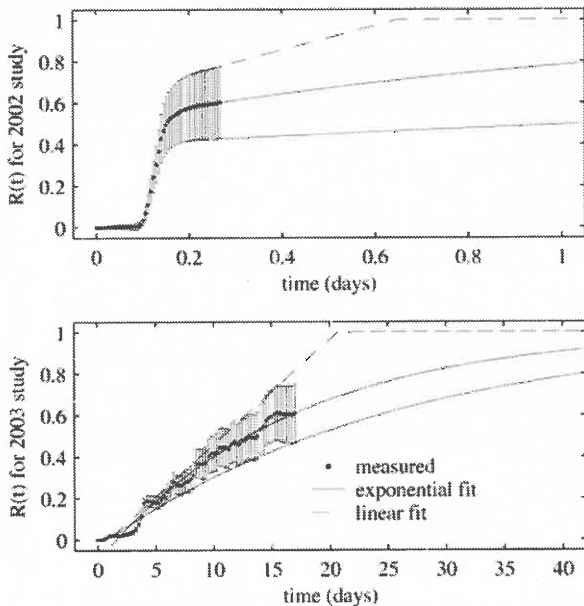
Figure 5. Measured CRTD with error bars for the 2002 and 2003 experiments along with extrapolated tails. The tail of the expected value and the lower bound are extrapolated exponentially while the tail for the upper bound is extrapolated linearly to give a conservative estimate of the lower bound on mean residence time.

DEAD-ZONE MODEL

For the 2002 experiment, a dead-zone model was fitted to the data in order to explore the physical processes and extrapolate the tail of the RTD. This type of model was developed to explain enhanced dispersion in rivers with side-lobes (e.g. Valentine and Wood 1977) and further developed for use in wetlands by Andradóttir and Nepf (2000a,b). The idea is that a channel exhibiting classic plug-flow with longitudinal dispersion is coupled to a stationary "dead zone" through bulk diffusion. The model equations for transport of a conservative passive tracer are given by Eqs. 8 and 9 where C_c is the tracer concentration in the channel, C_d is the tracer concentration in the dead zone, u is longitudinal velocity, L is the length of the system, $q = A_c / (A_c + A_d)$ where A_c and A_d are the cross-sectional areas of the channel and dead zone, respectively, K_x is longitudinal dispersion, and $\alpha^* = \Delta Q / Q$ is the ratio of the volumetric channel/dead zone exchange rate, ΔQ, and the channel flow rate, Q.

$$\frac{\partial C_c}{\partial t} + u \frac{\partial C_c}{\partial c} = K_x \frac{\partial^2 C_c}{\partial^2 x} + \frac{\alpha^* u}{L} (C_d - C_c) \tag{8}$$

$$\frac{\partial C_d}{\partial t} = \frac{\alpha^* u}{L} \frac{q}{1-q} (C_d - C_c) \tag{9}$$

Equations 8 and 9 were solved using an upwind differencing scheme with time-dependent velocity and longitudinal dispersion. Length L was taken to be $835m$, corresponding to the distance between DR and FB. Time-dependent velocity was computed from the outflow and cross-sectional area measured at site FB by $u = Q/(\theta A_{FB})$, where θ is a dimensionless parameter relating the time-dependent area of the channel under the footbridge, A_{FB}, to the mean cross-sectional area of the channel, A_c. Time-dependent longitudinal dispersion was computed from velocity by $K_x = \gamma h u$, where $h = 2m$ is the estimated average depth of the channel and γ is a dimensionless constant which in a natural stream is about 0.6 (Fischer et. al. 1979).

The equations were solved on a domain of length $3L$ and the concentration gradient was set to zero on the boundaries. The concentration fields were initialized at zero with the exception of the channel concentration at $x = L$, which was initialized at $V_0 /(\Delta x \theta A_{FB})$. The time series of concentration at $x = 2L$ was compared with the measured time series of concentration at site FB, and the model was fitted to the data by varying the parameters γ, α^*, q, and θ to minimize the sum-square error. Andradóttir and Nepf (2000b) suggest that during periods of high flow, $\alpha^* \approx 1$ and q may be roughly predicted from the length-to-width ratio, L/W, of the wetland (or

149

SP this works out to $q \approx 0.15$. These estimates were used as a starting point in the search for a best fit. The sum square residual was minimized by the parameters $\gamma = 4.5$, $\alpha^* = 0.55$, $q = 0.25$, and $\theta = 4$. All of these parameters are within an order of magnitude of the values predicted by simple scaling analysis.
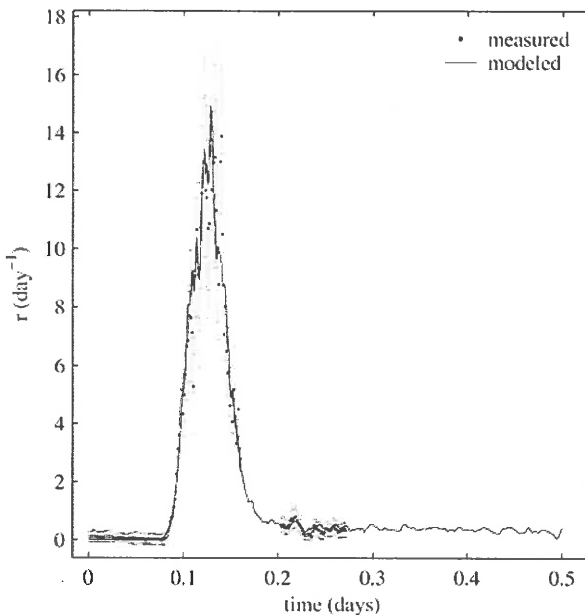
Figure 6. Measured RTD with error bars (indicating total instantaneous uncertainty) for the 2002 experiment along with the best-fit dead-zone model solution. Time 0 is the dye release time.

The dead zone model fits the data splendidly and provides a more physically based means to extrapolate the tail of the measured RTD. Solving the best-fit dead zone model using flow rates measured after the end of the dye study yields a mean residence time of $0.88 days$. The mean residence time is quite sensitive to model parameters, and for other solutions falling within the error bounds of the measured data, mean residence times between 0.6 and $1.8 days$ are obtained. This uncertainty is due to the sensitivity of mean residence time to the shape of the RTD tail and to the fact that the experiment was terminated before the shape of the tail was well-established. Towards the end of the residence time curve for the dead zone model, exponential decay is approached, but along the way the decay rate itself decays – we may now see that this is the reason exponential extrapolation of the 2002 RTD without the conservation of mass constraint failed. We observe that with the constraint of mass conservation, exponential extrapolation of the CRTD predicts mean residence time within 60 % of that predicted by the dead-zone model for the 2002 experiment. This gives us some estimate of our confidence in the extrapolated 2003 RTD.

150

CONCLUSIONS

The dye studies and extensive macrophyte surveys discussed herein comprise a unique data set for investigating flow and transport through macrophyte-dominated coastal embayments and wetlands. Scaling analysis suggests that barotropic forcing from the watershed and both barotropic and baroclinic forcing from the adjacent lake can all be important in this type of system. Mean residence time scales were estimated for two different forcing regimes and a dead-zone model was used to explain the physics in one of the experiments where barotropic watershed forcing dominated. The measured residence time distributions are integrated measures of embayment hydrodynamics and can be used in the future to calibrate and verify models accounting explicitly for the effect of macrophytes.

REFERENCES

ANDRADÓTTIR, H. Ó. AND H. M. NEPF. 2000a. Thermal mediation by littoral wetlands and impact on lake intrusion depth. Limnol. Oceanogr. 36: 725-735.

ANDRADÓTTIR, H. Ó. AND H. M. NEPF. 2000b. Thermal mediation in a natural littoral wetland: measurements and modeling. Limnol. Oceanogr. 36: 2937-2946.

FISCHER, H. B., E. J. LIST, R. C. Y. KOH, J. IMBERGER, AND N. H. BROOKS. 1979. Mixing in Inland and Coastal Waters. Academic.

HAMBLIN, P. F. 1982. On the free surface oscillations of Lake Ontario. Limnol. Oceanogr. 27: 1039-1049.

HILTON, A. B. C., D. L. MCGILLIVARY, AND E. E. ADAMS. 1998. Residence time of freshwater in Boston's inner harbor. J. Waterw. Port Coast. Eng. 124: 82-89.

LIGHTBODY, A. F., AND H. M. NEPF. 2006. Prediction of velocity profiles and longitudinal dispersion in emergent salt march vegetation. Limnol. Oceanogr. 51: 218-228.

LOHRMAN, A., B. HACKETT, AND L.P. RØED. 1990. High resolution measurements of turbulence, velocity and stress using a pulse-to-pulse coherent sonar. J. Atmos. Ocean. Technol. 7: 19-37.

MONSEN, N. E., J. E. CLOERN, L. V. LUCAS, AND S. G. MONISMITH. 2002. A comment on the use of flushing time, residence time, and age as transport time scales. Limnol. Oceanogr. 47: 1545-1553.

NEPF, H. M. 1999. Drag, turbulence, and diffusion in flow through emergent vegetation. Water Resources Res. 35: 479-489.

RUEDA, F. J., AND E. A. COWEN. 2005. Exchange between a freshwater embayment and a large lake through a long, shallow channel. Limnol. Oceanogr. 50: 169-183.

RUEDA, F. J., AND E. A. COWEN. 2005. Residence time of a freshwater embayment connected to a large lake. Limnol. Oceanogr. 50: 1638-1653.

THACKSTON, E. L., F. D. SHIELDS JR., AND P. R. SCHROEDER. 1987. Residence time
    distributions of shallow basins. J. Environ. Eng. 113: 1319-1332.
VALENTINE, E. M., AND I. R. WOOD. 1977. Longitudinal dispersion with dead zones.
    J. Hydraul. Div. Am. Soc. Civ. Eng. 103: 975-990.
WÜEST, A. AND A. LORKE. Small-scale hydrodynamics in lakes. 2003. Annu. Rev.
    Fluid Mech. 35: 373-412.

DENSITY CURRENT BETWEEN REED BELTS AND OPEN WATER – HEAT BUDGET CALCULATIONS

Charlotta Borell Lövstedt[1]

(1) Department of Water Resources Engineering, Lund University, Box 118, 221 00 Lund, Sweden
E-mail: charlotta.borell_lovstedt@tvrl.lth.se

INTRODUCTION

Reed belts are important structures in the shallow lake ecosystem. Here, juvenile fish seeks protection from predating fish and birds (Okun et al. 2005; Okun and Mehner 2005). The exchange of water with the open water mass is therefore of importance for the transport of oxygen, nutrients and other dissolved constituents that keep the environment within the vegetation healthy.

The most obvious driving force for this exchange is the wind, but a density-driven current induced by differential heating of the water surface can also be of importance. This current is a consequence of the shading of the water surface by the reed vegetation. The surface water within the reeds therefore tends to be colder than the surface water outside, and a density-driven surface current from the open water to the reed belt is induced. Simultaneously a current out from the reeds below the surface current must be created to keep the mass in balance. During the night the open water surface cools faster that the surface within the vegetation and a reverse density current can be induced.

There have been studies of other density-induced currents in lakes. These are for example a) currents between shallower and deeper parts, since the shallower parts heat and cool faster (Farrow and Patterson 1994; Horsch and Stefan 1998; James and Barko 1991; James et al. 1994; Monismith et al. 1990), b) currents between wind sheltered and wind mixed areas (Finlay et al. 2001; Nepf and Oldham 1997; Schlatter et al. 1997), and c) currents between clear and turbid areas, where the turbid water absorbs more heat (Dale and Gillespie 1977). Further, density-induced currents caused by shading from floating mats of vegetation have been shown to be sufficient to supply the vegetation with the needed phosphorus (Coates and Patterson 1993).

In a previous conference paper, measurements of the surface current and the driving parameters (temperature profiles and solar radiation) have been described (Lövstedt 2004). These measurements showed that the current occurred during days that was characterized by sunshine and low wind speeds (<2 m s^{-1}). The temperature gradient was around 0.5°C and the surface current speed was 1.5-2.8 cm s^{-1}, directed towards the reeds. The main difficulty in analyzing the driving parameters is that the

temperature profiles are already affected by the current, and it is not possible to model the current if the initial driving forces are not fully understood.

Therefore, the aim of this paper is to calculate the heat budget of the water within the reeds and the water outside the reeds. The calculated values are compared to measured temperatures. Finally, a few heat budget scenarios are used to determine the probable maximum difference between the open water and the reed belt and the effect of different shading conditions. This heat budget will also make it possible to predict when and where the density current will occur, even if water temperature data is not available.

METHOD

To compare the difference in stored heat in the open water and in the water within the reeds, a two-box model was developed as shown in Figure 1. The left box is the open water and the right box is the water in the reeds. In the open water the heat budget is calculated in a standard way where heat is gained through solar radiation (R_S), long-wave radiation from the atmosphere ($R_{L(atm)}$), and sensible heat (H_{sens}) (if the air is warmer than the water), and lost through reflection of solar radiation ($R_S\alpha$), long-wave back radiation from the water surface (R_B), latent heat flow from evaporation (H_{lat}) and sensible heat (if the water is warmer than the air). The result is a change in heat content which can be translated to a change in temperature.

For the water within the reed belt, the standard heat budget has to be modified in three ways. First, the shading effect from the vegetation means that much solar radiation is absorbed within the reeds before it reaches the water surface (R_SC_S), second, the long-wave radiation does not come directly from the atmosphere, but from the vegetation ($R_{L(veg)}$), and third, the change in heat content is also affected by the heat exchange with the open water (H_Q). This term is not important for the open box since the total volume of open water is much larger than the volume within the reeds. Further, the evaporation will be less in the vegetation than from the open water surface since the solar radiation and wind speeds are less. The smaller wind speed will also decrease the sensible heat transfer within the vegetation. The water is chosen to be somewhat deeper in the open box than in the reed box, which will be explained in the following description of the model.

154
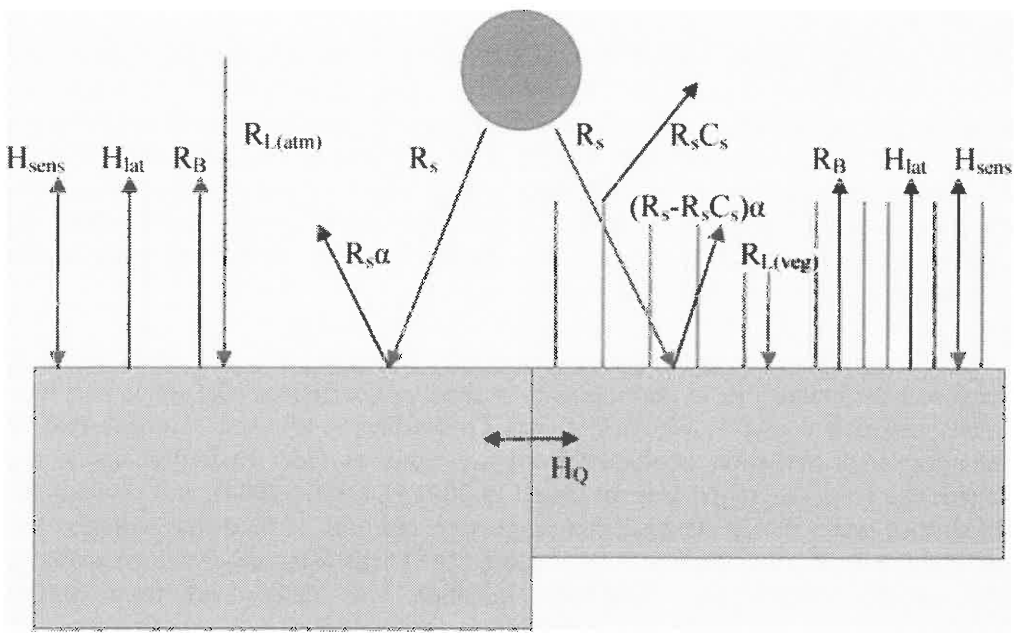
Figure 1. Heat budget components. The left box symbolizes the open water and the right box the water within the reed belt.

The change in stored heat integrated over the depth can be described with the following equation.

$$\rho \cdot c_p \int_0^h \frac{\partial T}{\partial t} dz = R_{net} - H_{lat} - H_{sens} + H_Q \tag{1}$$

where ρ is the density (kg m^{-3}), c_p is the specific heat capacity for water ($4.18 \cdot 10^3$ J (kg K)$^{-1}$), h is the water depth (m), T is the temperature ($^{\circ}$C), t is the time (s), z is the vertical distance from surface (m), R_{net} is the net radiation (W m^{-2}), H_{lat} is the latent heat (from evaporation) (W m^{-2}), H_{sens} is the sensible heat (from convection, added if the air is warmer) (W m^{-2}) and H_Q is the lateral heat flow (W m^{-2}) related either to the open water width or to the reed belt width. The heat exchange with the sediments can sometimes be included, but it is often neglected if the lake is not ice-covered. The lateral heat flow, H_Q, will not be included in the calculations. In the open water this term will be assumed to be zero as discussed above. In the reed however, the difference between the heat budget calculations and the measurements will be the indication of how large the exchange with the open water is (H_Q).

To estimate a change in temperature that could be compared to the measured values, the right-hand side of Eq. 1 was divided by the density, the specific heat capacity of water, the water depth and then multiplied by seconds per 30-minutes, resulting in a change in the depth-averaged temperature over 30 minutes, ΔT_{30}:

155

$$\Delta T_{30} = \frac{R_{net} - H_{lat} - H_{sens} + H_Q}{\rho \cdot c_p \cdot h} \cdot 1800 \qquad (2)$$

ΔT_{30} can be compared to the difference between the depth-averaged temperatures measured in 30-minutes intervals. Note that H_Q will not be included directly in the calculations as discussed above. The mean water depth of Lake Krankesjön, where the measurements were taken is 0.7 m, and the depth in the reeds where the temperature was measured was 0.5 m, therefore, these depths are used in the calculations.

Radiation balance was computed with α=0.05 (albedo) for water (Shaw 1994). In the reed heat budget, R_S is multiplied by a shading coefficient, C_S, which can have values between 0 and 1, where 0 means no shading at all, and 1 means that all incoming solar radiation is shaded from the water surface. Radiation inside and outside the reed vegetation was measured in 2001 (Lövstedt 2004), and showed that the surface water inside the reed in average received only 15 % of the radiation that reached the open water surface. The shading coefficient is therefore approximated to 0.85 in the calculations. Longwave radiation was determined from Stefan-Boltzmann's equation, with the emissivity, ε, for a clear sky calculated to be 0.8-0.815 using:

ε=0.740+0.0049·e (Anderson, 1952), $\qquad (3)$

where e is the vapor pressure of the air (mb). The emissivity for water is 0.96 (Bengtsson 1997), whereas ε for the reed that is used to calculate R_L inside the reed belt is more difficult to predict. Other values found in the literature are for example ε for fields and croplands $\approx$0.95, ε for dense forest $\approx$1, ε for different types of vegetation and soil 0.9-0.95 (Bengtsson 1997), and ε=0.98 for growing wheat (Mo and Liu 2001). The emissivity for the reed was set to 0.98 according to these values. The temperature of the reed vegetation was approximated to the temperature of the air. For cloudy conditions the emissivity, ε_{cloudy}, can be determined using:

ε_{cloudy}= $\varepsilon(1+a'N^{b'})$ (Raphael 1962) $\qquad (4)$

where N is the part of the sky that is cloud covered (0-1), a' is 0.17, and b' is 2. Latent heat was determined from the evaporation, which was directly calculated by the weather station data program (Penman's combined formula depending on air temperature, relative humidity, average wind speed and solar radiation). In the reeds the evaporation was recalculated with Penman formula, but with *wind speed=0* (based on observations) and *net radiation=0.15·net radiation in the open water* (according to measurements described above). This resulted in evaporation in the reeds corresponding to approximately 25% of the evaporation from the open water, which was the relation that was used in the calculations as a simplification. Bowen's ratio, B was used to calculate the sensible heat:

$$H_{sens} = B \cdot H_{lat}. \qquad (5)$$

The temperature measurements that are used to compare with this heat budget were taken continuously from 2 July to 11 November in 2004. Ten temperature loggers (StowAway TidbiT) were installed to measure the vertical gradient 3 m outside the edge of the reeds, and the vertical gradient 1 m inside the reeds, with five loggers in each vertical with 10 cm distance between the loggers. Measurements were taken every 30 minute.

OBSERVATIONS AND DISCUSSION
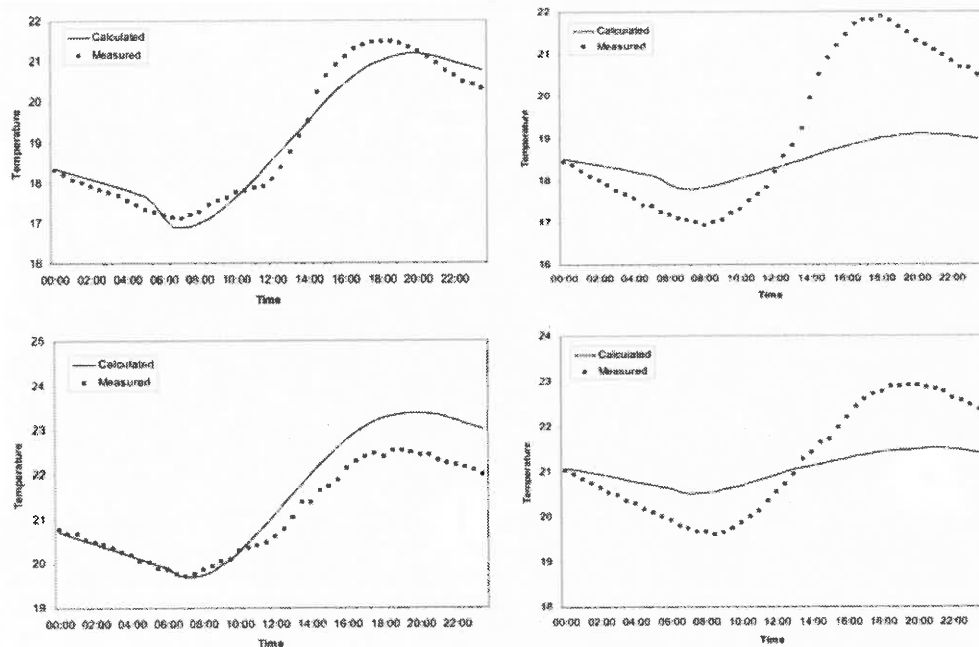
Figure 2. Calculated and measured depth-averaged temperatures during two sunny and calm days. The left column shows the open water and the right column the water in the reed belt. First row is 17 July 2004, and second row is 29 July 2004.

The temperature change, ΔT_{30}, was calculated for the days during the summer of 2004. The most interesting results are from the calm and sunny days, since these have the best conditions for the density-driven current to develop. The results from the two days with the most solar radiation together with the lowest wind speeds are shown in Figure 2. The heat budget calculations were further tested during days with other weather conditions, and results from the most extreme days are presented in Figure 3 (sunny and windy, cloudy and calm, and cloudy and windy). Different values of the shading coefficient were also tested, which will be discussed in the next section.

157
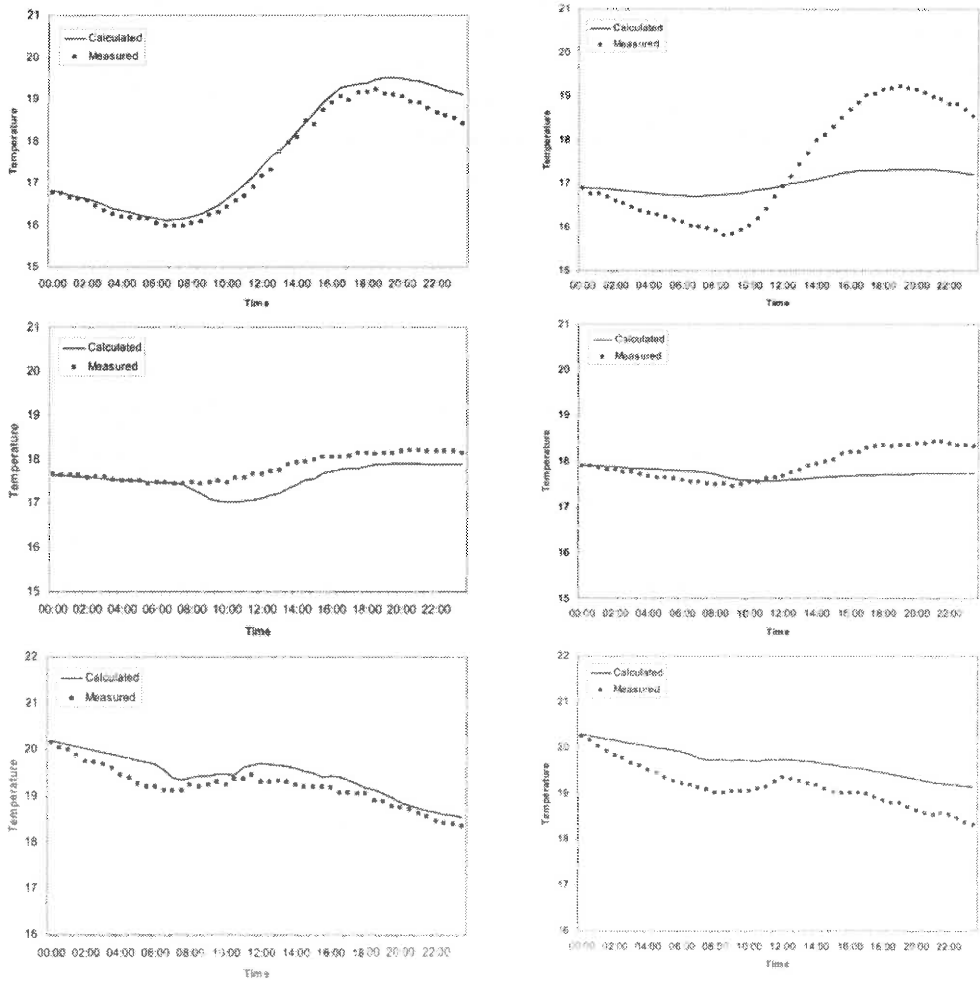
Figure 3. Measured and calculated temperatures during different weather conditions. The left column shows the open water and the right column the water in the reed belt. First row is a sunny and windy day (16 July 2004), second row is a cloudy and calm day (22 July 2004), and third row is a cloudy and windy day (25 July 2004).

In the open water during the sunny and calm days (Figure 2), the calculations are good estimations of the measured temperatures. During the second day in Figure 2, the temperature increase is slightly overestimated in the open water which results in a difference of 1°C between the model and the measurements in the end of the day. This could be explained by that the evaporation, which is very difficult to estimate, could be underestimated. The right-hand subfigures in Figure 2 show the calculations and the measured temperatures in the reed belt. The difference between the calculations and the measurements is an indication of how large the exchange with

the open water, H_O, is. Until the middle of the day the exchange transport colder water into the reed belt, and in the afternoon until the night, warmer water is transported into the reed belt.

The first row in Figure 3 shows the results from a sunny and windy day, which is similar to the results from the sunny and calm days. The main difference is that the exchange here is probably also driven by wind-induced currents. A calm and cloudy day is presented in the second row in Figure 3. During this day the temperature in the water is fairly constant during the day and the calculations is a good approximation of the measured values in the open water. The calculations in the reed during this day indicates that there is a similar pattern as for the sunny days, with colder water flowing in during the morning, and warmer flowing in during the afternoon, but much weaker. This is probably explained by that the open water surface still receives more solar radiation than the reed surface water even when sun is shaded by clouds, which can also be seen if the measured temperatures in the open water are compared to the measured temperatures in the reed belt. In the last row in Figure 3, data and calculations from a cloudy and windy day is shown. The water temperature is decreasing in both the open water and within the reed belt this day, since the water is warmer than the air temperature is during this day. The calculations in the open water are following the measurements well. The surface water in the open water is heated slightly in the morning, which is followed by a slight increase in temperature in the reed belt after about 2 hours. According to the calculations the water cools more effective in the open water, and this colder water is then mixed with the water in the reed belt and this is shown by the difference between the calculations and the measurements in the reed belt.

SCENARIOS AND DISCUSSION

The results from different shading scenarios are presented in Figure 4. The shading coefficient is very important for how large the temperature differences between the open water and the reed belt will be. The basic data that is used is from 17 July 2004, the same as the first row in Figure 2, with a modification of the solar radiation so that it is simulating a perfect clear sky (compare Figure 4b) and the first row in Figure 2). If the reed shades 100% of the incoming solar radiation, the maximum temperature difference between the open water and the reed belt (if there was no exchange) is 4.6°C (Figure 4a)). If the reed shades 85% of the solar radiation (as in the calculations above) the maximum temperature difference is 2.6 °C, which is 0.5 °C higher than in the calculations with the real solar radiation shown in Figure 2. If the shading coefficient is further decreased the temperature difference decrease fast as is seen in Figure 4c) and d). When the reeds shade 60% of the incoming solar radiation, the water temperature in the reed belt is estimated to be warmer than the water outside. This is probably not realistic but can be explained by that other factors in the calculations also must change if the reed is not considered as dense as in the

first calculations. For example is the emissivity of the reed larger that the emissivity of the atmosphere, and when the reed vegetation is less dense, then the emissivity of the atmosphere must affect the water in the reed also. Further, evaporation and sensible heat flow will also increase and become more similar to the calculations in the open water if the vegetation is less dense. Anyway, the results in Figure 4 show that the shading coefficient is an important parameter in the calculations.
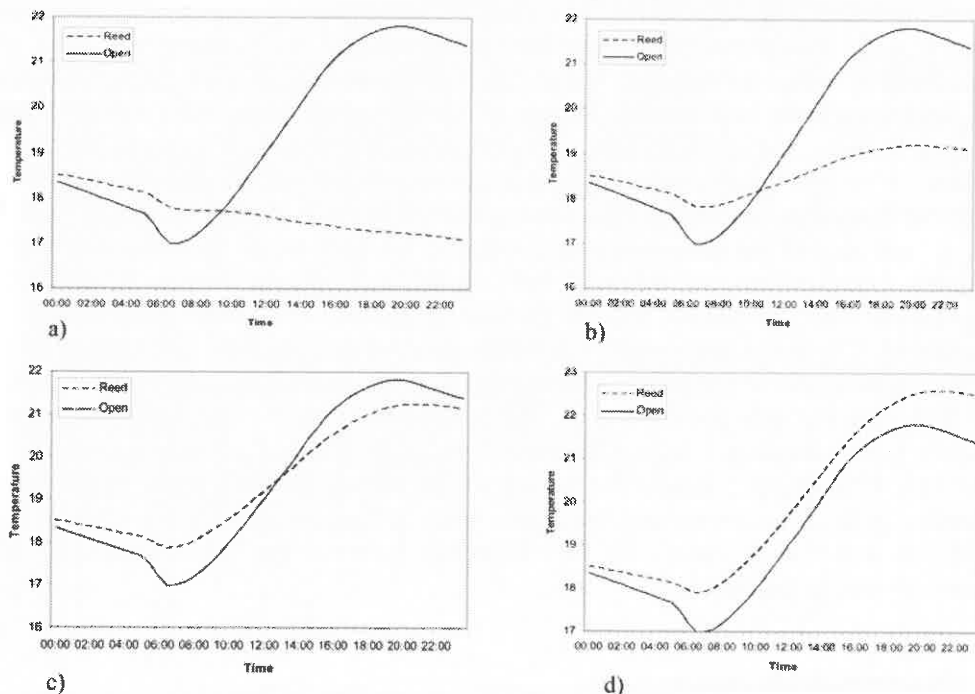
Figure 4. Calculated temperatures during a perfect sunny day with different shading coefficients, C_S: a) C_S=1, b) C_S=0.85, c) C_S=0.7, and d) C_S=0.6.

This heat budget calculations shows that if the temperatures is not known, but weather data and an approximated shading coefficient is available, the temperature differences that can drive a density current can be estimated.

CONCLUSIONS

The main conclusions from these heat budget calculations for open water and the water within the reed belt are a) the difference between the calculations and the measured temperatures in the reed belt gives an indication of the exchange of water between the open water and the reed belt, b) the shading coefficient is very important for the calculations in the reed. But the coefficient should not be changed

160

substantially without changing other parts of the heat budget calculations, and c) heat budget calculations can be used to determine conditions for density currents to occur between open water and areas that are shaded by above surface vegetation.

REFERENCES

ANDERSON, E.R. 1952. Energy-budget studies from water loss investigations. Lake Hefner studies Techn. Rep., US Geol. Surv. Circ 229, Washington: 71-119.

BENGTSSON, L. 1997. Hydrologi – teori och processer. Svenska Hydrologiska Rådet, Teknisk vattenresurslära Lunds Universitet, Lund, Sweden [in Swedish]

COATES, M. AND PATTERSON, J.C. 1993. Unsteady natural convection in a cavity with non-uniform absorption of radiation. J. Fluid Mech. 256: 133-161.

DALE, H.M. AND GILLESPIE, T. 1977. The influence of submersed aquatic plants on temperature gradients in shallow water bodies. Can. J. Bot. 55: 2216-2225

FARROW, D.E. AND PATTERSON, J.C, 1994. The daytime circulation and temperature structure in a reservoir sidearm. Int. J. Heat Mass Transfer 37: 1957-1968.

FINLAY, K.P., CYR, H. AND SHUTER. B.J. 2001: Spatial and temporal variability in water temperatures in the littoral zone of a multibasin lake. Can. J. Fish. Aquat. Sci.58: 609-619.

HORSCH, G.M. AND STEFAN, H.G. 1988. Convective circulation in littoral water due to surface cooling. Limnol. Oceanogr. 33: 1068-1083.

JAMES, W.F. AND BARKO, J.W. 1991. Estimation of phosphorus exchange between littoral and pelagic zones during nighttime convective circulation. Limnol. Oceanogr. 36: 179-187.

JAMES, W.F, BARKO, J.W. AND EAKIN, H.L. 1994. Convective water exchanges during differential cooling and heating: implications for dissolved constituent transport. Hydrobiologia 294: 167-176

LÖVSTEDT, C. 2004. Density driven currents induced by heterogeneous solar radiation between open water and reeds (*Phragmites australis*). In: Proceedings of 8th European Workshop on Physical Processes in Natural Waters. Lund Univ.19-24.

MALM, J. 1994. Thermal bar dynamics – spring thermo- and hydrodynamics in large temperate lakes. Ph.D thesis. Lund Univ.

MO, X. AND LIU, S. 2001. Simulating evapotranspiration and photosynthesis of winter wheat over the growing season. Agric. Forest Meteorol. 109: 203-222.

MONISMITH, S.G., IMBERGER, J. AND MORISON, M.L. 1990. Convective motions in the sidearm of a small reservoir. Limnol. Oceanogr. 35: 1676-1702.

NEPF, H.M. AND OLDHAM, C.E. 1997. Exchange dynamics of a shallow contaminated wetland. Aquat. Sci. 59: 193-213.

OKUN, N., LEWIN, W-C AND MEHNER, T. 2005. Top-down and bottom-up impacts of juvenile fish in littoral reed stand. Freshwater Biol. 50: 798-812.

OKUN, N. AND MEHNER, T. 2005. Distribution and feeding of juvenile fish on invertebrates in littoral reed (*Phragmites*) stands. Ecol. Freshwater Fish 14: 139-149.

RAPHAEL, J.M. 1962. Prediction of temperature in rivers and reservoirs. Proc. J. Power Div. ASCE 2: 157-181.

SCHLATTER, J.W., WÜEST, A. AND IMBODEN, D.M. 1997: Hypolimnetic density currents traced by sulphur hexafluoride (SF6). Aquat. Sci. 59: 225-242.

SHAW, E.M. 1994. Hydrology in Practice. Chapman & Hall, London.

EFFECTS OF SMALL-SCALE TURBULENCE ON PLANKTON DYNAMICS IN A COASTAL ECOSYSTEM

Peters, F.[1]

(1) Institut de Ciències del Mar (CSIC), Barcelona, Catalunya, Spain. cesc@icm.csic.es.

INTRODUCTION

Turbulence is ubiquous in aquatic systems. As an environmental variable that depends on the type and intensity of energy inputs into a system, turbulence can potentially affect the organisms living within the water. Effects of small-scale turbulence on biological organisms and processes has been a subject of study for over 20 years (Rothschild & Osborn 1988 and many others). Inertial forces seem to generate the stronger signals from biological organisms albeit microorganisms well below the Kolmogorov and Batchelor scales often show signals most probably related to the remaining shear (Peters & Marrasé 2000). Effects on planktonic micro-organisms are usually measured in terms of altered growth rates for osmotrophs (organisms growing on dissolved substances) (e.g. Arin et al. 2002) and increased encounter probabilities of predators with their prey particles for phagotrophs (organisms feeding on particles) (e.g. Kiørboe & MacKenzie 1995). For osmotrophs in diffusion-limited conditions the theory shows that an increase in flow relative to an organism will alter the gradient of nutrients from the far field to the cell, making it steeper and thus increasing the flux of nutrients towards the cell (Karp-Boss et al. 1996). An increased nutrient supply should translate into higher growth rates. This process depends on turbulence intensity and cell size and thus, in general, the increase in flux is significant only for the larger microorganisms such as net phytoplankton. We have observed this increased growth repeatedly in experiments and we and others have also shown that the most benefitted phytoplankters are the larger ones (Peters et al. 2006). In addition we have shown that the nutrient uptake is indeed enhanced under turbulence for the osmotrophs larger than 10 μm in average cell size.

In natural ecosystems, even coastal ones, small phytoplankton tends to dominate the community while these organisms seem to be weakly affected by turbulence. Thus, system level responses to turbulence are expected to be hard to see as compared to the laboratory where turbulence levels tend to be somewhat higher. In addition, in ecosystems that hold a multitude of different organism populations and the consequent ecological interactions, the overall system response to turbulence can not be clearly foreseen.

Besides the processes mentioned above, the availability of inorganic nutrients is a necessary requirement for osmotrophic organisms to grow and turbulence may help bring nutrients to the water column through resuspension. It may also help entrain atmospheric nutrients into the water which can be an important nutrient source under some circumstances such as in industrialized coastal systems (nitrogen oxides that can turn into nitrate) or under storms carrying suspended particles (for instance Saharan dust in the Mediterranean coastal regions). We have started an effort to look into the effects of these forcing factors, namely nutrient load and turbulence, in a NW mediterranean coastal ecosystem.

MATERIAL AND METHODS

A monthly sampling was carried out for one year in Blanes Bay (100 km north of Barcelona, Spain). We analyzed inorganic nutrients, chlorophyll and other chemical and biological variables. Turbulence was derived from wind measurements from a nearby automatic meteorological station and estimated using the equations in MacKenzie and Leggett (1993). Two one week long sampling efforts were carried out in the coast of Barcelona (November 2005 and April 2006). Here we sampled three to four times per day for chemical and biological variables. In addition CTD cast were done at the station and at two more stations located nearby. Turbulence was measured continuously with a Vector acoustic doppler velocimeter (Nortek AS) deployed 3 m deep. Turbulence was estimated from spectral analysis of velocity time series.

RESULTS

In a monthly time series of inorganic nutrient samples in Blanes Bay, the amount of nitrate and of silicate in water was related to the average turbulence intensity of the previous seven days (Table 1). In addition, silicate was also related to the accumulated rainfall during the previous two weeks. The signal of these nutrients is thus related to resuspension from the sediment and river discharge in a system where the nearby Tordera river runs dry most of the year. An increase of nutrient availability in the water column can then translate into higher system production.

Nutrient	Variable	R^2
Nitrate	-TEMP, **TURB7**	0.775
Nitrite	-TEMP	0.620
Ammonium	TEMP? (0.054)	0.281
Phosphate	-	-
Silicate	**TURB7, RAIN14**, -IR1	0.682

Table 1. Relationships between nutrient concentrations and environmental variables such as temperature (TEMP), average turbulence in the previous 7 days (TURB7), accumulated rainfall in the previous 14 days (RAIN14) and irradiance (IR1).

164

In the coastal location in Barcelona nutrient concentrations in the water were difficult to interpret since the coast has several drainage water outfalls and atmospheric deposition can also be an important source of nitrate. It seems that primary production responds to overall nutrient avaialbility (Fig. 1), mainly through the larger phytoplankton in Nov 05. A nutrient input peak in Apr 06 seemed to have a "sewage-like" signature but it was short-lived and probably was advected away before the local system could significantly repond.
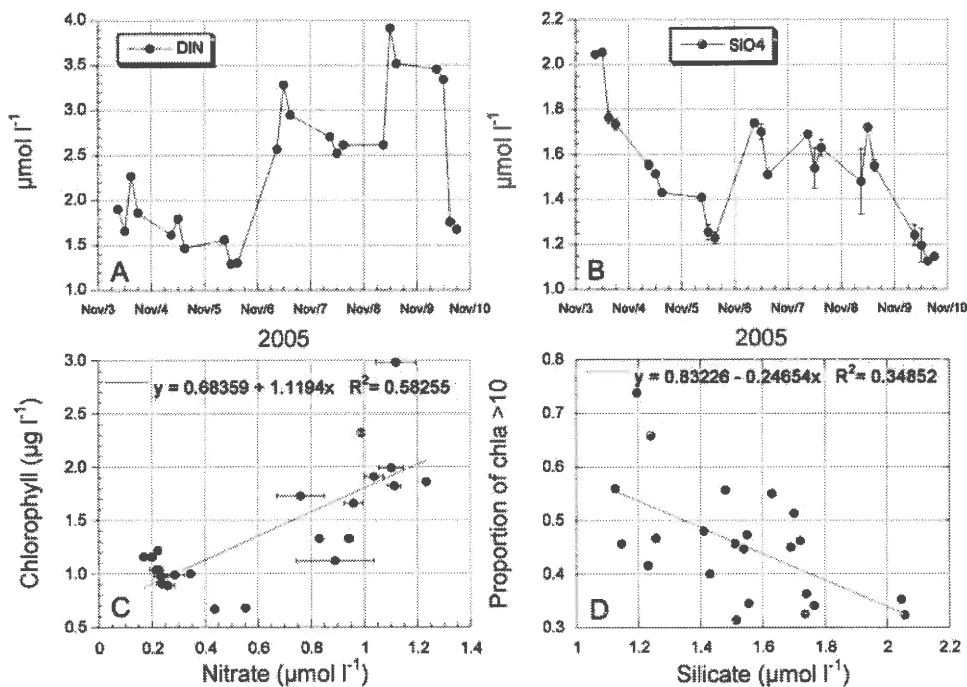
Figure 1. Data from the one week long sampling effort in Nov 05 in the coast of Barcelona. A: Dissolved inorganic nitrogen over time. B: Dissolved silicate over time. C: Chlorophyll versus nitrate concentration. D: The proportion of chlorophyll larger than 10 μm with respect to silicate concentration.

We had mostly calm weather in Nov 05, while we had a storm in the middle of our sampling effort in Apr 06. This storm seems to have resuspended the sediments and a clear signal of fluorescence is observed in the water column and especially near the sediment bed. Aerial pictures and he fact that the signal started just somewhat earlier at a shallower station and just somewhat later at a deeper station strengthen the resuspension view (Fig. 2). Whether this is growth responding to increased nutrient concentrations (the turbidity signal is weaker than the fluorescence signal) or mostly resuspension of non-living organic matter and/or benthic phytoplankton biomass remains to be seen. For both sampling efforts chlorophyll is either unrelated or is

negatively related to turbulence. A statistically significant, positive response of chlorophyll to turbulence is observed with a time lag between 39 and 54 h (Fig. 3).
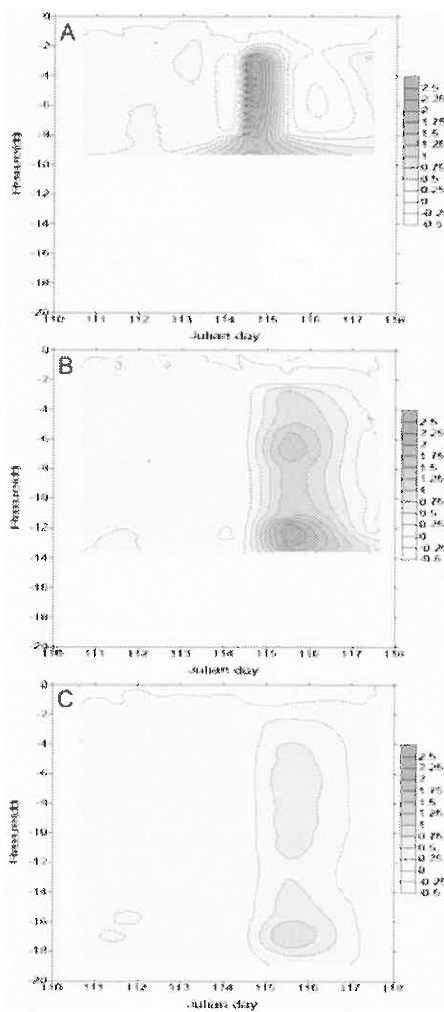
Figure 2. Contour plots of the fluorescence signal distribution in depth for the Apr 06 sampling effort. A: A station nearer to the shore than our reference station. B: the reference station. C: A station further away from the shore tha our reference station.

DISCUSSION

It should be normal to find a time lag of the response of chlorophyll to turbulence since organisms have to respond to turbulence by growing and this takes some time. The variability in this response is also understandable if one takes into account the variability in previous physiological histories, different phytoplankton taxa, and

166

variations in other environmental variables, such as temperature and irradiance for instance. The negative correlation observed in Nov 05, when no time lag is considered between chlorophyll and turbulence, is puzzling. Recent studies show that turbulence may actually increase the settling velocity of phytoplankton particles (Ruiz et al. 2004). It could be that under turbulence a portion of the particles settle downward reducing the chlorophyll signal and that once turbulent conditions subside, phytoplankton is stimulated most likely also owing to higher inorganic nutrient concentrations or a higher resource ratio. In Apr 06 correlations are not significant for time lags less than 36 h.
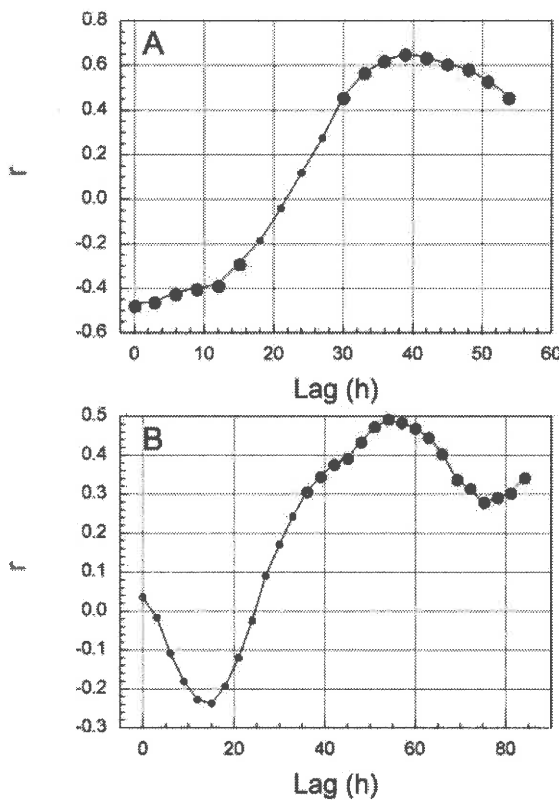
Figure 3. Crosscorrelograms of turbulence and chlorophyll for the Nov 05 (A) and the Apr 06 (B) sampling efforts. Blue dots show significant correlations (P < 0.05).

As has been already shown with laboratory experiments nutrient availability is highly determinant for system production. Turbulence is an additional factor that seems to act directly and indirectly upon osmotrophic organisms, although with a weaker signal. Continuous in situ measurements of turbulence, nutrients and chlorophyll fluorescence are needed to discern the effect and interactions of each forcing factor on coastal ecosystem production. Ideally, records should cover several years at an hourly or higher frequency, and we are making progress towards that goal.

ACKNOWLEDGMENTS

REFERENCES
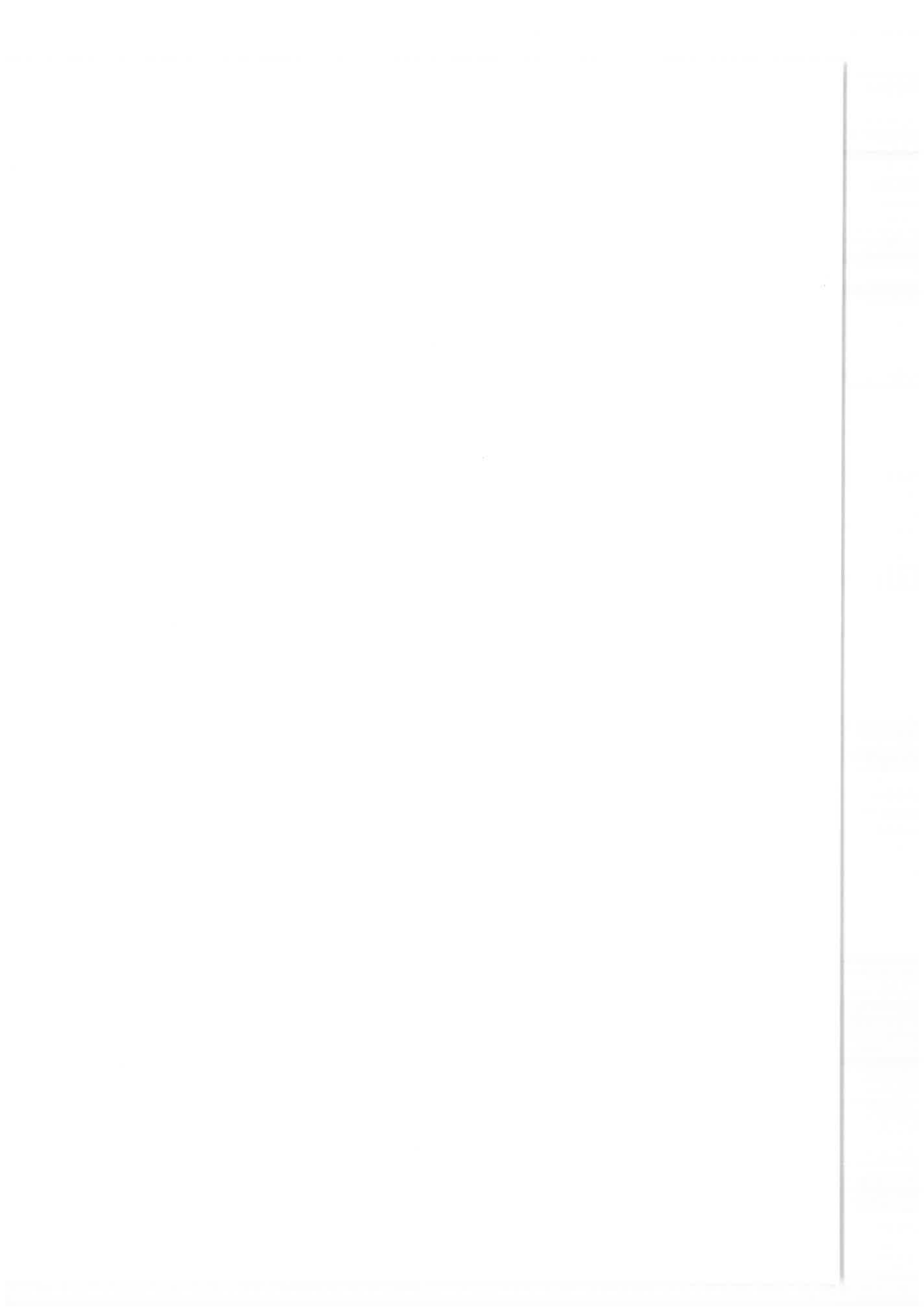
ARIN, L., C. MARRASÉ, M. MAAR, F. PETERS, M.M. SALA, AND M. ALCARAZ. 2002. Combined effects of nutrients and small-scale turbulence in a microcosm experiment. I. Dynamics and size distribution of osmotrophic plankton. Aquat. Microb. Ecol. 29: 51-61.

KARP-BOSS, L., E. BOSS, AND P.A. JUMARS. 1996. Nutrient fluxes to planktonic osmotrophs in the presence of fluid motion. Oceanography and marine Biology: An Annual review. 34: 71-107.

KIØRBOE, T., MACKENZIE, B. 1995. Turbulence-enhanced prey encounter rates in larval fish: effects of spatial scale, larval behaviour and size. J. Plankton Res. 17: 2319-2331.

MACKENZIE, B.R., AND W.C. LEGGETT. 1993. Wind-based models for estimating the dissipation rates of turbulent energy in aquatic environments: empirical comparisons. Mar. Ecol. Prog. Ser. 94: 207-216.

PETERS, F., AND C. MARRASE. 2000. Effects of turbulence on plankton: an overview of experimental evidence and some theoretical considerations. Mar. Ecol. Prog. Ser. 205: 291-306.

PETERS, F., L. ARIN, C. MARRASÉ, E. BERDALET, AND M.M. SALA. 2006. Effects of small-scel turbulence on the growth of two diatoms of different size in a phosphorus-limited medium. J. Mar. Syst.

ROTHSCHILD, B.J. AND T.R. OSBORN 1988. Small-scale turbulence and plankton contact rates. Journal of Plankton Research. 10: 465-474.

RUIZ, J., D. MACÍAS, F. PETERS. 2004. Turbulence increases the average settling velocity of phytoplankton cells. Proc. Nat. Acad. Sci. USA. 101: 17720-17724.

THE IMPACT OF WATER LEVEL FLUCTUATIONS AT DIFFERENT TEMPORAL AND SPATIAL SCALES ON ABIOTIC AND BIOTIC PROCESSES

Hilmar Hofmann; Andreas Lorke, A.; Frank Peeters[1]

(1) Environmental Physics Group, Limnological Institute, University of Konstanz, Konstanz, Germany

Water level fluctuations (WLF) of surface water bodies generated by internal and external physical processes, such as long-term precipitation, high discharge events, basin-scale oscillations, or short-term surface waves, affect especially the littoral zone. These processes occur at various temporal and spatial scales, which can be divided into a macro scale and a micro scale. The macro scale describes well known long-term temporal (days to years) and wide-ranged spatial (meters to kilometres) scales. The micro scale, on the other hand, is characterized by short-term temporal (seconds to hours) and locally limited (centimetres to meters) spatial scales. The impacts of micro scale WLF on habitat and organisms are often underestimated due to a lack of appropriate measurements. Although the forcing at both scales is different and hence interactions between them are limited, their superposition has major consequences for the interface between the aquatic and the terrestrial ecosystems. The understanding and consideration of WLF at a wide range of temporal and spatial scales allows to understand changes of abiotic and biotic processes, e.g. resuspension, sediment transport, migration of fishes, phytoplankton growth and abrasion or coverage of biofilms in the shallow littoral zone.

THE INFLUENCE OF STRATIFICATION AND MIXING PROCESSES ON THE VERTICAL DISTRIBUTION OF NUTRIENTS IN A SMALL, EUTROPHIC LAKE

H. Miller[3], I. Jones[1], A. Folkard[2], S. Maberly[1]

(1) Centre for Ecology and Hydrology, Lancaster Environment Centre
(2) Department of Geography. Lancaster University
(3) Lancaster, LA1 4AP UK

During the summer, the development of temperature stratification can play an important role in the distribution of nutrients within a lake (Wetzel, 1983). Stratification leads to a partitioning of the water column into a relatively well mixed surface layer and a deeper layer of cooler water, separated by a thermocline (Kalff, 2002). In the deeper layer of cooler water there is characteristically much less turbulence than in the surface mixed layer (Kalff, 2002) and respiratory processes dominate (Stumm & Morgan, 1996). The decrease in the turbulent mixing imposed by the stratification means that the respired oxygen is not rapidly replenished from the surface. This sometimes leads to the bottom waters of the lake becoming anoxic (Wetzel, 1983) leading to surface sediment anoxia. Oxidized substances are then reduced in the sediment leading to phosphorus diffusing from the sediment into the overlying water and resulting in a build up of phosphorus in the water at the bottom of the lake (Bostrom *et al.*, 1988).

In order to calculate the thermal stability of the stratification, a determination of the amount of work required by the wind to destratify a lake without the addition or subtraction of heat is needed (Idso, 1973). This can be calculated using the Schmidt stability, Equation [1], which represents the susceptibility of the whole water column to wind mixing (Hutchinson, 1957) and the likely mixing of deep water and nutrients into the surface mixed layer (Kalff, 2002).

The Wedderburn number, Equation [3], is the ratio of depth-based buoyancy to the length-based wind mixing (Kalff, 2002). When W < 3-4, appreciable upwelling is caused up wind in a small lake (Thompson and Imberger, 1980). Tilting of the isopycnals occurs with the interface approaching the surface at W < 6 but not many significant upwelling events occurred above W = 6 in Chain Lake, British Columbia, a short shallow lake, similar to the one studied in this work (Stevens and Lawrence, 1997). W < 10 indicates evidence of shear stress and above W = 10 surface stirring dominates mixing (Schallenberg et al., 1999).

MATERIAL AND METHODS

Esthwaite Water is a glacial lake in the English Lake District approximately 1 km² in area with maximum and mean depths of 15.5 m and 6.4 m respectively (Ramsbottom, 1976). Water samples were taken with a 1L friedinger on a weekly basis at 0.5 m depth and then every 2 m down to a depth of 14.5 m from the 16th June to 13th October 2004 and every 1 m down to a depth of 14 m from the 1st June to 26th September 2005. Water samples were analyzed for total phosphorus (TP) following the method of Eisenrich (1975). Temperature data were collected every meter between 1 and 12 m depth from a thermistor chain and wind data were collected from a height of 2 m from a buoy on Esthwaite Water. The data were collected on a minute-by-minute basis and averaged to give daily means.

The stratification of the lake was quantified using the Schmidt stability of the lake, S, calculated per unit area from the thermistor data collected at the buoy,

$$S = -\frac{g}{A_0} \int_0^{z_m} (z - z_g) A_z (\rho_{max} - \rho_z) dz \qquad [1]$$

where A_0 is the surface area of the lake, A_z is the area of the lake enclosed by a contour of depth z, g is acceleration due to gravity (9.81 ms⁻²), ρ_{max} is the maximum density of the water (999.9749608 kg m⁻³), ρ_z is the density of water at depth z and z_m is the maximum depth (Hutchinson, 1957). A_0 and A_z were obtained from Ramsbottom (1976). The depth to the centre of gravity of the lake, z_g, is given by,

$$z_g = \frac{1}{V} \int_0^{z_m} z A_z dz \qquad [2]$$

where V is the volume of the lake. The temperature data were used to calculate the density of the water using the method of UNESCO (1981).

To quantify the tilting of the isopycnals, and determine whether upwelling of water from the metalimnion was taking place, the Wedderburn Number, W, was calculated as the ratio of the buoyancy to the wind induced friction velocity over the lake surface,

$$W = \frac{g' h_1}{u_*^2} \frac{h_1}{L} \qquad [3]$$

where g' is the modified gravity given by $(\Delta\rho/\rho_0)g$, with $\Delta\rho$ being the density difference across the thermocline and ρ_0 the water density at the bottom of the lake, L is the fetch ($\sqrt{A_0}$) and u_* is the wind induced friction velocity on the lake surface,

$$u_* = \left(\frac{\rho_a}{\rho_w} C_D U^2 \right)^{\frac{1}{2}} \qquad [4]$$

172

where ρ_w is the density of water, ρ_a is the density of air, C_D is the drag coefficient at a height of 2 m and U is the wind speed at a height of 2 m.

RESULTS

Esthwaite Water became stratified at the beginning of May in 2004 and 2005 (Figure 1). Between the 9th and 11th July 2004 (days 191 and 193) the surface mixed layer of the lake deepened to a depth of approximately 4 m. This part of the summer was cooler with some wet and windy weather. The stratification in the lake was re-established as the weather became warmer again. Between the 9th August and 26th September 2004 (days 222 and 260) the stratification became weaker and the lake overturned between the 16th and 26th September 2004 (days 260 and 270).
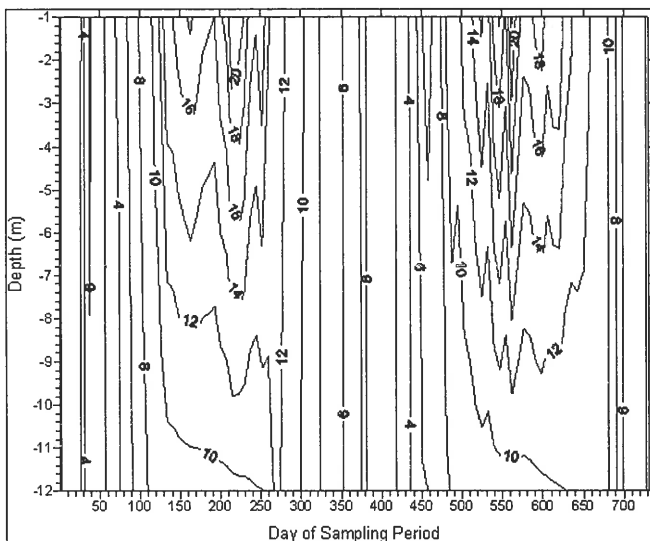
Figure 1. Temperature (°C) measured from 1st January 2004 to 31st December 2005 down a vertical profile at the buoy on Esthwaite Water. The contour lines are drawn every 2°C between 4 and 20°C.

Between 14th and 19th June and 8th and 10th July 2005 the surface mixed layer of the lake deepened from a depth of approximately 2 m to 5 m (Figure 1). On 29th July and 28th August 2005 there were shorter mixing events causing the surface mixed layer of the lake to deepen to a depth of approximately 6 m. During 2005 there were more mixing events and the temperature structure of the lake appeared to be less stable than in 2004. Between 7th September and 17th October 2005 the stratification became weaker and the lake overturned between the 2nd and 17th October 2005, 20 days later than in 2004.

173

The temperature data (Figure 1) were used to calculate the Schmidt stability of Esthwaite Water for 2004 and 2005 (Figure 2). The stratification in the lake appeared from the beginning of April (approximately day 100) in both years. In 2004 there were two main periods of stratification with the Schmidt stability reaching 120 J m^{-2} on 8th June (day 160) and 145 J m^{-2} on 12th August (day 225). Between these dates the lake partially destratified with the Schmidt stability decreasing to 60 J m^{-2} on 8th July (day 190).
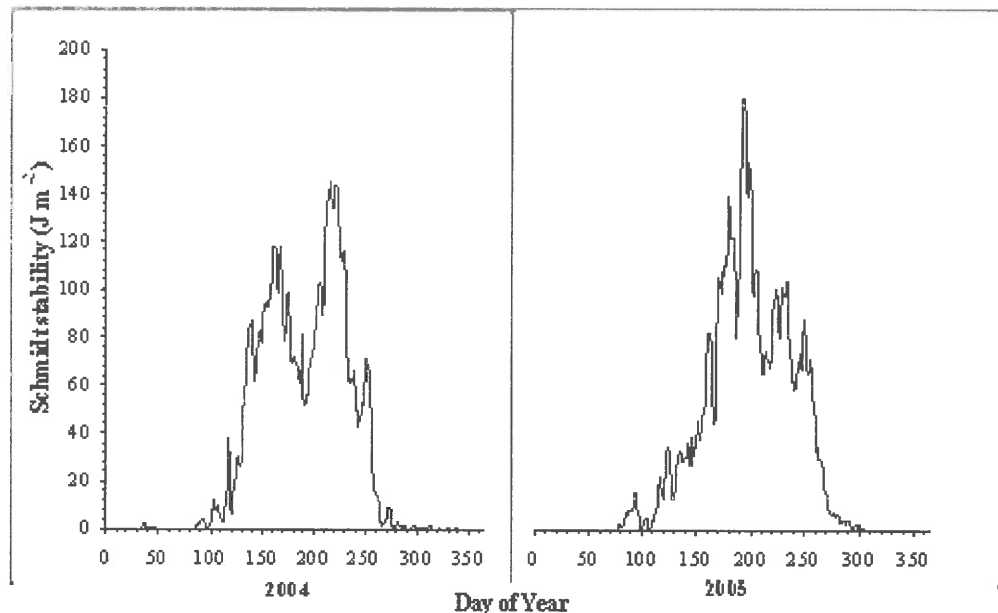
Figure 2. Daily averaged Schmidt stability for 2004 and 2005 calculated using the temperature data collected from the thermistor chain on the Esthwaite Water buoy.

In 2005 the stratification in the lake built up more slowly than in 2004. The general pattern in the Schmidt stability showed an increase to 180 J m^{-2} by 13th July (day 194) and then a decrease with the lake overturning in mid-October (day 285). The peak in the stability of the stratification in 2005 was higher than either of the peaks in the stability of the stratification in 2004. However, the period of stratification was more often interrupted by mixing events than in 2004 with noticeable decreases in the Schmidt stability on the 19th June, 9th and 29th July and 2nd September (days 170, 190, 210 and 245).

The Wedderburn Number (W) was calculated for each year on an hourly basis. In 2004 there were 10 days when upwelling of the metalimnion to the surface of Esthwaite Water occurred for an hour or more (W < 4), on 4 further days W < 6 and W < 10 on 11 further days. In 2005 there were 7 days when W < 4, 17 further days when W < 6 and 7 further days when W < 10.

174

The relationships of the Schmidt stability and the Wedderburn number with TP were not linear and so a linear regression could not be used to investigate the relationships. A Generalised Additive Model (GAM) was used instead. The models fitted to the TP data from the mixed layer indicated that the Schmidt stability model was significant during 2004 and the Wedderburn number model was significant during 2005. The TP data from below the mixed layer indicated that the Schmidt stability model was significant in both years.

DISCUSSION

The results from the GAM suggest that the Schmidt stability had a greater correlation with TP in 2004 than in 2005 and that the Wedderburn number was more highly correlated than the Schmidt stability for the surface mixed layer waters in 2005. A Pearson correlation between TP concentration and Schmidt stability at each sample depth down the water column was carried out. For the 2004 data the correlations were increasingly negative at and above 4.5 m and increasingly positive below 4.5 m. This relationship was significant with $r = 0.997$ ($F_{1,6} = 1011$, $p \ll 0.001$) implying that the TP concentration decreased with an increase in Schmidt stability at and above 4.5 m because of a decrease in mixing so less TP was being moved up from the bottom of the lake into the surface mixed layer. The increase in TP concentration with an increase in Schmidt stability below 4.5 m implies that the TP concentration was increasing because there is less mixing taking place to move the TP into the surface mixed layer. For the 2005 data the correlation between TP concentration and Schmidt stability did not show such a clear cut pattern.

The difference between the years could have been due to different patterns in the wind strength during 2004 and 2005 but analysis of the wind data did not indicate this (not shown). The Wedderburn number did differ between 2004 and 2005, however, with $4 < W < 6$ on 4 occasions in 2004 and 17 occasions in 2005. When the isopycnals tilt and the interface approaches the surface boundary mixing will occur at the side of the lake. Boundary mixing is important for the movement of nutrients in a stratified lake. If boundary mixing was occurring in 2005, eddy diffusivity values should be higher at the side of the lake where the thermocline intercepts the bank (MacIntyre, 1999).

These results imply that the mixing between the two years was different. Vertical mixing occurred in both years but there was more boundary mixing taking place in 2005. Future work will investigate the spatial distribution of diffusivity within Esthwaite Water and differences in surface heating between the years.

175

REFERENCES

HUTCHINSON, G.E. 1957. A treatise on limnology, Volume 1: Geography, physics and chemistry. Wiley.

IDSO, S. B. 1973. On the concept of lake stability. Limnol Oceanogr. 681-683.

KALFF, J 2002. Limnology. Prentice Hall.

MACINTYRE, S., FLYNN, K. M., JELLISON, R. AND ROMERO, R. 1999. Boundary mixing and nutrient fluxes in Mono Lake, California. Limnol Oceanogr. **44**: 512-529.

RAMSBOTTOM, A.E. 1976. Depth charts of the Cumbrian lakes. Freshwater Biology Association Scientific Publication No. 33.

SCHALLENBERG, M., JAMES, M., HAWES, I AND HOWARD-WILLIAMS, C. 1999. External forcing by wind and turbid inflows on a deep glacial lake and implications for primary production. New Zeal J Mar Fresh. **33**:311-331.

STEPHENS, K. 1963. Determination of low phosphate concentrations in lake and marine waters. Limnol Oceanogr. **8**: 361-362.

STEVENS, C. L. AND LAWRENCE, G. A. 1997. Estimation of wind-forced internal seiche amplitudes in lakes and reservoirs, with data from British Columbia, Canada. Aquat Sci. **59**: 115-134.

THOMPSON, R. O. R. Y. AND IMBERGER, J. 1980. Response of a numerical model of a stratified lake to wind stress. Proc. Int. Symp. Stratified Flows. 2nd Tronheim. **1**:562-570.

UNESCO 1981. Tenth Report for the joint panel on oceanographic tables and standards, Unesco Technical Papers in Marine Science, 36.

Wetzel, R.G. 1983. Limnology, second edn. Saunders College Publishing.

DYNAMICS OF A RIVER INFLOW INTO A RESERVOIR: CONSEQUENCES FOR THE PHYTOPLANKTON POPULATION

Javier Vidal, Xavier Casamitjana, Jordi Colomer and Teresa Serra[1]

(1) Institute of the Environment, University of Girona
Campus de Montilivi, 17071 Girona, Spain

INTRODUCTION

This paper investigates river inflow into the Sau Reservoir. During the last days of July 2005, the daily variation of the river temperature made the daily inflow response vary from overflow to interflow, and the reservoir was a highly dynamic system with increased mixing. Furthermore, during the overflow events nutrients from the river were introduced at the surface of the reservoir and a bloom of cyanobacteria was located in the mixing zone of these overflow events with the quiescent body of the reservoir, clearly linking physics and biology.

River valley reservoirs, such the Sau Reservoir, are often long and narrow, receiving water from a single river inflow; these reservoirs have important longitudinal changes controlled by the river intrusions into them (Hejzlar & Straskraba, 1989). These characteristics allow reservoirs to be defined as hybrid systems between rivers and lakes (Margalef, 1983), showing a progressive transformation from river to lake system, not only in the environmental variables but also in their morphology and hydrodynamic characteristics. In general, a reservoir can be divided along its longitudinal axis into three zones (Kimmel et al., 1990): the riverine, the transition and the lacustrine zones. The riverine zone is characterized by higher flow, short residence time, and high values of nutrients and suspended solids. The transition zone where the river meets the reservoir is characterized by high phytoplankton productivity, decreasing flow velocity, increased water residence and high sedimentation. Finally, the lacustrine zone is related with the area near the dam with longer residence time, less available nutrients and less suspended matter. The boundaries between the three zones are not well defined and can be highly dynamic, responding to inflow characteristics.

Sau is a canyon-shaped reservoir, 18.5 km long and deep (up to 80m), located in the central part of the Ter River, which is 200 km long and has its source in the Pyrenees in the northeast of Spain. Because of its morphology (Fig. 1), it can be divided into three hydrodynamic zones (Fig. 1). The hydrodynamics of the lacustrine zone are mainly dominated by the wind that generates wind driven currents and

internal waves (Vidal et al. 2005). The riverine and transition zones, however, are narrow and meandering zones sheltered from the wind; here, the hydrodynamics are mainly dominated by the river inflow.
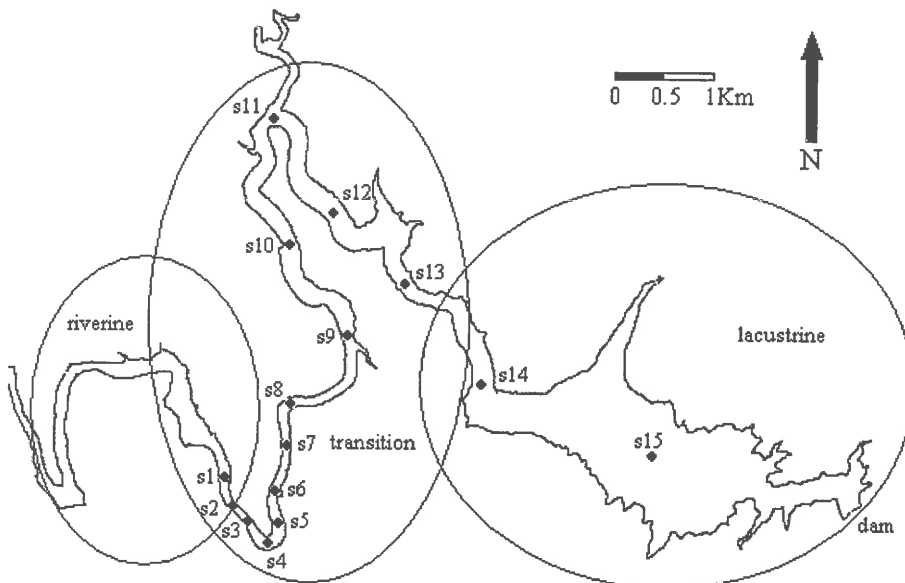
Figure 1. Location of the measuring stations along the Sau Reservoir. The reservoir has been divided into riverine, transition and lacustrine zones.

Armengol et al. (1999) studied the long term longitudinal processes associated with the river circulation patterns in the Sau Reservoir. They described the annual pattern of the inflow circulation based on the density differences between the inflow and the main body of the reservoir. In winter, the inflow temperature is colder than that of the reservoir and the circulation is that of an underflow. This deep circulation remains until February, when the river temperature rises faster that the surface water of the reservoir and an overflow occurs. From February to April-May the surface circulation corresponds to the start of the spring phytoplankton bloom due to the injection of nutrients into the photic zone. The transition between spring and summer is characterized by an interflow that sinks progressively until mid November when it reaches the bottom as an underflow.

We will show in this paper that the hydrodynamics of the river inflow into the Sau Reservoir are not only affected by seasonal, but also by short term variations; that the quick response of the river temperature to variations from days to weeks also makes it a highly dynamic system; and that there are related consequences for phytoplankton population.

MATERIAL AND METHODS

CTD profiles were carried out at measuring stations s1 to s15 (Fig. 1) every 2 days from 26th July to 1st August 2005 (Julian days 207-213); a thermistor string and an ADCP were also deployed at s6. The thermistor string was composed of ten thermistors measuring every half a meter between 0.5 m and 5 m with a sampling interval of 2 minutes. The ADCP was deployed on the water surface with the beams looking downward and an interval rate of 10 min and a cell size of 20 cm. Meteorological data was supplied from a nearby automatic meteorological station on the Ter River; and the temperature, conductivity and nutrients of the river were obtained from an automatic station placed on the Ter River near the reservoir.

RESULTS

The inflow dynamics of the river into the reservoir are governed by the density difference between them, and temperature is the main factor controlling that density. The river temperature is highly dependent on the air temperature, responding quickly to short term variations of it (Fig. 2A). During the survey the river inflow was around 2-3 $m^3 \cdot s^{-1}$ (Fig. 2B) and the outflow was intermittent and normally higher than the inflow; because of this, the water level was decreasing. Conductivity (Fig. 2C) can be used as a tracer, and phosphorous, which is usually the limiting factor of the algal growth in Sau is shown in Fig 2D.
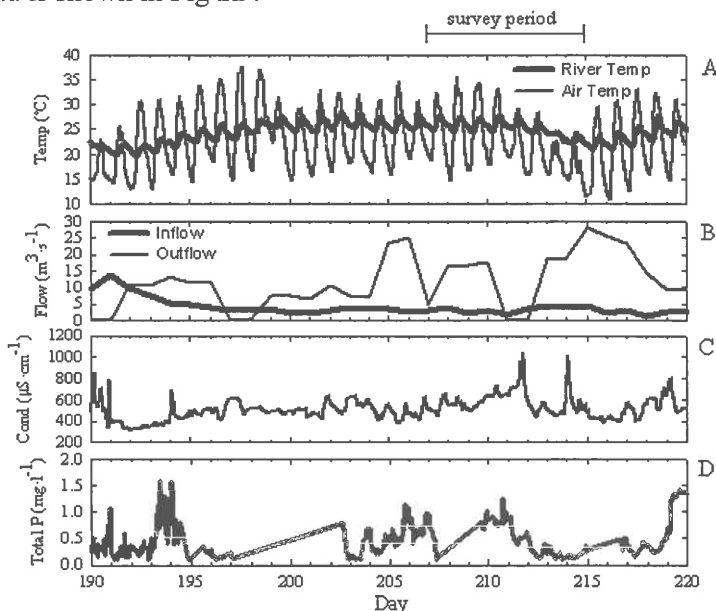
Figure 2. Evolution of (A) river temperature and air temperature from Julian day 190 (2005) to 220 (2005); (B) inflow and outflow; (C) river conductivity; and (D) concentration of total phosphorus in the river.

During the last days of July 2005 an overflow situation was alternating with an interflow situation. Throughout the day the river was getting warmer and its temperature reached similar values as those found on the surface of the reservoir, generating an overflow. However, during the night the river was getting colder than the water surface and an underflow took place, intruding at approximately 7-8 meters depth, where the density of the river reaches the density of the reservoir. During the survey, the intersection of the river with the reservoir was located between s2 and s3 (Fig. 1) where the plunge point occurs. The changing dynamics of the inflow can be observed by looking at the data from the ADCP and the temperature string, deployed at s6 (Fig. 3). Figure 3B shows the velocity profile during three days, with positive values following the direction of the river towards the dam. Here it is clear how the inflow varies from an underflow to an overflow with positive velocity values changing from the bottom to the surface respectively.

The river intrusion depth has been estimated by comparing the river density with the reservoir density obtained from the thermistor string at s6, and by taking into account the introduced delay due to the time needed for the river to travel from the automatic measuring station to s6. Black lines in Figures 3A and 3B show the estimated intrusion depth that roughly corresponds to the inflow position (see Fig. 3B), as expected. Figures 3C and 3D show a drawing of the alternation between overflow and interflow with a 12h delay. During the underflow episodes cold dense water from the river is entering into the warmer water of the reservoir; and during the overflow episodes warm water from the river displaces the surface water of the reservoir.

The estimated position of the river inflow during the overflow events is approximately 1m deep and for that reason it is not a real overflow, although the nearness of the surface allows the inflow to also reach the surface. In both processes an upstream is generated and water from the reservoir is entrained in the inflow, especially at the plunge point where the mixing is greater. That is, during the overflow events cold water from lower layers is traveling upstream (Fig. 3C) and during the interflow events (Fig. 3D) water from the surface of the reservoir travels upstream. In s6, the water column stratifies during overflow and underflow events, and mixes during the transition of such events (Fig 3A).
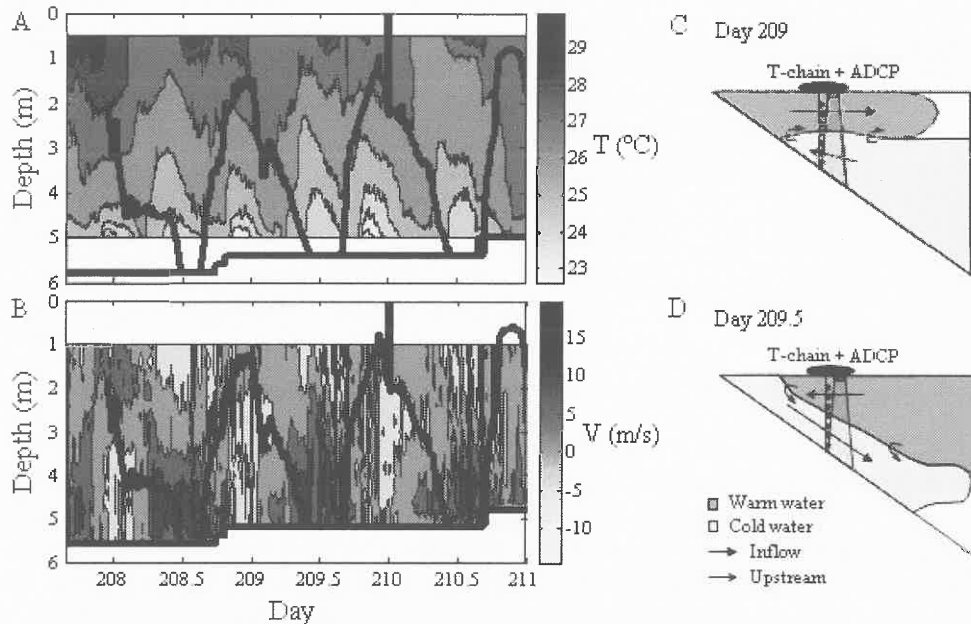
Figure 3. (A) Evolution of the temperature column at station 6. (B) Evolution of the velocity in the water column at station 6. (C) and (D) represent a draft of the overflow and interflow events occurring on days 209 and 209.5, respectively. Black lines in (A) and (B) show the estimated intrusion depth.

From a water quality point of view, it is important to know how the river nutrients will be distributed along the reservoir and the effect of such nutrients on the phytoplankton populations. Conductivity from the river inflow is generally higher than the reservoir and can be used as an inflow tracer. Figure 4A shows the conductivity in a longitudinal section following the thalweg profile carried out at midday on day 209. The conductivity distribution is not only due to present events but also to background events. The alternation between the overflow and the interflow means that, in the first kilometers, water from the inflow is distributed all along the water column and not only in the positions of the present overflow and interflow events.

181
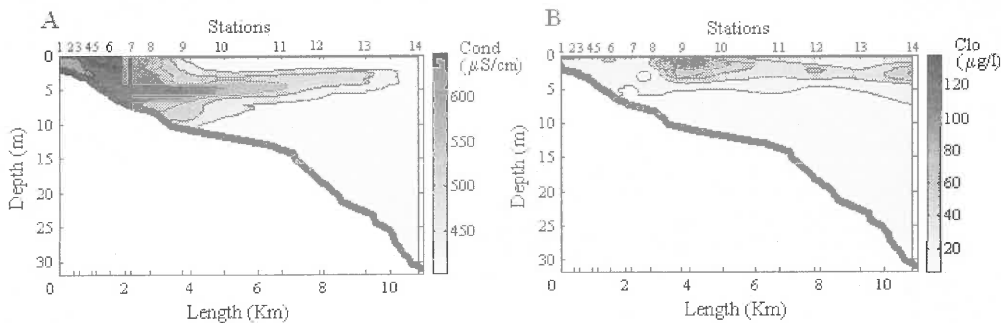
Figure 4. Longitudinal profile of (A) conductivity and (B) Chlorophyll following the thalweg during day 209.

It is expected that nutrients from the river will have a similar distribution as the conductivity. If we look at the water surface in Figure 4A there is a big gradient around s9, where the front of the overflow episodes is located. This well located zone is characterized by water from the river, rich in nutrients, mixed with water from the reservoir that is also characterized by being quite eutrophic. In such conditions, the nutrients injected from the overflow events into that zone of the reservoir, together with the sunny conditions, developed a bloom of Cyanobacteria in this well located zone (see Fig. 4B), clearly linking physics and biology.

REFERENCES

ARMENGOL, J., AND OTHERS. 1999. Longitudinal processes in canyon type reservoir: The case of Sau (N.E. Spain), p. 313–345. *In* J. G. Tundisi and M. Straskraba [eds.], Theoretical reservoir ecology and its applications. Backhuys Publishers.

HEJZLAR, J. AND STRASKRABA, M., 1989. On the horizontal distribution of limnological variables in Rimov and other stratified Czechoslovak reservoirs. Arch. Hydrobiol. Beih. Ergebn. Limnol., 33:41-55.

KIMMEL, B. L., LIND, O. T. AND PAULSON, L. J., 1990. Reservoir Primary Production. pp. 133-193. In K. W. Thornton, B.L. Kimmel and F. E. Payne (eds.), Reservoir limnology. Ecological perspectives, John Wiley & Sons, Inc., NY.

MARGALEF, R., 1983. Limnologia, ed. Omega, Barcelona.

VIDAL, J., CASAMITJANA, X. COLOMER J. AND SERRA T., 2005. The internal wave field in Sau reservoir: Observation and modeling of a third vertical mode. Limnol. Oceanogr, 50: 1326–1333.

VERTICAL STRUCTURE OF ALGAL POPULATIONS WITH CONTRASTING BUOYANCY: PHYSICAL VS. BIOLOGICAL DRIVERS IN A CANYON-SHAPED RESERVOIR

Rafael Marcé [1]*, Claudia Feijoó [1], [2], Enrique Navarro[1],
Jaime Ordóñez[1], and Joan Armengol[1]

(1) Fluvial Dynamics and Hydraulic Engineering (FLUMEN), Department of Ecology, University of Barcelona, Spain.
(2) Programa de Ecología Acuática, Universidad Nacional de Luján, Argentina.
* rafamarce@ub.edu

INTRODUCTION

The spatial distribution of algal populations in lakes and reservoirs is the outcome of the summation of several processes: biological growth and decay, sedimentation, turbulence motion, and advective currents. The presence of wind-driven internal seiches and their associated currents poses the algal populations in a challenging situation: they must counteract the effects of advective movements and the competition for light and nutrients with other algal populations to perennate.

Keeping this in mind, Mediterranean canyon-shaped reservoirs share some interesting features: they are elongated reservoirs with strong winds showing a remarkable periodicity in direction and intensity. This frequently excites seiches modes resonant with the wind field. In addition, their eutrophic state severely limits the light ambient of the water body. Taking Sau Reservoir (Spain) as a prototype of this kind of systems, we show results from a 3-day experiment with 4-h periodicity to exemplify how vertical structures can arise in connection with a noisy horizontal pattern, and how biological activity interacts with the physical forces to produce non-intuitive vertical algal distributions.

STUDY SITE AND EXPERIMENTAL APPROACH

Sau Reservoir is a canyon-shaped, eutrophic reservoir located on a middle stretch of the Ter River (Northeast Spain). The reservoir has two main sectors: an upstream elongated section highly influenced by the river inflow, and a deep lacustrine section near the dam (Fig. 1), where a marked daily wind pattern promotes the presence of internal seiches of several modes (Vidal et al. 2005).
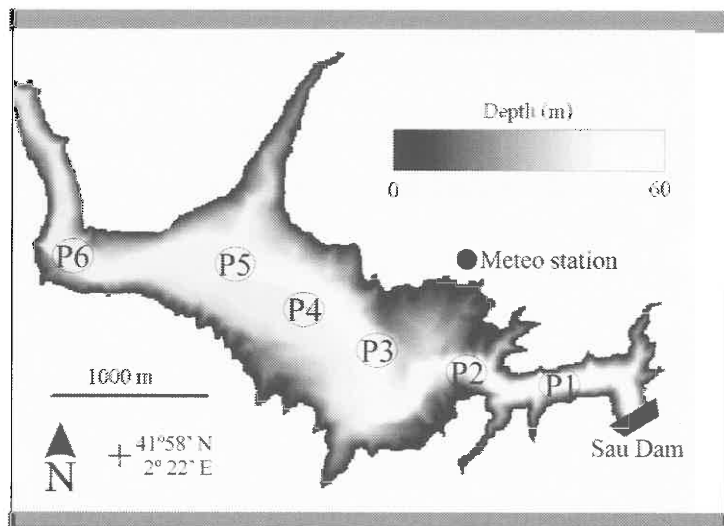
Fig. 1. Lacustrine section of Sau Reservoir, with location of the meteorological station and of the sampling points.

We sampled 6 stations (Fig. 1) with 4 h periodicity during 3 days along the main axis of the lacustrine section, in order to describe the longitudinal properties of the internal wave that was present during these days in the reservoir. We focused on the end-wall side of the reservoir, although one station (P6, Fig. 1) was located in the West end of the lacustrine section, where it joins the riverine section of the reservoir.

In each station we collected vertical profiles of temperature and algal abundance with a field fluorometric probe (bbe Fluoroprobe), which was previously calibrated with algae obtained from cultures based on autochthonous populations. Since we were interested in the algal motion in the surface layer, the vertical profiles were 10 m deep, just to cover the most accessible picnocline.

Simultaneously, ten drogue-release experiments were performed to assess the effect of the wind on the movement of the surface layers of the reservoir. The drogues were 5 L plastic containers filled with water and appropriately ballasted, linked by a very thin line to flat, non wind-drifted buoys. They were released at 0, 1, 3 and 5 m depth, using three replicates for each level, and the drifting time varied between two

184

and four hours. They were tracked using the release and gathering points recorded with a GPS receiver.

Hourly-averaged meteorological data were obtained from a station located in the shoreline at ca 10 m above the level of the reservoir.

THE SEICHE MODE

The drogue-release experiments reinforced the conclusion already reached by Vidal et al. (2005) that the surface water movements in Sau Reservoir are directly linked to the wind forcing. Table 1 shows the correlations found between the vector of movement calculated for the drogues at different depths and the vector of the measured wind during the drifting time. Since we are mainly interested in the water movements along the reservoir, only the projection on the main axis of the reservoir (imaginary line connecting P2 and P6 in Fig. 1) was used. The high correlation values strongly support the hypothesis that the wing forcing controls surface water movements in the reservoir.

Drogue depth (m)	Pearson r	Spearman R	pvalue for R
0	0.99	0.97	< 0.001
1	0.98	0.95	< 0.001
3	0.96	0.85	0.004
5	0.90	0.68	0.042

Table 1. Correlations between drogue vector and wind vector during drogue-release experiments.

Taking into account the principal effect of the wind on water movements in the reservoir and the daily pattern of the wind vector in Sau Reservoir, the presence of internal waves resonant with the wind field is not surprising. Actually, plotting the depth of the isotherm that best characterize the most superficial thermocline during the experiment, the presence of an internal seiche with the node between stations 4 and 5 is obvious (Fig. 2).
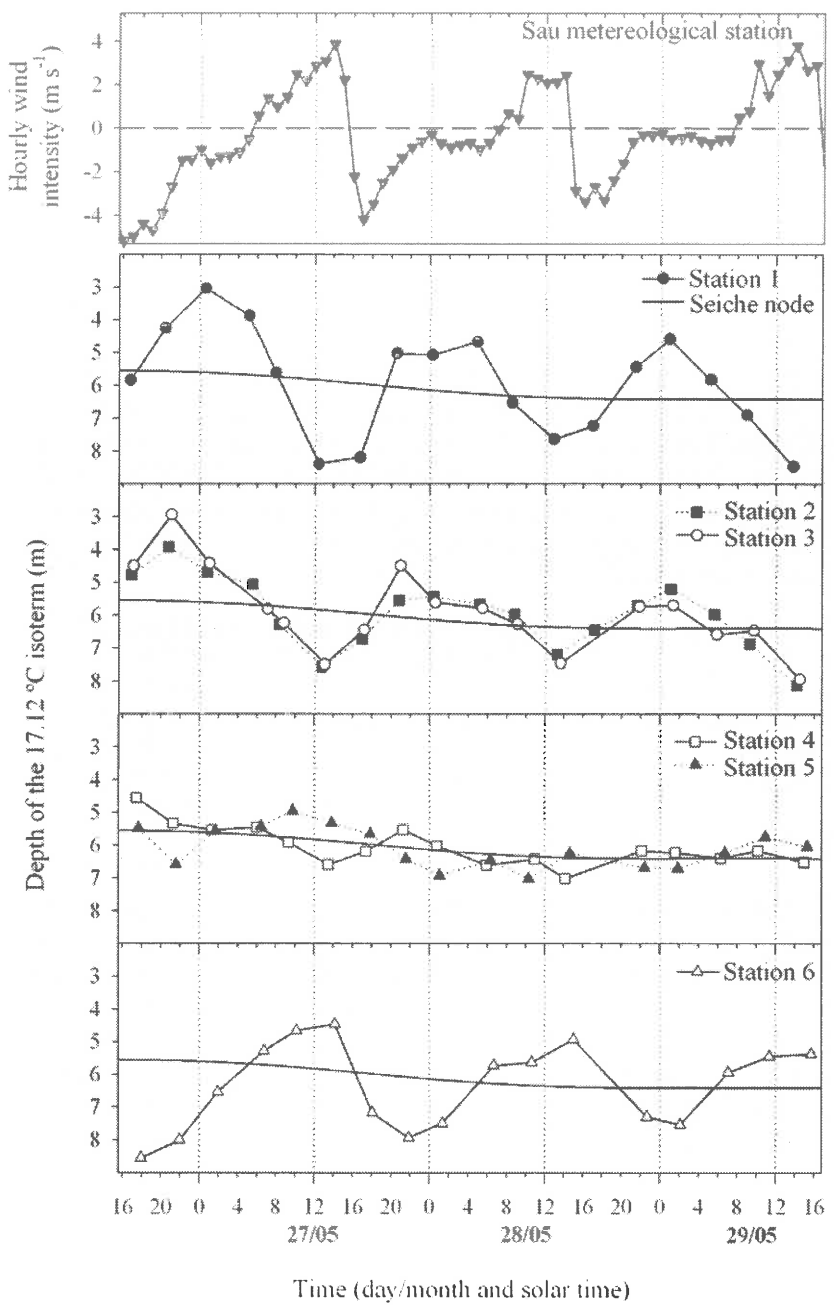
Fig. 2. Wind velocity vector projected on the main axis of the reservoir (negative to the West), and oscillations of the thermocline in the different sampling stations during the experiment. The location of the seiche node was estimated fitting a spline to data from stations 4 and 5.

186

A Maximum Entropy Spectral Analysis (MESA) stressed the relationship between the wind regime and these oscillations (Fig. 3). A main peak at 24 h and its harmonics were present for the wind time-series, and it was coincident with the main period showed by the thermocline oscillations, especially in those stations located in the extremes of the seiche.
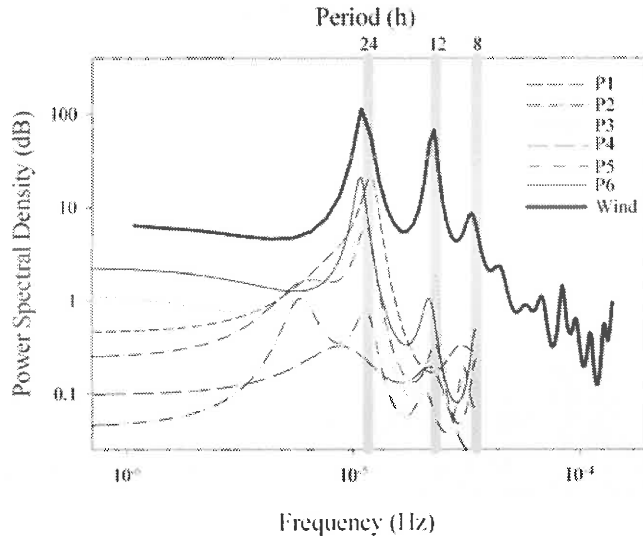
Fig. 3. MESA for the wind time-series and the oscillations of the thermocline showed in Fig. 2.

To fully describe the internal wave field in the reservoir during these days, we extended the analysis to the deep layers of the reservoir solving the Münnich et al.'s (1992) eigenvalue problem with the help of a temperature profile from surface to the bottom measured just before the beginning of the experiment. The theoretical periods for the first four vertical modes in Sau Reservoir with the given temperature profile are detailed in Table 2. From this result, we conclude that the surface oscillation detected with the temperature profiles is most probably the first vertical oscillation of a V3H1 mode, because this is the mode with the period closest to the observed period of thermocline oscillation.

Seiche mode	Oscillation period (h)
V1H1	8.32
V2H1	14.12
V3H1	21.59
V4H1	37.81

Table 2. Theoretical periods for the first four vertical modes in Sau Reservoir during the sampling days.

In addition, we calculated the theoretical maximum amplitude of the oscillations for the different seiche modes in Sau Reservoir, and we compared this with the observed oscillations for the surface thermocline. We found that the results agreed with the presence of a V3H1 mode (Fig. 4). It is worthy to mention that this mode has been already described in this reservoir (Vidal et al. 2005).
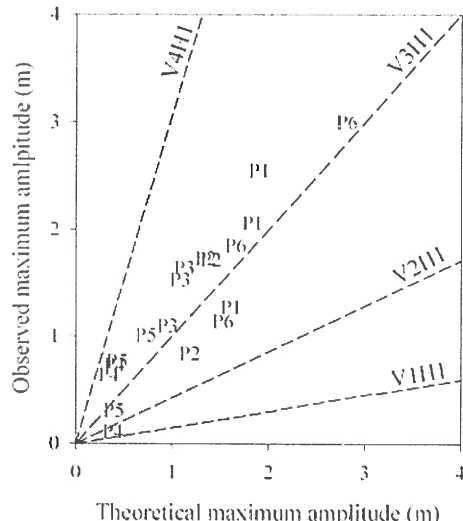
Fig. 4. Theoretical maximum amplitude for thermocline oscillations for different modes, calculated solving the Münnich et al.'s (1992) eigenvalue problem, against observed oscillations in the sampling stations.

ALGAE DISTRIBUTION

During the sampling days the epilimnetic algal community was composed by diatoms and chlorophytes almost in the same proportion (ca 16 g chl-a L $^{-1}$). Although a priori we expected the existence of marked longitudinal gradients in the distribution of the different algae, this was not the case during the experiment. In theory, when the wind blows in one direction, the algae should distribute following its buoyancy properties, with the positively buoyant species in the downwind shore and the negatively buoyant ones in the opposite side (Reynolds 1997). However, to form this "conveyor belt" the wind should blow in the same direction during time and intensity enough, to allow particles to cross the system before the wind pattern changes (Verhagen 1994). We calculated the minimum water velocity needed to form a conveyor belt in Sau Reservoir along its main axis in a 12 h period, and the resultant velocity (0.09 m s^{-1}) is almost two times the observed (0.046 m s^{-1}). Thus, during the sampling days the wind forcing was not high enough to form a "conveyor belt" during each 12 h period in which wind blows in the same direction (Fig. 2).

188

Consequently, a time-series plot of algal abundance in an extreme of the seiche in Sau Reservoir did not shown a 24 h cycle expected for a "conveyor belt", but a noisy trace around a mean value (Fig. 5).
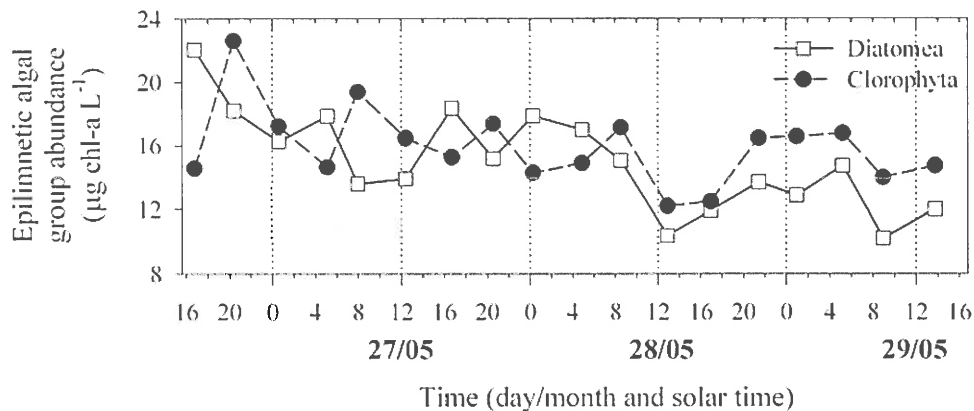
Fig. 5. Time-series of algal abundance (expressed as pigment concentrations) in Station 1.

By contrast, vertical distribution patterns with a strong periodicity were present during the study. To avoid being disturbed by the noisy nature of the algal horizontal distribution, we characterized the vertical distribution of diatomea and chlorophyta calculating the difference between the depth of the thermocline and the depth where the 95% of the algal biomass accumulated. The results for the 6 stations are shown in Fig. 6.

The diatoms and the chlorophytes behaved in a very different way. Green algae showed a dynamics similar to that expectable for a neutrally buoyant particle. The oscillations of the thermocline and associated advective movements did not affect its vertical distribution, most probably because green algae are almost homogeneously distributed all through the epilimnion. However, diatoms showed a very interesting pattern, changing the depth at which most part of the biomass accumulated in the form of a daily cycle. The pattern is consistent throughout the reservoir, although the cycle is much clearer in the Eastern side of the seiche. The dynamics of the open Western side (station 6) departs from the above description, probably due to riverine hydrodynamic processes overlapped to the seiche oscillation.

189
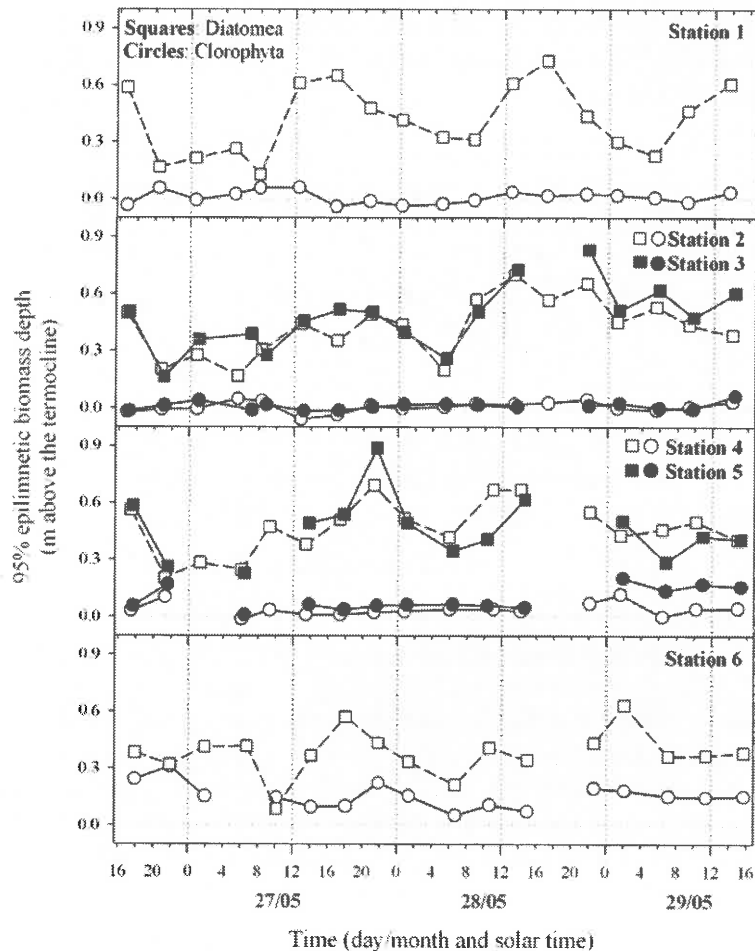
Fig. 6. Vertical distribution of the algal epilimnetic biomass respect the depth of the thermocline in the 6 sampling stations.

The link between thermocline oscillations and the wind regime allowed us to establish a direct causal relationship between the wind direction and the vertical disposition of the diatom assemblage (Fig. 7). Thus, the diatom community is spatially rearranged in a short time period by changes in the wind regime.

190
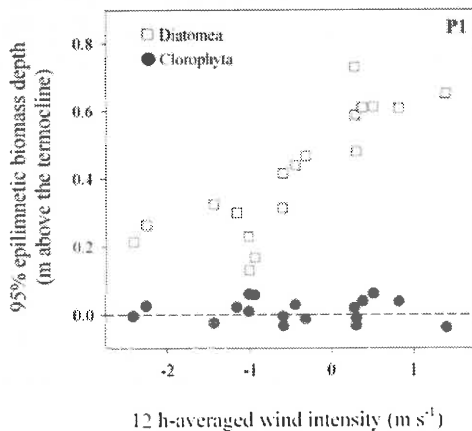
Fig. 7. Relationship between the vertical structure of phytoplankton groups and the wind regime.

MODELLING THE ALGAE MOTION

The differences found between the behavior of diatoms and chlorophytes in the preceding section were attributed to differences in the sinking rate, because the effect of growth and decay are not probable at this time scale. To test this hypothesis we modeled the algae motion modifying the modeling framework proposed by Huisman et al. (2002) in order to include the water advective motion induced by seiching:

$$\frac{\partial \omega}{\partial t} = (\tau - \nu)\frac{\partial \omega}{\partial z} + D\frac{\partial^2 \omega}{\partial z^2} \tag{1}$$

where ω is phytoplankton density, τ is the vertical water advective velocity induced by seiching, ν is the sinking velocity of phytoplankton, and D is the turbulent-diffusion coefficient. Since our simulations will extent only 12 h (i.e. the time that the thermocline takes for raising or deepening), in our model the biological growth and decay are not included in the equation. Raw D profiles were estimated following Wüest et al. (2000), and scaled by an adjustable parameter. τ vectors were taken from the eigenvalue problem above, and were also scaled by an adjustable parameter. ν velocities where left as adjustable parameters. We run one simulation for thermocline rising, and another for thermocline deepening. ν values where identical in both scenarios, since the fitting was performed simultaneously.

The fitting proceeded reasonably well (Fig. 8), and gave ν = 12.45 μm s^{-1} for diatoms and 5.04 μm s^{-1} for chlorophytes. This confirms our expectation, and stresses the fact that the biological features of algae combined with complex hydrodynamic

191

settings can lead to non-intuitive vertical algal distributions. In this case, the accumulation of diatoms biomass in the upper layers during thermocline deepening is an observation that only takes sense after considering all the system's complexity.
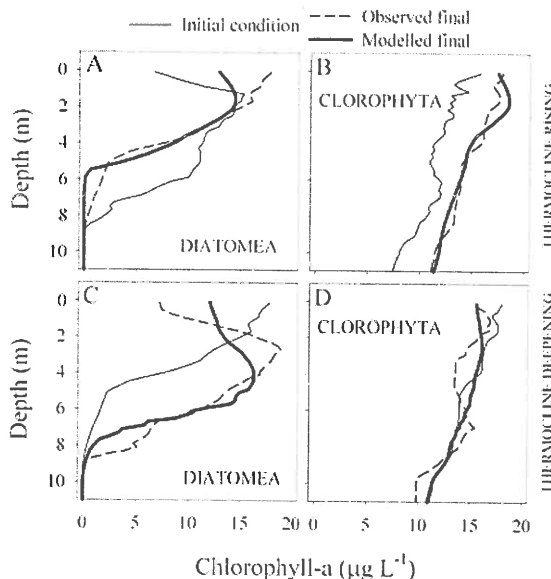
Fig. 8. Outcomes of the modified Huisman approximation for the modeling of the phytoplankton community in Sau Reservoir.

REFERENCES

HUISMAN, J., M. ARRAYÁS, U. EBERT, AND B. SOMMEIJER. 2002. How do sinking phytoplankton species manage to persist? Am. Nat. 159: 245-254.

MÜNNICH, M., A. WÜEST, AND D.M. IMBODEN. 1992. Observations of the second vertical mode of the internal seiche in an alpine lake. Limnol. Oceanogr. 37: 1705-1719.

REYNOLDS, C. S. 1997. Vegetation processes in the pelagic: a model for ecosystem theory. Ecology Institute, Oldendorf Luhe, Germany.

VERHAGEN, J.H.G. 1994. Modeling phytoplankton patchiness under the influence of wind-driven currents in lakes. Limnol. Oceanogr. 39: 1551-1565.

VIDAL, J., X. CASAMITJANA, J. COLOMER, AND T. SERRA. 2005. The internal wave field in Sau reservoir: Observation and modeling of a third vertical mode. Limnol. Oceanogr. 50: 1326–1333.

WÜEST, A., G. PIEPKE, AND D.C. VAN SENDEN. 2000. Turbulent kinetic energy balance as a tool for estimating vertical diffusivity in wind-forced stratified waters. Limnol. Oceanogr. 45: 1388–1400.

BIOLOGICAL CONSEQUENCES OF TURBULENCE AND MIXING IN LAKES

Josef Daniel Ackerman[1] and Mark R. Loewen[2]

(1) Physical Ecology Laboratory, Department of Integrative Biology and Faculty of Environmental Sciences, University of Guelph, Guelph, Ontario, Canada V2N 4Z9, ackerman@uoguelph.ca
(2) Civil and Environmental Engineering, University of Alberta, Edmonton, Alberta, Canada T6G 2W2

Fluid dynamic factors control the transfer of scalars such as nutrients as well as other ecological processes (e.g., suspension feeding) in aquatic ecosystems (Fischer et al. 1979; Wetzel 2001). In the water column (or pelagic) planktonic organisms will theoretically experience steady state conditions even in a turbulent environment, if they are smaller than the Kolmorogov length scale (λ) – the scale of the smallest turbulent eddies that dissipate energy through the energy cascade (Imboden and Wüest 1995). Such organisms experience the forces of lift, drag, and gravity, depending on their excess density. Near the bottom or benthos, the environments is controlled by the benthic boundary layer (BBL) and the velocity gradients that occur around benthic organisms (Boudreau and Jørgensen 2001; Okubo et al. 2002; Wüest and Lorke 2003). In this case, in addition to lift and drag, organisms also experience shear stress ($\tau = \rho u_*^2$; where ρ is the density and u_* is the friction velocity). Shear stress is always present in the benthos and this is a major distinction between benthic and pelagic environments. Aquatic ecosystems represent an environment where physical and biological features are linked.

TURBULENCE IN THE PELAGIC ZONE

The ultimate source of energy is solar radiation, wind stress, and in large lakes, the earth's rotation. Turbulence in lakes is driven primarily by wind stress acting on the lake surface, which can be estimated by recalling that $\tau = \rho u_*^2$,

$$u_* = (C_d \rho_{air} / \rho_{water})^{\frac{1}{2}} w_{10}$$

where C_d is the drag coefficient, ρ_{air} and ρ_{water} are the density of the air and water, respectively, and w_{10} is wind speed at 10 m. The energy dissipation rate (ε) in the epilimnion likely varies as a function of u_*

$$\varepsilon \approx u_*^3 / L$$

where L is the turbulent length scale. The shear rate (γ) is a function of the energy dissipation rate (ε) and the kinematic viscosity (ν)

$$\gamma = (\varepsilon / \upsilon)^{1/2}$$

Given that dissipation is proportional to the square of the shear rate and the smallest turbulent eddies are defined by the Kolmogorov length scale (λ)

$$\lambda = (\upsilon^3 / \varepsilon)^{1/4},$$

which are likely on the order of mm (Mitchell et al. 1985).

PLANKTONIC ORGANISMS

The majority of productivity in lakes is driven by the relatively small photosynthetic phytoplankton (cyanobacteria and unicellular and colonial algae) and larger heterotrophic zooplankton (a variety of organisms and larvae), which transfer the production through aquatic foodwebs (Wetzel 2001). These organisms do not have sufficient propulsion to overcome currents, but they can use various techniques to alter their position in the water column. Turbulence is considered to be of importance for mixing phytoplankton within the water column, which affects their productivity through their transport into regions with different light environments (MacIntyre 1993); although blooms can form with and without stratification (Huisman et al. 1999). Water column turbulence can also affect encounter rates of zooplankton and hence trophic (feeding) interactions through a dome-shaped relationship (e.g., MacKenzie et al. 1994). Moderate levels of turbulence enhance encounter rates whereas large levels are inhibitory. Importantly, the theoretical concept that organisms smaller than λ are not affected by turbulence does not appear to hold (Peters and Marrasé 2000). Energy expenditure increase with turbulence and concomitantly, growth rates decrease, and the response can vary among types of organisms. Small-scale unsteady motion and length scales other than organism size are likely to be more relevant to certain ecological processes (Peters and Marrasé 2000). Further research into this area is warranted and anticipated.

AGGREGATES

The ultimate fate of organic matter from planktonic organisms, which is deposited throughout the water column as particulate organic matter (POM), is to the benthos (Wetzel 2001). Most of the POM is in > 500 μm diameter aggregates that are comprised of microorganisms, inorganic particles, transparent exopolymer particles (TEM), and detritus. There are four types of aggregates found in lakes: algal-derived aggregates; zooplankton exoskeleton-derived aggregates; cyanobacterial-derived aggregates; and those aggregates of unknown origin (Grossart et al. 1997). Aggregates in rivers are less diverse with both inorganic material and detritus contained in a microfibril matrix of microbial origin (i.e., TEM; Droppo et al. 1997). Similar patterns of diversity have been found in marine systems, where the aggregates are also referred to as marine snow (e.g., Alldredge et al. 1990; Kiørboe et al. 1998). Aggregates are important because they *create* spatial patchiness that affect nutrient cycling and the downward flux, and potential retention of autotrophic production in the well-mixed zone (Kiørboe et al. 1998; Okubo et al. 2002).

The role of physical processes in the formation of aggregates has long been noted as has their complex formation involving biological, chemical, and physical factors (Droppo et al. 1997). The formation of algal aggregates has been modeled using a coagulation process, involving Brownian motion, fluid shear, and differential sedimentation of particles, in which shear coagulation is thought to be of importance in the formation of aggregates in the upper ocean (Jackson and Burd 1998). Fluid shear (i.e., shear rate) can be both positive in that it provides the collisions need for coagulation, and negative in that it may lead to the destruction of aggregates; the latter process also includes sedimentation, degradation by organisms, dissolution, fragmentation, pressure fluctuations, and fracture (Alldredge et al. 1990). The destruction of aggregates appears more likely to be driven by biological processes such as grazing by organisms (e.g., Kiørboe 2000). In addition, aggregates appear to accumulate at physical discontinuities in the water column associated with density stratification (MacIntyre et al. 1995). Regardless of the mechanism involved, the persistence of aggregates at discontinuities may be on the order of hours to days, which would have important ecological implications for trophic transfer.

TURBULENCE IN THE BENTHIC ZONE

A small fraction of the energy in lake environments extends downward from the surface to the bottom or benthic zone; the vast majority of this energy is transferred to the benthic boundary layer (BBL) by the various mechanisms including seiches, Kelvin waves, high frequency internal waves, shear instabilities near the benthos, and the interactions of the thermocline with the bottom under stratified conditions. The

important issue is that fluid shear is always present in the benthos. Shear stress (τ) in the BBL is usually modeled via the law of the wall,

$$u(z) = \frac{u_*}{\kappa} \ln\left(\frac{z}{z_0}\right)$$

where κ is the von Karman constant (= 0.41) and z_0 is the roughness height, recognizing that $\tau = \rho u_*^2$ (Ackerman and Hoover 2001). However given that the physical conditions and consequently velocity vary temporally and spatially, it is often difficult to apply the law of the wall model to data (e.g., Ackerman et al. 2001).

SUSPENSION FEEDING

As indicated above, the ultimate fate of material is deposition in the benthos, but it should be recognized that benthic organisms, and the processes that occur on and in lake sediments, are also relevant to lake ecosystems (Wetzel 2001). Suspension-feeding benthic organisms such as bivalves provide an excellent example of how grazing of water-borne biological productivity links the pelagic and benthic zones. A case in point is given by zebra mussels (*Dreissena polymorpha*), which have been introduced into Europe and North America and have been effective in clearing near-shore regions and water column in shallow lakes (Ackerman et al. 2001). Much of our understanding of benthic-pelagic coupling in lakes is limited to small-scale laboratory experiments and synoptic surveys that do not account for the influence of turbulence and mixing on lakes, which are generated by the interaction of a number of forcing functions including wind-generated waves, stratification, and surface-gravitational seiching (Fischer et al. 1977).

The mass transport of seston (concentration C) to suspension-feeding bivalves can be modeled by the advection-diffusion-reaction equation,

$$u\frac{\partial C}{\partial x} + w\frac{\partial C}{\partial z} = \frac{\partial}{\partial z}\left((D + K_D)\frac{\partial C}{\partial z}\right) + R$$

where u and w are the velocities in the downstream (x) and vertical (z) directions, D and K_D are the molecular and turbulent diffusivities and R describes the reaction of the mussels (e.g., Koseff et al. 1993; O'Riordan et al. 1995). A number of "reactions" are known including how mussel size, mussel density, velocity, seston quality and quantity affect suspension feeding (Ackerman 1999). In this case, we have to consider how the momentum and wave boundary layers affect the development of the concentration boundary layer (CBL) over mussel beds. Turbulence and mixing could have several influences including the renewal of depleted resources and the forcing of

reactions in mussel beds. Unfortunately as indicated above, these physical forcing issues are complex in the benthos and as yet not well understood (Wüest and Gloor 1998; Wüest and Lorke 2003).

The situation in shallow lakes is relatively complex as many of the formulations of mixing processes have been developed for density-stratified conditions (e.g. Imboden and Wüest 1995). Unfortunately, shallow lakes are likely to be polymictic on a diel and/or periodic basis, which complicates the analysis. Indeed rather than being well-mixed (e.g., Schertzer et al. 1987), the western basin of Lake Erie (average depth of 10 m) appears to have density gradients of sufficient magnitude to inhibit vertical mixing (Ackerman et al. 2001). In other words, diurnal stratification may inhibit mixing even in the absence of a seasonally stratified water column. This has important implications for benthic suspension feeders as the time scale for clearing a stratified water column is approximately equal to the time scale for turbulent diffusion to replenish the depleted materials. Consequently, it is possible to detect a CBL above mussel beds, which indicates that well-mixed reactor models are inappropriate for application in these conditions (Ackerman et al. 2001). Importantly, the relative strength of the stratification responsible for this result will be related to the strength of the density gradients that stabilize the water column and the turbulent kinetic energy that mix the water column (Imboden and Wüest 1995).

NEAR-BED HYPOXIA

Another important consequence of stratification is the potential for hypoxia ($O_2 < 7$ mg l^{-1}) given that the downward transport of oxygen from the surface is inhibited and there is potential for biochemical oxygen demand (BOD) by the sediments. It is relevant to examine the nature of aquatic sediments. Sediments are affected by advective transport of POM and inorganic matter to and beneath the surface, turbulent diffusion, and biologically-mediated diffusion via bioturbation especially near the sediment surface. The vertical structure in the sediments includes the nepheloid layer at the sediment surface where sediment resuspension occurs; the relatively thin Brinkman layer, which is subject to porewater processes; the mixed layer where bioturbation can still occur; and a deeper layer where conditions are relatively stable (Boudreau and Jørgensen 2001). Coincident with this vertical structure is a shift from oxic to anoxic conditions, and near-bottom turbulence due to high frequency mixing in the BBL can affect the oxygen flux into the sediments (e.g., Darcy flow; Lorke et al. 2003).

The relative impact of hypoxia can also be exacerbated by the decomposition of organic matter in the sediments that creates a sediment oxygen demand at the sediment-water interface. If conditions at a given location are such that the water column is stratified for a sufficient duration, the sediment oxygen demand will gradually reduce oxygen concentrations in the hypolimnion until local hypoxia occurs

197

(Wetzel 2001). However, if enough turbulent kinetic energy is available to mix the water column, the thermocline will be obliterated and the likelihood of local hypoxia will be reduced greatly.

As an example, measurements of water-column conditions in the western basin of Lake Erie reveal that the vertical transport of oxygen and heat is controlled by the complex interaction of several physical mechanisms. Generally when the wind speed was > 7 m s^{-1} and the air was cooler than the water, the water column was well mixed due to turbulent mixing. However, when wind speeds were < 7 m s^{-1} turbulence was found to be too weak to overcome the stratification and mix the water column. Strong stratification occurred approximately 5% of the time when the rate of vertical mixing, as indicated by the vertical eddy diffusivity (K_z), was reduced by three orders of magnitude compared to unstratified conditions (i.e., $K_z \sim 10^{-3}$ vs. 10^{-6} m^2 s^{-1}). The probability that hypoxia due to stratification and sediment oxygen demand (SOD) will occur during these time periods was assessed. Results indicate that there is strong probability of hypoxia given the turbulent diffusivities (i.e., < 10-6 m^2 s^{-1}) and SOD (i.e., 0.1 to 1 g m^{-2} day^{-1}) that have been reported for the western basin of Lake Erie. The environmental implications of stratification to water quality and its effects on benthic organisms, requires further considerations in shallow lake basins like western Lake Erie. There is much to gain from an understanding of the biological consequences of turbulence and mixing in lakes.

REFERENCES

ACKERMAN, J.D. 1999. The effect of velocity on the filter feeding of zebra mussels (*Dreissena polymorpha* and *D. bugensis*): Implications for trophic dynamics. *Can. J. Fish. Aquat. Sci.* 56:1551-1561.

ACKERMAN, J.D. AND T. HOOVER. 2001. Measurement of local bed shear stress in streams using a Preston-static tube. *Limnol. Oceanogr.* 46:2080-2087.

ACKERMAN, J.D., LOEWEN, M.R., AND P.F. HAMBLIN. 2001. Benthic-pelagic coupling over a zebra mussel bed in the western basin of Lake Erie. *Limnol. Oceanogr.* 46:892-904.

ALLDREDGE, A.L., T.C. GRANATA, C.C. GOTSCHALK, AND T.D. DICKEY. 1990. The physical strength of marine snow and its implications or particle disaggregation in the ocean. *Limnol. Oceanogr.* 35:1415-1428.

BOUDREAU, B.P., AND B.B. JØRGENSEN. 2001. The Benthic Boundary Layer. Oxford University Press.

DROPPO, L.G., G.G. LEPPARD, D.T. FLANNIGAN, AND S.N. LISS. 1997. The freshwater flow: A functional relationship of water and organic and inorganic floc constituents affecting suspended sediment properties. *Water Air Soil Poll.* 99:43-54.

FISCHER, H.B., LIST, E.J, KOH, R.C.Y., IMBERGER, J., AND BROOKS, N.H. 1979. *Mixing in Inland and Coastal Waters.* Academic, San Diego.

GROSSART, H.P., M. SIMON, AND B.E. LOGAN. 1997. Formation of macroscopic organic aggregates (lake snow) in a large lake: The significance of transparent exopolymer particles, phytoplankton, and zooplankton. *Limnol. Oceanogr.* 42:1651-1659

HUISMAN, J., P. VAN OOSTVEEN, AND F.J. WEISSING. 1999. Critical depth and critical turbulence: Two different mechanisms for the development of phytoplankton blooms. *Limnol. Oceanogr.* 44:1781-1787.

IMBODEN, D.M., AND A. WÜEST. 1995. Mixing mechanisms in lakes, P. 83–138. In A. Lerman, D. Imboden, and J. Gat [eds.], *Physics and Chemistry of Lakes.* Springer-Verlag.

JACKSON, G.A., AND A.B. BURD. 1998. Aggregation in the marine environment. *Environ. Sci. Technol.* 32:2805-2814.

KIØRBOE, T. 2000. Colonization of marine snow aggregates by invertebrate zooplankton: Abundance, scaling, and possible role. *Limnol. Oceanogr.* 45:479-484.

KIØRBOE, T., P. TISELIUS, B., MITCHELL-INNES, J.L.S. HANSEN, A.W. VISSER, A.W., AND X. MARI. 1998. Intensive aggregate formation with low vertical flux during an upwelling-induced diatom bloom. *Limnol. Oceanogr.* 43:104-116.

KOSEFF, J.R., J.K. HOLEN, S.G. MONISMITH, AND J.E. CLOERN. 1993. Coupled effects of vertical mixing and benthic grazing on phytoplankton populations in shallow estuaries. *J. Mar. Res.* 51:843-868.

LORKE, A., B. MÜLLER, M. MAERKI, AND A. WÜEST 2003. Breathing sediments: The control of diffusive transport across the sediment–water interface by periodic boundary-layer turbulence. *Limnol. Oceanogr.* 48:2077–2085.

MACINTYRE, S. 1993. Vertical mixing in a shallow, eutrophic lake: Possible consequences for the light climate of phytoplankton. *Limnol. Oceanogr.* 38:798-817.

MACINTYRE, S., A.L. ALLDREDGE, AND C.C. GOTSCHALK. 1995. Accumulation of marine snow at density discontinuities in the water column. *Limnol. Oceanogr.* 40:449-468.

MACKENZIE, B.R., T.J. MILLER, S. CYR, AND W.C. LEGGETT 1994. Evidence for a dome-shaped relationship between turbulence and larval fish ingestion rates. *Limnol. Oceanogr.* 39:1790-1799.

MITCHELL, J.G., A. OKUBO AND J.A. FUHRMAN. 1985. Microzones surrounding phytoplankton form the basis for a stratified marine microbial ecosystem. *Nature* 316:58-59.

OKUBO, A., J.D. ACKERMAN, AND D.P. SWANEY. 2002. Passive Diffusion in Ecosystems. pp. 31-106 in A. Okubo and S. Levin (eds.) *Diffusion and Ecological Problems: New Perspectives*, 2nd Ed. Springer Verlag.

O'RIORDAN, C.A., S.G. MONISMITH, AND J.R. KOSEFF. 1995. The effect of bivalve excurrent jet dynamics on mass transfer in the benthic boundary layer. *Limnol. Oceanogr.* 40:330-344.

PETERS, F., AND C. MARRASÉ. 2000. Effects of turbulence on plankton: an overview of experimental evidence and some theoretical considerations. *Mar. Ecol. Prog. Ser.* 205: 291–306.

SCHERTZER, W.M., J.H. SAYLOR, F.M. BOYCE, D.G. ROBERTSON, AND F. ROSA. 1987. Seasonal thermal cycle of Lake Erie. *J. Great Lakes Res.* 13: 468-486.

WETZEL, R.G. 2001. *Limnology 3rd Ed.* Academic, San Diego.

WÜEST, A., AND M. GLOOR. 1998. Bottom boundary mixing: The role of near-sediment density stratification, p. 485–502. In J. Imberger [eds.], *Physical Processes in Lakes and Oceans*. American Geophysical Union.

WÜEST, A. AND A. LORKE. 2003. Small-scale hydrodynamics in lakes. *Ann. Rev. Fluid Mech.* 35: 373–412.

USING AIRBORNE REMOTE SENSING TO STUDY THE MIXING CHARACTERISTICS OF LAKES AND RESERVOIRS

D.G. George[1]

(1) Centre for Ecology and Hydrology. Lancaster, UK

INTRODUCTION

The physical processes that regulate the mixing characteristics of lakes cover a wide range of spatial and temporal scales. Airborne remote sensing provides the ideal means of analysing these patterns and relating them to prevailing weather conditions. Here, I present a series of Case Studies to show how these techniques can be used to study the impact of wind-induced mixing on the physical and biological characteristics of lakes. The studies formed part of the remote sensing campaigns organized by the Natural Environment Research Council in the UK. Most of the examples are taken from aerial surveys of Esthwaite Water, a small, thermally stratified lake in the English Lake District. One example is based on a synoptic survey of Llyn Peris in North Wales, a lake that forms part of major hydroelectric scheme.

THE AIRBORNE SURVEYS AND GROUND-TRUTH MEASUREMENT

The instrument used was a Daedalus 1268 Airborne Thematic Mapper mounted in a twin-engined, Piper Navahoe Chieftain aircraft. This instrument acquires data in eleven spectral bands ranging from the 'blue' visible to the thermal infrared. The visible bands were calibrated using a calibration system supplied by the National Physical Laboratory (Rollin and Milton 1988). The thermal band measurements were converted to a brightness temperature using the calibration procedure described by Wilson (1986). The Daedalus scanner has been specifically designed to operate over water and can measure the temperature of the surface with an absolute accuracy of 0.2°C and a relative accuracy of 0.1°C. All the surveys described were flown between 10.00 and 15.00 hours GMT to minimise the effects of sun-glint. Preliminary image processing was carried out at the Institute of Terrestrial Ecology in Bangor using an International Imaging Systems (I^2S) Model 75 processor. Selected 512 x 512 images were then transferred to floppy disk for processing on an R-CHIPS system at the Institute of Freshwater Ecology in Windermere. Only five of the eleven channels were used to produce the lake images. These included Band 2 (450-520 nm), Band 3

(520-600nm), Band 5 (630-690), Band 8 (910-1050 nm) and Band 11 (8500-13000 nm). Bands 2 and 3 were used for chlorophyll retrieval, bands 5 and 8 for sediment retrieval and Band 11 for mapping the surface temperature. A description of the chlorophyll retrieval algorithms used is given in George (1997). High concentrations of chlorophyll were estimated using the reflectance measured in Band 3 and lower concentrations using a ratio of the measurements in Band 3 and Band 2.

Ground truth surveys were organized to coincide with each over-flight. Surface and subs-surface temperature measurements were recorded with a Windermere Profiler and samples of water collected for chlorophyll measurements and suspended sediment determinations. Chlorophyll *a* concentrations were estimated using the procedure described by Talling and Driver (1963) and the suspended sediment concentration estimated gravimetrically using pre-weighed Whatman GF/F filters. Measurements of the upwelling and downwelling radiance were recorded at selected stations using a Spectron SE 50 scanning radiometer with a nominal sampling interval of 3 nm.

THE CASE STUDIES

The five Case Studies have been designed to illustrate the different ways in which the airborne measurements were used to visualize the mixing processes and explore their biological effects. Each case study includes a brief description of the methods used and an example image to illustrate the patterns recorded.

Case Study 1: Using reflective drogues to track the trajectory of surface currents

Fig.1. A remote sensing image of a line and a 'patch' of drogues drifting in Esthwaite Water.

The first remote sensing studies conducted on Esthwaite Water were designed to quantify the spatial variation in the wind-driven currents. Passive remote sensing techniques cannot be used to measure surface currents but they can be used to track drogues and record the variations in the surface temperature. In Esthwaite Water, surface currents were mapped by tracking lines and patches of free-floating drogues.

Each drogue was made from a square of plywood measuring 60 x 60 cms fixed to an upturned plastic bucket. The plywood squares were painted white to increase their reflectance and the bucket acted as a 'sea anchor' that minimized the direct effect of the wind on the surface float. The drogues were tracked by identifying the most reflective pixels in the aerial imagery and their positions at selected times checked with an electronic distance meter fixed to a theodolite. Since Esthwaite Water is only 2.5 km long, most drogue experiments were completed in less than two hours. Overflights were organized at intervals of 10-15 minutes and the drogues removed before they reached any shallow water.

Fig.1 shows a line and a patch of drogues drifting in the open water. The bright area inside the patch is a slug of dye used to estimate the direct effect of wind on the surface floats. The line was used to map the trajectory of the surface currents and the dispersion of the patch used to estimate the horizontal eddy diffusivity. The results showed that the complex topography of the basin had a major effect on the circulation pattern. Thermal 'fronts' were periodically recorded in the larger bays and were frequently associated with areas of high shear along their relatively stable boundaries. The dispersion rates of the drogues in the 'patches' showed that the scale of turbulent mixing in Esthwaite Water was much smaller than those recorded in large lakes. Their average rate of dispersion was lower than that predicted by the Batchelor model (Batchelor 1952) and appeared to be constrained by the 'diffusion floor' formed by the shallow thermocline (George and Allen 1994). The integral scale of turbulence was about 40 m and the drogues reached their asymptotic rate of dispersion in 10-15 minutes.

Case Study 2: Coriolis effects on the spatial distribution of cyanobacteria
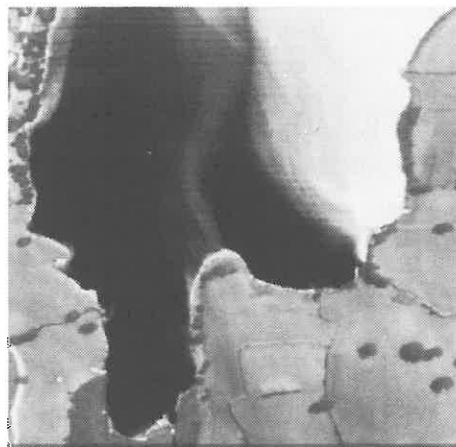
Fig. 2. A remote sensing image of a cyanobacterial bloom in Esthwaite Water showing the Coriolis defle-ction of the wind-driven currents.

Wind-induced water movements have a major effect on the horizontal as well as the vertical distribution of phytoplankton. Plankton patches usually form when motile or buoyant species regulate their depth and accumulate in areas of downwelling water (George and Edwards 1976; George and Heaney 1978). The best known examples of phytoplankton patches are those reported in lakes dominated by blue-green algae (cyanobacteria). Many species of blue-green algae contain gas vacuoles that allow them to float to the surface during calm periods (Reynolds 1987). Light winds then carry these aggregations towards the shore where they accumulate to form unpleasant algal 'blooms'. In 1987, a series of multi-temporal surveys were organized in Esthwaite Water to study the formation and dissolution of these near-surface accumulations.

In Esthwaite Water, the general circulation pattern can best be described as a 'conveyor belt' where the wind drift is balanced by a deep return flow. When the wind speed is relatively high, this conveyor belt is aligned with the prevailing wind. When the wind speed is low, the circulation pattern is modified by the Coriolis force which deflects the flow to the right of the wind (Ekman 1905). A more detailed account of these rotational effects can be found in a papers published by George and Heaney (1976) and Falconer et al. (1990).

Fig. 2 is a remotely sensed image of a cyanobacterial bloom in Esthwaite Water. The original false colour image was produced by displaying the outputs from ATM Bands 11, 3 and 8 on the red, green and blue channels of the display monitor. Warm water containing relatively low concentrations of phytoplankton thus appeared red whilst cooler water containing relatively high concentrations of phytoplankton appeared green. In the black and white copy, the brightest areas in the image show the high concentrations of cyanobacteria that had accumulated in the large bay. At the time of sampling, the wind was blowing along the axis of the lake (i.e. from top to bottom) but Coriolis effects were deflecting the near-surface currents towards the right-hand shore.

Case Study 3: The development of 'dead zones' in the shallow littoral.
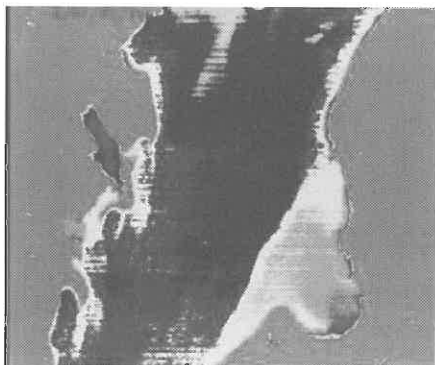

Fig.3. A remote sensing image of Esthwaite Water showing a poorly mixed area of water ('dead zone') in a shallow bay. This thermal image (ATM Band 11) has been density-sliced at intervals of *ca.* 0.5°C.

204

In recent years, it has become clear that traditional Fickian models of dispersion cannot explain the spatial distribution of phytoplankton in fast-flowing rivers. In the UK, most rivers are too short to sustain substantial growths of planktonic algae. 'Patches' of phytoplankton may, however, appear in meandering sections where some pools are partially isolated from the main flow. The physical dynamics of these 'dead zones' have been described in a number of publications and Reynolds et al (1991) have also explored their biological significance. Their intensive studies on the River Severn showed that some 'dead zones' can remain intact for several weeks and support substantial populations of growing phytoplankton.

In a topographically complex lake, like Esthwaite Water, very similar 'dead zones' periodically develop in the more sheltered bays. Fig. 3 is a thermal image of Esthwaite Water recorded on a day when the wind speed was relatively low. In this image, the bright area in the right hand bay is more than 2°C warmer than the darker areas in the open-water. At the time of sampling, the wind was blowing along the lake but the thermal 'fronts' that had formed on the edge of this bay effectively isolated the littoral zone from the open water. George (2000) has shown that these littoral areas often contain increased concentrations of dissolved reactive phosphorus. There has been no systematic study of their effect on the development of phytoplankton, but they could serve as a 'refugium' for slow-growing species, like the blue-green algae.

Case Study 4: Monitoring the discharge of water from a hydroelectric plant
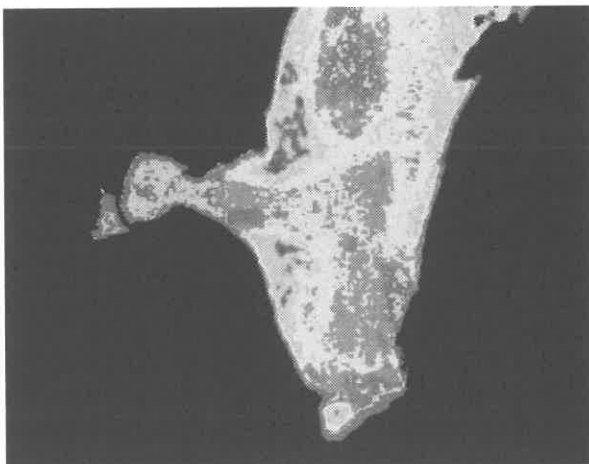
Fig. 4. A remote sensing image showing the plume of turbid water discharged into Llyn Peris by the Dinorwig pump storage plant. The image is based on the ratio of the reflectance measured in ATM Bands 5 and 3.

In the 1970's, the electricity generating authority in the UK recognized that there was a need for 'standby' systems that could quickly transfer power to the national grid when there was an increase in demand. Hydro-electric pumped storage schemes

provide a very effective way of meeting these short-term requirements. They work by using the water pumped into an upper reservoir to 'store' the excess energy produced by conventional power stations. At peak periods, this water is discharged through turbines which are later reversed to pump the water back into the upper reservoir. Llyn Peris in Snowdonia is now used as the lower reservoir in the Dinorwig pumped storage scheme. This power station can produce 1.320 megawatts of electricity when the water is drained from the upper reservoir and reach full capacity in 12 seconds. Such a massive transfer of water has a direct effect on the physical characteristics of Llyn Peris and an indirect effect on its chemistry and biology.

In 1995, an airborne survey of Lyn Peris was organized to quantify the effect of this discharge on the temperature of the water and the concentration of sediment. The flight was timed to coincide with the discharge of water from the upper reservoir and supported by detailed ground-truth measurements in the lower lake. Water samples were collected from a number of locations in and around the plume and the spatial variations in the water temperature recorded with a Windermere Profiler.

Measurements of the water temperature in and around the discharge plume showed that the water in the plume was 1-1.5°C warmer than that in the receiving basin. In hydraulic terms, the dispersal characteristics of a plume are controlled by the ratio of the forces of momentum and buoyancy i.e. the Froude number. Jets with a low Froude number are less energetic and reach the surface after a much shorter time than those with a high Froude number. At the time of the overflight, only two of the six generators were operating at full capacity so the warm water reached the surface very close to the point of discharge. Fig. 4 shows the effect that this discharge had on the spatial distribution of the suspended sediment. The darker areas in this density sliced image show the areas with the highest concentrations of suspended sediment. The observed variations were not very large but the highest concentrations were recorded in the centre of the basin and the points where the leading edge of the plume reached shallow water.

CONCLUSIONS

Airborne remote sensing techniques provide the ideal means of monitoring the mixing characteristics of freshwater lakes and reservoirs. They are most effective when supported by intensive ground truth measurements and used to visualize specific mixing processes. Instruments of the kind used in these NERC campaigns are invariably costly and cannot always be deployed in a flexible way. Simpler systems, based on an array of CCD cameras, provide a convenient alternative and can be quite effective in aquatic applications where a precise 'pixel-by-pixel' matching of the acquired images is not usually necessary.

REFERENCES

BATCHELOR, G.K. 1952. Diffusion in a field of homogeneous turbulence. II The relative motion of particles. Proc. Cam. Phil. Soc., 48, 345-362.

EKMAN, S. 1905. On the influence of the earth's rotation on ocean currents. Ark. Mat. Astr. Fys., 11, 52 pp.

FALCONER, R.A., D.G. GEORGE, and P. HALL. 1991. Three dimensional numerical modelling of wind driven circulation in a shallow homogeneous lake. J. Hydrol. 124, 59-79.

GEORGE, D.G. 1997. The airborne remote sensing of phytoplankton chlorophyll in the lakes and tarns of the English Lake District. Int. J. Rem. Sens., 18 (9), 1961-1975.

GEORGE, D.G. 2000. Remote sensing evidence for the episodic transport phosphorus. Freshwat. Biol., 43, 571-578.

GEORGE, D.G. and R.W. EDWARDS. 1976. The effect of wind on the distribution of chlorophyll a and crustacean plankton in a shallow eutrophic reservoir. J. Appl. Ecol., 13, 667-690.

GEORGE, D.G. and S.I. HEANEY. 1978. Factors influencing the spatial distribution of phytoplankton in a small productive lake. J. Ecol., 66, 133-155.

GEORGE, D.G. and C.M. ALLEN. 1994. Turbulent mixing processes in a small Cumbrian lake. In K. Beven, P.Chatwin and J. Millbank [eds.]. Physical mechanisms of transport and dispersion in the environment. Wiley, 3-15.

GEORGE, D.G. and C.M. HAPPEY-WOOD. 1996. The remote sensing of a power station plume in Llyn Peris, Snowdonia. Proc. 22nd Ann. Conf. Rem. Sens. Soc., Durham, 11-14th September 1996, 325-332.

REYNOLDS, C.S. 1987. Cyanobacterial water blooms. Adv. Bot. Res., 13, 67-143.

REYNOLDS, C.S., P.A. CARLING, and K.J. BEVEN. 1991. Flow in river channels: new insights into hydraulic retention. Arch. Hydrobiol., 121, 171-179.

ROLLIN, E.M. and E.J. MILTON. 1988. Intercalibration between the Daedalus AADS 1268 ATM scanner and two NERC field spectroradiometers. Proc. NERC 1986 Airborne Campaign Workshop, NERC, Swindon, 207-218.

TALLING, J.F. and D. DRIVER. 1963. Some problems in the estimation of chlorophyll a in phytoplankton. Proc. Conf. Primary Productivity Measurement (Marine and Freshwater), TID-7633, US Atomic Energy Commission (Washington D.C.), pp 142-146.

WILSON, A.K. 1986. Calibration of ATM data. Proc. NERC 1985 Airborne Campaign Workshop, NERC, Swindon, E25-E40.
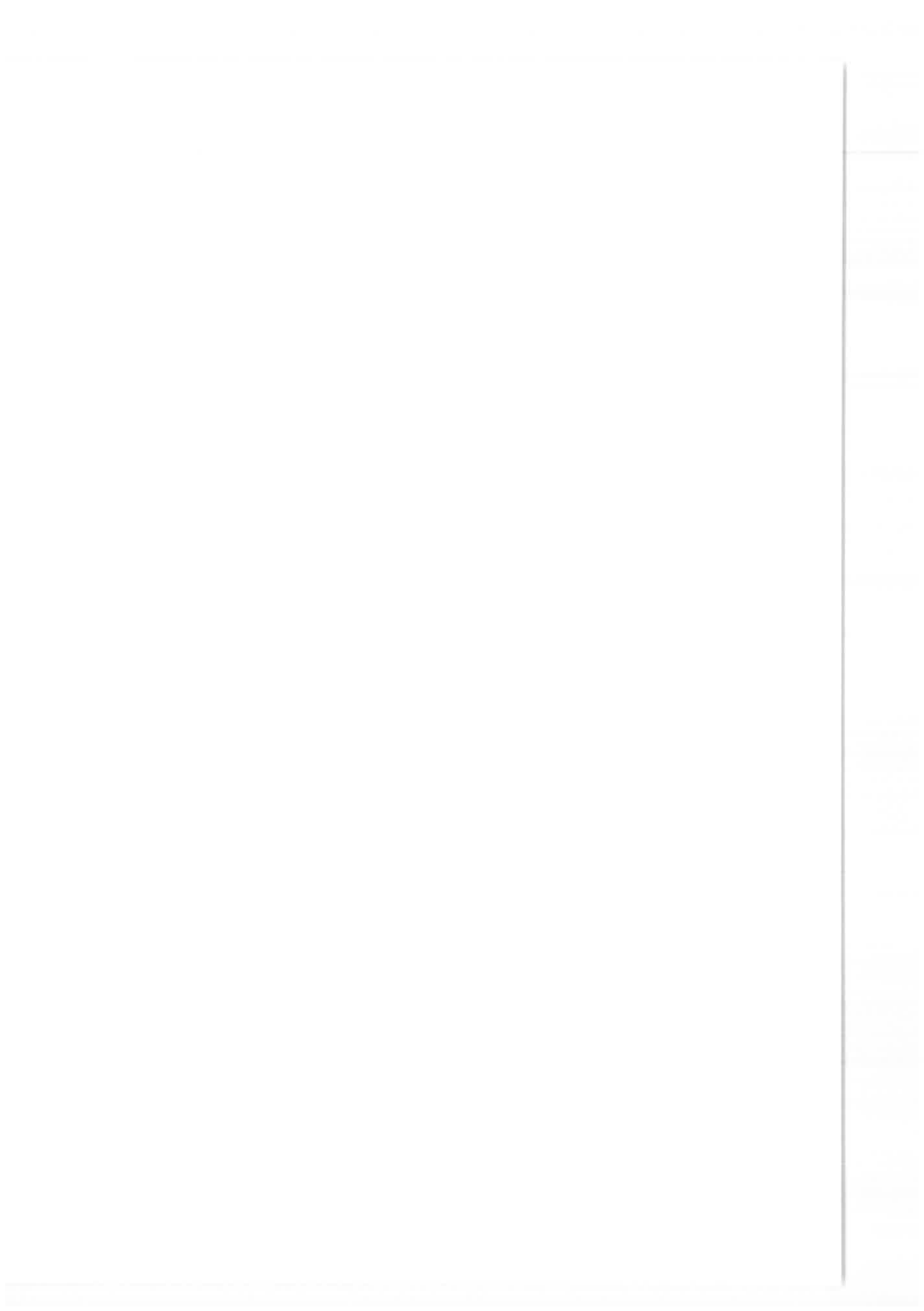
DIMENSION ANALYSIS AS APPLIED TO THE LAKE ECOSYSTEM MODELING

Sergey Golosov[1],[2]; A. Tolmachev[1]; G. Kirillin[2]; and E. Shipunova[1]

(1) Institute of Limnology, Russ. Acad. Sci., 196105 St. Petersburg, Russia
(2) Institute of Water Ecology and Inland Fisheries, Berlin, Germany

The water quality in freshwater reservoirs in many respects is determined by the intensity of organic matter producing due to phytoplankton photosynthesis, so-called "primary production" (PP). The level of PP in lakes defines such peculiarities of chemical regime as over/ undersaturation of the water by the dissolved oxygen, presence/absence of nutrients in the upper layers, formation of the oxygen depletion in the near bottom zone, etc. Moreover, PP of high intensity is capable to change the mixing conditions in a lake due to absorption of the solar radiation in the upper water layers. To represent the PP in ecological models, the Michaelis – Menten equations are usually applied. Equations of this type describe the algae photosynthesis in dependence on factor limiting the algae growth and contain at least two unknown empirical parameters, so called "half-saturation constant" and "maximal rate of algae growth". In natural conditions both parameters vary in the range of several orders of magnitude in dependence on environmental conditions and species of phytoplankton. The last often leads to erroneous evaluations of the PP in ecological models. In fact, the mentioned parameters serve as fitting empirical constants, providing accordance between measured data and results of calculations. In this case the forecasting value of the ecological models becomes negligible. A new parameterization of the PP in lakes is developed on the basis of the principles of dimension analysis. The parameterization was verified against field data collected in more than 30 lakes located in different regions over the world. Results of verification show that the new representation of PP allows avoiding the traditional mistakes at calculating of the phytoplankton photosynthesis in ecological models.

THE LIGHT ATTENUATION AND ABSORPTION COEFFICIENT FUNCTION IN THE METHOD TO ESTIMATE CHL *A* CONTENT IN A LAKE SURFACE LAYER USING WATER COLUMN TEMPERATURE AND METEOROLOGICAL FLUXES

Sri Adiyanti[1]

(1) Centre for Water Research. University of Western Australia. 35 Stirling Hwy. Crawley. 6009. WA. Australia. adiyanti@cwr.uwa.edu.au

INTRODUCTION

In most natural waters chl *a*, a commonly used primary productivity parameter, is the most variable light absorption component compared to others (water, dissolved organic matter and detritus). The proportion of Photosynthetically Available Radiation (PAR; 0.36 -0.76 μm) absorbed by phytoplankton is highly variable, ranging from a few percent in oligotrophic lakes to as high as 20-40% in highly productive lakes (Smith et al 1989). The absorbed energy leaves the excited pigment cells (chl *a* and accessory pigments) in various ways (Smith et al 1989); most are converted into heat within less than mille seconds. Besides being absorbed, photons in PAR can also be scattered which increases the probability of photons being absorbed by other molecules (Kirk 1981). In turbid water the chance of photons being scattered and then absorbed is high (Kirk 1984). All of these attenuate the penetrating short-wave radiation in a lake surface layer. The degree of light attenuation is commonly parameterized using total diffuse attenuation coefficient for the underwater irradiance or $K_d(PAR)$, as it is usually called.

A method to derive $K_d(PAR)$ values from water column temperature and meteorological fluxes has been proposed (Adiyanti & Imberger, submitted manuscript). The method was tested and analysed in Lake Kinneret (Israel), Valle de Bravo Reservoir (Mexico) and Winam Gulf, a side arm of Lake Victoria (Kenya) using water column temperature and meteorological fluxes measured by a Lake Diagnostic System. The method worked reasonably well for the case when the photic depth (i.e. the depth at which the irradiance is reduced to 1% of the surface reading) is deeper than the surface mixed layer (Imberger 1985) during the stratification period and when the activity of internal waves is weak enough to strain the base of the

surface layer. Further, it is possible to estimate chl a concentration from $K_d(PAR)$ using bio-optical property approach; most errors resulted from this model reached less than 10% (Adiyanti & Imberger, in prep.).

The chl a model (Adiyanti & Imberger, in prep.) relies on successfully converting a value of $K_d(PAR)$ to total absorption coefficient (a) and then decomposes this total value into its components (phytoplankton, dissolved organic matter, water and detritus). In the conversion of $K_d(PAR)$ to total absorption coefficient (a), a Monte Carlo procedure (Kirk 1981 & 1984) was applied to 1, 2, 25, and 100 millions of photons to form an explicit function of a, b and $K_d(PAR)$, hereafter called $K_d(PAR) = f(a,b)$, where b is the total scattering coefficient. Here $K_d(PAR)$ was defined as the irradiance-weighted (w) value integrated over the photic depth ($^w K_d(av, z_{eu})$), to take into account the non-homogenous vertical light distribution in this zone, defined as:

$$^w K_d(av, z_{eu}) = \frac{\int_{0^+}^{z_{eu}} K_d(z) Q(z) dz}{\int_{0^+}^{z_{eu}} Q(z) dz} \tag{1}$$

where $Q(z)$ is the irradiance at the depth z and $K_d(z)$ is the $K_d(PAR)$ at depth z. Values of $Q(z)$ and $K_d(z)$ were calculated from the Monte Carlo simulation for given ranges of the scattering/absorption ratio (b/a) values. The resultant function is:

$$^w K_d(av, z_{eu}) = f(a,b) = \frac{1}{\mu_o}\left[a^2 + G(\mu_o)ab\right]^{1/2} \equiv \frac{1}{\mu_o}\left[a^2 + (1.0251\mu_o - 0.19825)ab\right]^{1/2}$$
$$\tag{2}$$

where μ_o is the cosines of the incident photons just below the surface, calculated based on day, time, latitude and longitude (TVA 1972).

The numerical coefficients in the linear equation of Eq. (2) ($G(\mu_o)$) are different to Kirk (1984) values:

$$K_d(av, z_{eu}) = f(a,b) = \frac{1}{\mu_o}\left[a^2 + G(\mu_o)ab\right]^{1/2} \equiv \frac{1}{\mu_o}\left[a^2 + (0.425\mu_o - 0.190)ab\right]^{1/2}$$
$$\tag{3}$$

where $K_d(PAR)$ was not irradiance-weighted, i.e. $K_d(av, z_{eu}) = \frac{1}{z_{eu}} \int_0^{z_{eu}} K_d(z) dz$. Later, Kirk (2003) showed that the irradiance-weighted average coefficient ($^w K_d(av, z_{eu})$) values from a Monte Carlo simulation was more accurate than other definitions of $K_d(av)$. However, until now an explicit function of $K_d(PAR) = f(a,b)$ for $^w K_d(av, z_{eu})$, Eq. (2), had not been derived.

The study presented herein shows the comparison of errors resulted from the application of Eq. (2) and Eq. (3) to the method of estimating chl a from water column temperature and meteorological fluxes (Adiyanti & Imberger, 2006). Based on this, the appropriate way of defining the light attenuation coefficient ($K_d(PAR)$) in the method is suggested.

METHOD

The study was conducted on data sets obtain from Valle de Bravo Reservoir (Mexico) in 2004. The concentration of chl a was analysed spectrophotometrically from water samples taken at 11, 13, and 16 hours from 1, 2.5, 7 m depths. The water sample collection, pigment extraction, chl a determination and DOM analysis were conducted using the APHA method (1998). A vertical profile of the underwater PAR was measured using the diffuse light sensor installed in the LICOR light meter.

Values of $K_d(PAR, z)$ for 3 sampling depths (1, 2.5, 7 m), photic depth (z_{eu}) and mid photic depth (z_m) were derived as localized values such that:

$$K_d(PAR, z) = -\frac{0.5}{z^+ - z^-} \log \frac{Iz^+}{Iz^-} \tag{4}$$

where z is depth of interest; z^+ and z^- are +/- 10% of z, I_z^+ and I_z^- are the corresponding irradiance values.

Inputs for the chl a model (Adiyanti & Imberger, in prep.) include $K_d(PAR)$, blue and red peak ratio for phytoplankton, a knowledge of phytoplankton composition and dissolved organic matter concentration from 3 sampling depths. The model was modified with different function of $K_d(PAR) = f(a, b)$, i.e. using Eq. (2) or Eq. (3). The simulation was run 10 times with different seed numbers for creating random numbers in the optimisation scheme. Detailed method is described elsewhere (Adiyanti & Imberger, in prep.).

RESULTS & DISCUSSION

The result (Figure 1) shows the dependency of the mean error (%) of the simulated-observed chl a concentration to the photic depth. When the photic depth is shallower than the sampling depth the chl a simulation resulted in maximum error in both cases, i.e. application of Eq. (2) and Eq. (3). Errors of simulation at time 13 and 16 hours at depth 7 m are examples of this. The photic depths were only 4.7 m and

213

3.7 m, respectively. These indicate the function of $G(\mu_o)$, i.e. effect of average cosines (μ_o), was irrelevant for the case where photic depth is very shallow, simply because not enough radiant flux penetrated into the bottom layer. This was also observed by Duntley (1963).

The application of Eq. (2) into the $K_d(PAR)$- chl a model (Adiyanti & Imberger 2006) resulted in less error than the application of Eq. (3). The error resulted from the application of Eq. (3) may be intensified in a very turbid water.

However, when the sampling depth is either close to mid photic depth z_m (case at time 13 hours at 2.5 m depth, z_m=2.6 m) or photic depth z_{eu} (case at time 11 hours at 7 m depth, z_{eu} = 7.1 m), the application of Eq. (3) resulted in less error that Eq. (2). This was because the nature of Kirk's definition of $K_d(av, z_{eu})$ is as same manner as Eq. (4) which was used to calculate $K_d(PAR, z_m)$ and $K_d(PAR, z_{eu})$.
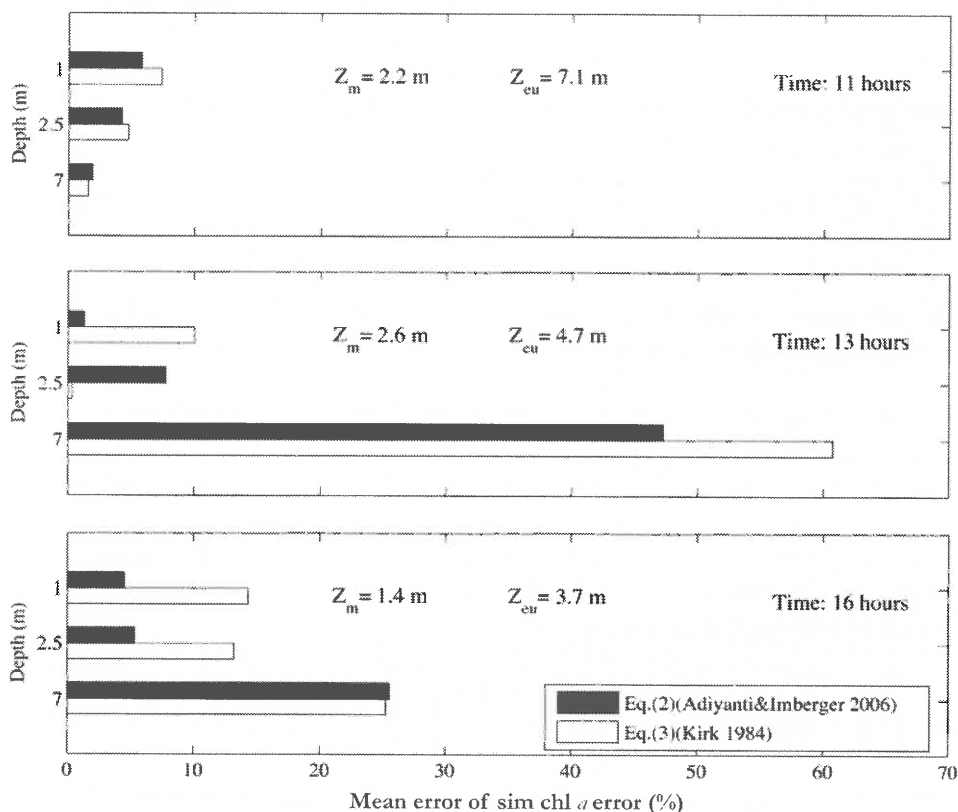

Figure 1. Comparison of mean error (%) of simulated-observed chl a concentration resulted from the application of equation (2) and equation (3) to the $K_d(PAR)$- chl a model (Adiyanti & Imberger 2006). The value is an averaged error over 10 simulations. z_m is mid photic depth (10% light), z_{eu} is photic depth (1% light).

214

The depth of interest in the method to estimate chl a from water column temperature and meteorological fluxes needs to be shallower than the photic depth (Adiyanti & Imberger 2006), i.e. the surface layer is comparable to the photic depth. Based on this it is more appropriate to use the irradiance-weighted averaged light attenuation coefficient of $K_d(PAR)$ ($^wK_d(av, z_{eu})$) of photic depth, i.e. Eq. (1), in the method. This definition may also be more useful for any study where the depth of interest is less than photic depth.

This study also shows that the coefficients in function of $G(\mu_o)$ depend significantly on how it is calculated, whether using irradiance-weighted average or non-weighted average.

CONCLUSION

In this study we have shown the error resulted by using two definitions of $K_d(av, z_{eu})$ in the chl a model (Adiyanti & Imberger, in pres). We proposed the irradiance-weighted average coefficient of light attenuation integrated over photic zone ($^wK_d(av, z_{eu})$) to be a more appropriate for the method to estimate chl a from water column temperature and meteorological fluxes.

REFERENCES

ADIYANTI, S. & IMBERGER, J. 2006. Derivation of total diffuse attenuation coefficient from water column temperature data and meteorological water surface fluxes: A simple management tool. [Submitted manuscript, April 2006]

ADIYANTI, S. & IMBERGER, J. 2006. A method to estimate total chlorophyll a in the surface layer of a stratified lake from a knowledge of the diffuse light attenuation coefficient. [In prep.]

IMBERGER, J. 1985. The diurnal mixed layer. *Limnol. Oceanogr.,* 30, 737-770.

KIRK, J. T. O. 1981. Monte Carlo procedure for simulating the penetration of light into natural waters. CSIRO Aust. Div. Plant Ind. Tech. Pap. 36, 1-16.

KIRK, J. T. O. 1984. "Dependence of relationship between inherent and apparent optical properties of water in solar altitude", *Limnol. Oceanogr.,* 29, 350-356.

KIRK, J. T. O. 2003. The vertical attenuation of irradiance as a function of the optical properties of the water. *Limnol. Oceanogr.,* 48, 9-17.

SMITH, R. C., MARRA, J., PERRY, M. J., BAKER, K. S., SWIFT, E., BUSKEY, E., ET AL. 1989. Estimation of a photon budget for the upper ocean in the Sargasso Sea. *Limnol. Oceanogr., 34*(8), 1673-1693.

TENNESSEE VALLEY AUTHORITY. 1972. Heat and mass transfer between a water surface and the atmosphere. Lab. Report 14. Norris, Tennessee.

COUPLING HYDRODYNAMICS AND PHYTOPLANKTON: IMPACT OF EXOGENOUS PERTURBATIONS IN A MESOTROPHIC RESERVOIR IN SOUTHERN SPAIN (EL GERGAL, SEVILLE)

E. Moreno-Ostos[1],[2], F.J. Rueda[1], I. de Vicente[1],[3], J. Armengol[2],
D.G. George[4], C. Escot[5], A. Basanta[5] & L. Cruz-Pizarro[1]

(1) Instituto del Agua. Universidad de Granada. (Spain). enmoreno@ugr.es
(2) Dpto. Ecología. Universidad de Barcelona (Spain)
(3) Institute of Biology. University of Southern Denmark.. Odense. M (Denmark)
(4) Centre for Ecology and Hydrology. Lancaster Environment Centre. Lancaster (UK)
(5) Empresa Municipal de Abastecimiento y Saneamiento de Aguas de Sevilla (Spain)

INTRODUCTION

In spite of earlier assumptions on a rigid and predictable succession of community assembly controlled by the community itself (autogenic) that culminates in a well-established climax or equilibrium (Clements 1916), Margalef's revolutionary theory (1978) describe the phytoplankton succession as a two dimensional nutrient-turbulence domain in which the microalgae succession follows well defined paths strongly influenced by the external forcing. Margalef represented the habitat in which the phytoplankton develops into a mandala, an oriental symbolic figure that concentrates the whole cosmos order and behaviour (Figure 1a). Later on, Reynolds (1987, 1997) advanced in this subject by the incorporation of the functional group concept (Fig. 1b), based the classification of algae as a consequence of their primary life-history strategies (Grime, 1979). This classification establishes three different functional groups of phytoplankton:

1. Ruderals species (R), tolerant to external perturbations. They can even obtain benefits from unstable environments.

2. Colonizers species (C), characterised by a small size, high surface/volume ratio and fast-replication strategies (r-strategists)

3. Stress tolerators species (S), typically large-sized organisms, showing low replication rates and resistant to grazing (k-strategists).

217

In the classical seasonal succession concept, the different phytoplankton functional groups are replaced following a relatively well-defined sequence (R-C-S-R...). Thus, the first species in the annual cycle use to be the diatoms (R), followed by a variety of small fast-growing green algae (C). Finally, they are replaced by the large size cyanobacteria and dinoflagellates (S).
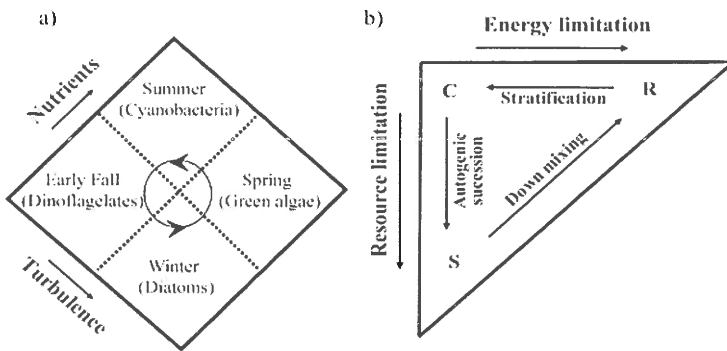

Figure 1. (a) The Margalef's phytoplankton *mandala*. (b) The Reynold's phytoplankton succession triangle.

Nevertheless, this long-term process is certainly more complex as the phytoplankton succession is frequently perturbed by the impact of short-term (days, hours) allogenic energy inputs (disturbances), such as wind events (Soranno 1997). Those disturbances, if intense and frequent enough, can separate shorter autogenic successional episodes. Thus, as expressed by Reynolds (1997) the degree of organisation and community development at any point in time is a measure of the effectiveness of the autogenic processes since the last disturbance. therefore, external disturbances plays a central role in the phytoplankton ecology: a frequent allogenic structural revision of the habitat keeps on arresting or setting back the progress of the self-organising autogenic process towards a climactic steady state (Fig. 2). In this sense, late-succession species fail to exclude precursor ones while disturbances keep re-opening habitat to more pioneer-like invaders (Reynolds, 1997).
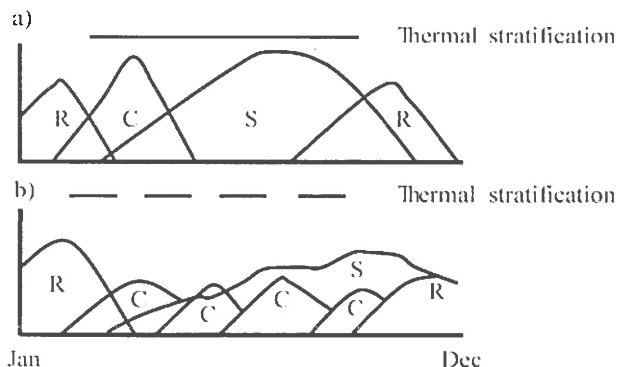

Figure 2. (a) Idealized phytoplankton seasonal succession model. (b) The succession model if the lake were submitted to intermediate perturbations during the themal stratification period.. Modified from Harris (1986).

If we accept these postulates as valid interpretations of succession in freshwater ecosystems, one necessarily concludes that the analysis and understanding of the functional structure of phytoplankton communities and its evolution needs to be grounded on the knowledge of the physical processes of transport and mixing determining turbulence levels and nutrient distribution in the water column.

With the new ACOHPLE project, we propose to study -at a range of spatial and temporal scales- the links between hydrodynamics (transport, turbulent mixing) and the phytoplankton community structure in a mid-size mesotrophic reservoir (El Gergal, Seville). Our working hypothesis (based in all the previously mentioned postulates) is that perturbations induced by hydrological/meteorological events in the three-dimensional patterns of water motion, on one hand, modify the light climate and the pathways of nutrients within the reservoirs, and may trigger changes in the structure (in terms of functional groups and size) of the phytoplanktonic community; and, also, that their frequency, intensity and persistence control the specific patterns of change exhibited by such communities. In this context, the present paper advances some observations on the impact of long-term and short-term physical processes on the phytoplankton community succession and composition in El Gergal.

EL GERGAL RESERVOIR

El Gergal is a medium-size canyon-type reservoir located on the Rivera de Huelva River, a tributary of the Guadalquivir River (Seville, South West Spain). A set of three more reservoirs located upstream completes the water-supply system to the city of Seville and some surrounding towns (c. 1.200.000 inhabitants).

The hydraulic management of El Gergal dam is based on the selective withdrawal of water at any of four different depths: the spillway (at 50 m.a.s.l) and a top (at 42.30 m.a.s.l), a medium (at 26.35 m.a.s.l) and a bottom outlet (at 18 m.a.s.l).

El Gergal reservoir thermal cycle depicts, over the years, a clear warm monomictic pattern, characterized by a long period of direct stratification which normally last from the end of February to middle of October. During June and, especially July and August, a well defined thermocline develops. Nevertheless, the depth and stability of the thermocline varies from year to year as a consequence of the different selective withdrawal operations adopted. The only period of complete isothermy takes place at the end of autumn-early winter (Moreno-Ostos, 2004).

The main physical determinants of phytoplankton seasonal succession are both the water column thermal structure and the hydraulic management strategies adopted each year (Moreno-Ostos, 2004). In general terms, the community evolves from winter ruderal groups (diatoms) through small non-motile green algae in spring and

flagellate volvocal chlorophytes at the beginning of summer to larger size stress-tolerators species of cyanobacteria during the maximum thermal stability period. In addition, short-term processes such as wind-induced mixing events, rainfall events and water transfers from other reservoirs in the catchment act as intermediate disturbances in the phytoplankton succession modifying the composition and dynamics of the phytoplankton community. Depending on their severity, extent and frequency, those events could induce just transitory states in the general algae succession or more dramatic changes in the paths followed by phytoplankton inside the mandala.

LONG-TERM PROCESSES: THE INFLUENCE OF THERMAL STRUCTURE ON PHYTOPLANKTON SUCESSION

As previously exposed, the different hydraulic management operations applied in El Gergal can significantly change the depth and stability of the seasonal thermocline. This physical variability has profound implications for the spatial and temporal dynamics of phytoplankton in the reservoir. When water is abstracted from the top layers of the water column, as during summer 2001, the thermal stability increases and the reservoir shows a well-developed thermocline at around 10 meters depth (Fig. 3a). This stable physical environment enhances the growth and development of stress-tolerators (S) phytoplankton species, such as the cyanobacteria *Aphanizomenon* sp (Fig. 3b). and the dinoflagellate *Ceratium hirundinella* (Fig. 3c). By contrast, the small diatom *Cyclotella* sp.(R) (Fig. 3d) only appears during the whole mixing-period.

On the other hand, when water is abstracted from the bottom layers on the water column (as during summer 2003) a less stable thermal structure results, characterised by a deeper thermocline and a wider metalimnion (Fig. 4a). This new hydrodynamical scenario results optimal for the small fast-growing *r*-strategist *Cyclotella* (Fig.4d), that develops in the reservoir during almost the whole annual cycle. Contrary, under the effect of the frequent turbulent mixing, *Aphanizomenon* populations depicted smaller densities even during summer (Fig. 4b) and dinoflagellates were virtually absent (Fig. 4c).
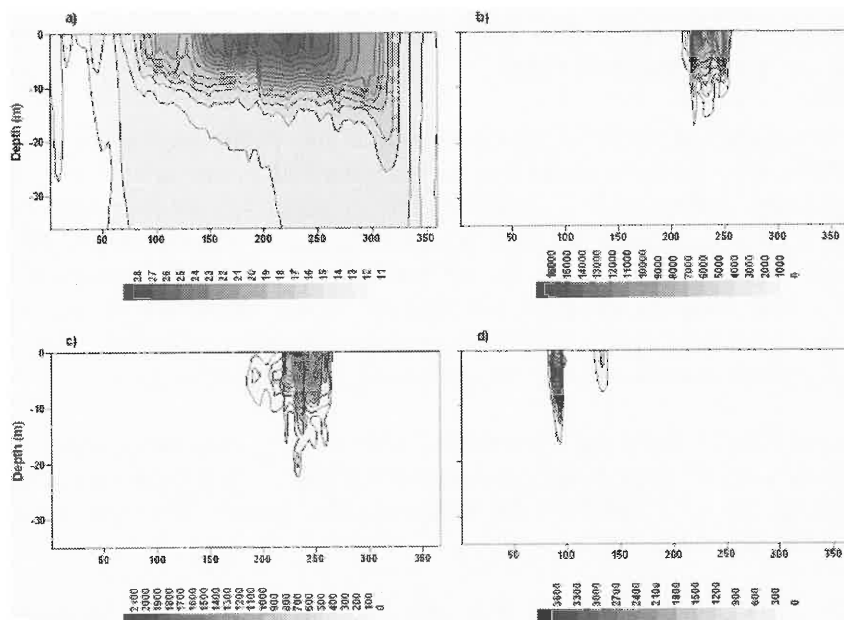
Figure 3. The spatio-temporal distribution of (a) water temperature (°C); (b) *Aphanizomenon* sp. (cells ml^{-1}); (c) *Ceratium hirundinella* (cells ml^{-1}) and (d) *Cyclotella* sp. (cells ml^{-1}) in El Gergal reservoir during 2001.
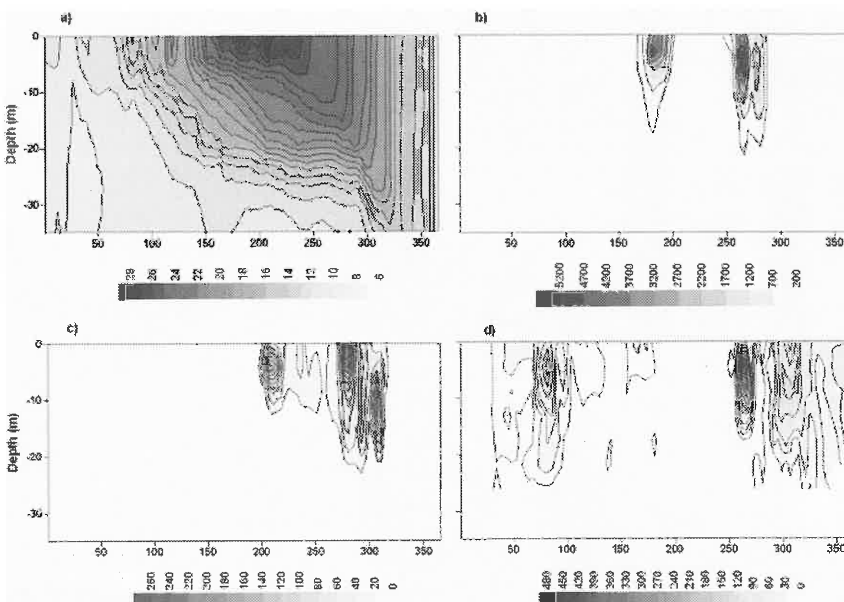

Figure 4. The spatio-temporal distribution of (a) water temperature (°C); (b) *Aphanizomenon* sp. (cells ml^{-1}); (c) *Ceratium hirundinella* (cells ml^{-1}) and (d) *Cyclotella* sp. (cells ml^{-1}) in El Gergal reservoir during 2004.

SHORT-TERM PROCESSES: THE IMPACT OF WIND-EVENTS ON PHY-TOPLANKTON COMPOSITION

As established in the Introduction section of this paper, phytoplankton temporal dynamics in lakes and reservoirs can be characterised by the alternation of relative stable periods, during which phytoplankton is submitted to long-term autogenic changes (succession) and short-term transitional and stochastic events, that induce sharply changes (or shifts) in the phytoplankton community composition. The frequency and intensity of such disturbances would determine if the ecosystem dynamics is governed by the relatively unpredictable external forcing or, by contrast, if is auto-organized itself and trends to an equilibrium or climax state.

Figures 5 and 6 show the dynamic response of three contrasting algae species in the epilimnion of El Gergal to the occurrence of wind events (wind speed above 7.0 m s^{-1}) during the 2002 and 2003 thermally stratified period. The three algae species considered in this study are:

(i)   The large filamentous and positively-buoyant cyanobacteria *Aphanizomenon* sp. (S group).
(ii) The small centric and negatively-buoyant diatom *Cyclotella* sp. (R group).
(iii) The small almost spherical neutrally-buoyant chlorococcal green algae *Sphaerocystis* sp. (C group).
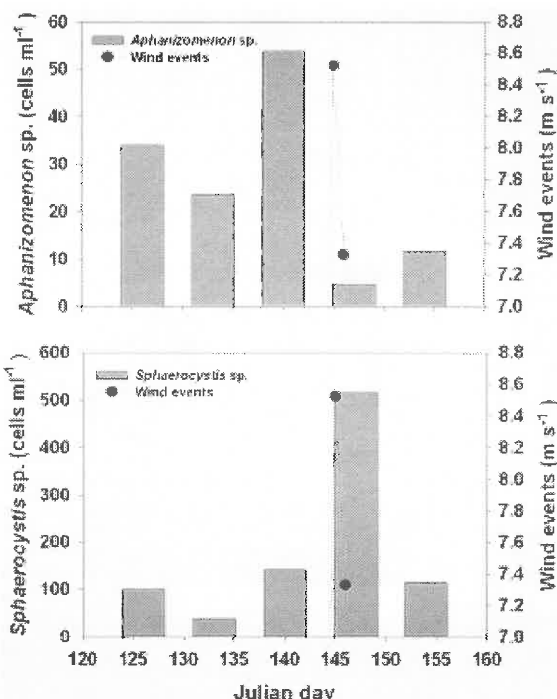
Figure 5. The impact of wind events on the populations of the cyanobacteria *Aphanizomenon* sp. (a) and the green algae *Sphaerocystis* sp. (b) during summer 2002.

222
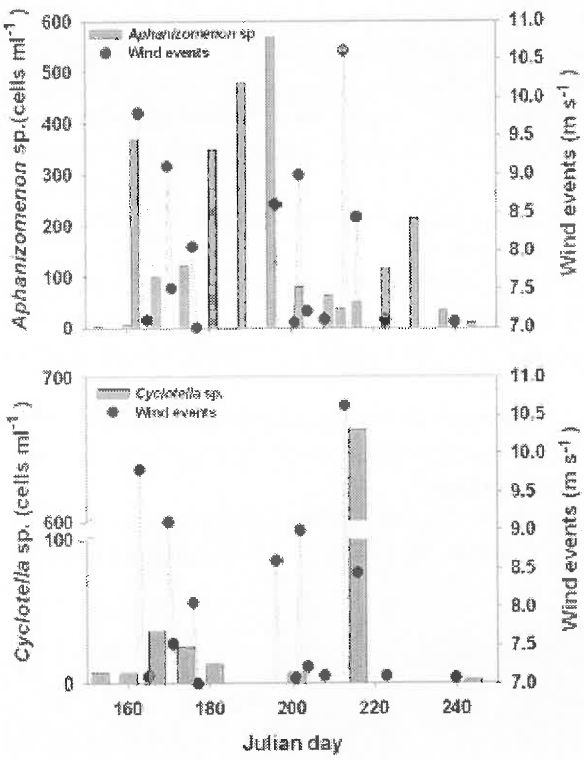
Figure 6. The impact of wind events on the populations of the cyanobacteria *Aphanizomenon* sp. (a) and the diatom *Cyclotella* sp. (b) during summer 2003.

In the two study cases, the lack of wind events enhanced the development of *Aphanizomenon* sp., a well-adapted species to live in low-turbulence and thermally stratified environments. However, the sudden occurrence of intense wind-induced turbulent mixing events supposed a marked decrease of the cyanobacteria population density and enhances the increase in biomass of the more appropriately adapted species development, such as *Cyclotella* sp. and *Sphaerocystis* sp., thus meaning a change in the original succession track represented in the Margalef's mandala.

ACKNOWLEDGMENTS

223

REFERENCES

CLEMENTS, F.E. 1916. Plant succession: an analysis of the development of the vegetation. Publs. Carnegie Instn 242: 1-512

GRIME JP. 1979. Plant strategies and vegetation processes. John Wiley and Sons.

Harris, G.P. 1986. Phytoplankton ecology. Structure, function and fluctuation. Chapman and Hall.

MARGALEF, R. 1978. Life-forms of phytoplankton as survival alternatives in an unstable environment. *Oceanol. Acta*, 1: 493-509.

MORENO-OSTOS, E. 2004. Spatial dynamics of phytoplankton in El Gergal reservoir (Seville, Spain). Ph D Thesis. Univ.of Granada.

REYNOLDS, C.S. 1997. Vegetation processes in the pelagic: A model for ecosystem theory. Ecology Institute.

REYNOLDS, C.S. 1987. Community organization in the freshwater plankton, p. 297-325. *In* J.H. R. Greene and P.S. Giller [eds], Organization of communities, past and present. Blackwell Scientific Publications.

SORANNO, P.A. 1997. Factors affecting the timing of surface scums and epilimnetic blooms of blue-green algae in a eutrophic lake. Can. J. Fish. Aquat. Sci. 54: 1965–1975 (1997).

SPATIALLY VARYING PROBABILITY OF SEDIMENT RESUSPENSION IN TWO SHALLOW COASTAL LAGOONS: IMPACT ON SEDIMENTARY NUTRIENTS DISTRIBUTION

I. de Vicente[1][2], Relaño-Pastor, C[1], E. Moreno-Ostos[1][3], F.J. Rueda[1] and L. Cruz-Pizarro[1]

(1) Water Research Institute- University of Granada - C/ Ramón y Cajal, 4- 18071 Granada, Spain
(2) Institute of Biology - University of Southern Denmark - Campusvej 55 - 5230 Odense M, Denmark
(3) Flumen Research Group - Department of Ecology - University of Barcelona- Av. Diagonal 645 - 08028 Barcelona, Spain

INTRODUCTION

Nowadays, eutrophication is a problem of major concern for the quality of natural and artificial water bodies (e.g. Sas, 1989; Ryding and Rast, 1992; Harper, 1992). Apart from external loading, nutrients availability in the water column of shallow lakes is, to a large extent, controlled by vertical exchange processes occurring at the water-sediment interface (internal loading). For the case of phosphorus (P), the internal loading has been identified as an important mechanism in delaying recovery of shallow lakes following reduced external P loading (Marsden, 1989; Søndergaard et al., 1992; Schauser et al., 2003, among others). As Golterman (1995) established, the P concentrations in the sediment and the overlying water are in a dynamic equilibrium where the position of this equilibrium, that controls whether input or output dominates, is determined by the interaction of multiple factors that may change over different time-scales. Among them, physical processes such as sediment resuspension, chemical reactions (e.g. oxidation vs reduction of P bound to Fe and precipitation vs dissolution of P bound to Ca) and biological mechanisms account for the instability and unpredictability of nutrients dynamics in shallow lakes (see de Vicente et al., 2004).

In shallow lakes, where sediment often undergoes continuous wave action, wind-induced resuspension usually plays a fundamental role in determining the nutrient dynamics (e.g. Kristensen et al., 1992; Nõges et al., 1999; Weyhenmeyer and Bloesch, 2001). Resuspension, which ultimately depends on lake bathymetry, on

sediment granulometry and also on the presence of cohesiveness agents (e.g. benthic algae), can determine the existence of erosion, transport and deposition areas in a particular lake. Despite of this, few studies consider the impact of sediment resuspension on the distribution of sedimentary nutrients. In this work, we estimate the spatial variability in the probability of sediment resuspension in two adjacent eutrophic lakes: Lake Honda and Lake Nueva (South Spain) that, as a consequence of their geographic proximity are subjected to the same meteorological forcing. These results are used for explaining the horizontal distribution of sedimentary nutrients both in dissolved (interstitial water) and in particulate pools.

STUDY SITE

The Albufera de Adra is composed of two small and shallow coastal lakes, Laguna Honda (LH) and Laguna Nueva (LN), which are located in south-eastern Spain (Fig. 1). High external and internal P loadings have induced eutrophic conditions in both lakes, especially in LH (de Vicente et al., 2001; de Vicente et al., 2003; Cruz-Pizarro et al., 2003; de Vicente and Cruz-Pizarro, 2003). Despite of their geographic proximity, LH and LN exhibit considerable differences in their morphometry and hydrological regime. LH has a larger catchment area. As a consequence, the turbidity level in LH is larger than in LN and it is subject to a continuous silting process. Submerged macrophytes are currently absent from LH due to the high turbidity level, while in LN macrophytes patches commonly develop in the littoral zone.
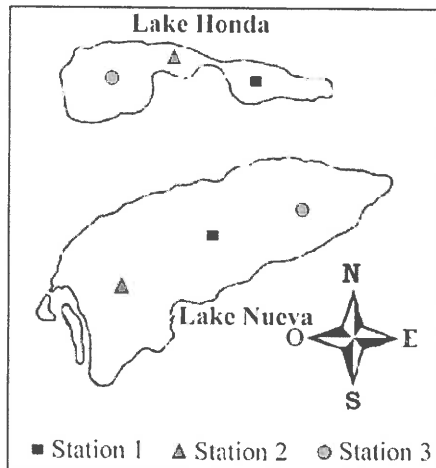

Figure 1. Location of the sites for sediment sampling.

226

Some of the most important morphometric features are summarised in Table 1. A measure of the bottom dynamics (Håkanson and Jansson, 1983) is given by the dynamic ratio. Its value is larger in LH, which suggest that resuspension may play a relatively major role in this lake compared to LN. In addition, a transversal section of the bathymetric maps show the existence of a flat bottom in LN while in LH two different basins can be distinguished: a much deeper east basin (Z_{max}, 3.19 m) and a much shallower (Z_{max}, 2.25 m) and larger west one (Fig. 2).

As a result of their shallowness, meteorological forcing plays a key role in the temporal fluctuations detected in the water column (Cruz-Pizarro et al., 2002). During most of the study period the wind speed was between 2 and 8 m s^{-1}, with maximum values exceeding 10 m s^{-1}. According to Cruz-Pizarro and others (2002), complete water column mixing in LH and LN occurs for wind speeds exceeding 3.9 and 4.2 m s^{-1} respectively. Hence, it appears reasonable to expect that resuspension events should be taken into account in studying nutrient dynamics.

	Honda	NUEVA
Lake area: A (m^2, 10^3)	77.19	259.21
Volume: V (m^3, 10^3)	84.90	589.84
Mean depth: $\overline{Z}$ = V / A (m)	1.10	2.28
Maximum depth: $Z_{máx}$ (m)	3.19	3.80
Maximum lengh: L_{max} (m)	586	759
Catchment area: A_c (m^2, 10^5)	137.2	5.0
Dynamic ratio ($\sqrt{A}$ / $\overline{Z}$)	253	223
$\overline{Z}$ / Z_{max}	0.34	0.60
A_c / A	177.73	1.93
A_c / V (m^{-1})	161.61	0.85
TP (µg l^{-1})[*]	98-529 (290)	22-245 (95)
P-PO$_4^{3-}$ (µg l^{-1})[*]	0-287 (75)	0-33 (4)
Chlorophyll a (µg l^{-1})[*]	2-409 (124)	4-136 (51)
Secchi depth (m) (annual mean)[*]	0.10-2.14 (0.62)	0.35-1.40 (0.80)

Table 1. Main morphometric and limnological features (June 2000-August 2001) (modified from de Vicente, 2004). [*]Max-Min (Average). Taken from de Vicente (2004).
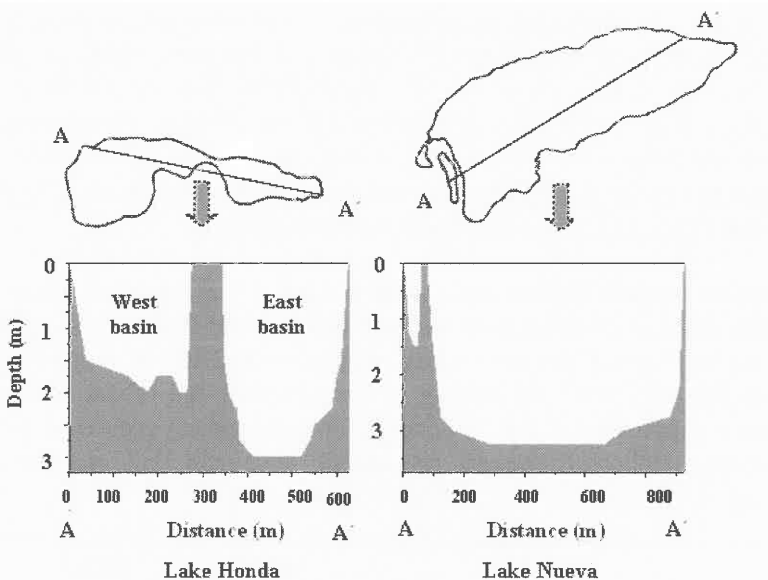
Figure 2. Cross-section of the study lakes. Taken from de Vicente (2004).

MATERIAL AND METHODS

Meteorologic and morphometric data - The wind speed data set consists of hourly wind-speed and direction records collected from 1991 to 2006 at the agricultural experimental station 'Las Palmerillas' (less than 5 km from the lagoons). Hypsographic curves and morphometric variables were derived from bathymetry maps (Cruz-Pizarro et al., 1992).

Sediment monitoring - Surface sediment samples (0-5 cm) were collected monthly, from July 2000 to August 2001, at three different sampling stations located along a longitudinal transect in both study lakes (Fig. 1), using an Ekman dredge. Within 24 hours, the interstitial water was separated from the sediment particles by centrifugation at 5000 r.p.m. during 10 min. (Enell & Löfgren, 1988). The supernatants were then filtered through Whatman GF/C filters. The wet sediments were kept at 4°C until they were fractionated 1-2 weeks later. No treatment (drying, freezing or sieving) was performed on the sediment samples before fractionation. In the interstitial water, the concentration of PO_4^{3-} (Murphy and Riley, 1962), NH_4^+ (Rodier, 1989) and inorg-C_{diss} (TC Autoanalyser, Dohrman, DC-190) was measured. In the particles, P-fractionation was performed following the EDTA method, based on a sequential extraction with chelating compounds (Golterman, 1996). TP was measured by spectrophotometry (Murphy & Riley, 1962) after an acid digestion (Golterman, 1996). Finally, the content of Total C and N was also measured by CNH Elemental Analyser. The granulometric composition of the surface sediment layer

was determined using the method proposed by Robinson (1922), basically based on the Stokes law.

Model to predict resuspension events - The empirical model proposed by Carper and Bachman (1984) were used to estimate whether resuspension occurs at any given point in each of the lakes. In that model wind-induced waves will induce resuspension at a given location when the water depth is less than half the wavelength (Carper and Bachmann 1984). The wave height is estimated as one-half of the wavelength L, which in turn is calculated as

$$L = \frac{gT^2}{2\,\pi} \tag{1}$$

Here, g is the acceleration of gravity, and T is the wave period, calculated as a function of wind speed (V, m s^{-1}) and of the effective distance over water that the wind blows (fetch, F, m), by the empirical formula:

$$\frac{gT}{2\,\pi\,V} = 1.20\tanh\left[0.077\left(\frac{gF}{V^2}\right)^{0.25}\right] \tag{2}$$

For any given location within the lake, the fetch depends on the wind direction and, of course, on the geometry of the lake itself. The fetches for each wind direction (from zero to 359 every 1 degree) and for every point on a grid of 1x1 m overlaid over the bathymetry maps, were calculated for LH and LN, following the method indicated in Carper and Bachmann (1984). From the fetch and the bathymetric information, for any given individual wind speed and direction record an index matrix was calculated with ones or zeros, depending on whether resuspension occurs or not, according to the algorithm proposed by Carper and Bachmann (1984). An index matrix was constructed for each individual record in the time series of wind speed and direction. The probability of resuspension was estimated on the 1x1 m grid by counting the number of times the index matrix is 1 at each cell and dividing by the number of records in the time series for wind.

Statistical analysis - Statistical analysis was performed using Statistica Program (6.0). For t- student test, unless otherwise stated, the significance level is established at $p < 0.05$.

RESULTS AND DISCUSSION

Spatially varying probability of sediment resuspension - The model of Carper and Bachmann (1984) predicts markedly differing behaviours for Lake Nueva and Lake Honda. For Lake Nueva, the probability of sediment

resuspension is nearly uniform in space, with values around 40% for most of the area. Values become higher near the shore where the lagoon is shallower (Fig. 3 - left). In Lake Honda, though, the probability of resuspension undergoes spatial variations, controlled by the more complex geometry of this water body. The probability ranges from 40% in the eastern basin to 50% in western basin, and reach values of up to 70% near the shore (Fig. 3 - right). The larger probability of resuspension in the western basin is due to being shallower than the eastern basin. In consequence, it is hypothesized that resuspension processes prevail in the western basin, while sedimentation will prevail in the eastern basin.
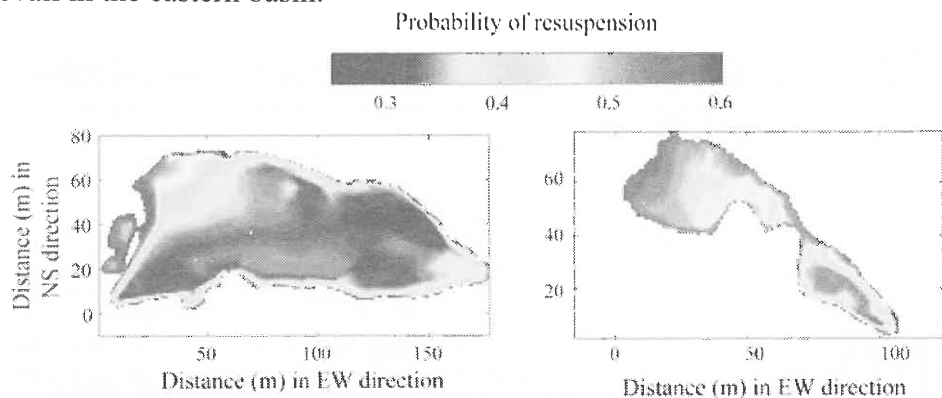

Figure 3. Probability of sediment resuspension in Laguna Nueva (left) and Laguna Honda (right) estimated from bathymetry maps and hourly wind records, using the method proposed by Carper and Bachman (1984)
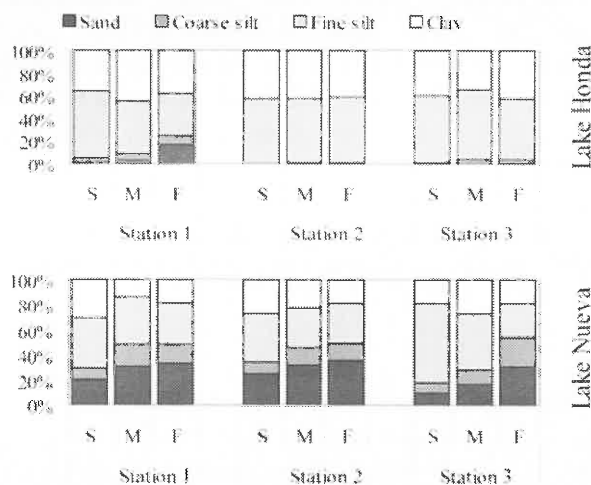
Figure 4. Granulometry of the surface sediment (0-5 cm).

230

Spatial distribution of sedimentary nutrients - The analysis of nutrients in the interstitial water and in the solid fraction of the sediment has revealed large differences between both study lakes (Table 2 and Figure 4). LH shows a very clear spatial heterogeneity, with maximum concentrations in the deepest basin (east basin), thus considered as an accumulation zone. Contrarily, LN is characterized by a homogeneous distribution of sediment nutrients. Accordingly, the Cluster analysis (Figure 5) revealed that the three stations located along the longitudinal transect in LN show similar values for nutrients concentrations in both sedimentary dissolved and particulate pools.
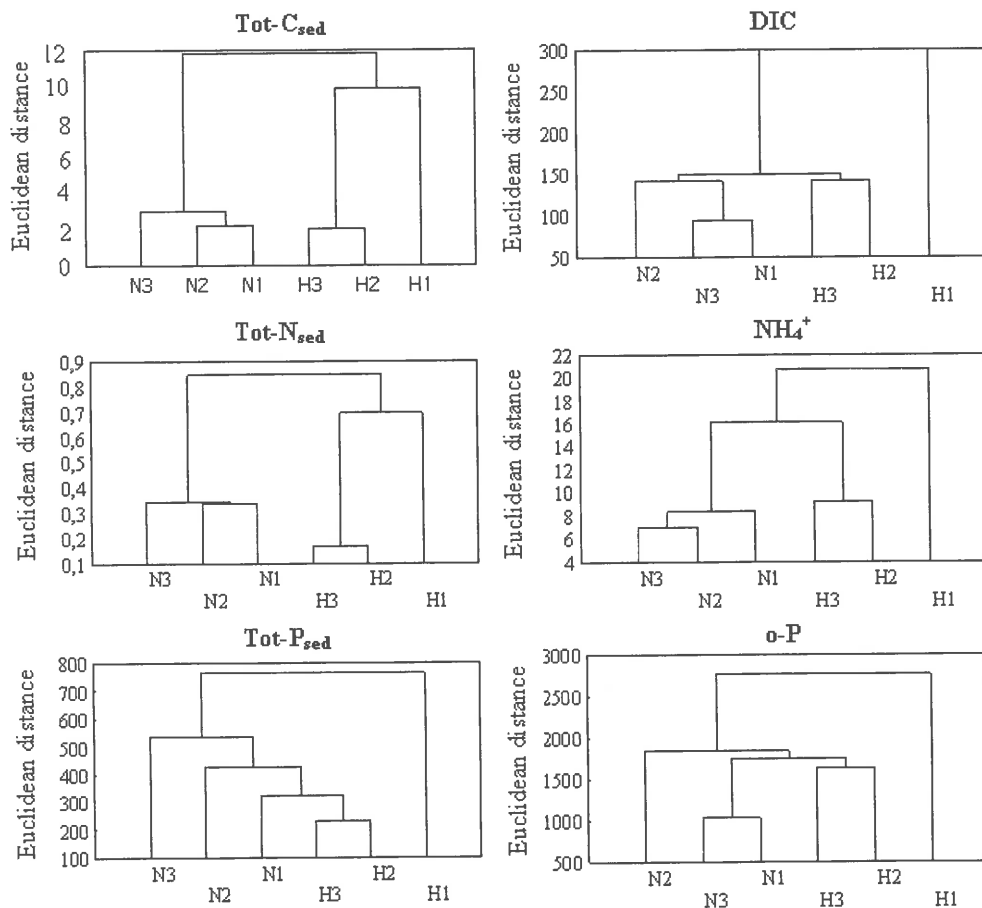
Figure 5. Results of the cluster analysis. Tot-C_{sed}, Tot-N_{sed}, Tot-P_{sed} are referred to sediment particles. DIC, NH_4^+ and o-P are referred to the interstitial water.

|		Lake Honda			Lake Nueva		
		Station 1	Station 2	Station 3	Station 1	Station 2	Station 3
Sediment	O.M (%)	9.6±1.6 (14)	3.8±0.8 (14)	3.7±1.1 (14)	16.3±2.0 (14)	15.9±2.4 (14)	17.4±2.0 (14)
	Tot-C (%)	8.41±0.49 (5)	3.46±0.61 (5)	4.10±0.83 (5)	13.65±0.34 (5)	14.11±0.79 (5)	14.18±1.35 (5)
	Tot-N (%)	0.48±0.05 (5)	0.13±0.02 (5)	0.18±0.07 (5)	0.86±0.08 (5)	0.84±0.10 (5)	0.93±0.13 (5)
	Tot-P[1]	703±97 (12)	460±75 (12)	447±67 (12)	398±126 (12)	469±187 (12)	468±225 (12)
	P ≈ FeOOH[1]	137±26 (12)	92±24 (12)	99±32 (12)	19±13 (12)	31±25 (12)	28±14 (12)
	P ≈ CaCO$_3$[1]	315±36 (12)	211±43 (12)	183±31 (12)	142±40 (12)	180±77 (12)	128±66 (12)
	Org-P$_{acid}$[1]	63±36 (12)	77±29 (12)	83±29 (12)	54±24 (12)	58±50 (12)	89±99 (12)
	Org-P$_{alk}$[1]	175±61 (12)	75±42 (12)	74±32 (12)	167±73 (12)	189±62 (12)	209±130 (12)
	Tot-Fe[2]	34.7±5.0 (12)	33.3±4.8 (12)	34.3±10.6 (12)	21.0±6.2 (12)	21.2±11.3 (12)	23.8±9.9 (12)
	FeOOH[2]	19.4±3.2 (12)	13.8±2.4 (12)	13.6±2.2 (12)	4.3±1.2 (12)	5.6±2.4 (12)	5.6±2.8 (12)
	Fe:P	82±28 (12)	88±29 (12)	84±36 (12)	207±196 (12)	184±207 (12)	145±103 (12)
Interstitial water	o-P[3]	1312±505 (14)	516±445 (14)	682±484 (14)	327±315 (14)	389±580 (14)	336±270 (14)
	NH$_4^+$[4]	11.26±4.56 (12)	7.18±3.94 (12)	5.26±3.55 (12)	4.27±2.83 (12)	3.41±2.91 (12)	3.68±2.23 (12)
	DIC[4]	121±59 (15)	95±47 (15)	84±22 (15)	45±22 (15)	72±38 (15)	54±18 (15)
	DOC[4]	39±12 (15)	32±9 (15)	34±13 (15)	17±7 (15)	20±6 (15)	20±7 (15)

Table 2. Chemical composition of the surface (0-5 cm). Mean ± SD (number of samples). Units: [1]µg g^{-1} DW; [2]mg g^{-1} DW; [3]µg l^{-1}; [4]mg l^{-1}.

232

CONCLUSIONS

Our results suggest that, apart from extrinsic factors (wind velocity), sediment resuspension depends on lake morphometry and sediment granulometry, factors which cause LH to be much more affected than LN by resuspension events. Thus, in LH a large proportion of the sediment is located at relatively low depth (Figure 4); by contrast, sediment resuspension in LN is ultimately limited by the relevant contribution of the sand-to-sediment mineral matrix (Figure 2) and also by its morphometry (Figure 4). In LH there is a clear spatial variability in the probability of sediment resuspension and hence, we have identified a west basin where resuspension occur and a east basin dominated by sedimentation processes. As a consequence, sedimentary nutrients in LH show a marked heterogeneous distribution characterized by maximum concentrations in the "sedimentation" basin while the impact of sediment resuspension in the east basin is responsible for a sharp decrease in sediment nutrients storage. By contrast, the morphometry and granulometry of LN account for an equal impact of sediment resuspension along the fetch, and accordingly a clear homogenous pattern of sedimentary nutrients distribution has been detected in this lake.

ACKNOWLEDGMENTS

REFERENCES

CARPER, G. L., AND R. W. BACHMANN (1984), Wind resuspension of sediments in a prairie lake. *Can. J. Fish. Aquat. Sci., 41,* 1763-1767.

CRUZ-PIZARRO, L., M. ARGAIZ, I. GARZÓN, AND J. LÓPEZ (1992), Batimetría de las lagunas de la Albufera de Adra. Technical Report, Water Research Institute, University of Granada.

CRUZ-PIZARRO, L., J. BENAVENTE, J. CASAS, V. AMORES, L. MAY, D. FABIÁN, M. RODRÍGUEZ, K. EL MABROUKI, I. RODRÍGUEZ, I. DE VICENTE, E. MORENO-OSTOS, S. L. Rodrigues da Silva, M. Bayo, A. Moñino, and M. Paracuellos (2002), Control de la eutrofización en las lagunas de las Albuferas de Adra. Diagnóstico, Evaluación y Propuesta de Recuperación. Final Report Project UE LIFE B4-3200/98/458. 349 pp.

CRUZ-PIZARRO, L., I. DE VICENTE, E. MORENO-OSTOS, V. AMORES, AND K. EL MABROUKI (2003), Estudios de diagnóstico y viabilidad en el control de la eutrofización de las lagunas de la Albufera de Adra. *Limnetica, 22,* 135-154.

DE VICENTE, I. (2004), Intercambio de nutrientes en la interfase agua-sedimento de dos lagunas costeras de elevado nivel trófico, Ph D. thesis, 287 pp, University of Granada, Granada.

DE VICENTE, I., V. AMORES, K. EL MABROUKI, E. MORENO-OSTOS, I. RODRÍGUEZ-PARÍS, AND L. CRUZ-PIZARRO (2001), Balance de fósforo en las lagunas de las Albuferas de Adra (Almería, España). *Actas del V Simposio sobre el Agua en Andalucía, 3,* 301-311.

DE VICENTE, I., L. SERRANO, V. AMORES, V. CLAVERO, AND L. CRUZ-PIZARRO (2003), Sediment phosphate fractionation and interstitial water phosphate concentration in two coastal lagoons (Albuferas de Adra, SE Spain). *Hydrobiologia, 492,* 95-105.

DE VICENTE, I., AND L. CRUZ-PIZARRO (2003), Estudio de la carga externa e interna de fósforo y aplicación de modelos empíricos de eutrofización en las lagunas de la Albufera de Adra. *Limnetica, 22,* 165-181.

ENELL, M., AND S. LÖFGREN (1988), Phosphorus in interstitial water: methods and dynamics. *Hydrobiologia, 170,*103-132.

GOLTERMAN, H. L. (1995), Theorical aspects of adsorption of ortho-phosphate onto iron-hydroxide. *Hydrobiologia, 315,* 59-68.

GOLTERMAN, H. L. (1996), Fractionation of sediment phosphate with chelating compounds: a simplification and a comparison with other methods. *Hydrobiologia, 335,* 87-95.

HÅKANSON, L., AND M. JANSSON (1983), *Principles of lake sedimentology.* 316 pp, Springer- Verlag, Berlin.

HARPER, D. (1992), *Eutrophication of freshwaters. Principles, problems and restoration.* Chapman & Hall. Londres.

KRISTENSEN, P., M. SØNDERGAARD, AND E. JEPPESEN (1992), Resuspension in a shallow eutrophic lake. *Hydrobiologia, 228,* 101-109.

MARSDEN, M.W. (1989), Lake restoration by reducing external phosphorus loading: the influence of sediment phosphorus release. *Fresh. Biol., 21,*139-162.

MURPHY, J., AND J. P. RILEY (1962), A modified single solution method for the determination of phosphate in natural waters. *Anal. Chim. Acta, 27,* 31-36.

NÕGES, P., L. TUVIKENE, T. NÕGES, AND A. KISAND (1999), Primary production, sedimentation and resuspension in large shallow Lake Võrtsjärv. *Aquat. Sci., 61,* 168-182.

ROBINSON, G. W. (1922), New method for mechanical analysis of soil and another dispersion. *J. Agr. Ac., 12,* 306-321.

Rodier, J. (1989), *Análisis de las aguas.* Omega. Barcelona.

Ryding, S.O., and W. Rast (1992), *El control de la eutrofización en lagos y pantanos.* Pirámide. Madrid.

SAS, H. (1989), *Lake restoration by reduction of nutrient loading: expectations, experiences, extrapolations.* Sankt Augustin: Akademia Verlag Richarz.

SCHAUSER, I., J. LEWANDOWSKI, AND M. HUPFER (2003), Decision support for the selection of an appropriate in-lake measure to influence the phosphorus retention in sediments. *Wat. Res., 37*, 801-812.

STATSOFT INC. (1997), Statistica for Windows (computer program manual). Tulsa, Oklahoma, USA.

SØNDERGAARD, M., P. KRISTENSEN, AND E. JEPPESEN (1992), Phosphorus release from resuspended sediment in the shallow and windexposed Lake Arresø, Denmark. *Hydrobiologia, 228*, 91-99.

WEYHENMEYER, G. A., AND J. BLOESCH (2001), The pattern of particle flux variability in Swedish and Swiss lakes. *Sci. Total Environ., 266,* 69-78.

HYDRODYNAMIC PROCESSES IN LAKE PAVIN (FRANCE)

Celine Bonhomme[1], Yannis Cuypers[1], B. Brigitte Vinçon-Leite[1],
Bruno Tassin[1] and M. Poulin[2]

(1) CEREVE, Centre d'Enseignement et de Recherche Eau-Ville-Environnement, ENPC, 6 av. Blaise Pascal, Champs sur Marne, F-77455, France
(2) CIG, Centre d'informatique géologique, ENSMP, 5 rue Saint Honoré, Fontainebleau, F-77305, France

The present study aims at understanding the main hydrodynamic processes which occur in the water column and especially between mixo and monimolimnion of Lake Pavin. Lake Pavin is a cone-shaped crater lake, very deep (100m) with regards to its surface (1.7 km^2). The 40 lower meters are never mixed and are highly anoxic (very steep oxycline around 50m). As shown by previous measurements (Summer 2005), the oxycline coincides with a cold temperature anomaly (-0.04°C) around 50 meters depth, and the water balance on the lake suggests this anomaly could be generated could be generated by sublacustre water intrusions. In year 1995, a thermistor string located in the upper part of the lake already showed the presence of different internal waves modes and their influence in depth due to low dissipation in the basin. In the frame of METANOX project, which aims at describing the main biogeochemical processes in the monimolimnion, a monthly survey of the lake comprising physical, chemical and biological parameters will take place between in 2006 and 2007. The deployment of high frequency response thermistor strings, SCAMP and CTD profiles and ADCP measures of currents permit us to quantify the dispersion coefficient in the water column and to identify the influence of internal waves, bottom friction and sublacustre sources in this coefficient. These measurements should help us to understand oxycline position and its fluctuations during the period of observation. First resultst of the field survey will be presented. At last, with the 3D physical model ELCOM developed at CWR (Australia), we would like to reproduce internal seiches and dispersion coefficient and test the role of water intrusions to stabilize or destabilize the interface mixo-monimolimnion.

RIVER DISCHARGE CONTROLLING THE NUTRIENT CONTENT IN AN ESTUARINE SYSTEM. CASE STUDY OF PALMONES RIVER

Avilés, A. and Niell, F.X.[1]

(1) Dept. of Ecology. Faculty of Science. University of Málaga. Campus Universitario de Teatinos S/N, 29071-Málaga, Spain.Tel. +34952131844 Fax. +34952137386
e-mail: aviles@uma.es

ABSTRACT

A two-year study was carried out in the lower part of the Palmones River to describe the role of a small dam controlling the nutrient fluxes to the estuary and the relationships between the properties of the estuarine sediment and the hydrological conditions. Results showed that the dam could be considered as an optimally dimensioned pre-dam. Therefore, it removed on average more than 25 % of total phosphorus (TP) reaching during the dry season values of 55 %. Palmones River exported 11.3 TonsP y^{-1} of TP and 72.1 TonsN y^{-1} of TN to the estuary showing important seasonal differences.

Floods are responsible for the variation in the concentration of different phosphorus forms obtained in the sediment of the estuary of Palmones River. The apatite forms (AIP) are the major ones. Noticeable changes in the concentration of different phosphorus forms are related with fine grain size sediment. In spite of different responses obtained along the estuary, the results reveal the possibility of using phosphorus concentration as a flood event index, discarding the use of phosphorus speciation for the same purpose.

KEYWORDS

Eutrophication, flooding, nutrient forms, Palmones River, pre-dam, estuarine sediment.

INTRODUCTION

Over the last few decades there has been an increased interest in quantifying the fluxes of nutrients into estuaries and the environmental effects such nutrients have on water quality (e.g. Nedwell et al., 2002).

Phosphorus is usually considered the limiting nutrient for primary producers in freshwater, while in marine systems it is nitrogen, thus their reduction from river channels is of paramount importance. Several studies have shown the application of pre-dams as traps, that reduce nutrients and suspended particulate matter (SPM) from the water column (e.g. Paul et al., 1998). In these small reservoirs, an important increase of the hydraulic retention time (HRT) is produced and consequently, settling of particles, interactions between sediment and water column and elimination of dissolved nutrients by the primary producers become stronger.

Estuarine sediments have a considerable influence on nutrient concentration in the overlying water, especially in shallow estuaries, because of their capacity to exchange P and N (e.g. Boström et al., 1988).

Climatic and geomorphic conditions have important influence on the behaviour of shallow estuaries in the South of Spain, since they are characterized by small catchment areas and a subarid climate, which implies unpredictable short and long drought seasons alternating with important flooding events. Palmones is a good example of a south Spanish Mediterranean river (Clavero et al., 1999).

The main objectives of this study are to describe the influence of a small dam in the seasonal variation of nutrient concentrations in the lowland catchment of Palmones River, quantify its role in the fluxes of phosphorus and nitrogen from the river to the estuary and describe the relationships between flooding events and the concentration of sediment phosphorus forms in the estuary.

MATERIALS AND METHODS
STUDY AREA

The Palmones River Estuary is located in the Algeciras Bay (southern Spain). It is 5.5 km long and has a surface area of 3.75 km^2. The flow of fresh water into the estuary is dominated by the Palmones River. In 1955 a small dam was built in the inner part of the estuary with the purpose of supplying freshwater to a cellulose pulp plant. Nowadays, in spite of it being out of function, it still acts as a barrier for seawater at high tide, allowing only freshwater discharge. Upstream from the dam, there is a small reservoir with a volume of 0.21 Hm^3, a length of 8.6 km and a mean

width of 32 m. The main sewage treatment works (STW) of the basin flows into the dammed water (Figure 1).
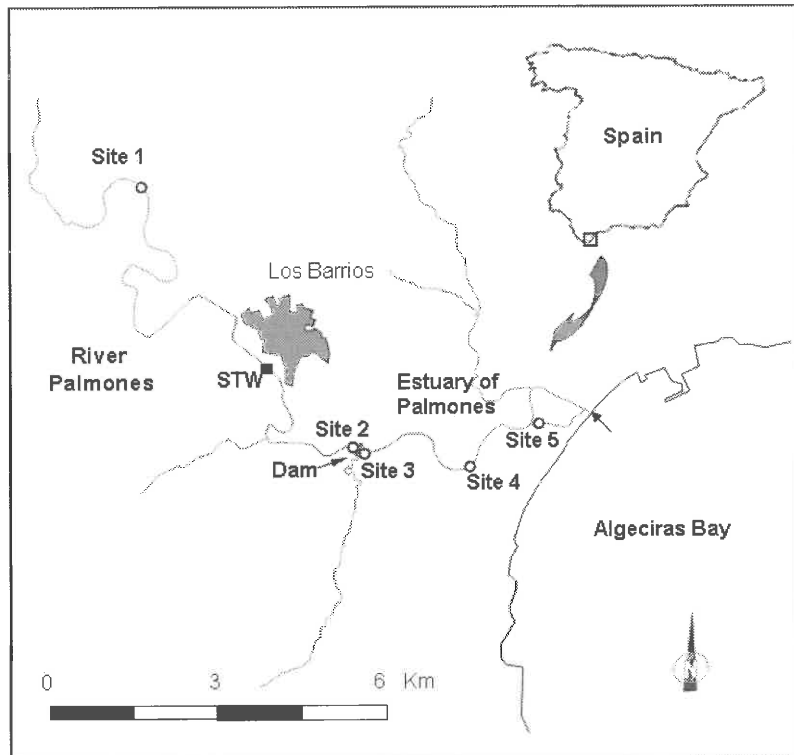

Figure 1. Map of the study area showing the location of sampling points.

SAMPLING AND ANALYTICAL METHODS

Two sampling sites (Site 1 and Site 2) were established upstream the dam and other three sampling sites (Sites. 3, 4 and 5) were established along the estuary from the inner to the lower part (Figure 1). The first two sites were selected in an attempt to characterize the role of the dam and the STW in the water quality and the nutrient fluxes to the estuary and the estuarine sites were taken in order to characterize the flooding effect in the sediment phosphorus concentration.

From April 1999 to May 2001, eight samples of water and six samples of sediment were collected with a frequency conditioned by river discharge and in order to complete periodical results of total nitrogen and phosphorus obtained by the Environmental Agency of the Junta de Andalucía.

241

Two litres of water were taken from each site and placed in ice for transport to the laboratory. For the determination of particulate forms of phosphorus and nitrogen, suspended particulate matter (SPM) and chlorophyll a (Chl a), subsamples of water were filtered through Whatman GF/F membranes, using the filtered water for the analysis of soluble nutrients, and unfiltered subsamples for the determination of total forms of phosphorus and nitrogen. Two replicate sediment cores (PVC, 10 cm diameter x 25 cm length) were collected in the intertidal sediment at each sampling site. Granulometric analysis was carried out combining dry and wet sieving. Phosphorus forms were extracted using the Pardo et al., (1999) method.

RESULTS AND DISCUSSION
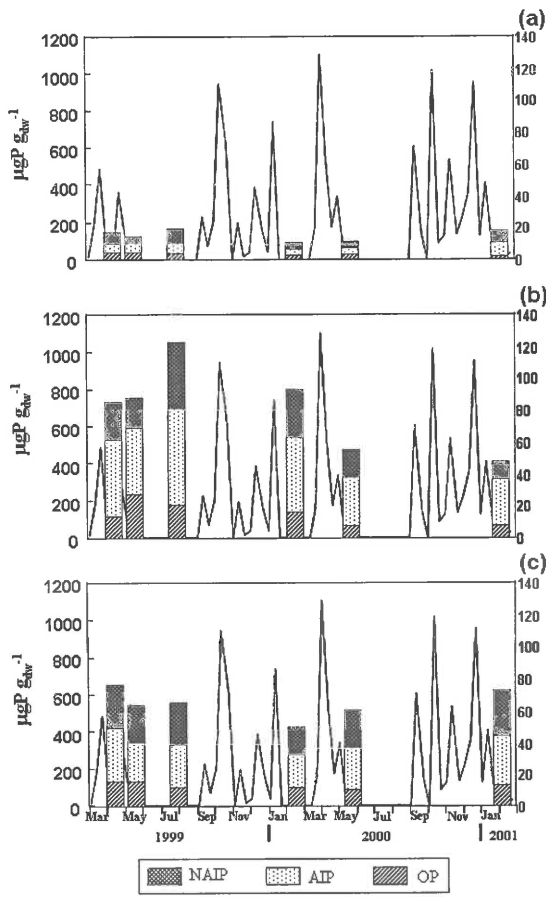
The Hydraulic Retention Time (HRT) values obtained in this study ranged between one hour and more than 1,000 hours. This extremely high seasonal variability produces important differences in the nutrient removal produced by the dam. The annual removal of total phosphorus (TP) was higher than 25 %, while no net removal was obtained for total nitrogen (TN) (Table Ia). Considering the seasonal variability, the average percentage of TP and TN loads removed from June to September were 55.4 and 79.8 %, respectively; while from February to May only a remove of 1.8 % of TP has been estimated and also an increase of 41.2 % of TN (Table Ib). Paul (2003) obtained that TP elimination did not outreach 25 % even in the largest pre-dams in summer, showing the great efficiency of the studied dam in the phosphorus elimination from the water column.

The annual river loads of TP and TN from Palmones River to the estuary during the study period being 11.3 TonsP y^{-1} and 72.1 TonsN y^{-1}, respectively. In spite of these results were lower than those obtained by Nedwell et al. (2002) in rivers with similar watershed areas, their effects over this shallow estuary are evident. In order to establish the variability of nutrient loads from the Palmones River to the estuary in relation with the hydrological conditions, a comparison between low flow (summer) and high flow conditions (January to March 2001) was made. In spite of the summer period accounting for 33 % of total sampling time (from June to September), TP and TN loads were lower than 8 and 5 % of total loads, respectively. On the other hand, in only three months (11 % of total sampling time) the loads of TP and TN corresponded to 23.6 and 64.5 % of total loads, respectively.

Results show the importance of the dam in the control of estuarine eutrophication, reducing the nutrient loads during the summer when the nutrient needs for primary production is highest.

Apatite inorganic phosphorus (AIP) is the dominant form of phosphorus in the sediment of the estuary of Palmones River, showing significant differences between stations that ranged from 30.8 $\mu gP\ g_{DW}^{-1}$ in Site 3 to 520.4 $\mu gP\ g_{DW}^{-1}$ in Site 4 (Fig.

2). Significant correlations with fine grain size ($< 63\ \mu m$) were observed for different phosphorus forms in agreement with other studies (e.g. McComb et al., 1998).

Figure 2. Distribution of sediment phosphorus concentrations of each fraction (NAIP, AIP and OP) at Site 3 (a), Site 4 (b) and Site 5 (c). Integrated ten day precipitation (continuous line) is superimposed.

Important seasonal changes in the sediment phosphorus forms were observed in Site 4, whereas at sampling point 3 and 5 were very low. The spatial heterogeneity makes difficult to determine the role of flooding events in the whole estuary. Nevertheless, it is possible to study this on the phosphorus fractions taking into account each sampling point.

Thus, Site 4 presented clear seasonal differences: in summer, concentrations higher than 500 $\mu gP\ g_{DW}^{-1}$ of AIP or 175 $\mu gP\ g_{DW}^{-1}$ of OP were obtained, followed by an important decrease, reaching a minimum in winter. The existence of intense

rainfalls during autumn and winter (which are depicted in Fig. 2) and subsequent increases of river discharges and scouring effects are responsible for these variations. It shows the great relationship between the river discharge and the sediment properties in Site 4. These results make possible to use the phosphorus concentration in the sediment as a flooding event index, taking into account its spatial heterogeneity.

(a)

	Inputs	Outputs	Removal
	Site 1+ STW	Site 2	%
TP (TonsP y^{-1})	15.1	11.3	25.2
TN (TonsN y^{-1})	71.9	72.1	-0.3

(b)

	June-Sept	Oct-Jan	Febr-May
TP (%)	55.4	44.0	1.8
TN (%)	79.8	-18.0	-41.2

Extract from: Avilés and Niell (in press)

Table I. (a) Annual percentage of total phosphorus and nitrogen removed by the dam and (b) seasonal variability of the removed percentage through the study period.

REFERENCES

AVILÉS. A., F. X. NIELL. 2005. Pattern of phosphorus forms in a Mediterranean shallow estuary: Effects of flooding events. Estuar. Coast. Shelf Sci. **64**: 786–794.

AVILÉS A., F. X. NIELL. (under revision). The control of a small dam in nutrient inputs to an hypertrophic estuary. Wat. Air Soil Poll.

BÖSTROM, B., J. M. ANDERSEN, S. FLEISHER, M. JANSSON. 1988. Exchange of phosphorus across the sediment-water interface. Hydrobiologia. **170**: 229-244.

CLAVERO, V., J. J. IZQUIERDO, L. PALOMO, J. A. FERNÁNDEZ, F. X. NIELL. 1999. Water management and climate changes increases the phosphorus accumulation in the small shallow estuary of the Palmones River (southern Spain). Sci. Total Environ. **228**: 193-202.

McComb, J. A., S. Qiu, R. J. Lukatelich, T. F. McAuliffe. 1998. Spatial and temporal heterogeneity of sediment phosphorus in the Peel-Harvey estuarine system. Estuar. Coast. Shelf Sci. **47**: 561-577.

Nedwell, D. B., L. F. Dong, A. Sage, G. J. C. Underwood. 2002. Variation of the nutrient loads to the mainland U.K. estuaries: Correlation with catchment areas, urbanization and coastal eutrophication. Estuar. Coast. Shelf Sci. **54**: 951-970.

Pardo, P., J. L. López-Sanchez, G. Rauret, V. Ruban, H. Muntau, Ph. Quevauviller. 1999. Study of the stability of extractable phosphate content in a candidate reference material using a modified Williams extraction procedure. Analyst. **124**: 407-411.

Paul, L., K. Schröter, J. Labahn. 1998. Phosphorus elimination by longitudinal subdivision of reservoirs and lakes. Wat. Sci. Tech. **37**(2): 235–243.

Paul, L. 2003. Nutrient elimination in pre-dams: results of long term studies. Hydrobiologia. **504**: 289–295.

VELOCITY PROFILES AND WATER LEVELS MEASUREMENTS IN A SHALLOW COASTAL LAGOON

Carmelo Nasello[1], Giuseppe Ciraolo[1], Goffredo La Loggia[1]

(1) Dipartimento di Ingegneria Idraulica ed Applicazioni Ambientali, Università di Palermo, Viale delle Scienze, 90128 Palermo, Italy. Email: giuseppe@idra.unipa.it; Fax: +390916657749

INTRODUCTION

The numerical modelling of the hydrodynamics in lagoons and coastal areas requires a sound knowledge of the *in-situ* dynamical behaviour of the simulated variables (velocities, water elevations, etc). These measurements are essential in calibration and validation procedures and they are also important to understand the physical system. This paper illustrates results of field measurements carried out in a shallow coastal lagoon, called *Stagnone di Marsala*, in the western part of Sicily (Italy). The water exchange with the Mediterranean Sea occurs through two openings in the basin: the northern one is narrower and shallower than the southern one: for this reason the main fluxes pass through the southern mouth.

Four field campaigns have been carried out: July 2003, July 2004, December 2004 and July 2005. In this paper results from the last field campaign will be compared with those already described in previous papers. The measured physical variables are: 1) tide at the lagoon mouths; 2) velocities and elevations in selected stations within the lagoon; 3) wind speed. During the 2005 field campaign, our attention has been focused on the velocity profiles over vegetated areas.

THE STUDY AREA

The *Stagnone di Marsala* is a shallow lagoon located in the western part of Sicily, delimited by the dry land and the *Isola Grande* island. This lagoon is 12 km² in area (1.8 km wide by 6.8 km long) (Fig. 1). Within the lagoon there are two small islands (*Mothia* and *Santa Maria*). From ecological viewpoint, the Stagnone di Marsala is considered a environment peculiar within the Mediterranean Sea owing to the particularity of vegetal and animal species living in it. The most important submerged vegetation is the *Posidonia oceanica*, a typical sea-grass (rooted marine macrophytes) in the Mediterranean Sea whose formations, in form of plateaus and barrier reefs,

247

largely contribute to the sustenance of lagoon ecosystems (Calvo *et al.*, 1996). For these reasons, the lagoon and the surrounding areas are a natural reserve.

The lagoon has a northern narrow and shallow mouth to the sea (400 m wide, 0.2-0.3 m deep) and a southern wider and deeper one (1200 m wide, 1.0-1.5 m deep). At the left end of the northern mouth a 20 m wide and 1 m deep channel was dredged, somehow enhancing the local flushing capability (see inset in Fig. 1).

In order to calibrate an *in-house* hydrodynamic numerical models (Balzano *et al.* 2002), a meteorological station and tidal gauges have been installed in the lagoon in 2002. A first measurement campaign was carried out in July 2003 to measure velocities in 4 sites (Nasello and Ciraolo, 2004). Three other measurements campaigns were performed in July and December 2004 and in July-August 2005. In particular, the results of processed data from last campaign are reported here.
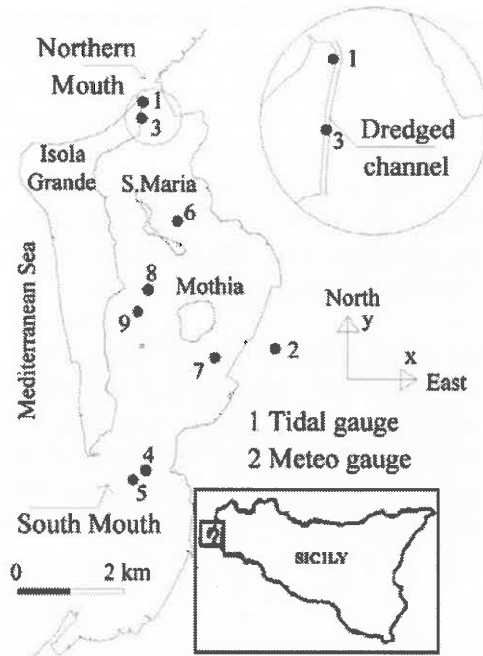

Figure 1. The Stagnone di Marsala lagoon and the experimental stations with measurement sites.

THE EQUIPMENTS

The tidal data have been acquired using a float-operated Shaft Encoder (Ott Thalimedes), located in a box connected with the dredged channel of the northern mouth (station 1, Fig.1). The sea level is measured every minute and the mean value is recorded every 5 minutes.

The meteorological gauge is located over a building at about 10 m above the ground in the mid lagoon (station 2, Fig. 1). This weather station is able to record several climatic data: in particular wind speed and direction are measured every 5 seconds and the mean values for each sector are recorded every 15 minutes. Figure 2a shows the intensity and directions of the prevalent sector of the July 2004 campaign. The wind speeds (Fig. 2b) are typically low overnight and increase during the morning; in particular, on 23rd July 2004 a daytime northerly wind blew with intensity from 5 up to 10 m/s.

During the December 2004 survey (Fig. 2c and 2d), a south-easterly wind blew on the first day of measurements and a north-westerly wind blew in the subsequent two days. The wind intensity increased from 5 to 15 m/s during these three days. During the summer 2005 survey the wind intensity was generally below 5 m/s.

Water velocities have been measured using two electromagnetic sensors and two ultrasonic sensors. Special platforms rising above the sea surface were designed for each instrument and built using aluminium metal tubes (3 m times 3 m). The platforms enabled us to shift the instrument upwards and downwards to record velocities at selected water depths.

Two electromagnetic velocimeters (Valeport 808 EM) are two-dimensional (V_{est} and V_{north}). The maximum acquisition rate is 0.5 Hz, *i.e.* with velocities recorded every 2 s. The first velocimeter was located in the dredged channel at the northern mouth (station 3 of Fig. 1). The second electromagnetic velocimeter was installed next to the southern mouth (stations 4 and 5 of Fig. 1). These instruments are able to measure the water depth h above the gauge using a pressure sensor and thus detect level oscillations.
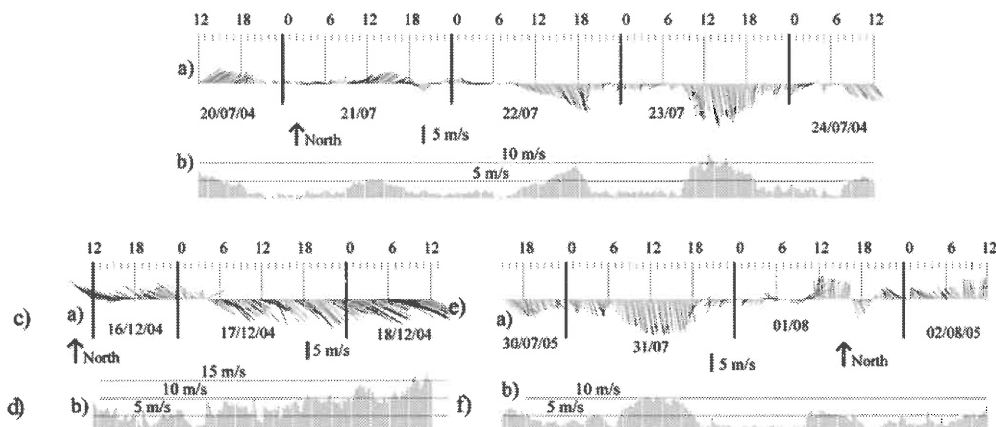

Figure 2. Wind direction and intensity during the 2004 and 2005 surveys.

One of the three-dimensional ultrasonic velocimeters, a Vector by Nortek, is able to measure and record the three water velocity-components with a sampling rate of 1 up to 16 Hz. This instrument is also able to measure the instantaneous water level. The Vector was located south-east of Mothia in July 2004 and 2005 and north-west of it in December 2004 (stations 7 and 8 of Fig. 1). The second three-dimensional acoustic velocimeter is an ADV by Nortek; the acquisition rate is between 1 and 25 Hz. This instruments was always positioned west of Mothia (station 9 of Fig. 1).

VELOCITY PROFILES

In the station 9 on 31st of July and 1st of August 2005 velocities at different depth were recorded using the ADV, in order to describe the shape of the velocity profiles in a point within the lagoon. The acquisition rate was set up at 25 Hz and we recorder for 3-8 minutes velocities in each point of the profile. We take about 30 minutes. In the station 9, during the acquisition time, the mean sea level over the bottom was of 140 cm and the vegetation (*Cymodocea nodosa*) height was 45 cm. Both profiles were collected during flowing out tide. The main difference between the two days was the wind condition. During the 31st (10:30 am) a strong wind (9.5 m/s) generated wind waves that propagate in the north-south direction. On the 1st of August (9:30 am) we found low wind (1.7 m/s) and flat sea surface.

In Figure 3 we report the velocities components recorded under windy condition, in three points. The first point is located near the water surface ($z=117$ cm, $z/H=0.84$ - Fig. 3a); the second point is located in the central part of the water column ($z/H = 0.43$ - Fig. 3b); the third point is located within the vegetation ($z/H= 0.13$ – Fig. 3c). Velocities components were filtered with a lowpass digital filter (cut off frequency of 2 Hz).

Near the surface is evident the influence of wind waves on the velocity field (Nasello and Ciraolo 2004, 2005). The three velocity components show the typical oscillating behaviour of the orbital motion of a velocity field influenced by wind waves (Kundu and Cohen, 2002; Nasello and Ciraolo, 2004; Nasello et at., 2005). The period of these oscillations is about one second (like the wind waves). The Vz component oscillates around zero, so that the mean flow in the vertical directions is almost insignificant. The velocity vector in the horizontal plane shows a surface flow southwards.

The analysis of velocities measured as deep as the mid water column ($z/H=0.43$) shows two main facts (fig. 3b): 1) the influence of the wind waves is still evident there and the period of the oscillations is about 1 second; 2) the velocity intensities are lower than the near-surface values and only the Vy component oscillates around a non zero value (fig. 3c).

250
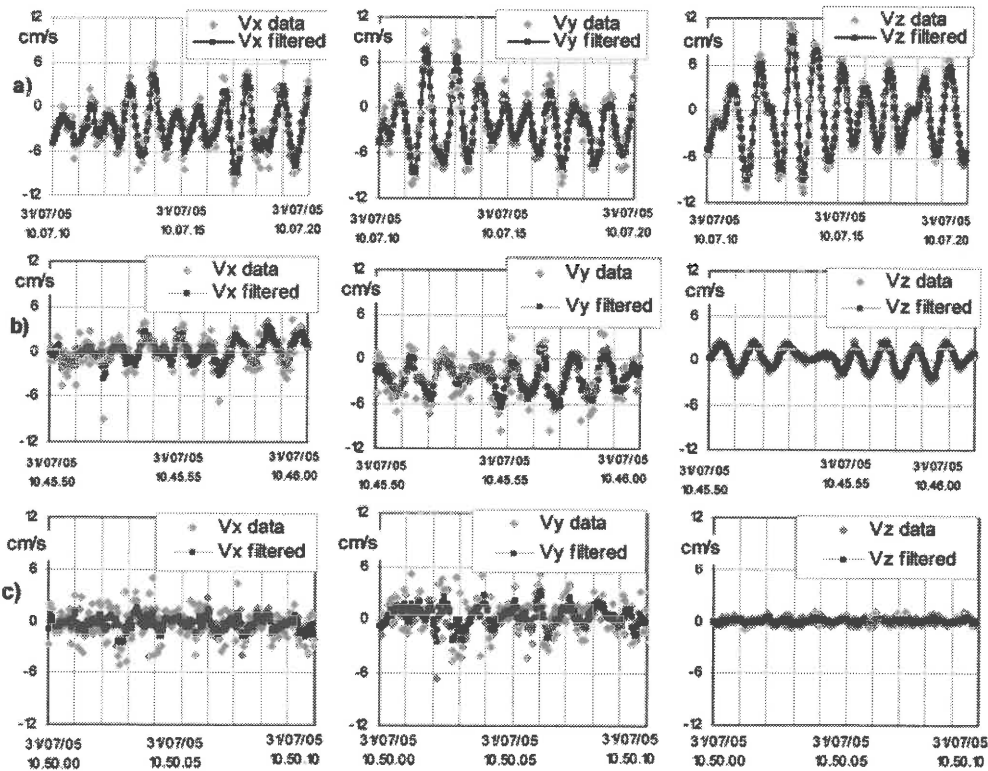
Figure 3. Velocity Components Vx, Vy, Vz; a) z/H=0.84; b) z/H=0.43; c) z/H=0.13.

The velocities measurements performed under calm condition, showed the absence of the orbital oscillations of wind waves (z= 117 cm, z/H = 0.84, Fig. 4). Also in this case the main flow is southward (tide flowing out).
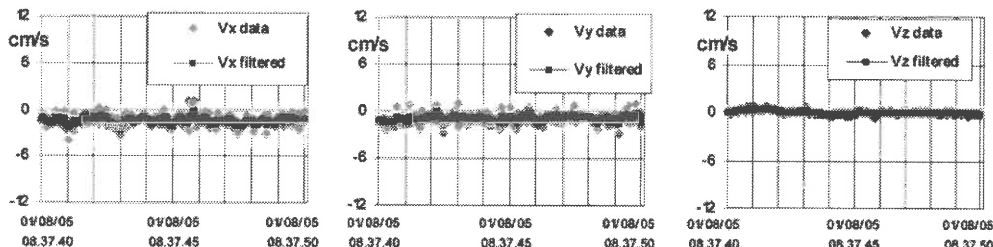

Figure 4. Velocity Components Vx, Vy, Vz; at z/H=0.84 in calm condition

Figure 5 shows the profile of the mean velocity components *Vx*, *Vy* during windy (Fig. 5a top) and calm (Fig. 5b top) condition . The deviations around the mean value (Fig. 5 middle) and the turbulence intensity (Fig. 5 bottom) are also plotted.

251

The *Vy* component is directly related with tide (negative values means that the flux is going in the south direction according with the lowering tide). The turbulence intensity is highest near the surface and decreases downwards. As also found by other authors (Yang 1998, Leonard and Reed 2002), the velocities and turbulence strongly decrease close to the vegetated layer (*z*=45 cm, vertical segment in fig. 5). It is possible to distinguish two different layers of the flow-field: the upper one characterized by larger velocities and the lower vegetated layer characterized by low and uniform velocities (Christiansen *et al.* 2000).

In the transition zone between these two layers a mixing layer should occur. This layer is subject to Kelvin-Helmholtz instability, which produces coherent eddies with cross-stream vorticity. In fact, similar studies of uniform flow in the presence of aquatic (Ghisalberti and Nepf, 2002) vegetation have shown that the roughness sublayer at the top of the canopy takes the form of a mixing layer, rather than a boundary layer in which the velocity profile has of a shear layer containing an inflection point. Further measurements will be carried out in order to focus this aspect.
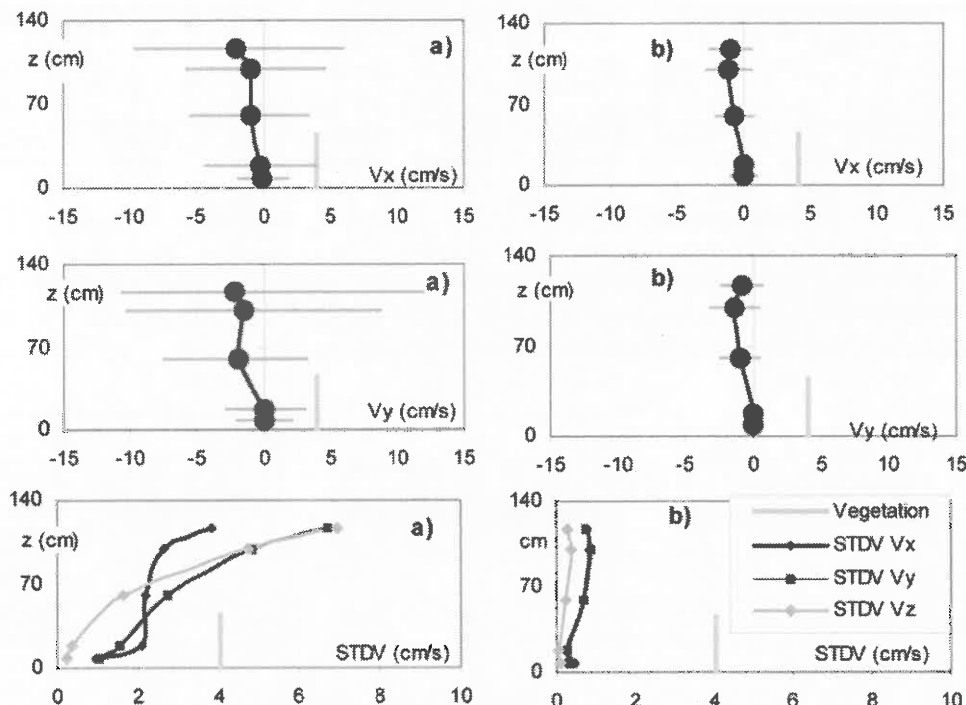

Figure 5. Velocity profiles components and turbulence intensity: a) windy conditions; b) calm.

A Fast Fourier Transform (FFT) algorithm applied to the three velocity components confirms the influence of wind waves on the flow field (Fig. 6a). The

power spectra of these near-surface velocity components (z/H=0.84) show a peak at 1 Hz, which is similar to frequency of the wind waves. This suggests that some fraction of water-current kinetic energy is related to the orbital eddies generated by the wind action. Part of this kinetic energy is then transferred to small vortices where is dissipated and for this reason is not available for the deeper layers. The peak attenuates going downwards and so do the large eddying caused by wind waves. Arguably, part of the kinetic energy of the eddies went into dissipation and part was transferred into turbulence structures of smaller scale (Pope, 2000).

Because of the wind waves, the flow field near the surface is anisotropic. The −5/3 slope of the Kolmogorov law does not fit the experimental spectra power (Kundu and Cohen, 2002) (Fig. 6a). At a lower relative-depth (z/H=0.13), instead the Kolmogorov law and experimental data fit well. This suggests that the flow field near the bottom is more isotropic in nature that the near-surface one.

In calm condition the FFT analysis does not show any significant peak (Fig. 6b).
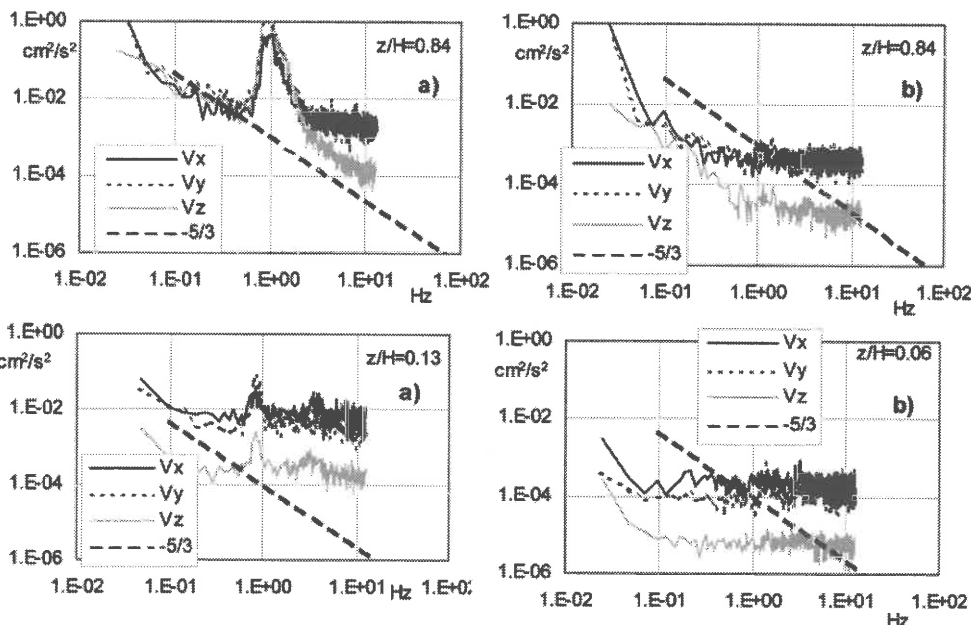
Figure 6. Power spectra of Vx, Vy and Vz for different relative depths under windy (a) and calm (b) conditions

WATER LEVELS IN THE LAGOON AND AT THE TWO MOUTHS

Tidal oscillations were recorded continuously at the Station 1 near the northern mouth. These oscillations have been filtered using a digital low-pass filter (1st order

Butterworth) using a cut-off frequency of 10^{-4} Hz . We assume that the Station 1 has recorded the tide levels because of its proximity to the open sea: thence, we also suppose that this signal is the same as that at the southern mouth. In line with the Newton theory, we observed the highest tide level occurring during the night when the meridian crossing the lagoon is internal to the moon-earth alignment.

In general, the comparison of water levels recorded near the mouths and those recorded in the inner stations shows that the water oscillations inside the lagoon are smaller than outside. Furthermore, there occurs a temporal shift between the water-level minima and maxima recorded in the two locations: the water-level peak near Mothia shows a time lag of about 30 minutes with respect the 'open sea' peaks, while the time lag of the minima increases up to 1 hour. This means that, when the water at the lagoon boundary is at its lowest level and the tide starts rising, the water level are still decreasing inside the lagoon.

RECORDS AT THE SOUTHERN MOUTH

As representative case, we report the velocities measured near the southern mouth (station 4) using the two-dimensional electromagnetic Velocimeter, in July 2004. The mean depth of Station 4 is 118 cm; the measurement point was located at 70 cm above the bottom (z/H=0.59) and the recording rate was 20 s. Fig. 7 shows two days of recordings: h is the depth of the pressure sensor below the free surface; Vx and Vy are positive eastwards and northwards respectively. Each of the three parameters shows a sinusoidal behaviour clearly related to the tide oscillations. The effect of wind waves is superimposed to the tide signals. A low-pass digital filter with cut-off frequency $6 \cdot 10^{-5}$ Hz has been applied to extract the some information on the mean flow.

The northward component Vy is strongly influenced by the tide: when tide enters the lagoon, Vy is positive: the opposite happens when the tide flows out. As recognized by other authors, the maximum velocities measurements are expected approximately when the water level takes minimum or maximum values (Leonard *et al.* 1995; Christiansen *et al.*, 2000).
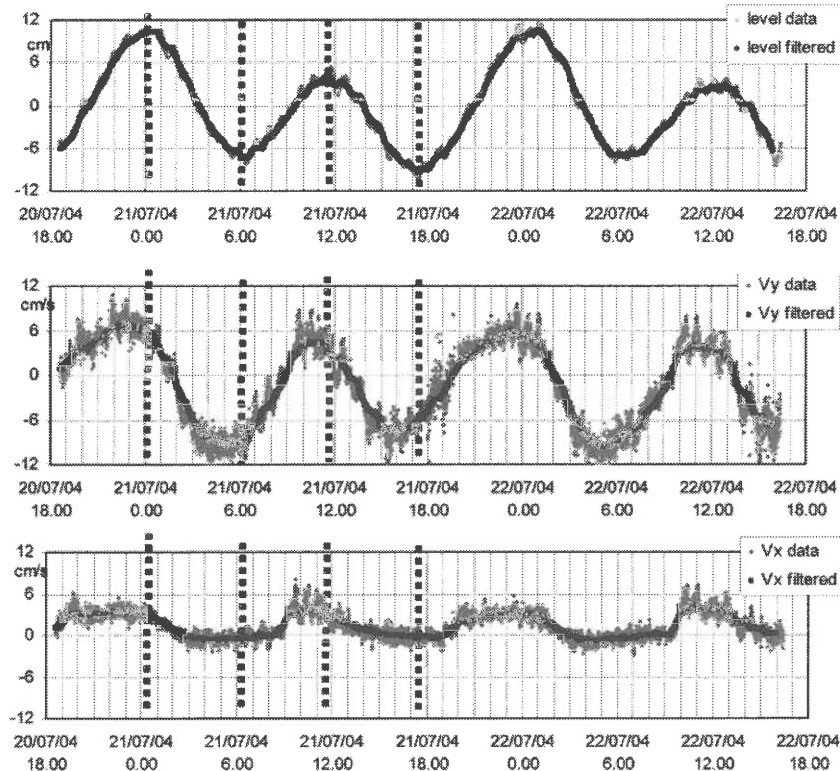
Figure 7. Levels and velocities in the southern Mouth (z=70 cm)

In our case, the levels and velocities are not in phase. When h reaches the maximum (e.g. 00:00 of 21 July, Fig. 7) and begins to decrease, Vy is still positive, which means water flowing northwards. This process carries on as long as the water level of the Southern mouth is larger than the one inside the lagoon.

Comparing the filtered water-oscillations h and the filtered Vy's at the southern mouth and near Mothia (sites 4 and 7), it is possible to recognise that, if the water level at the inner station is higher than that at the southern mouth, then the Vy values are negative, *i.e.* water is flowing out. The opposite occurs when the water level of the inner station is lower than at the lagoon boundary. An analogous behaviour has been recorded in the dredged channel at the northern mouth.

In the same station, under strong wind conditions (as during the night of the 18 dec. 2004) the instantaneous value of Vx increased whilst the mean values of Vy display lower values than the previous days characterised by low wind intensities. This could be explained by the fact that, when wind waves occur, the total kinetic energy and turbulence intensity increase. In this condition, the quantity of turbulent kinetic energy transferred from the mean flow and the large-scale turbulent structures

255

to the small-scale fluctuations increases. This causes the reduction of the kinetic energy of the mean flow field (Curto and Napoli, 2004). Other authors similarly explained the mean-flow deceleration as caused by the increase of turbulent intensity because of wind (Li and Zhang, 1996; Davies *et al.*, 1997).

CONCLUSIONS

During the three field campaigns performed in the *Stagnone di Marsala* lagoon, velocities and levels have been measured near the two mouths and within the lagoon and in the inner region. The levels oscillations recorded in these sites showed that the flow is governed by the difference between the inner points levels and the boundary levels. When the tide level is minimum at the two mouths and the tide starts rising, the water fluxes are still flowing out. This because the waters levels inside the lagoon are higher than the mouths levels. After a lag time, tide fluxes start flowing inside the lagoon. Because this time shift, the levels oscillations inside the lagoon are shorter than the one of the mouths.

The measured velocity profiles showed that, near the water surface, some fractions of water-current kinetic energy is related to the orbital eddies generated by the wind action. Part of this kinetic energy is then transferred to small vortices where it is dissipated and for this reason it is not available for the deeper layers.

As regards the mean flow field, that is the main field reproduced by numerical models, all the measurements showed that the trend of mean velocities is sinusoidal (with a semi-diurnal period) and strictly related with the tide oscillations. When wind waves occur, an orbital signal is superimposed on the tide signal, especially near the water surface.

When wind intensity increases over certain level, it is evident the increasing of signal amplitudes due to wind waves and, at the same time, a reduction of the mean flow. The reduction of the kinetic energy of the mean flow field, could be explained by the fact that, when wind waves occur, the total kinetic energy and turbulence intensity increase: in these conditions, the quantity of turbulent kinetic energy transferred from the mean flow and the large-scale turbulent structures to the small-scale fluctuations increases.

REFERENCES

BALZANO, A., CIRAOLO, G., NASELLO, C. Hydrodynamic Finite Element Numerical Simulations in a Shallow Coastal Lagoon of Sicily. Atti della *Fifth International Conference on Hydroinformatics*. Vol. 1, pp. 358-364. Cardiff (UK), July 1 –5, 2002.

CALVO, S., CIRAOLO, G., LA LOGGIA, G., MALTHUS, T. J., SAVONA, E. AND TOMA-SELLO, A. Monitoring posidonia oceanica meadows in the mediterranean sea by means of airborne remote sensing techniques. Second International *Airborne Remote Sensing Conference and Exhibition*. San Francisco, California, 24-27 June, 1996.

CHRISTIANSEN, T., WIBERG, P. L., MILLIGAN, T. G. Flow and Sediment Transport on a Tidal Salt Marsh Surface. *Estuarine, Coastal and Shelf Science* (2000) 50, 315–331.

CURTO, G. AND NAPOLI E. *Idraulica*. Vol. primo, Editoriale Bios, 2004.

DAVIES, A. M., JONES, J.E., XING, J. Review of recent developments in tidal hydrodinamic modeling. I: spectral models. *Journal of Hydraulic Engineering*, Vol. 123, No. 4, April 1997, pp. 278-292.

GHISALBERTI, M. AND NEPF, H.M. (2002). "Mixing layers and coherent structures in vegetated aquatic flows." *J. Geophys. Res.*, 107(C2),1-11.

LABVIEW 7.0: *User Manual*, National Instruments, April 2003.

LI, Y.S., AND ZHANG, M.Y. A semi-implicit three-dimensional hydrodynamic model incorporatine the influence of flow-dependent eddy viscosity, bottom topography and wave-current interaction. *Applied Ocean Research*. 18 (1996), 173-185.

LEONARD L.A., HINE A.C., LUTHER M.E., STUMPF, R.P., WRIGHT, E.E. Sediment Transport Processes in a West-central Florida Open Marine Marsh Tidal Creek; the Role of Tides and Extra-tropical Storms. *Estuarine, Coastal and Shelf Science* (1995) 41, 225–248.

LEONARD, L.A., REED., D.J. Hydrodynamics and Sediment Transport Through Tidal Marsh Canopies. *Journal of Coastal Research*. Special Issue 36, pp. 459-469, 2002.

KUNDU, P.K. Cohen I.M, *Fluid Mechanics*, Academic Press, 2002.

Nasello, C. and Ciraolo, G. Misure idrodinamiche nello Stagnone di Marsala. Atti del *XXIX Convegno di Idraulica e Costruzioni Idrauliche*. Trento, settembre 2004.

POPE, S. *Turbulent flows*. Cambridge University Press, 2000.

YANG, S.L. The Role of Scirpus Marsh in Attenuation of Hydrodynamics and Retention of Fine Sediment in the Yangtze Estuary. *Estuarine, Coastal and Shelf Science* (1998) 47, 227–233.

SPATIAL RESPONSE CALIBRATION
OF A MICRO FLUOROMETER

Fabian Wolk[1], Hidekatsu Yamazaki[2], Hua Li[3], Rolf G. Lueck[4]

(1) Rockland Oceanographic Services Inc., Victoria, British Columbia, V9A 4B6, Canada
(2) Department of Ocean Sciences, Tokyo University of Marine Science and Technology, Tokyo, 108-8477, Japan
(3) Alec Electronics Co. Ltd., Kobe, 651-2242, Japan
(4) School of Earth and Ocean Science, University of Victoria, Victoria, British Columbia, V8V 2Y2, Canada

ABSTRACT

This article describes an experimental method to establish the spatial resolution of bio-optical sensors. The spatial calibration method is demonstrated on an in-situ fluorometer that measures the structure of the fluorescence field at small spatial scales. To establish the size of the sampling volume and the amount of spatial averaging, the fluorometer and a fast response thermistor are towed repeatedly through a warm, fluorescent plume in a tow tank. The ratio of the measured fluorescence and temperature spectra determines the wavenumber response of the fluorometer. For the sensor used in this experiment, the measured spectral ratio is well described by the transfer function of a first order, low-pass filter with a half-power point at 22 cycles per meter. The equivalent spatial resolution is 7 mm. The transfer function model can be used to correct measured fluorescence spectra for the limited wavenumber response of the sensor.

OPERATING PRINCIPLE OF THE SENSOR

The high resolution optical sensor is an open-path fluorometer, which is deployed on free-falling profiling instruments (Wolk et al. 2002). Typical profiling speeds are 0.5 to 1 m s^{-1}. The sensor travels in the r-direction (Figure 1), which minimizes the distortion of the flow field due to flow blockage by the sensor housing.

A set of light emitting diodes produces the blue light required for fluorescence excitation (400 – 480 nm). The LEDs are arranged in a circle and are tilted 30° towards the centre of this circle so that their light beams intersect (Figure 1). The intersection of the light beams creates a nearly conical, blurred sampling volume in front of the receiver diode. The re-emitted light from fluorescent material is collected

by the receiver diode, located at the center of the diode circle. The receiver has an optical pass-band of 640 – 720 nm and an opening view angle of 45°. The point of the highest light intensity is 14 mm in front of the receiver diode, where the center lines of the excitation light beams intersect. The light intensity away from the intersection point decreases most strongly in the radial direction (r). The complex geometry of the light sources makes it difficult to analytically predict the shape and size of the sampling volume, both of which determine the amount of spatial averaging.
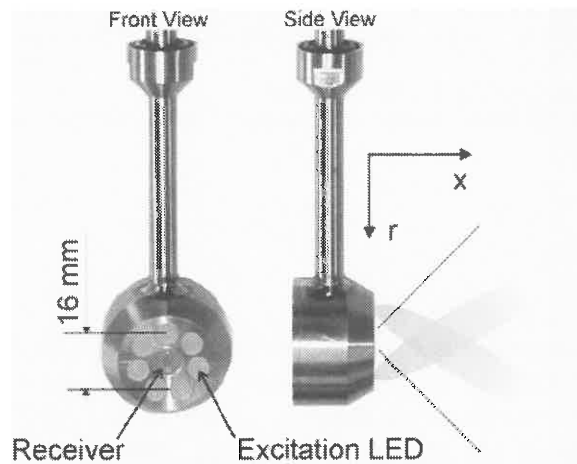

Figure 1. The front view of the sensor (left) shows the excitation LEDs and the center receiver LED. The side view (right) shows the approximate beam pattern for two of the excitation LEDs. The dashed lines indicate the receiver diode's field of view. During deployment, the sensor travels in the r-direction.

EXPERIMENTAL SETUP

To determine the composite spatial response of the sensor, the fluorometer signal was compared to that of a fast-response thermistor (Thermometrics FP07), for which the spatial response is known. Both sensors were mounted on a carriage and towed in a tank through a warm, fluorescent plume. The distance between the two sensors was 20 mm, while the sensing tip of the FP07 was within 5 mm of the center of the focal point of the light beams of the fluorescence sensor. As the carriage moved at a constant speed of 0.1 ms^{-1}, the fluorescent plume was created by pouring a stock solution of sodium fluorescein (concentration ~600 parts per billion) into the tank just in front of the moving carriage. The stock solution was heated to ~5 °C above the water temperature in the tank. Average frequency spectra for each experimental run were computed from the measured time series. Based on the sampling frequency ($F_s = 256\,\text{Hz}$) and the carriage speed, the resolved wavenumber range was between 0 and 1280 cpm.

260

RESULTS AND DISCUSSION

a. Spatial transfer function

In order to obtain the transfer function of the fluorescence sensor, it is assumed that (i) temperature variations can be used as a proxy tracer for variations fluorescein concentration, (ii) the transfer function of the temperature measurement system is unity.

With these assumptions, the spatial transfer function $H^2(k)$ of the sensor can be estimated from the ratio of the fluorescence and temperature spectra

$$H^2(k) = \Phi_{FF}(k)/\Phi_{TT}(k) \, , \qquad (1)$$

where $\Phi_{FF}(k)$ and $\Phi_{TT}(k)$ are the auto spectra of fluorescence and temperature, respectively, and k is the cyclic wavenumber given by $k = f/U$.
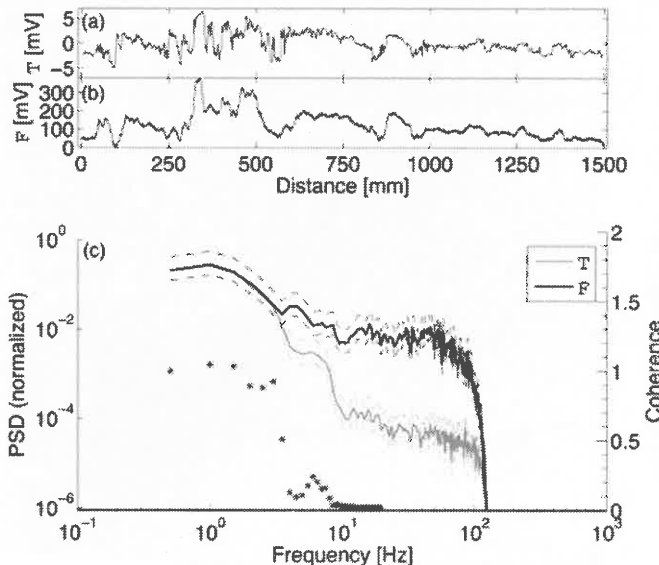

Figure 2. Time series of temperature (a) and fluorescence (b), and power spectral density (c) of fluorescence and temperature of run #4 of the tank experiment. The time series are shown as output by the data recorder, in units of mV. The spectra are normalized by their respective total power. The temperature spectrum is corrected for the frequency response of the FP07 sensor. The frequency dependent coherency between the F and T signals is shown as asterisks.

To account for response limitations of the temperature sensor, the temperature spectrum shown in Figure 2c is boosted by dividing the spectrum by the response function (Gregg, 1999)

$$H_{FP07}^2(f) = \frac{1}{[1+(2\pi\tau f)^2]^2},\tag{2}$$

where $\tau = 0.01\,\mathrm{s}$ is the time constant of the FP07 sensor.

A typical example of the signals and spectra of F and T is shown in Figure 2. The fluorescence signal traces the slowly varying part of the temperature signal, but small scale details of the temperature signal are not reflected in the fluorescence signal. The power spectra (Figure 2c) corroborate this observation; they agree at frequencies up to 3 Hz and deviate at higher frequencies. Both spectra flatten above 10 Hz, indicating the noise floor of their sensor-electronics systems. At ~80 Hz, the anti-aliasing filters of the recording systems sharply reduced the signal variances. The dashed lines indicate the approximate 95% confidence intervals for the spectra. The coherence spectrum, shows that the signals are coherent up to 3 Hz (or $k = 30$ cpm), which is equivalent to a length scale $L = k^{-1} = 0.033\,\mathrm{m}$. This length scale is consistent with the separation of the temperature and the fluorescence sensors (20 mm).
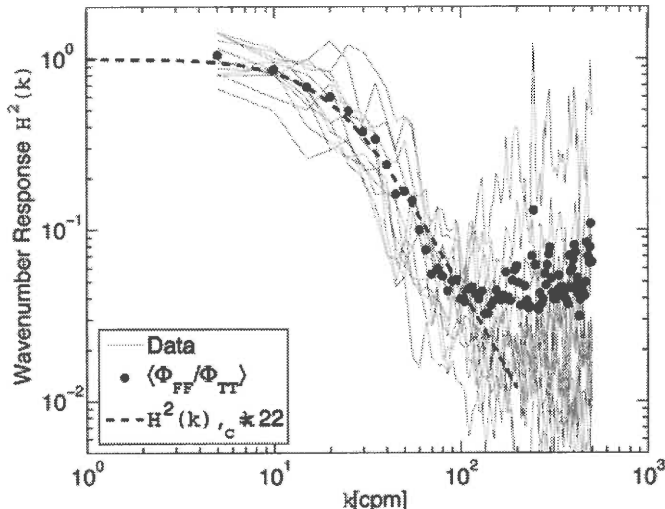

Figure 3. Average wavenumber response (●) and model (dashed line). The grey lines are the transfer functions from individual runs. Frequency is converted to wavenumber using $k = f/U$. The spectra are truncated at 400 cpm.

The transfer functions for eight experimental runs computed from (1) are shown in Figure 3. The average transfer function is well approximated by the filter model

262

$$H^2(k) = \frac{1}{1+(k/k_c)^{2N}},$$

(3)

with a half-power point at $k_c = 22$ cycles per meter (cpm) and $N = 1$. The parameters k_c and N were determined by minimizing the sum of the squared difference between the average transfer function and the model (3). This model is a first-order low-pass filter, or Butterworth filter. Since the transfer function is estimated based on the ratio of the output and input spectra of the measurement system (i.e., the sensor and its electronics), incoherent noise in the system introduces an asymptotic bias in the spectral ratio (1). This bias is evident in the measured transfer function above 100 cpm (Figure 3), i.e. where the dotted curve of the average transfer function flattens. Below 100 cpm (or 10 Hz) both $\Phi_{FF}(k)$ and $\Phi_{TT}(k)$ are clearly above the noise (Figure 2c) and so the asymptotic noise bias does not affect our transfer function estimate. The fitted transfer function model indicates a half-power point at 22 cpm, which is well below the wavenumber band affected by the bias. At 22 cpm the power of $H^2(k)$ is a factor 10 above the noise.

b. Averaging length scale

The 3 dB point of the transfer function (4) at $k_c = 22$ cpm determines a characteristic length scale over which the sensor will average in space. Intuitively, this "averaging scale" can be understood as the spatial scale below which the sensor will not be able to detect fluorescence variations. The transfer function model (3) describes a first-order system, for which

$$H^2(k) = \frac{1}{1+(k/k_c)^2} = \frac{1}{1+(kl_c)^2},$$

(4)

where $l_c = (2\pi k_c)^{-1}$ can be defined as a "response distance", analogous to a time constant τ for time-domain systems. By this definition, the "response distance" or averaging scale for the fluorometer, based on $k_c = 22$ cpm, is

$$l_c = \frac{1}{2\pi k_c} = 0.0072 \quad [\text{m}].$$

(9)

c. Spectra signal correction

The closed analytical form of the transfer function model (3) can now be easily used to correct measured fluorescence spectra for the effects of the sensor's spatial averaging. The response corrected spectrum Φ_{corr} is obtained by dividing the measured spectrum by the transfer function model, i.e.,

263

$$\Phi_{corr}(k) = \Phi_{FF}(k)\left[1 + (k/22)^2\right].$$

$$(10)$$

Because of the noise considerations discussed above, we recommend that such a correction should only be applied up to a maximum wavenumber. This maximum wavenumber depends on the concentration of the fluorescence in the sample. A high concentration improves the signal to noise ratio and pushes the point where the spectrum reaches the noise floor to higher wavenumbers.

ACKNOWLEDGEMENTS

REFERENCES

GREGG, M. C., 1999: Uncertainties and limitations in measuring ε and χ_T, J. Atmos. Ocean Tech., 16, 1483 – 1490.

WOLK, F., L. SEURONT, AND H. YAMAZAKI, 2001: Spatial resolution of a new micro-optical probe for chlorophyll and turbidity. J. Tokyo Univ. Fish., 87, 13–21

WOLK, F., H. YAMAZAKI, L. SEURONT, R. G. LUECK, 2002: A new free-fall profiler for measuring biophysical microstructure, J. Atmos. Ocean Tech., 19, 780 – 793.